

University of Sheffield

The University of Sheffield

Department of Civil and Structural Engineering

USE OF CEMENT BYPASS DUST AS A SUSTAINABLE CEMENT REPLACEMENT

A thesis presented for the degree of

Doctor of Philosophy in Civil and Structural Engineering

By

Ahmad Mahmoud Kobeiter Abiad

Supervisors:

Dr Kypros Pilakoutas

Dr Maurizio Guadagnini

Dr Hajime Kinoshita

January 2024

To my parents, thank you for your love, support and encouragement
To my brother, thank you for being my biggest source of inspiration
To my uncle, thank you for pulling me through my most difficult times
To all my family and friends who have supported me during my life

Table of Contents

Acknowledgements.....	xiviv
List of Abbreviations.....	xv
Abstract.....	xvi
Chapter 1 – Introduction	1
1.1 Background of the Research	1
1.2 Research Aims and Objectives.....	4
1.3 Research Significance	5
1.4 Outline of Thesis	5
Chapter 2 – Literature Review	7
2.1 Portland Cement.....	7
2.1.1 Manufacture of Portland Cement	7
2.1.2 CO ₂ Emissions Due to Cement.....	7
2.2 Supplementary Cementitious Materials	8
2.2.1 GBFS and Fly Ash.....	8
2.2.2 Metakaolin	8
2.3 Alkali Activated Materials	9
2.3.1 What is an AAM?	9
2.3.2 One-Part and Two-Part AAMs	9
2.3.3 Environmental Impact of AAMs	10
2.4 Cement Kiln Dust and Cement Bypass Dust	10
2.5 Cement Waste Dust Composition	13
2.6 Toxicity of CKD and CBPD	14
2.7 Fineness and Specific Gravity.....	14
2.8 Loss on Ignition.....	15
2.9 Uses of Cement Bypass.....	15
2.9.1 Soil Stabilisation.....	15

2.9.2 Land Application	16
2.10 Properties of CBPD Mortar/Concrete	17
2.10.1 Rheology and Setting Time	17
2.10.2 Strength of Binders	18
2.10.3 Durability of CBPD Mortar/Concrete	20
2.10.4 Shrinkage	21
2.10.5 Hydration	22
Chapter 3 – Effectiveness of Cement Bypass Dust in Heat and Ambient Temperature Cured Slag-Based Mortars	24
3.1 Introduction	25
3.1.1 Background.....	25
3.1.2 Cement Bypass Dust.....	25
3.2 Materials and Methods	27
3.2.1 Materials	27
3.2.2 Mortar Mixing Procedure	29
3.2.3 Characterisations	30
3.2.4 Life Cycle Assessment	32
3.3 Results and Discussion.....	32
3.3.1 Standard Consistency and Setting Time	32
3.3.2 Workability	33
3.3.3 Effect of heat curing on the volume of mortar samples	34
3.3.4 Bulk Density	35
3.3.5 Heat of Hydration	35
3.3.6 Compressive Strength.....	37
3.3.7 X-Ray Diffraction.....	38
3.3.8 Fourier Transform Infrared Spectroscopy	42
3.3.9 Differential Scanning Calorimetry	44

3.3.10 Thermogravimetric analysis	45
3.3.11 Mercury Intrusion Porosimetry	47
3.3.12 Scanning Electron Microscopy	48
3.4 Hydration Reaction	49
3.5 Life-Cycle Analysis Results.....	50
3.6 Technical Feasibility	51
3.7 Conclusions	52
Chapter 4 – The effect of CBPD Composition on the properties of Slag-based Mortars.....	54
4.1 Introduction	55
4.2 Experimental Work	58
4.2.1 Materials	58
4.2.2 Specimen Preparation	60
4.2.3 Test Methods	61
4.3 Results and Discussion.....	63
4.3.1 Flow Diameter, Standard Consistency and Setting Time.....	63
4.3.2 Heat of Hydration	64
4.3.3 Density and Ultrasonic Pulse Velocity	68
4.3.4 Compressive and Flexural Strength.....	69
4.3.5 XRD Analysis.....	72
4.3.6 FTIR Analysis.....	76
4.3.7 TGA/DTG Analysis.....	79
4.3.8 Chemical Shrinkage.....	84
4.3.9 Total Shrinkage.....	88
4.3.10 CBPD Classification.....	89
4.4 Conclusions	90
Chapter 5 – Carbon Curing of Cement Bypass Dust	92
5.1 Introduction	92

5.2 Methodology	95
5.2.1 Materials	95
5.2.2 Curing and Casting Procedure	96
5.2.3 Analytical Techniques	98
5.3 Results	99
5.3.1 Mass Gain	99
5.3.2 Density and Water Absorption	101
5.3.3 Compressive Strength.....	102
5.3.4 XRD.....	105
5.3.5 Thermogravimetric Analysis	107
5.3.6 Scanning Electron Imagery	112
5.3.7 Technical Feasibility.....	113
5.3.8 Sustainability	114
5.4 Conclusion.....	115
Chapter 6 – Mechanical and Durability Properties of Ternary Blends of Milled CBPD-GBFS- Metakaolin	117
6.1 Introduction and Background.....	118
6.1.1 Effect of Milling on CBPD.....	119
6.1.2 CBPD-Metakaolin Binders.....	119
6.1.3 Corrosion due to CBPD.....	120
6.1.4 Effect of Metakaolin on Corrosion Resistance.....	121
6.1.5 ASR in CBPD binders	122
6.1.6 ASR in Metakaolin Binders.....	122
6.2 Research Significance	123
6.3 Materials and Methodology	123
6.3.1 Material Properties	123
6.3.2 Mix Designs and Preparation	124

6.3.3 Experimental Methodology	125
6.4 Results	128
6.4.1 Effects on Milling on CBPD	128
6.4.2 Workability	131
6.4.3 Heat of Hydration	132
6.4.4 Density.....	133
6.4.5 Compressive Strength.....	134
6.4.6 X-Ray Diffraction.....	136
6.4.7 CBPD-Metakaolin Thermogravimetric Analysis	139
6.4.8 Total Shrinkage.....	141
6.4.9 Alkali-Silica Reaction.....	143
6.4.10 Corrosion Resistance	146
6.5 Conclusions	152
Chapter 7 – Life Cycle Assessment of CBPD Binders.....	154
7.1 Introduction	154
7.1.1 Background.....	154
7.1.2 Research Gap.....	154
7.2 Methodology	155
7.2.1 Mortar Mix Description.....	155
7.2.2 Life Cycle Assessment	155
7.3 Results	159
7.3.1 Compressive Strength of Binders	159
7.3.2 LCA Results	160
7.3.3 Cost Analysis.....	164
7.3.4 Total Efficiency	165
7.4 Conclusion.....	166
Chapter 8 - Conclusion and Recommendations.....	168

8.1 Introduction	168
8.2 Main Conclusions.....	168
8.2.1 Effectiveness of Cement Bypass Dust in Heat and Ambient Temperature Cured Slag-Based Mortars	168
8.2.2 The Effect of CBPD Composition on the Properties of GBFS-based mortars.....	169
8.2.3 Carbon Curing of CBPD-Slag Binders.....	170
8.2.4 Mechanical and Durability Properties of Ternary Blends of Milled CBPD-GBFS- Metakaolin	171
8.2.5 Life-Cycle Assessment of CBPD Binders.....	172
8.3 Recommendations for Future Research	173
References.....	175
Appendix.....	204
Appendix A: Chapter 3 Data	204
Appendix B: Chapter 4 Data.....	212
Appendix C: Chapter 5 Data	239
Appendix D: Chapter 6 Data	245

List of Figures

Figure 1-1 – Worldwide CO ₂ emission forecast from cement by 2050 (Global Carbon Budget, 2023)	1
Figure 1-2 – Expected CO ₂ reduction through different mitigation strategies (International Energy Agency and Cement Sustainability Initiative, 2018).....	2
Figure 1-3 - Yearly Scopus results for search terms 'Cement Kiln Dust' and 'Cement Bypass Dust' since 2015	4
Figure 2-1 - Cement kiln with bypass system showing location of CBPD and CKD (Global Cement and Concrete Association, 2020).....	11
Figure 2-2 - Estimated CKD and CBPD production since 2010 (Jaganmoham, 2024)	12
Figure 2-3 - Range of CBPD and CKD composition (Adaska & Taubert, 2008)	13
Figure 2-4 – Variation of loss on ignition with free lime (Todres et al., 1992).....	15
Figure 3-1 - Particle size distribution of GBFS, OPC and CBPD	28
Figure 4-1 – Graphical abstract presented in published journal paper	55
Figure 4-2 – XRD images of OPC, GBFS, CBPD R & CBPD L (l = lime, g = gypsum, s = sylvite, b = belite, a = alite, c = calcite, q = quartz and p = portlandite)	59
Figure 4-3 – Particle size of GBFS, OPC, CBPD R & CBPD L	60
Figure 4-4 – Relative change in flow of mix designs containing CBPD compared to OPC ...	63
Figure 4-5 – Heat of hydration for CBPD R, CBPD L & OPC pastes	65
Figure 4-6 - Heat of hydration for SB50R and SB50L.....	66
Figure 4-7 - Heat of hydration for SB30R and SB30L.....	67
Figure 4-8 – Heat of hydration for SB10R and SB10L	68
Figure 4-9 – Linear relationship between UPV and density showing a correlation of 99% ...	69
Figure 4-10 – Compressive strength results of all investigated mixes at 3, 7, 28 and 90 days	70
Figure 4-11 – Flexural strength results of all investigated mixes at 3, 7, 28 and 90 days.....	71
Figure 4-12 – XRD results of SB50R and SB50L (p = portlandite, c = calcite, e = ettringite, f = friedel’s salt, a = alite, q = quartz and s = syngenite).....	72
Figure 4-13 - XRD results of SB30R and SB30L (p = portlandite, c = calcite, e = ettringite, f = friedel’s salt and a = alite)	73
Figure 4-14 - XRD results of SB10R, SB10L and OPC (p = portlandite, c = calcite, e = ettringite, f = friedel’s salt, a = alite, g = gypsum and q = quartz)	74
Figure 4-15 – Simplified hydration model of CBPD-GBFS-OPC Binders (Jo et al., 2017)...	76
Figure 4-16 – FTIR results for SB50R and SB50L	77

Figure 4-17 – FTIR results for SB30R and SB30L	78
Figure 4-18 – FTIR results for SB10R, SB10L and OPC	79
Figure 4-19 - TGA results for the investigated mix designs (a) SB50R and SB50L (b) SB30R and SB30L (c) SB10R, SB10L and OPC.....	80
Figure 4-20 – DTG results for the investigated mix designs (a) SB50R and SB50L (b) SB30R and SB30L (c) SB10R, SB10L and OPC.....	82
Figure 4-21 – CBPD R, CBPD L and OPC chemical shrinkage results.....	85
Figure 4-22 – SB50R and SB50L chemical shrinkage results.....	86
Figure 4-23 – SB30R and SB30L chemical shrinkage results.....	87
Figure 4-24 - SB10R, SB10L and OPC chemical shrinkage results.....	87
Figure 4-25 - Total shrinkage strains for all investigated mix designs.....	88
Figure 5-1 - Publications related to carbon curing of cement since 2015	92
Figure 5-2 – Particle size of raw materials	95
Figure 5-3 - XRD patterns of raw materials (p=portlandite, q = quartz, g = gypsum, b = belite, l = lime, a = alite, s = sylvite, c = calcite).....	96
Figure 5-4 - Carbonation curing set-up.....	97
Figure 5-5 - Mass gain over time of SB50L	100
Figure 5-6 - Water absorption over time of the specimens.....	101
Figure 5-7 - Density results for CBPD and control mix at 28 days.....	102
Figure 5-8 - Compressive strength results	103
Figure 5-9 - Correlation between mass and strength gain (%)	104
Figure 5-10 - XRD patterns for SB50L and SB50L-C (c = calcite, p = portlandite)	105
Figure 5-11 - XRD patterns for SB50R and SB50R-C (c = calcite, p = portlandite).....	106
Figure 5-12 - XRD patterns of OPC and OPC-C (c = calcite, p = portlandite).....	107
Figure 5-13 – TGA results of SB50L and SB50L-C	108
Figure 5-14 – TGA results of SB50R and SB50R-C.....	109
Figure 5-15 – TGA results of OPC and OPC-C	109
Figure 5-16 – DTG results of SB50L and SB50L-C	111
Figure 5-17 – DTG results of SB50R and SB50R-C.....	111
Figure 5-18 – DTG results of OPC and OPC-C	112
Figure 6-1 - Chloride content in CBPD from different sources of literature.....	121
Figure 6-2 – XRD of CBPD, metakaolin, GBFS, and OPC (p = portlandite, q = quartz, g = gypsum, s = sylvite, l = lime, c = calcite, b = belite, a = alite, i = illite, m = muscovite, k – kaolinite).....	123

Figure 6-3 - Total shrinkage testing using a length comparator	126
Figure 6-4 - Bars cast for ASR testing	127
Figure 6-5 – Particle size distribution of CBPD at different milling times	129
Figure 6-6 - X-Ray diffraction of milled CBPD and unmilled CBPD	130
Figure 6-7 - Diffractograms showing peak reduction after milling (A) calcite (B) gypsum.	130
Figure 6-8 - Heat of hydration for SB50 vs SB50M.....	132
Figure 6-9 - Heat of hydration for metakaolin CBPD binders.....	133
Figure 6-10 - Percentage strength increase of mix designs between 7 and 28 days.....	135
Figure 6-11 - Relationship between density and compressive strength.....	136
Figure 6-12 - Diffractogram for SB50 and SB50M (e = ettringite, p = portlandite, a = alite, q = quartz, s = syngenite, f = friedel's salt and c = calcite).....	137
Figure 6-13 – XRD patterns SB50M, SB50M 10MK & SB50M 20MK at 7 days (a) 5-60° (b)17-19° (e = ettringite, p = portlandite, a = alite, q = quartz, s = syngenite, f = friedel's salt and c = calcite).....	138
Figure 6-14 – XRD patterns SB50M, SB50M 10MK & SB50M 20MK at 28 days (a) 5-60° (b) 17-19° (e = ettringite, p = portlandite, a = alite, q = quartz, s = syngenite, f = friedel's salt and c = calcite).....	139
Figure 6-15 - TGA of the investigated mix designs	140
Figure 6-16 - DTG results for investigated mix designs (a) 35-1000°C (b) 350-500°C.....	141
Figure 6-17 – Drying shrinkage of SB50 and SB50M binders.....	142
Figure 6-18 – Drying shrinkage of CBPD-GBFS-metakaolin binders and OPC	143
Figure 6-19 - ASR expansion of OPC, SB50M, SB50M 10MK, and SB50M 20MK	144
Figure 6-20 - XRD of pastes submerged in NaOH and water (a) OPC (b) SB50M (c) SB50M 10MK (d) SB50M 20MK.....	145
Figure 6-21 - Minor corrosion due to water curing	146
Figure 6-22 – View of the external corrosion of the prisms	147
Figure 6-23 - Corrosion of prisms (a) near surface corrosion of fibres (b) cross-sectional view	147
Figure 6-24 - SB50M following 8 months of corrosion	148
Figure 6-25 - SB50M showing signs of rust in the centre of the prism.....	148
Figure 6-26 - Compressive strength of mixes following corrosion simulation at 4 and 8 months.....	149
Figure 6-27 - Flexural strength of mixes following corrosion simulation at 4 and 8 months.....	150

Figure 6-28 - Residual strength of main mixes following corrosion simulation at 4 and 8 months (a) SB50M (b) OPC (c) SB50M 10MK (d) SB50M 20MK.....	151
Figure 7-1 – Cradle to gate system boundary of CBPD-GBFS-OPC mix.....	156
Figure 7-2 - Mechanical efficiency scores.....	160
Figure 7-3 (a) GWP of OPC and AAM (b) contribution of inputs.....	160
Figure 7-4 - (a) GWP of CBPD-GBFS, CBPD-GBFS and milled CBPD mixes (b) Contribution of inputs.....	161
Figure 7-5- (a) GWP of CBPD-metakaolin mixes (b) Contribution of inputs	162
Figure 7-6 – (a) GWP of the studied binders (b) Efficiency of CBPD binders vs OPC.....	162
Figure 7-7 - Normalised impact scores of CBPD binders relative to OPC	163
Figure 7-8 - (a) Cost efficiency (b) Contribution of inputs to cost.....	164
Figure 7-9 - Total efficiency of CBPD binders relative to OPC.....	166

List of Tables

Table 3-1 - Mix designs investigated.....	29
Table 3-2 - Life cycle inventory	32
Table 3-3 – Setting times and standard consistence of CBPD binders.....	33
Table 3-4 - Overall densities of CBPD binders at 3,7 and 28 days	35
Table 3-5 – Location of functional groups on the FTIR spectra.....	44
Table 4-1 – Peak areas of main peaks for CBPD R and CBPD L determined using peak deconvolution.....	58
Table 4-2 – Mix Design. Sample ID: S refers to Slag, B refers to Bypass Dust. The number refers to the quantity of each (50 = 50% Slag and 50% Bypass Dust). R and L refer to CBPD from Rugby and Latvia, respectively	61
Table 4-3 – Standard consistencies, setting times and flowability of all the investigated mix designs.....	64
Table 4-4 – UPV and Density results of all the investigated binders	69
Table 4-5 – Main peak area ratio for all investigated mix designs at 28 days determined using peak deconvolution of main peaks.....	75
Table 4-6 - Functional groups classification for the FTIR results for all mix designs	76
Table 5-1 – Mix designs investigated	96
Table 5-2 - Mass gain of SB50L with different W/C ratios	99

Table 5-3 – Mass gain of each mix design after CO ₂ mass gain	100
Table 5-4 – Density increase of the CO ₂ cured mixes relative to non-CO ₂ cured mixes	102
Table 5-5 – Strength increase of the CO ₂ cured mixes relative to non-CO ₂ cured mixes	104
Table 5-6 – Peak quantification of calcite and portlandite	107
Table 5-7 - TGA mass loss results	110
Table 6-1 – Mix designs investigated	124
Table 6-2 – Gradation of the aggregate used for durability tests.....	127
Table 6-3 - Flow diameter, standard consistency, and density of investigated mix designs .	131
Table 6-4 – Compressive strength of investigated binders	134
Table 7-1 – Investigated mix designs	155
Table 7-2 – GWP and transport data of the raw materials investigated	157
Table 7-3 – Compressive strength results	159
Table 7-4 – Cost of the investigated binders	164
Table A.3-0-1 - KGA strength and density results	208
Table A.3-0-2 - KGH strength and density results	208
Table A.3-0-3 - KGCA strength and density results.....	209
Table A.3-0-4 - KGCH strength and density results.....	209

Acknowledgements

Firstly, I would like to express my deepest gratitude to my supervisors, Professor Kypros Pilakoutas, Dr Maurizio Guadagnini, and Dr Hajime Kinoshita, for their continued support, patience, and advice.

I would like to thank the Engineering and Physical Sciences Research Council (EPSRC) for funding my research which allowed me to carry out my PhD.

A special thank you to all the technical staff in all the many labs I have had the pleasure to work in. Particularly Kieran Nash and Samuel Gibson, who despite their busy schedules and difficult jobs, always found the time to help me with my work.

I would like to thank all the former and current researchers that are part of the Concrete and Earthquake Engineering research group. I appreciate the wonderful time and discussions we have had together. I would also like to thank all my friends who have helped me through my PhD journey.

Finally, my deepest thanks to my family, who I owe everything to.

List of Abbreviations

OPC	Ordinary Portland Cement
GBFS	Ground Granulated Blast Furnace Slag
CBPD	Cement Bypass Dust
CKD	Cement Kiln Dust
ASTM	American Society for Testing and Materials
XRD	X-Ray Diffraction
TGA	Thermogravimetric Analysis
FTIR	Fourier Transform Infrared Spectroscopy
SEM	Scanning Electron Microscopy
MIP	Mercury Intrusion Porosimetry
CSH	Calcium Silicate Hydrate
LCA	Life Cycle Analysis
AAM	Alkali Activated Materials

Abstract

Cement bypass dust (CBPD) is a waste dust extracted from rotary cement kilns at around 2% of cement clinker by weight. CBPD is often landfilled due to its excessive contents of chlorides, sulphates, and high alkalinity, at high monetary and environmental cost. Due to its high pH and lime content, it is hypothesized that CBPD could be used as a cement replacement with activating potential to make a sustainable binder. The aim of this research is to create a sustainable binder composed of CBPD and pozzolanic materials that can perform similarly to OPC. This was achieved through extensive lab work, including a thorough microstructural analysis to properly characterise the behaviour of binders.

Preliminary investigations showed that ambient temperature cured binders composed of CBPD and granulated ground blast furnace slag (GBFS) at ratios of 1:1 are possible. Heat curing proved to worsen the long-term strength benefits of CBPD binders, leading to lesser hydration products and a more porous microstructure. This is primarily due to accelerated hydration leading to uneven reaction products and consequently a less dense microstructure. Results also indicated that the inclusion of 20% cement content enhanced properties such as strength and workability.

Further research investigated the differences between CBPDs sourced from different locations. It was found that CBPDs with high free lime contents lead to deleterious expansion causing poor mechanical properties. It was also identified that the strength of CBPDs largely comes from its ettringite content. Following this, research involving carbonation curing revealed that the free lime content of CBPDs can be exploited due to the reaction of lime and CO₂. Thus, the properties of the lime rich CBPD binders were significantly enhanced relative to the sulphate rich CBPD. This showed that different forms of curing may be more suitable for different types of CBPD.

A milled CBPD mix composed of 10% metakaolin, 45% CBPD and 45% GBFS showed optimum mechanical and durability properties outperforming the control cement mix. CBPD mixes generally outperformed OPC when tested for alkali-silica reaction. Chlorides from CBPD binders did not cause any significant corrosion to steel fibres. Life cycle analysis indicates that all the studied binders had significantly less global warming potential than OPC.

This work shows that a cementless, environmentally friendly binder that can perform similarly to OPC is possible with CBPD. This can lead to reductions in landfilling and to make cement manufacture overall more efficient and less polluting.

Chapter 1 – Introduction

This chapter gives the background, aims and objectives of the study and the layout of the thesis.

1.1 Background of the Research

Rapid population growth and urbanization have increased massively the demand for construction materials, particularly concrete, which uses Portland cement as its main binder. Currently, about 25 billion tonnes per annum of cement are produced worldwide (US Geological Survey, 2020) and that contributes to circa 8% of the world’s anthropogenic carbon dioxide emissions (Habert and Ouellet-Plamondon, 2016). Global cement production is forecast to increase between 12-23% by 2050 (IEA, 2018). The total CO₂ emissions of cement were of 1.7 billion tonnes in 2021 with projections showing a steep rise by 2050 as reflected in Figure 1-1 (Global Carbon Budget, 2023).

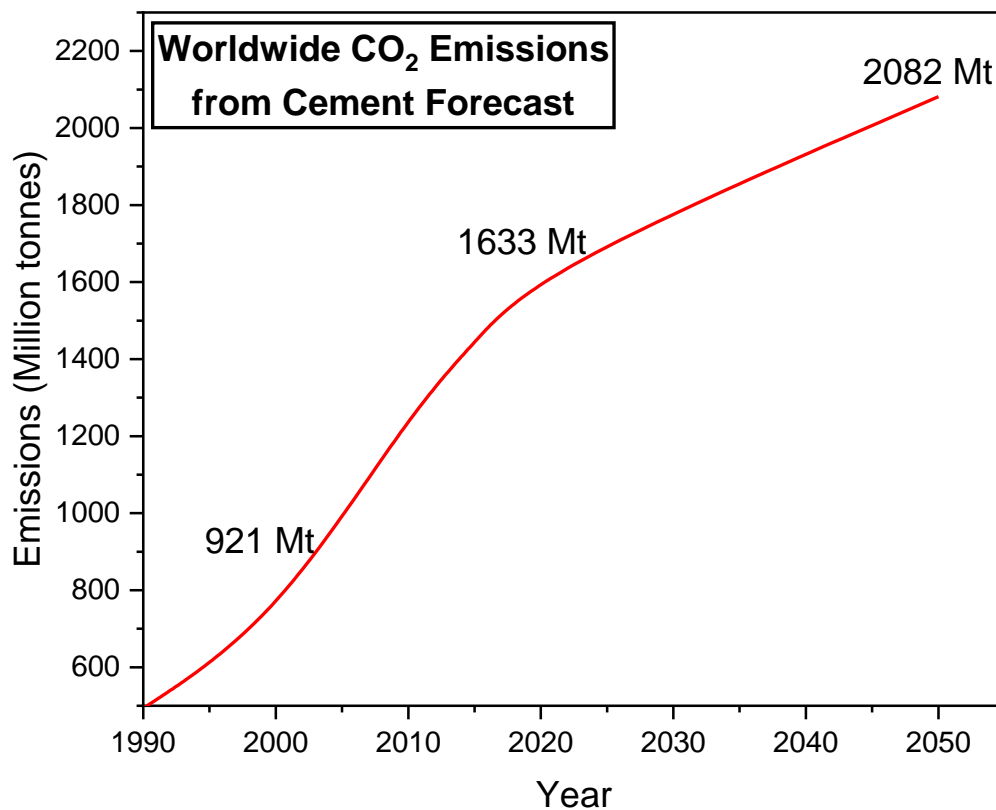


Figure 1-1 – Worldwide CO₂ emission forecast from cement by 2050 (Global Carbon Budget, 2023)

In 2008, the UK introduced the Climate Change Act which was the first ever legally binding framework for tackling climate change. This act set to cut greenhouse gas emissions by 34% by 2020 and 80% by 2050 relative to 1990 levels. This policy was updated in 2019 where the Committee on Climate Change (CCC) set a target of ‘net zero’ greenhouse gas emissions by

2050 (Climate Change Act, 2008). To meet new national and international targets to lower carbon dioxide emissions, the construction industry urgently needs to act.

Figure 1-2 identifies three scenarios that indicate environmental steps that can be taken to limit global temperatures to an increase of 2°C (International Energy Agency and Cement Sustainability Initiative, 2018). These scenarios are a) reference technology scenario, b) two-degree scenario, and c) beyond two-degree scenario. This illustrates how challenging it is to achieve this ‘net zero’ carbon goal, but it is clear from the graph how imperative it is to reduce the usage of clinker in building materials.

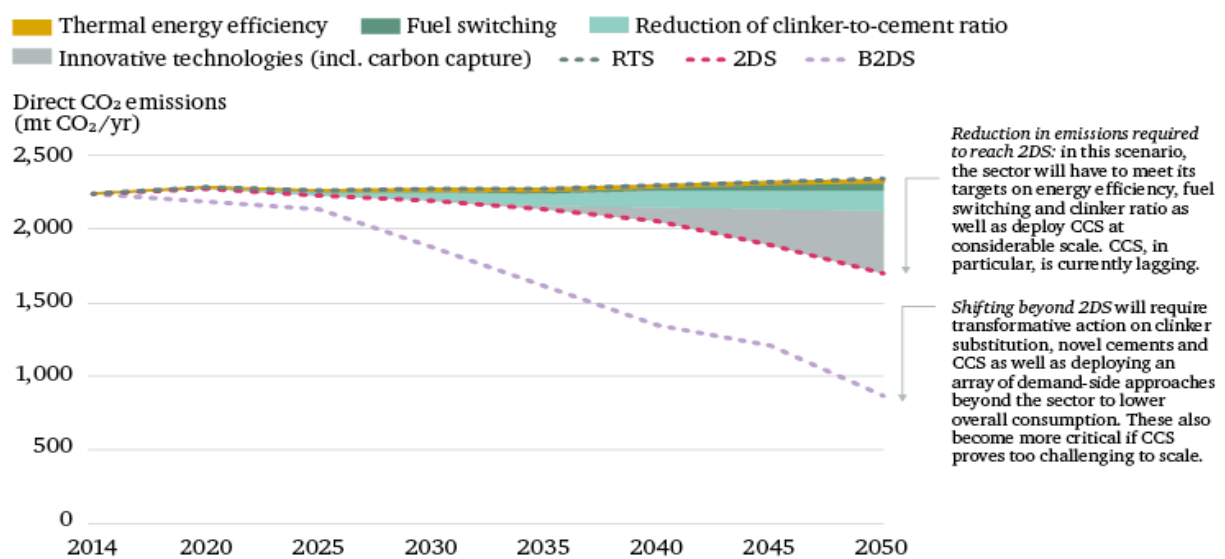


Figure 1-2 – Expected CO₂ reduction through different mitigation strategies (International Energy Agency and Cement Sustainability Initiative, 2018)

OPC is made by heating a mix of raw materials in a kiln at about 1450°C. The main source of carbon dioxide emissions in concrete lies in the cement production process, more specifically the decalcination process of limestone. This leads to the decomposition of limestone producing calcium oxide, one of the main components of cement, and carbon dioxide.

A promising method for reducing global cement use involves alkali-activated materials (AAMs). AAMs are formed by reacting a solid aluminosilicate powder (precursor) with a dissolved alkali metal (activator). Common precursors include ground granulated blast-furnace slag (GBFS), fly ash, silica fume, and metakaolin (Fernández-Jiménez, 2017), with GBFS, fly ash, and silica fume being readily available (Provis, 2014). Typical activators are sodium hydroxide and sodium silicate, though other alkalis may be used (Provis, 2014). A key drawback to AAMs is the environmental impact of alkali activators, particularly sodium

silicate, which has a high global warming potential. Life cycle assessments show varying emission reductions for AAMs, highlighting the need for more sustainable alternatives (Habert and Oullet, 2016; Habert and Oullet, 2015).

CKD (cement kiln dust) and CBPD (cement bypass dust) are waste dusts that have high alkalinity and could be used as alkali activators and cement replacements. The differences between both materials will be discussed in Chapter 2. Figure 1-3 shows the documents found through the Scopus search engine when searching for the key words ‘cement kiln dust’ and ‘cement bypass dust’. In total, 143 and 6,025 documents were found for cement bypass dust and cement kiln dust, respectively, since 2015. The trend indicates that these wastes are becoming more researched through the years. Despite this, there is still a long way to go to fully understand and standardise these materials.

Cement Bypass Dust (CBPD) is a waste product that is generated during the clinker manufacturing process. This material is characterised by having a significant amount of alkalis, sulphates and chlorides leading it to be mainly disposed of in landfills. Very few efforts have been made to utilise CBPD with a combination of other industrial by-products, such as fly ash and slag, to develop a binder for sustainable concrete. Limited research (Barnat-Hunek et al., 2018) has shown that there is potential for CKD to act as an alkaline activator and as a cement replacement, however much more work is required on CBPD. The current state of the research in this field is presented in Chapter 2 of this thesis.

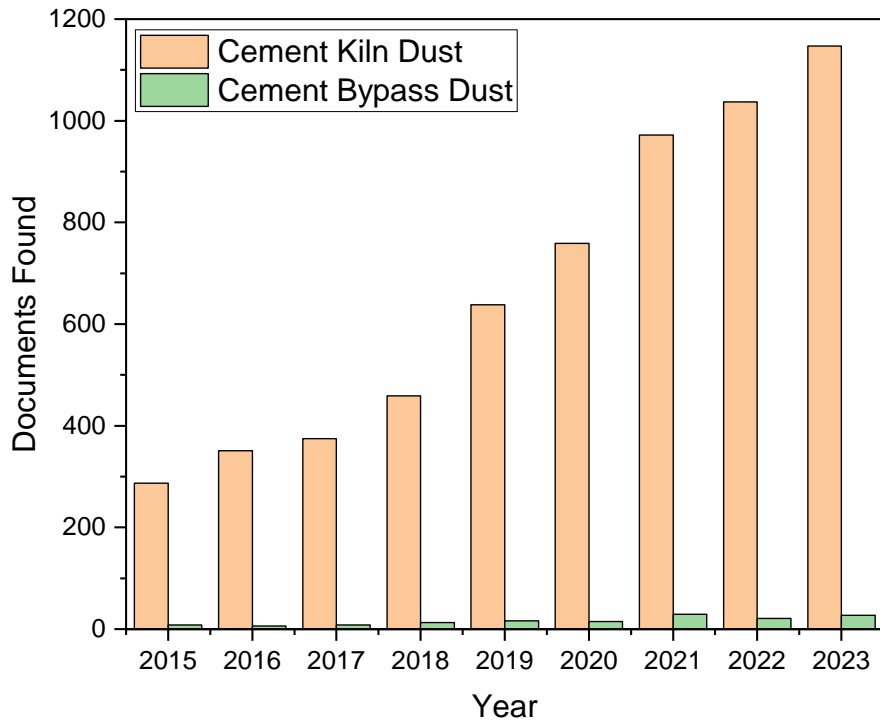


Figure 1-3 - Yearly Scopus results for search terms 'Cement Kiln Dust' and 'Cement Bypass Dust' since 2015

1.2 Research Aims and Objectives

The aim of this project is to study the potential of CBPD as cement replacement with potential to activated pozzolanic materials to achieve a sustainable, cementless mix with suitable physical, mechanical, and durability properties that can be comparable to OPC. Generally, mortars and pastes were tested, and the results were used to make recommendations on the binders used.

The following objectives are set for this project:

- 1) Develop CBPD based pastes and mortars in combination with GBFS, metakaolin and cement, and evaluate their fresh and hardened state properties including setting time, workability, heat of hydration, standard consistency, density, compressive strength, and flexural strength.
- 2) Examine the hydration mechanism and microstructural characteristics of the CBPD binders through different analysis techniques such as X-Ray Diffraction (XRD), Scanning Electron Microscopy (SEM), Thermogravimetric Analysis (TGA), and Fourier Transform Infrared Spectroscopy (FTIR).

- 3) Examine different curing techniques for CBPD binders such as heat curing, ambient temperature curing, and carbon curing.
- 4) Examine the durability properties of CBPD based paste and mortars by investigating drying and chemical shrinkage, corrosion, and alkali silica reaction.
- 5) Demonstrate the environmental credentials of the new binders through a lifecycle assessment (LCA) and an efficiency study.

1.3 Research Significance

Extensive research has already been carried out on the development of AAMs using waste materials; however, difficulties arise due to the required complex production processes. Furthermore, there is uncertainty regarding carbon footprints of AAMs, primarily due to their alkali activator. This work addresses the knowledge gaps on cementitious binders activated by CBPD and evaluates the mechanical and durability properties of these novel binders. The use of waste materials and industrial by-products, such GBFS and CBPD, will contribute to the development of a sustainable alternative to OPC, with a just-add-water formulation. This will bring a tremendous environmental advantage considering that CBPD is a waste material, since it will have much lower CO₂ to AAMs and can provide an alternative to landfilling of this waste dust.

1.4 Outline of Thesis

This thesis consists of eight chapters. Three chapters (Chapters 3, 4 and 6) have been prepared as standalone research journal papers (ready to be submitted to peer-reviewed journals), while the remaining chapters are presented following a conventional thesis format. Additional information is provided in the appendices.

Chapter 2: This chapter presents a review of the relevant literature used for this research.

Chapter 3 (Paper-based): *“Effectiveness of Cement Bypass Dust in Heat and Ambient Temperature Cured Slag-Based Mortars”*. The research explores the nature of CBPD and the difference between heat-curing and ambient temperature curing of binders composed of CBPD-GBFS and CBPD-GBFS-OPC. It aims to identify if a cementless binder composed of GBFS and CBPD can be made. This study lays the groundwork for the additional work carried out in this research project and presented in the following chapters.

Chapter 4 (Paper-based): *“The effect of CBPD Composition on the properties of Slag-based Mortars”*. This research discusses the differences between two types of CBPD by examining

the fresh and mechanical properties, as well as shrinkage. It also explores the microstructure of the different materials to identify the different properties and potential applications of CBPDs.

Chapter 5: “*Carbon-Curing of CBPD*” provides further research on the CBPD binders from Chapter 4. This research explores accelerated carbon-curing of CBPD binders and their potential for carbon capture.

Chapter 6 (Paper-based): “*Mechanical and Durability Properties of Ternary Blends of Milled CBPD-GBFS-Metakaolin*”. This research explores the milling of CBPD and use of metakaolin in GBFS-CBPD binders. It examines mechanical properties, hydration, and durability. This research aims to identify if CBPD binders can be made in a way that is comparable to OPC.

Chapter 7: “*Life Cycle Assessment of CBPD Binders*” explores the sustainability of the examined binders and compares them to OPC. Through the analysis of cost, strength and global warming potential, the efficiency of each binder relative to OPC is also assessed.

Chapter 8: This chapter presents the conclusions drawn from the entire research and presents recommendations for future work.

References: All the references used for this thesis can be found after chapter 8.

Appendix: Supplementary data that could not be included in the main body of the thesis will be found in the appendix.

Chapter 2 – Literature Review

This chapter focuses on the current state of research of CBPD and its uses. This helps identify the current gaps in knowledge and the need for this research.

2.1 Portland Cement

2.1.1 Manufacture of Portland Cement

The raw materials for cement manufacture are a mixture of limestone and clay, containing approximately 75% calcium carbonate, 15% silicon dioxide, 3% aluminium oxide, and 2% iron oxide. Portland cement also has many minor constituents that make up less than 5% of its weight including magnesium, sulphur, and potassium (Santagata et al., 2006). The limestone and clay are obtained by blasting rock quarries using explosives. The large, fragmented rock is then transported to the cement plant where it is crushed and pounded until it is about four centimetres in size. The raw material is placed in silos, so that it can be added in specific amounts depending on the type of cement that is being produced. For further processing the raw material is grinded within a vertical steel mill, where the pressure exerted is from three conical steel rollers and horizontal mills. Following pulverisation, the raw meal is homogenised within a silo. The material is then ready to be calcined in a rotary kiln (CEMEX, 2020). The rotary kiln produces cement and waste dusts.

2.1.2 CO₂ Emissions Due to Cement

The global cement industry is responsible for approximately 8% of global CO₂ emissions which accounts for 0.5-0.6 tons of CO₂ per ton of cement production (Hanifa et al., 2023) Since the beginning of the 21st century, global cement emissions have almost tripled and have increased sixfold since 1990 (Science & Nature, 2022). The main causes of these emissions are the following:

- 1) Calcination – Decomposition of Limestone into Calcium Oxide and Carbon Dioxide
- 2) Kiln – Combustion of fuel in the kiln
- 3) Other – Manufacturing operations, milling and transportation

Worldwide, the main contributors are dominantly China, followed by India, Europe, and the United States (Mohamad et al., 2022). Several technologies are currently being tested to mitigate these emissions.

2.2 Supplementary Cementitious Materials

2.2.1 GBFS and Fly Ash

Supplementary cementitious materials (SCMs) are materials added in different quantities to cementitious blends due to increased durability, improved mechanical properties, recyclability and more. The most common SCMs are fly ash, granulated blast furnace slag (GBFS), and other natural pozzolans such as metakaolin.

Fly ash is a by-product of the coal industry, with an estimated 500 million tonnes being produced annually (Mathapati et al., 2022). An inert material, fly ash is very typically recycled into concrete at dosages ranging from 15-20% by mass of cementitious binder giving beneficial effects on economy, cost, and durability (Wang et al., 2004).

GBFS is a by-product of the steel industry, which has been shown to develop excellent cementitious properties when combined with OPC (Hwang et al., 1986) due to its calcium content and reactivity among other factors. GBFS can substitute cement up to 95% by mass in concrete in CEM III type cement (EN-197, 2000).

An environmental evaluation by Turk et al. (2015), assessed the environmental performance of several green concretes and found that fly ash and slag concretes had a reduced impact of 25% and 5%, respectively. Due to their classification as by-products, rather than waste, they have CO₂ emissions associated with them.

2.2.2 Metakaolin

Metakaolin is a form of calcined clay formed through the calcination of kaolin clay at temperatures up to 800°C (Siddique & Klaus, 2009). Due to this calcination, it has higher associated emissions than other SCMs (Heath et al., 2014). It is a natural material rather than a by-product, which differentiates it from GBFS and fly ash.

The effect of metakaolin replacement on mortars and concretes has been studied extensively in the past. Bredy et al. (1988) investigated the microstructure and porosity of metakaolin-OPC pastes with up to 50% metakaolin content by mass. The compressive strength results showed improvements of up to 90%, however at higher replacements (40-50%) the strength gain over time was no longer appreciable. This is due to some metakaolin remaining unreacted and only acting as filler. The main reaction that takes place is between the portlandite and the metakaolin, and at 50% replacement there isn't sufficient portlandite to react with all the metakaolin. Poon et al. (2001) studied the strength of cement paste replaced between 5-20%

by metakaolin and found improvements at all replacement levels relative to the control, with the replacement level of 10% achieving the highest strength. The metakaolin was shown to benefit the early age strength the most due to its high initial reactivity. This was also shown to lead to a lower porosity overall. Guneyisi et al. (2007) investigated the effect of cement replacement with metakaolin on strength, drying shrinkage, and pore structure of concrete. Their results found up to a 30% increase in strength and a remarkably lower shrinkage for cements with up to a 20% replacement level. This was attributed to both due to physical and chemical effects. The physical effect was due to the fineness of the material filling voids and densifying the microstructure of the concrete matrix. The chemical effect was attributed to a faster reaction of water with metakaolin. Furthermore, during the chemical reaction the calcium hydroxide is precipitated into secondary CSH leading to a more refined pore structure and less portlandite.

2.3 Alkali Activated Materials

2.3.1 What is an AAM?

Alkali Activated Materials (AAMs) offer a promising solution for reducing global cement consumption by utilizing aluminosilicate precursors like ground granulated blast-furnace slag (GBFS), fly ash, silica fume, and metakaolin (Fernández-Jiménez et al., 2017). Common activators include sodium hydroxide and sodium silicate, though other alkali forms such as hydroxide, carbonate, and sulphate can be used (Provis, 2014). AAMs aim to enhance both sustainability and mechanical performance, with advantages like fire resistance (Abd-Razak et al., 2022), reduced shrinkage (Sagoe-Crentsil et al., 2013), and potentially higher strength compared to Ordinary Portland Cement (OPC). Depending on the activator's condition, AAMs can be categorized as one-part or two-part systems.

2.3.2 One-Part and Two-Part AAMs

One-part Alkali Activated Materials (AAMs) offer an innovative approach by using a dry mix of solid alkaline activators, aluminosilicates, and water, simplifying application and integration with current cement production processes. Askarian et al. (2019) achieved a 28-day compressive strength of 38 MPa using calcium hydroxide and sodium silicate, while Nematollahi et al. (2017) developed a fiber-reinforced AAM reaching 52.5 MPa with sodium metasilicate. Similarly, Matakah et al. (2017) reported 35 MPa strength with fly ash-based one-part AAMs using calcium oxide, sodium hydroxide, and magnesium oxide. Refining one-part AAMs for improved fluidity, strength, and durability remains a focus (Ma et al., 2019).

Habert et al. (2015) highlighted their potential due to manufacturing similarities with Ordinary Portland Cement (OPC) and lower global warming potential.

Two-part AAMs combine a concentrated alkaline solution with a solid aluminosilicate precursor (Provis & van Deventer, 2014). This method has industrial applications, such as the 70,000 tonnes of AAM concrete used at Brisbane Airport in 2014, praised for its strength and low shrinkage (Geopolymer Institute, 2014). Despite successful use, handling concentrated solutions on-site limits two-part AAMs to precast applications. Research is underway to develop dry powder-based binders, similar to OPC production (Luukkonen et al., 2018).

2.3.3 Environmental Impact of AAMs

The environmental impact of Alkali Activated Materials (AAMs) compared to Ordinary Portland Cement (OPC) has shown mixed results in research. Studies like Turner and Collins (2013) and Weil et al. (2006) report CO₂ emission reductions for AAMs ranging from 10% to 70%, depending on factors like curing methods and precursor types (Yang et al., 2013). However, AAMs' environmental footprint extends beyond CO₂ emissions. Habert and Oullet (2016) pointed out negative impacts on factors like abiotic depletion, ozone depletion, human toxicity, and eutrophication, largely due to the reliance on commercial activators like sodium silicate.

The production of sodium silicate through the Solvay process emits significant CO₂ due to high-temperature calcination (Torres Carrasco et al., 2015). Sodium hydroxide and sodium silicate emit approximately 1.1 kg and 1.2 kg of CO₂ per kg, respectively. McLellan et al. (2011) identified sodium hydroxide as a major emissions source in geopolymer mixes, stressing the need for sustainable alternatives. Provis (2018) also emphasized the need for more eco-friendly activators and cement replacements that maintain early strength development comparable to sodium hydroxide and sodium silicate. Many potential alternative materials currently being landfilled could be used in AAMs and OPC binders.

2.4 Cement Kiln Dust and Cement Bypass Dust

CKD is a waste material produced inside the kiln during the cement manufacturing process (Siddique, 2009). The raw materials enter the top of the kiln at a rate dependent on the rotation of the kiln. In the hottest region of the kiln, elements such as potassium, sodium and chlorine are volatilized, and can't pass into the clinker. The gas and continuous raw feed agitation results in a large amount of particulates being present within the combustion gases. The gas carries burned raw and volatilized material up the kiln. The CKD is captured by exhaust gases or the

kilns bypass system and is then collected in cyclones, electrostatic precipitators, or baghouses (Adaska and Taubert, 2008).

CBPD is collected from the kiln's bypass system at the bottom. This is shown in figure 2-1. The bypass system often is used to extract process gases that are high in chlorine, sulphur, and alkalis. Therefore, bypass dust tends to be much more alkaline than cement kiln dust. Additionally, since CBPD is produced at higher temperatures (up to 1000 degrees Celsius), it is much more calcined than CKD and contains higher levels of free lime relative to CKD. CBPD has a similar composition to cement, since it is generated in the hottest part of the kiln, however it has different proportions, primarily higher amounts of sodium, chloride, and potassium compounds. In the past, it has been used to enhance the qualities of some grades of cement due to reduced setting times (Siddique, 2009).

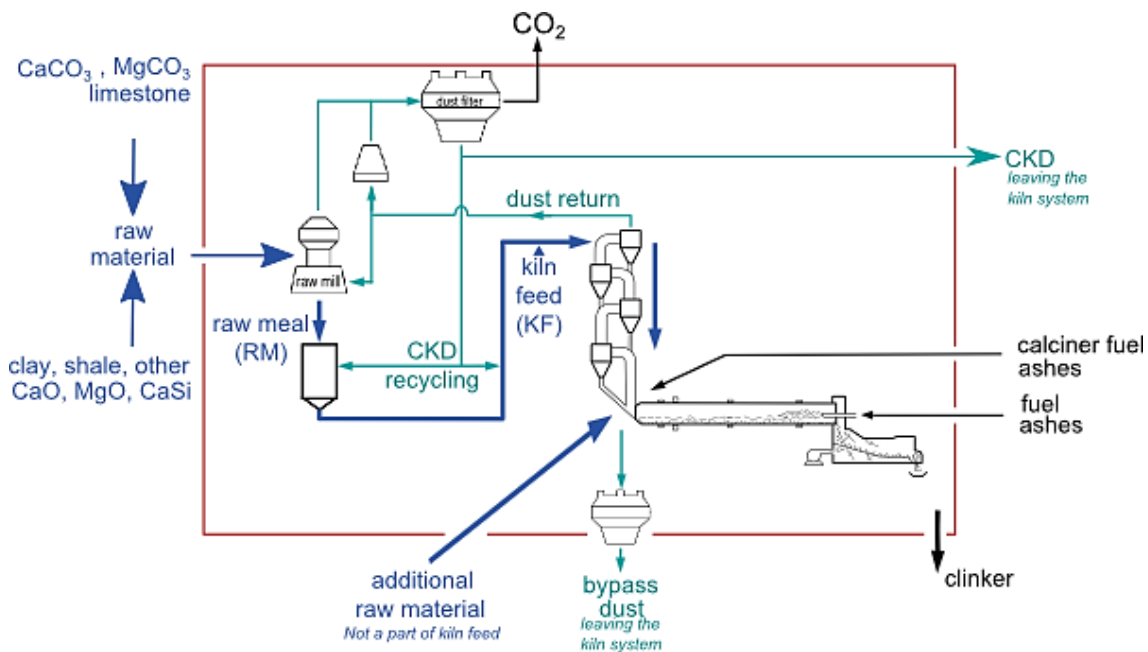


Figure 2-1 - Cement kiln with bypass system showing location of CBPD and CKD (Global Cement and Concrete Association, 2020)

Substantial quantities of CKD are produced each year where for every tonne of clinker, 50-200 kg of CKD is produced (Seo et al., 2019). The quantity of dust produced varies tremendously based on the kiln performance and the collection systems in the cement plant. Long dry kilns generate the largest amount of dust since the gas velocities within these kilns tend to be higher (Adaska et al., 2008). Preheated kilns tend to produce less dust since the feed load is high, and wet kilns produce the least amount of dust (Steuch, 1992).

CBPD accounts for approximately 2% of clinker production by weight and typically is much more landfilled than CKD due to its composition (Hanein et al., 2020). Based on clinker production statistics, the total quantity of CKD and CBPD per year can be estimated from these percentages (Tkachenko et al., 2023). Assuming that the material can't be recycled, approximately 60 million metric tonnes of CBPD are unused and unexploited each year. Based on UK cement production statistics, 1,678 thousand metric tonnes of CBPD were produced in 2022 (Jaganmohan, 2024) with the primary production location being the CEMEX cement plant in Rugby, Warwickshire (CEMEX, 2023). Figure 2-2 presents the yearly estimates of CKD and CBPD production.

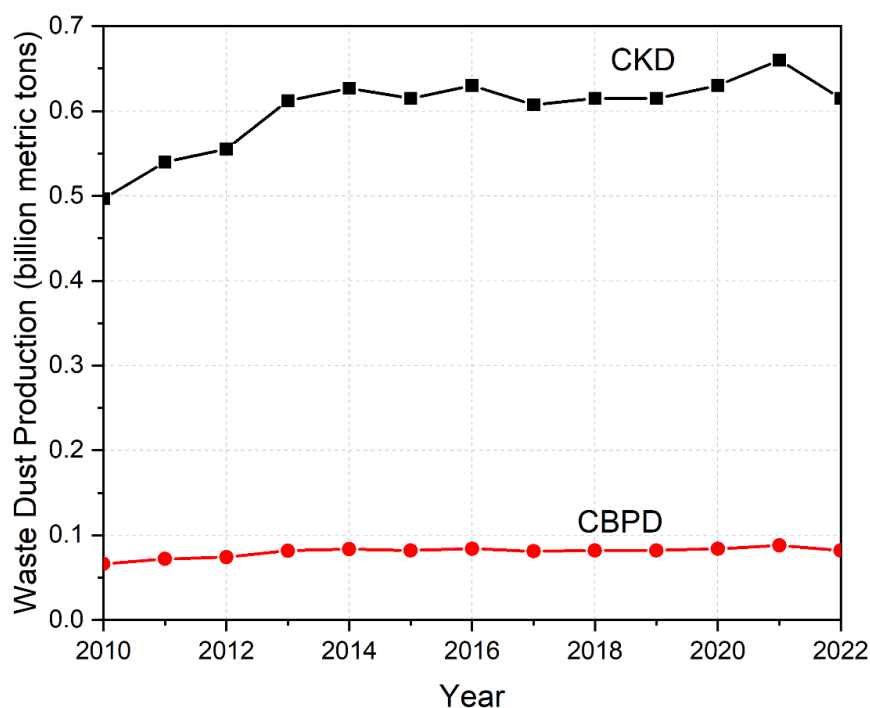


Figure 2-2 - Estimated CKD and CBPD production since 2010 (Jaganmoham, 2024)

Kessler (1995) summarised the main causes to produce CKD and CBPD into three main factors: mechanical limitations, operating stability, and product quality considerations. Currently, it is possible to collect waste dusts and recycle it into the kiln when this is practical, however in many cases, mainly for CBPD, this is not possible due to inadequate handling systems or reintroduction equipment hence mechanical limitations are a limiting factor. Operation stability is also an issue when the dust is too concentrated with volatile compounds which can cause plugs in the kiln system. Not recycling CBPD and CKD can be costly, however returning too much into the kiln can lead to system stability, hence a proper balancing system

needs to be calculated. Finally, waste dust needs to be removed when considering product quality especially when the target is to make a low alkali clinker (Kessler, 1995).

2.5 Cement Waste Dust Composition

The chemical composition of ordinary Portland (OPC) cement is very consistent for the most part. This is not the case for CKD/CBPD where very significant variations in chemical compositions and physical characteristics are observed in the material from plant to plant. Figures 2-3 the variation in the chemical compositions for different types of CKD/CBPD reported in literature from a wide array of sources that are included in the reference section at the end.

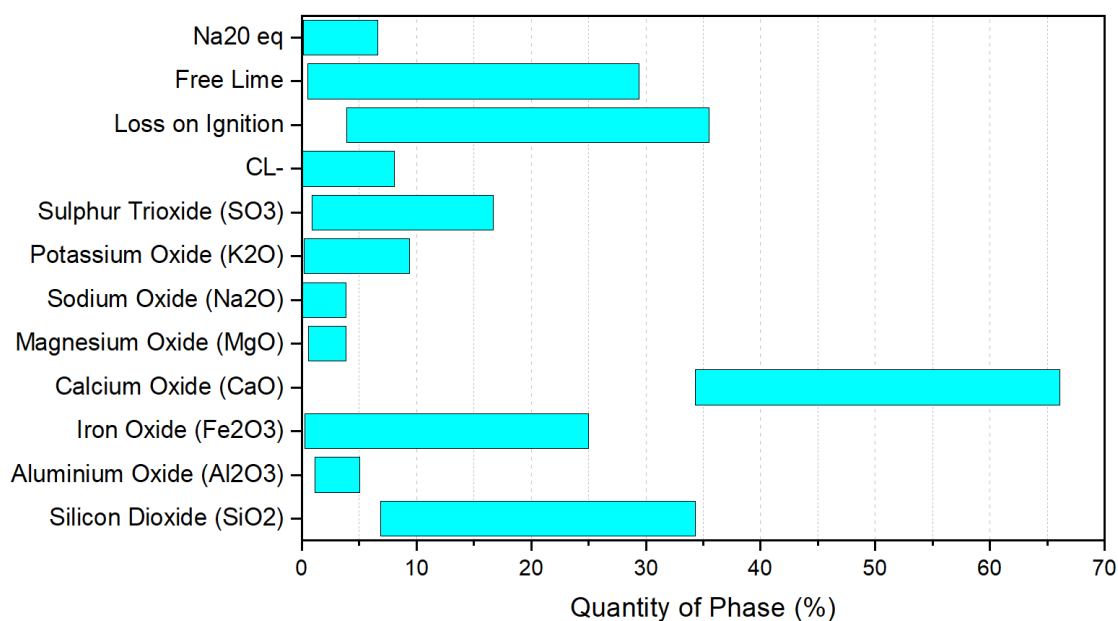


Figure 2-3 - Range of CBPD and CKD composition (Adaska & Taubert, 2008)

Calcium oxide and silicon dioxide are the major constituents of all CBPD as shown in figure 2-3, however there is a range in variation from all the oxides, as well as the loss on ignition (LOI), the free lime content, and the alkalinity of the material. The median free lime content reported was of 5.21% by weight; however, the free lime content values ranged from 0% to 29.14%. Higher free lime contents are representative of CBPD and lower are more representative of CKD. Furthermore, there is a large variation in the L.O.I where the values ranged from 3.92% and 30.94%.

Many factors affect the chemical composition of CKD/CBPD. Whiteley et al. (2015) listed them to be:

- Type of kiln
- Dust extraction system and bypass system
- Temperature in the kiln
- Input materials
- Fuel type

Special consideration is given for the fuel type due to the large number of alternative fuels from waste used in cement plants.

Ultimately the data reflects the fact that there is no real ‘mean’ CBPD and CKD composition and each source needs to be considered unique based on its own properties. The variability in composition indicates the importance of characterising the CBPD in order to properly assign its ideal use (Sreekrishnavilasam, 2006).

2.6 Toxicity of CKD and CBPD

Both cement kiln dust and bypass dust are alkaline in nature, with a pH of around 13 (Siddique, 2009). Metals within these dusts vary based on the cement plant, with volatile metals such as lead being the most susceptible to variation. Research by DEFRA (2015) found that CKD and CBPD contain low concentrations of organic contaminants meaning that they were unlikely to cause a significant risk.

Certain samples presented high concentrations of lead, barium and chromium in CBPD and molybdenum and lead in CKD. Additionally, CKD leachate contains highly soluble salts which can influence the dissolution of other elements within CKD (DEFRA, 2015). In general, it has been found that leachable concentrations of metals in CKD and CBPD are low based on literature, therefore the reuse of these materials in cementitious binders is a viable option.

2.7 Fineness and Specific Gravity

CBPD consists largely of calcium carbonate and silicon dioxide, much like ordinary Portland cement, however, it has a higher amount of alkalis, chlorides, and sulphates. The specific gravity of CBPD is typically in the range of 2.6 – 2.8 (Baghdadi, 1990) which is less than that of Portland cement (circa 3.15). Blaine fineness values for the dust varies between 2300 cm²/g and 14000 cm²/g, which is generally higher than that of OPC (3000-5000 cm²/g).

CKD tends to be fine, however the particulate size is dependent on the type of kiln, where both wet and semi-wet kilns produce a fine size with a median of 9.3 microns and dry kilns produce

CKD with a median of 3 microns (Todres et al., 1992). On the other hand, CBPD from an alkali by-pass kiln tends to have a median particulate size of 22.2 microns (Adaska & Taubert, 2008).

2.8 Loss on Ignition

Loss on ignition (LOI) is the loss of mass due to heating. In CBPD, the LOI is due to the chemically bound water, carbon dioxide and noncarbonated carbon. Thermogravimetric analysis can help identify the contribution of each of these compounds. Haynes et al. (1995) carried out this experiment by gathering 113 fresh CBPD samples and found the following:

- Carbon dioxide ranged between 4.4 to 34.4%
- Chemically bound water ranged from 0.4 to 3.8%
- And non-carbonated carbon ranged from 0.01 to 1.83%

Bhatty et al. (2010) suggested that the high LOIs occur primarily in CBPDs with a high level of carbonate and a low level of free lime. This relationship is reinforced in the figure 2-4. Typically, the LOI of CBPD ranges between 20-35%, the main cause of variance being the plant operation. Todres et al. (1992) observed CBPD from three different kiln types and found that long wet and long dry kilns had a significantly higher LOI than alkali bypass systems. Additionally, landfilled CBPD tends to have a higher LOI than non-landfilled CBPD.

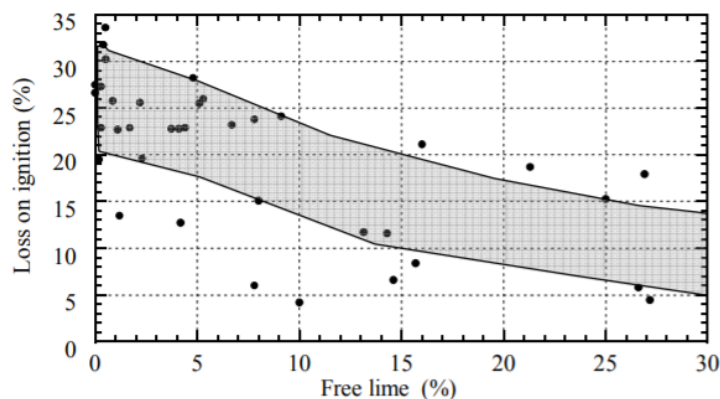


Figure 2-4 – Variation of loss on ignition with free lime (Todres et al., 1992)

2.9 Uses of Cement Bypass

2.9.1 Soil Stabilisation

Due to its high pH and level of free lime, CBPD has been shown to be a good wastewater stabiliser. In 2015, Shaheen et al. assessed the effectiveness of CBPD, activated carbon, and sawdust for removal of cadmium (Cd), copper (Cu), lead (Pb), and Zinc (Zn) from wastewater through sorption. Results indicated that CBPD had the highest affinity out of these materials,

where the average metal removal was 74%, 61%, and 60% for Cd, Cu, and Zn respectively. The authors recommended CBPD as a low-cost sorbent for removal of toxic metals from wastewater.

Research by Sulaymon et al. (2015) and Sorvari and Wahlstrom (2014), showed that CBPD could remove metals like copper and zinc from wastewater. Additionally, Waly et al. (2010), and Salem et al. (2015), showed that the pH of CBPD can be exploited to remove heavy metals such as manganese, zinc, nickel, and iron to neutralise wastewater. Since CBPD is an adsorbent material, it can be used in sewage treatment and is an effective antibacterial agent due to its ability of scavenging heavy metals (Salem et al., 2015).

Mackie et al. (2009) performed research on CBPD for its reuse in acidic wastewater. The high CaO content of CBPD can be used to replace lime in the treatment of acidic wastewaters. Their investigation indicated that the conductivity, pH, and calcium concentration of slaked CBPD and quicklime indicated the reactivity of CBPD. They went on to state that slaking CBPD enabled CBPD to have similar characteristics to commercial quicklime samples typically used in wastewater stabilisation. Ultimately, their acid neutralisation trials suggested that CBPD can be effective at neutralising acidic wastewater.

2.9.2 Land Application

CBPD can be used in land applications due to its chemical and physical properties. CBPD is used to stabilize and raise the pH of acidic soil and can be used as a fertilizing agent due to the presence of potassium and sulphur. Reports state that CBPD tend to contain a higher proportion of nutrients than other liming materials typically used for soil stabilization, however CBPD has a lower neutralizing value. Despite this a smaller particle size compared to liming materials, indicates that CBPD can be just as effective at altering the soils pH as it can be easily incorporated into the soil (DEFRA, 2015). Adaska and Taubert (2008), reported that out of 1,160,011 tonnes of beneficially reused CBPD from 10 different states in the USA, 46% of it went to soil stabilisation indicating its benefits in this industry. While this is the case, the material has yet to reach the level of support or evidence to be included in most construction guidelines in the United States (Bandara et al., 2020). In the UK, CBPD has been applied to land at a rate of circa 4.5 tonnes per hectare, at intervals of 3 years, where it is mostly applied in arable land in autumn (DEFRA, 2015).

2.10 Properties of CBPD Mortar/Concrete

2.10.1 Rheology and Setting Time

CBPD/CKD has been used as a cement replacement in previous research. Kounadis et al. (2023), assessed rheology of self-compacting concrete composed of CBPD, marble powder and OPC. They found a significant decrease in workability; this was attributed to the low roundness of CBPD particles and the K_2O in the CBPD leading to an accelerated setting and lower water demand. Wojtacha-Rychter et al. (2022), found up to an 11% increase in water demand in their OPC binders replaced by 30% CBPD. Gdoutos et al. (2002) determined that when CBPD is incorporated with GBFS, an OPC-CBPD-GBFS paste displays stiff and viscous flow properties, meaning a superplasticiser will possibly be required to achieve the required flowability. Bondar et al. (2014) stated that using CBPD reduced initial setting times in their CBPD-fly ash-OPC mixes by up to 32%. Chaunsali and Peethamparan (2011) found that the formation of portlandite and ettringite lead to early stiffening of neat CBPD pastes, however the addition of GBFS delayed the setting time due to the dilution effect in the CBPD-GBFS blend. Sreekrishnavilasam et al. (2006) deemed that cements with only additives such as CBPD have decreased workability and setting time. Marku et al. (2012) showed that the density of CBPD is lower than that of OPC, meaning that when it is used to replace OPC, more CBPD particles are required which worsens the rheological properties of the paste. CBPD particles also are very fine and may agglomerate reducing the workability. Ravindrarah (1982) stated that CBPD replacement of 15% reduced the workability and increased the water demand. Abo-El-Enein et al. (1994) stated that initial and final setting times would be reduced due to high free lime contents in the CBPD. The formation of ettringite was also stated to reduce the setting time, due to the enhancement of early age strength (Gdoutos et al., 2002) coinciding with Chaunsali and Peethamparan's research. Kalina et al. (2018) combined CBPD with sodium carbonate as alkaline activators, and what they found was that the addition of CBPD into AAM systems decreases workability due to the rapid early hydration of lime, leading to the systems inhomogeneity.

Contrary to these results, Aggarwal et al. (2023) investigated the compatibility of CBPD with foundry sand in controlled low strength materials, where their binders replaced OPC by up to 100%. Their results showed a higher flowability as CBPD content increased. This was attributed to the fineness of the material, where they explained that the fineness lead to filling of voids and consequently a release of the entrapped water enabling a more flowable mix.

2.10.2 Strength of Binders

CBPD has been utilised as an additive in previous studies, where it was shown that additions up to 10% did not negatively affect the mechanical properties of cement mortars. Siddique and Kunal (2016) claimed that this level of addition hardly affected cement properties, however an increase to 15% resulted in slight deterioration of these parameters. Reportedly, the main issue with the replacement of CBPD in concrete is its high chloride concentration and alkalinity (Danuta Barnat-Hunek et al., 2018). High chloride concentration is known to cause rust in steel reinforcement, significantly reducing the design life.

Wojtacha-Rychter et al. (2022), explored the replacement of 42.5R OPC with up to 30% CBPD. They found reductions in strength at all replacement levels, however 10% replacement did not lead to a considerable drop. Reductions in strength were attributed to an increased w/c ratio of CBPD binders, due to the higher water demand of CBPD. Another factor was the dilution effect of CBPD, which was less reactive than the clinker used. Al-Aleem et al. (2005) performed research on CBPD replacements up to 10% and 20% in OPC cement and slag cement pastes, respectively. They found that the compressive strength increased up to 6% in the OPC mortar, however decreased sharply at any replacement level higher than that. This was also true with slag cement, where beyond 10% replacement showed a significant decrease. All samples except the 20% replacement reached 25+ MPa by 28 days, and by 100 days all samples had exceeded this value, which can be attributed to the slow pozzolanic hydration. This agreed with the work undertaken by Al-Harthy et al. (2003) where they found that 5% replacement provided the best results for compressive strength, flexural strength, and toughness. Aggarwal et al. (2023), replaced cement by up to 100% with CBPD in their controlled low strength binders, where they found dramatic drops in strength at every replacement interval. They assumed this to be partly due to the inertness of the CBPD they were utilizing.

There is literature involving fired Aswan clay replaced by up to 25% by CBPD to fabricate roof tiles (Naggar et al., 2023). The results showed that replacing clay by up to 8% CBPD produced favourable breaking strength results and was a suitable option for reuse of the waste.

Most researchers agree that better results are obtained when CBPD is combined with a pozzolan due to its qualities as an activator. CBPD solution has a high pH (12-14), which can be exploited for the dissolution of pozzolanic materials when their glass network is disintegrated due to the penetration of OH⁻ ions. GBFS does not dissolve at a pH lower than

11.5 (Santagata et al., 2006). High sulphate content can also promote the formation of ettringite (Chaunsali and Peethamparan, 2011) which was shown to benefit the strength development of their CBPD/pozzolan binders. The reactive free lime from the CBPD leads to the creation of calcium silicate binder phases and benefits the development of strength in pozzolanic binders due to the availability of Ca^{2+} ions (Shi, 2001).

Kounadis et al. (2023), found high strengths in their marble powder-CBPD-OPC mixes. They attributed the strength partly to the chlorides in the CBPD system accelerating the hydration of alite. They also stated that the presence of gypsum led to faster hydration of C_3S . Gayathri et al. (2002) found a significant increase in compressive strength when replacing cement blends with 20% CBPD and 10% Silica fume reaching a 28-day compressive strength of 50.66 MPa. Coakley et al. (2016) combined 55% fly ash, 15% CBPD and made a concrete that surpassed 50 MPa at 28 days, reaching a very comparable strength to the pure OPC control mix. They also found that the early age strength increased due to the faster dissolution rate of the pozzolanic additives when combined with highly alkaline CBPD. Bondar et al. (2014) found that incorporating a low percentage of gypsum into their fly ash-OPC-CBPD mixes enhanced the late age strength. Gdoutos et al. (2002) concurred with this and achieved a 28-day compressive strength of 30.1 MPa in a 50% slag and 50% CBPD mix. Combinations with OPC up to 30% significantly improve strength while also drastically reducing carbon dioxide emissions due to reduced use of clinkers.

CBPD has also been used in AAMs. Heikal et al. (2020), activated a ternary blend of GBFS, CBPD and microsilica with sodium silicate and sodium hydroxide. Their results showed that 20-30% CBPD replacement with slag achieved the strongest AAMs. They attributed the strength to the alkali content of CBPD and the portlandite formation of the binder. Bilek et al. (2021), also investigated GBFS-CBPD binders activated with sodium silicate and CBPD. They found strengths of up to 57 MPa when the AAM had an increased activator content. This was due to an increase in the number of silicates in the system leading to the formation of more CASH gel.

In 2019, Vinai and Rafeet developed industrial scale CBPD/FA/GGBS. They developed nearly 400 blocks with the dimensions 440 x 215 x 100mm with varying water to binder ratios. Their blocks were tested at 4 days and 7 days and achieved a range of 1-1.5 MPa and 2-2.5 MPa respectively, which were very low values. Their reasoning for these results was the sub-par weather conditions and the extra water from the aggregate and the environmental moisture

could have hindered the reaction. More control will be required during the mixture procedure to achieve satisfactory results.

2.10.3 Durability of CBPD Mortar/Concrete

Several studies agree that excessive substitution of OPC with CBPD can deteriorate the durability properties of concrete. Much like with the strength properties, research carried out by El-Sayed et al. (1991) and Batis et al. (2002), found the optimum replacement to be circa 5%. It was found by Maslehuddin et al. (2009) that a 5% replacement can even improve properties such as chloride permeability, however there was a decrease in electrical resistivity which could be explained by the excessive chloride ions in the CBPD.

Hakkomaz et al. (2022), researched the carbonation and elevated temperature resistance of OPC binders replaced by up to 20% CBPD. Their carbonation depth increased from 8.1mm to 12.2mm with 20% CBPD addition. This was attributed to the higher porosity and permeability of the mortar, which resulted in CO₂ reacting with the portlandite in the CBPD-OPC system, causing a higher carbonation depth. Negligible reductions in strength were observed when the binders were exposed to high temperatures. Bilek et al. (2020), researched the freeze-thaw and aggressive solution resistance of alkali activated CBPD-GBFS binders. A significant drop in dynamic modulus was experienced after 250 cycles, however the AAM blocks had good resistance after 125 cycles. In terms of aggressive solution exposure, the blocks showed good resistance, except when exposed to acetic acid, which fully degraded an AAM block by 50 days exposure.

Ashteyat et al. (2019), researched the durability properties of white CBPD roller-compacted concrete replacing cement by up to 40% reinforced by polypropylene fibres. Their freeze-thaw investigation showed a reduction in dynamic modulus of elasticity (up to 27%) as the CBPD replacement ratio increased. They attributed this to the increased porosity and water absorption with increasing CBPD. They did note that there was a significant improvement when the concrete was reinforced with polypropylene fibres and overall, despite the worse performance, the CBPD binder provided satisfactory results.

The addition of pozzolanic materials to the cementitious blends tends to counteract several of the negative effects in CBPD-OPC binders. Kunal et al. (2016) found that there is a possible increase in the alkali-aggregate reaction when no pozzolanic additives are included, however these are drastically reduced with the addition of fly ash or GBFS. More work is required on the effect chlorides and sulphates have on the durability of concretes containing CBPD. Barnat-

Hunek et al. (2018) carried out some research on the durability of these concretes. They found that CKD addition of above 10% could lead to significant freezing and thawing along with the formation of significant salt crystals that affect the mechanical parameters of the concrete. Replacement of 20% CBPD also limits the efficiency of hydrophobization. They also stated that CBPD should not exceed 20% of the concrete composition. More research is required on durability of pozzolanic-CBPD binders.

2.10.4 Shrinkage

In terms of shrinkage, Daugherty and Funnel (1983) stated that a 10% replacement of CBPD in cementitious binders did not have an adverse effect on shrinkage. Contrarily, Wang and Ramakrishnan (1990) replaced an OPC binder with 5% CKD and found a slight increase in shrinkage. These results were corroborated by Masluheddin et al. (2008) where they found that the shrinkage strain in their OPC- CBPD blends increased with time and quantity of CBPD where the highest shrinkage strain was found in samples with 15% CBPD.

El-Mohsen et al. (2014), investigated the shrinkage properties of self-consolidating concrete containing cement kiln dust. They replaced OPC up to 40% with CBPD and tested the total shrinkage along a 120-day lifetime. They found that mixes containing 10% CBPD had very similar shrinkage strain to 0% CBPD mixes and 50% of the total shrinkage, circa 0.0003, was achieved in the first 28 days. Shrinkage strain for mixes containing 20% and 40% CBPD had 0.00035 and 0.00039 strain respectively.

A recent investigation by Kounadis et al. (2023), researched the drying shrinkage of ternary binders composed of CBPD, OPC and Marble Powder and compared them to OPC-Marble Powder binders. They found improvements in shrinkage in the ternary CBPD blend. They attributed this to the high free lime content and the carbonation associated with this phase. They also theorised that the coarse granulometry of the dust, led to lower capillary pressures in the microstructure of the mix.

Czapic et al. (2020), in their hydration investigation of CBPD, found that CBPD does not shrink but in fact expands. The expansion occurs particularly during the first 5 hours and stabilises after 21 hours. This was largely attributed to the hydration of CaO. The final volume increase reached up to 209%.

2.10.5 Hydration

Few studies have been made investigating the hydration of concretes incorporating CBPD. The studies that do, however, seem to all agree that the formation of an ettringite phase has a positive effect on the strength development of CBPD binders. Chaunsali and Peethamparan (2011) discovered that even if CBPD has a low free lime content, a high sulphate and alkali content was effective in hydrating GBFS and fly ash. They developed a CBPD-FA binder that achieved a compressive strength of 30 MPa (heat cured at 75 degrees Celsius). They determined that the early age strength development was largely due to the ettringite. This correlates with Coakley and Sadique (2016) where their quaternary blend containing GBFS-fly ash-OPC-CBPD reached a higher compressive strength than the pure OPC control mix. They attributed the enhanced strength gains, particularly early age strength gains, to the ettringite formation. Chaunsali and Peethamparan (2011) also determined that the CBPD with a lower sulphates content decreased the ettringite. Siddique (2014) also found that an addition of an alkali or a high alkali content could reduce the strength of CBPD binders as it hinders the formation of ettringite.

Czapik et al. (2020) found that the primary product in CBPD hydration was portlandite and additionally Freidel's salt was present too. While the hydration of cementitious binders is typically due to calcium silicate, alite and belite, CBPD's hydration was primarily due to CaO hydration. The calorimetric curve shows a rapid increase in heat release initially, due to the hydration of the CaO, however this is followed by a rapid decrease and a stabilization period around 11.3 hours followed by another decrease. In CBPD the clinker phase found was of C_2S which had an accelerated hydration due to the formation of portlandite due to free CaO hydration. They concluded that CBPD hydration with a high content of CaO lasted up to 7 days and that portlandite is the primary hydration product.

Chaunsali and Peethamparan (2011) also agree with this when they confirmed the presence of a potassium peak in the reaction product structure. They additionally identified the formation of different phases such as the CSH, CASH, portlandite, and AFm (ettringite) phases, stating that CASH gel appeared due to a pozzolanic reaction and a high free lime content. This corresponds with the typical reaction products of high calcium AAMs (Provis et al., 2014).

Gdoutos et al. (2002) researched the hydration of OPC, CBPD, and slag binders and found that the ratio between alkalis and silica has an important role in early age hydration. As the alkali-silica ratio increases, the time for the ion dissolution is elongated, and the rate of ion dissolution

increases. They also deemed in a 2004 paper, that the main factors affecting the initial hydration and activation were alkali concentration, fineness, and the presence of sulphates. Coakley and Sadiques' (2016) research coincide with this as the finer CBPD they utilised showed higher early age strength.

Chapter 3 – Effectiveness of Cement Bypass Dust in Heat and Ambient Temperature Cured Slag-Based Mortars

(Paper submitted to Resources, Conservation and Recycling awaiting decision)

Abstract

The climate impact of Ordinary Portland Cement (OPC) is mounting concern due to its substantial contribution to greenhouse gas emissions. Researchers and the industry are seeking alternative materials to either replace or augment OPC. Materials like fly ash, slag, and natural pozzolans show promise in reducing carbon emissions associated with OPC, but often require alkali activators. This study centres on Cement Bypass Dust (CBPD), a waste product of the cement industry rich in alkalis, free lime, and chlorides. The aims are to utilise CBPD as a value-added substitute for OPC. Given the high alkalinity of CBPD, the research investigates its efficacy as a cement replacement in combination with ground granulated blast furnace slag (GBFS) for producing mortar under ambient ($20 \pm 2^\circ\text{C}$) and elevated temperature ($65 \pm 2^\circ\text{C}$) curing conditions. Two distinct binder compositions are examined: (1) CBPD:GBFS = 1 : 1 and (2) CBPD:GBFS:OPC = 1:1:0.5 with a constant mass ratio of binder, sand and water at 1:3:1. Results of the physical and mechanical properties reveal that CBPD based mortars with 20% OPC can achieve compressive strengths of 7.5 and 9 MPa after 28 days of curing at ambient and elevated temperature, respectively. While heat curing benefits early age strength for both mix proportions, it proves less suitable for long-term mechanical performance, as it retards strength development compared to ambient temperature curing. Analysis through Mercury intrusion porosity (MIP), scanning electron microscopy (SEM), x-ray diffraction (XRD) and thermogravimetric analysis (TGA) reveals that ambient temperature cured mortars exhibit higher density, a less porous microstructure, and a more extensive formation of hydration products after 28 days of curing. This research contributes to the reduction of carbon emissions associated with the use of cement while concurrently addressing the challenge of waste disposal in landfills.

Keywords: Cement mortar, Bypass dust, Blast furnace slag, GBFS, Waste utilisation, Microstructure

3.1 Introduction

3.1.1 Background

The growing global demand for construction materials, particularly cement, driven by rapid population growth and urbanization, has significant environmental implications. The cement production process, due to its high energy demand and the release of CO₂ during limestone decarbonation, contributes to approximately 8% of global anthropogenic CO₂ emissions (Olivier et al., 2017). It is estimated that 4.3 billion tonnes of cement were produced worldwide in 2021 (International Energy Agency, 2022). As a result, it plays a substantial role in climate change acceleration. To address these concerns, the construction industry faces pressure to adopt more sustainable practices, including reducing energy consumption, developing eco-friendly materials, and using waste products, which can also lead to cost savings.

Industrial by-products such as fly ash, ground granulated blast furnace (GBFS), and silica fume are already being used as supplementary cementitious materials (Zhu et al., 2014; Nedunuri et al., 2020). Additionally, mineral wastes are used for developing cementless construction products through alkali activation and geopolymerization. An alkali activated material (AAM) is formed by the reaction of a solid aluminosilicate powder (precursor) with a dissolved alkali metal (activator). The common precursors used in AAMs are GBFS, fly ash, silica fume, and metakaolin (Fernández-Jiménez et al., 2017). Due to being completely cementless, they are expected to be one of the feasible solutions to reduce concrete carbon footprint (Provis et al., 2016). Other sustainable alternatives involve technologies like calcined clay limestone cement (Scrivener et al., 2018), hybrid mortars with low cement content (Batuecas et al., 2021), carbonation curing (Sharma et al., 2018), and energy-saving techniques such as hydrothermal synthesis (Jo et al., 2017).

Despite the potential of the above technologies, in many cases the cost and true extent of CO₂ reduction remain uncertain. This is particularly true with AAMs where the environmental impact of the chemical activator is often high and there are difficulties in implementing the technology. Furthermore, AAMs require the use of large amounts of corrosive alkali and an overhaul of the manufacturing line, which limits their use in the precast industry (Alnahhal et al., 2021). Sustainable activators sourced from waste streams may be viable options to address some of these concerns.

3.1.2 Cement Bypass Dust

Due to the introduction of chemicals such as chlorides into the kiln from alternative fuels, cement plants around the world have been introducing bypass systems into their kilns to reduce

the impurities going into their clinker. The dust that is collected from the bypass system is classified as cement bypass dust (CBPD). Though CBPD has a similar chemical composition to cement, it also has some significant differences such as, higher alkalinity (pH 11-14), and high sulphate and chloride content, making it difficult to recycle back in the kiln. The composition of CBPD varies from plant to plant depending on factors such as the fuel type, raw materials used, and kiln type (Adaska et al., 2008). The amount of CBPD produced is about 2% by weight of clinker meaning that several million tonnes of CPBD are produced each year worldwide (Hanein et al., 2020). CBPD is typically landfilled at a large cost to the cement manufacturers due to collection and transportation. The disposal of CBPD also leads to unnecessary use of land and the contamination of surface and ground water by heavy metal leaching (Siddique, 2006). If airborne, it can also affect human health by causing asthma, skin irritation, and eye problems, hence it is classified as a material that has potential to be hazardous to human health (EPA, 2016).

The significant quantity of CBPD generated, approximately 2% of clinker weight, necessitates large-scale disposal, often in landfills. This disposal is costly and leads to land use and groundwater contamination issues. Additionally, airborne CBPD can negatively impact human health. Therefore, research efforts have explored ways to reuse CBPD in cementitious binders as a filler or cement replacement, with some studies demonstrating its positive effects on mechanical strength. Combining CBPD with pozzolans has shown even more promising results.

El-Awney et al. (2005) investigated the behaviour of OPC mortars made with up to 20 % CBPD replacement and found that up to 10 % CBPD replacement enhanced mechanical strength. Al-Harthy et al. (2003) found similar results where they found a 5 % replacement of cement with CBPD in concrete led to an improvement in compressive and flexural strength. The benefits increase when CBPD is mixed with a pozzolan. Sadique and Coakley (2016) made a concrete using 55 % fly ash, 15 % CBPD and 30 % OPC that achieved 50 MPa compressive strength after 28 days curing, a very comparable result to typical concrete. Gayathri and Rajasekhar (2017) found a significant increase in compressive strength in their ternary blends of CBPD, silica fume and cement, reaching a compressive strength of 51 MPa. Bondar and Coakley (2014) also found favourable results in fly ash-OPC-CBPD-gypsum mixes. More recently, CBPD has been demonstrated to have potential as an alkali activator of aluminosilicates (Barnat-Hunek et al., 2018).

Though it is urgent that more sustainable construction materials are developed, it is also important to avoid large changes to the typical manufacturing process to avoid extra capital cost. The use of CBPD as a cement replacement in concrete manufacture is not expected to require any changes in the production process. However, the influence of key parameters, such as fineness, free lime content and alkalinity, in determining the effectiveness of CBPD as an activator of pozzolanic materials is not fully understood. There is a significant gap in literature addressing the potential of CBPD as a cement replacement and the waste material is currently primarily unexploited and disposed of in landfill.

Hence, this paper aims to investigate the effectiveness of CBPD in combination with GBFS as binder in producing mortar at ambient and elevated temperature curing conditions in which CBPD can act as a cement replacement with activating potential. The recycling of CBPD in a mortar binder would lead not only to the environmental benefits and promotion of a circular economy, but also to cost savings for the construction industry. To the author's knowledge, research of this kind is not currently available, where CBPD is primarily replaced at very small quantities in the literature available. Two mortar mixes, one cementless and one with 20% OPC are investigated. The chemical and physical properties of the powders and pastes are examined to determine their chemical composition and particle size distribution and microstructural properties using XRD, FE-SEM, TGA and MIP. The fresh and hardened state properties are examined to determine standard consistency and setting times, flowability, density, heat evolution and compressive strength.

3.2 Materials and Methods

A systematic experimental procedure was developed to produce a cementless mortar composed of GBFS and CBPD as well as a GBFS-OPC-CBPD mortar. Mortar samples were characterized in terms of their flowability, density, mechanical strength, and microstructure.

3.2.1 Materials

All mixes in this project contained CBPD and GBFS. The CBPD used in this study was used as received and was obtained from the CEMEX Rugby plant. GBFS was obtained from a Scunthorpe plant. CEM II 32.5R provided by CEMEX, UK was also used for ternary mixtures.

Locally available building sand was used as a fine aggregate for the mortars. Its specific gravity and water absorption capacity were measured to be 2.6 and 2.5%, respectively; these conform to the limits specified in BS EN 1097-6:2000. The sand conformed to the standard for the preparation of a plastering mortar with a targeted strength of 7.5 MPa in accordance with BS EN 998-1. The water used for the mortar was regular tap water at a temperature of 20 ± 2 °C.

The particle size distribution of CBPD, OPC and GBFS was determined using a laser particle size analyser and the results are shown in Figure 3-1. GBFS is shown to be the finest material with a median particle size of 12.9 μm . OPC and CBPD had median sizes of 20.9 and 46.5 μm , respectively. The CBPD used is relatively coarse when compared to previously reported data with a median particle size of circa 22.2 μm (Todres et al., 1992).

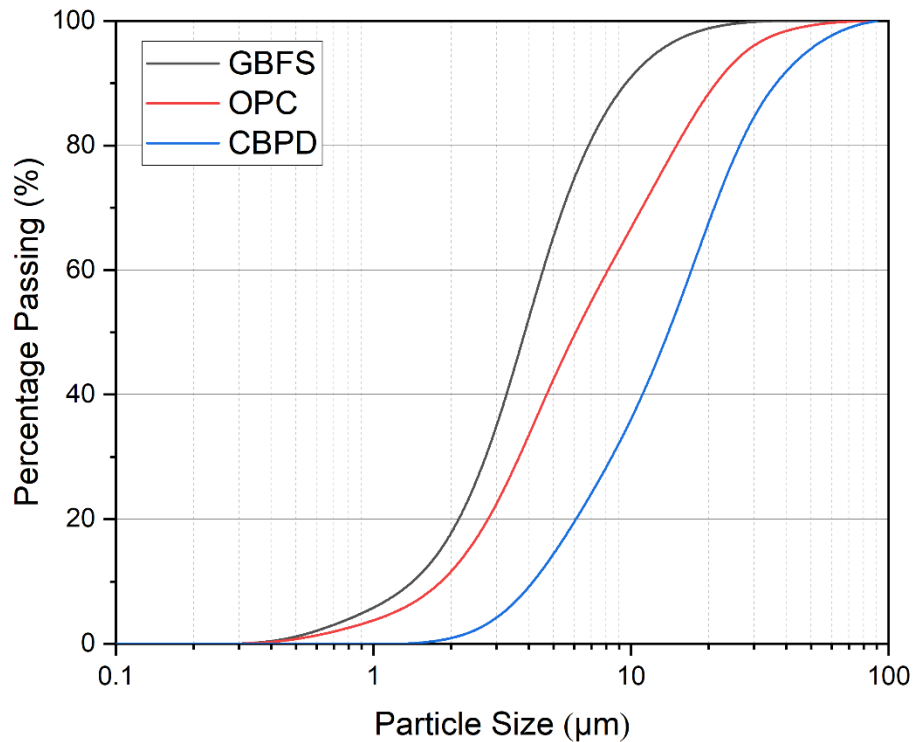


Figure 3-1 - Particle size distribution of GBFS, OPC and CBPD

The mineralogical characterisation of the raw materials was conducted using X-Ray Diffraction (XRD) as seen in Figure 3-2. The peaks were characterised using Diffrac.Eva software. The main crystalline phases present in CBPD were lime (CaO), gypsum ($\text{CaSO}_4 \cdot 2\text{H}_2\text{O}$), sylvite (KCl), quartz (SiO_2), and calcite (CaCO_3), with lime being the major crystalline phase. Sylvite provides the CBPD with a significant amount of alkalinity, which can be utilised to activate GBFS (Kalina, 2018). Cement on the other hand was mainly composed of calcite, alite (C_3S), and belite (C_2S). GBFS presented a very broad diffuse band indicating that it contained a very large amount of amorphous material.

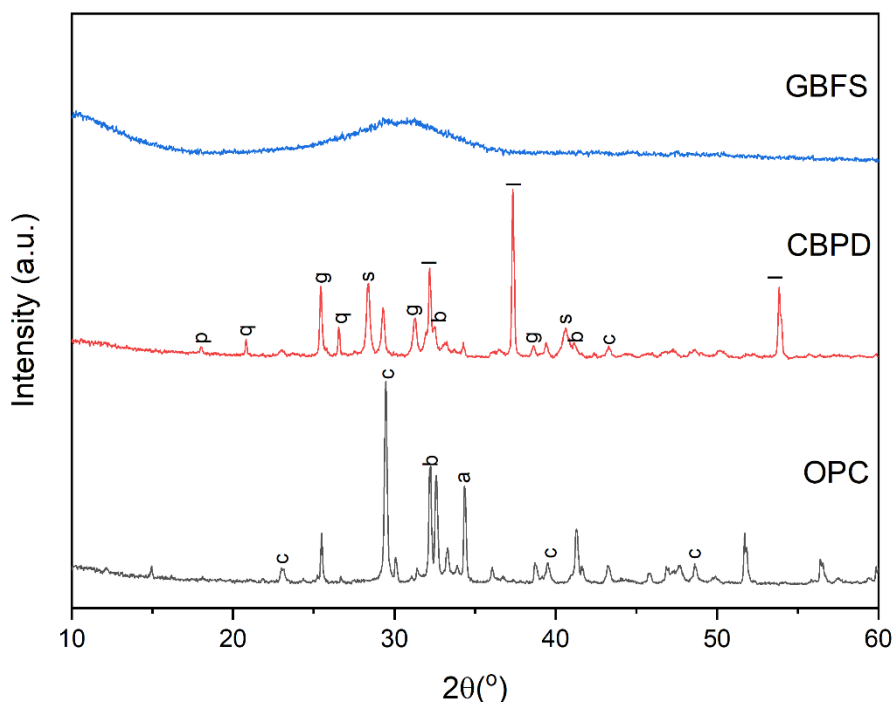


Figure 3-2 - XRD patterns of GBFS, CBPD and OPC (c=calcite, b = belite, a = alite, l = lime, s = sylvite, g = gypsum, p = portlandite, q = quartz)

3.2.2 Mortar Mixing Procedure

The CBPD-GBFS based mortar was prepared using a pan concrete mixer. Table 3-1 shows the mix proportion of the binder ingredients (CBPD, GBFS and OPC), fine aggregate, and water content. Two different mix designs were used, the first consisting of 50% CBPD and 50% GBFS and the other of 20% OPC, 40% CKD, and 40% GBFS. The binder to aggregate ratio was kept constant at 1:3. The water to binder ratio for with no admixtures was kept at 1.

Table 3-1 - Mix designs investigated

Mix Design	CBPD (kg/m ³)	GBFS (kg/m ³)	OPC (kg/m ³)	Fine aggregate (kg/m ³)	Water/Binder Ratio	Curing Temperature
KGA	225	225	-	1344	1	20 °C for 24h
KGH	225	225	-	1344	1	65°C for 24h
KGCA	180	180	90	1344	1	20°C for 24h
KGCH	180	180	90	1344	1	65°C for 24h

The dry material was mixed in the pan mixer first for homogeneity. Subsequently, the water was added and mixed continuously for a minimum of 120 seconds and until the mix was wet throughout. Following this, the plastic mortar mixture was cast into 50 mm cubic moulds in three layers and vibrated between each layer to release any entrapped air. Two methods of curing were used:

1) Heat-Curing: the moulds were placed in a climatic chamber at 65 ± 2 °C and 95% relative humidity for 24 hours. The samples were then de-moulded and cured in a water tank (21 ± 2 °C) until the desired age of testing.

2) Ambient Temperature Curing: Moulds containing the mortar samples were covered with a polyethylene sheet and allowed to set at ambient conditions (20 ± 2 °C) for 24 hours before being de-moulded and cured in a water tank (21 ± 2 °C) until testing.

3.2.3 Characterisations

3.2.3.1 Fresh and hardened state properties

The standard consistency and the setting times of CBPD based pastes were measured using a Vicat apparatus following BS 4550-3-3.5:1978 and BS EN 480-2:2006, respectively. Paste samples were cast in a Vicat mould and the time elapsed between the addition of water to the dry powder and the Vicat needle penetrating the paste at a 5 ± 0.5 mm depth was taken as the initial setting time. Following this step, a circular-end Vicat needle was released on the paste sample at ten-minute intervals, and the final setting time was determined once there was no imprint of the circular part of the needle left on the surface of the paste.

The flowability of the mortar samples was assessed using a flow table test following BS EN 1015-3:1999. The mortar was placed in a conical mould in three layers which was released after it was tamped down 25 times. Following this, the diameter of the mortar mix was measured in four different locations and recorded.

The density of the hardened mortar samples was determined prior to the compressive strength tests. The mass of the cubes was recorded when they were submerged in water. After this they were left to dry. Once dry, the mass of the samples was recorded again. The difference between the dry weight and submerged weight of the sample indicated the volume of the mortar cube by considering the specific gravity of water to be 1.

Temperature vs time measurements were carried out to investigate the heat evolution of CBPD binders. Paste samples were mixed and cast into plastic bags. The bags were then pierced with a thermocouple so that it was in contact with the paste. This was then placed in a semi-adiabatic container. Additional pastes of 100% OPC and 100% CBPD were cast and investigated for this test.

The compressive strength of the mortars was measured following ASTM C109/C109M - 21 using a 300 kN Universal Testing Machine. Three 50 mm mortar cubes from each batch (mix

design) were tested, with no prior preloading. The average compressive strength of all three specimens was considered as the compressive strength of that batch.

3.2.3.2 Microstructural Characterisation of CBPD samples

The CBPD pastes were prepared using the same binder composition of mortar. The paste samples were cast in glass containers and the curing method remained the same. After the desired hydration time, the samples were doused in isopropanol and ground into powder. Larger surface pieces were collected for SEM and MIP analysis. To prevent the creation of further pores, these pieces were collected by cutting the paste with scissors rather than hammering. Following this, the ground samples and chunks were placed in an oven at 65°C for 12 hours. This process was used to remove moisture and prevent further hydration.

3.2.3.2.1 X-Ray Diffraction (XRD)

X-ray diffraction of CBPD paste samples was carried out with a Bruker D-2 diffractometer. In this study, X-rays of 1.54 Å were generated by a Cu K α target and an Ni filter. The samples were analysed from 10° to 60° at a rate of 0.02° steps per second. The software used for peak identification was Diffrac.EVA by Bruker which has an ICDD library. Origin 2021 was used for Gaussian fitting of the main XRD peaks.

3.2.3.2.2 Scanning Electron Microscopy

The fractured surface of the CBPD based paste was observed using a FEI Inspect F field emission scanning electron microscope (FE-SEM). The microstructure was analysed at a voltage of 15 kV using a backscattering electron mode. Dried paste samples were fractured and mounted on an aluminium stub using carbon tape. The microstructure was then photographed in a vacuum.

3.2.3.2.3 Thermogravimetric Analysis

Thermogravimetric Analysis (TGA) was carried out using a Perkin Elmer Pyris 1 TGA. Samples were heated from 30°C to 1000°C degrees at a rate of 10°C per minute. In this study, 10 mg of the ground powder samples were used to investigate the thermal behaviour of CBPD paste.

3.2.3.2.4 Mercury Intrusion Porosimetry

Mercury Intrusion Porosimetry (MIP) was carried out using a Micrometrics Autopore V. This was used to evaluate the porosity, pore distribution and pore size of 28-days hydrated CBPD based paste. The MIP study was conducted assuming a 140° contact angle for mercury.

3.2.4 Life Cycle Assessment

Life cycle analysis (LCA) is a form of modelling that allows for the estimation of total CO₂ emissions and other impacts of a specific material or product from the manufacture till the disposal or recycling of it. This study aims to compare the environmental impact of the investigated mixes as well as to a representative OPC mix design. OpenLCA 2.0, an open source LCA modelling software, was used for the LCA analysis. The database used was Ecoinvent 3.8 and the LCA follows the standard ISO 14040 (2006). Global warming potential was the impact assessed.

The functional unit in this LCA was 1000 kg of mortar and the system boundary used was cradle-to-gate. The life cycle inventory includes all the raw materials and process necessary to fabricate the mortar mixes. CBPD had no emissions associated to it due to its classification as a waste according to the Waste Framework Directive of the European Union (2018). The GWP data for the raw materials was gathered entirely from the Ecoinvent database. Heat curing was assumed to be 180 kWh based on an industrial walk-in oven with a volume of 217 m³ (Kul et al., 2023). All the electricity data was gathered from the Ecoinvent database and was based on the UK grid. Transport distances were based on the researcher’s location and are shown in table 3-2. A freight lorry weighing 16-32 metric tonnes, from the Ecoinvent database, was assumed as the transporter of raw materials.

Table 3-2 - Life cycle inventory

Raw Material	Distance (km)
CBPD	100
OPC	18
GBFS	77
Sand	50
Tap Water	--

3.3 Results and Discussion

3.3.1 Standard Consistency and Setting Time

The standard consistencies and setting times for the tested samples are shown in table 3-3. The standard consistencies for KG and KGC pastes were determined to be 37%, and 35% respectively. The higher standard consistency of KG samples indicates that the combination CBPD and GBFS lead to an increased water demand relative to a mix with cement. There are several possible reasons for this high-water demand such as the higher alkali content (Bondar

and Coakley, 2014), the higher free lime content (Czapik et al., 2020), and the larger volume of CBPD particles in the binder due to its lower density relative to OPC. Another factor to consider is the inclusion of GBFS which could have also reduced the workability of the mixes due to its fineness. Generally, OPC is expected to have a standard consistency ranging from 25-35% (Bye, 2011).

The higher CBPD and GBFS content reduces the initial setting time of the binder mixtures. As observed, the initial setting time of KG is 140-minutes, whereas it is 223 minutes for the KGC mix. This is in line with previous research (Bondar et al., 2014), and can be attributed to the high free lime content and alkalinity of CBPD, which accelerate the hydration reaction. GBFS has also been shown to increase setting time due to its delayed reaction (Yun et al., 2020).

Table 3-3 – Setting times and standard consistence of CBPD binders

	KG	KGC
Initial Setting Time	140 min	223 min
Final Setting Time	395 min	415 min
Standard Consistency	37%	35%
Flow Table Value	150mm	158mm

3.3.2 Workability

As seen from table 3-3, the flow values correlate with the setting time results where it is found that the KG mixture possesses the lower flowability ($149.75 \text{ mm} \pm 0.4$). These results are in line with past research where it was found that the inclusion of CBPD or Cement Kiln Dusts lowers workability (Sreekrishnavilasam and Santagata, 2006; Ravindrarajah, 1982).

3.3.3 Effect of heat curing on the volume of mortar samples

Significant swelling was observed for both samples that were subjected to heat curing. Figure 3-3 shows the mix of KG with the heat cured specimen (a) and its ambient cured counterpart (b). While expansion may have occurred also in the ambient cured samples, the pop-out phenomenon (Lee and Lee, 2009) only visibly occurred in the heat cured samples. Significant cracking is also observed on the heat cured sample, likely due to this expansion as seen in Figure 3-4. No cracks are visible in the ambient cured sample. The same behaviour was observed for the KGC mixes (not shown).



Figure 3-3 - Side profile of CBPD binders (a) KGH (b) KGA

Expansive behaviour in the hydration of CPBD was also observed by Czapik et al. (2020), which resulted in a 55% of volumetric swelling. Swelling was also observed by Kalina et al. (2018) in their CBPD-GBFS-Sodium Carbonate binders. The main reason for this type of swelling is attributed to the free lime (CaO) content in CBPD, which when mixed with water leads to a heavily exothermic reaction (slaking reaction), where calcium hydroxide is formed (Ritchie and Bing-An, 1990). Furthermore, water particles act against binding forces within the mix, pushing the binder paste outwards, leading to the swelling (Neville., 2012). The ratio of volume change between calcium oxide and calcium hydroxide is 17/33 (Nagataki et al., 1998). Another reason for this could be the presence of excess sulphates, which increases the formation of ettringite that in turn leads to swelling of the cementitious system (Min and Mingshu, 1993). A significant presence of gypsum has been identified in the XRD data of the CBPD (Figure 3-2).

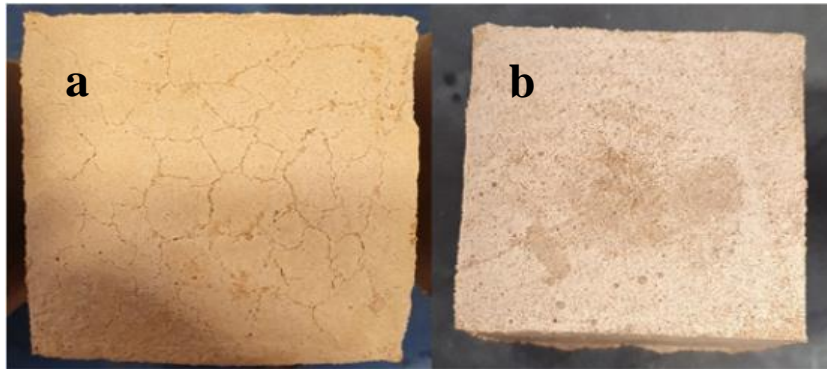


Figure 3-4 - Top-down view of CBPD mortar (a) KGH (b) KGA

3.3.4 Bulk Density

The densities of the heat and ambient cured samples at the age of 3, 7, and 28 days are presented in table 3-4. Overall, the densities of the mixes containing CBPD are lower than those typical in OPC mortar, which are normally higher than 2000 kg/m^3 (Bye, 2011). The high water to binder ratio is also a factor that needs to be considered. The highest bulk density was recorded for the KGCA mix, indicating a denser microstructure relative to the other samples, while KGH was the least dense. This indicates that the heat-curing regime negatively affected the microstructure development and led to a binder of lower density. The inclusion of cement in the KG mixes led to an overall increase in density likely due to better packing and denser hydration products formed.

Table 3-4 - Overall densities of CBPD binders at 3,7 and 28 days

Samples	Bulk Density (kg/m^3)		
	3 Days	7 Days	28 Days
KGA	1920 ± 25	1930 ± 30	1930 ± 50
KGH	1860 ± 35	1860 ± 45	1870 ± 10
KGCA	1960 ± 30	1960 ± 20	1960 ± 15
KGCH	1900 ± 15	1910 ± 20	1910 ± 20

3.3.5 Heat of Hydration

Figure 3-5 shows the temperature rise during hydration over time for KGA and KGCA, along with 100% OPC and 100% CBPD pastes.

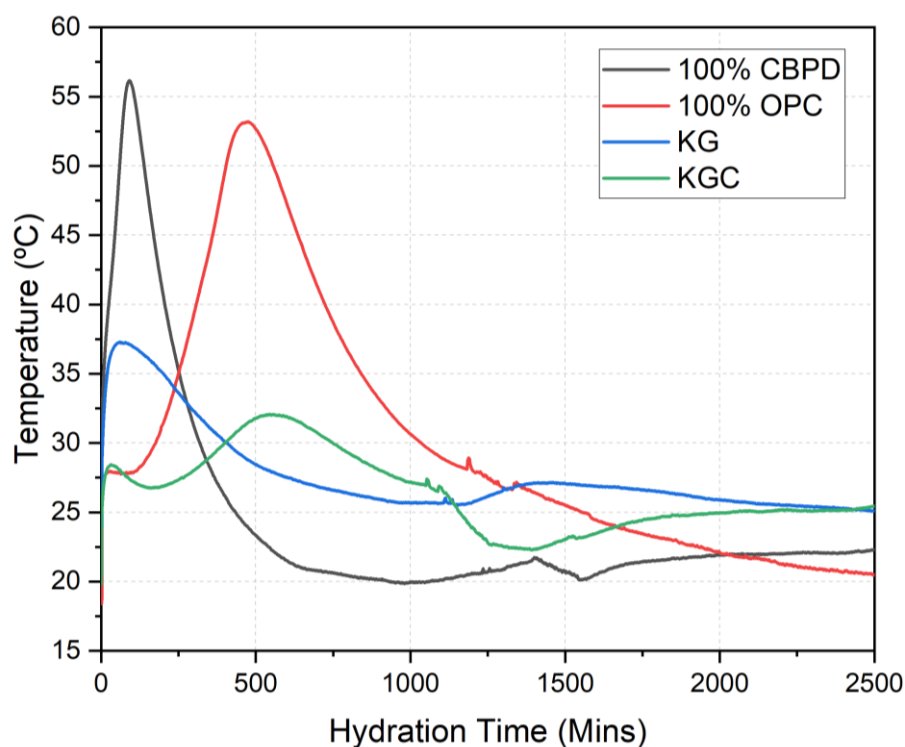


Figure 3-5 – Heat of hydration for KG, KGC, OPC and CBPD

Samples without cement (100% CBPD and KG) show a rapid increase in temperature, and no dormant period. 100% CBPD achieved its maximum temperature of 56.2°C after 91 minutes, whereas 100% OPC achieved its maximum temperature of 53.2°C after 460 minutes. A much faster decrease in temperature is also observed in the case of the CBPD. These findings agree with results by Czapik et al. (2020) where they also identified no dormant period in their CBPD heat of hydration results, rather just a rapid increase and decrease in heat evolution. Similarly, Wang et al. (2002) found that OPC-kiln dust binders have a much higher heat evolution compared to OPC and OPC-GBFS mixes. They attributed this to the alkalinity of the kiln dust.

The hydration behaviour for KG and KGC resembles that of CBPD and pure cement samples, respectively. Both mixes, however, show a significant decrease in temperature where KG and KGC reached max temperatures of 37.3°C and 32°C, respectively. This decrease in temperature is likely due to the latent hydration of GBFS, leading to an overall reduction of heat emitted (Moon et al., 2018). Both mixes showed slight increases in temperature following their main peaks, which could be attributed to the hydration of GBFS. The GBFS hydration begins earlier in the KG sample possibly due to the presence of the higher amount of alkalis given by the higher CBPD content in the mix. The hydration of GBFS is accelerated by the free lime content

due to the increase in alkalinity of the pore solution, leading to faster dissolution of GBFS particles (Kalina et al., 2018). This secondary peak can also be attributed to the secondary formation of Calcium Silicate Hydrate (CSH) gel. Additionally, KG showed no induction period due to the lack of rapid dissolution of the cementitious component and avoid formation of a layer on un-hydrated grains. Both mixes possess similar final temperatures after the measurements ceased and are still found to be higher than that of the 100% OPC and CBPD samples.

3.3.6 Compressive Strength

Figure 3-6 shows the compressive strengths achieved by the heat and ambient cured CBPD based samples. Heat curing is clearly beneficial at early age. KGH achieved a 3.8 MPa compressive strength after 3 days of curing, whereas KGA achieved 1.2 MPa. These results are expected as the hydration of the binders is accelerated by elevated temperature curing, which leads to an increase at the early age mechanical strength (Elkhadiri et al., 2009). A similar trend is observed for KGCH and KGCA mixes, which exhibited strength values of 4.6 MPa and 1.9 MPa, respectively, after 3 days of curing. The 3-day compressive strengths of KGCA and KGCH are found to be 62% and 22% higher than their cementless counterparts, respectively.

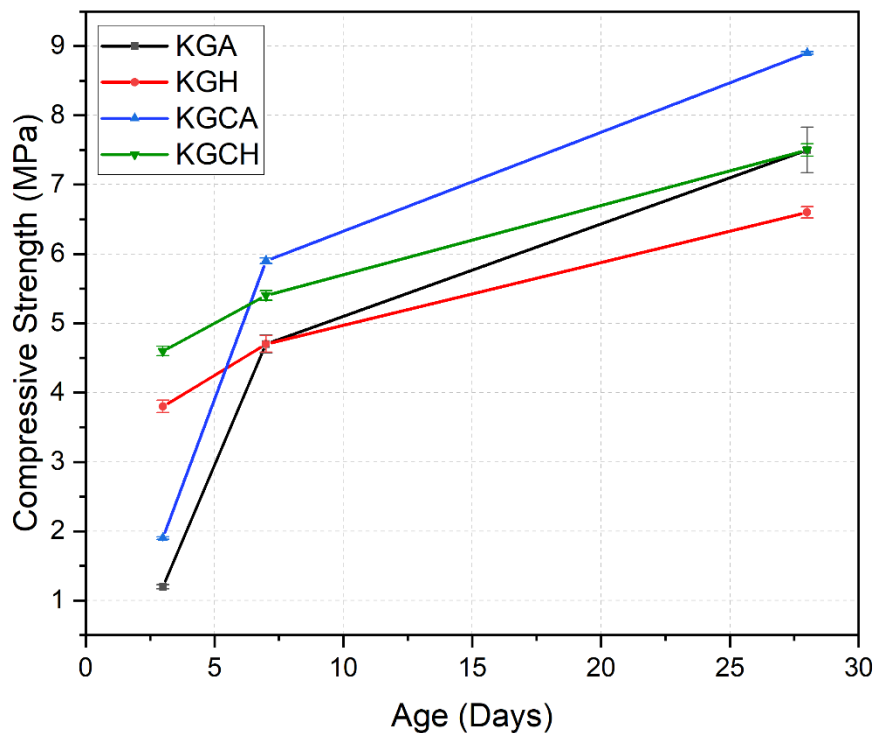


Figure 3-6 – Compressive strength results of CBPD binders

The benefits of heat curing on the mechanical properties are no longer valid at later ages, as ambient cured samples reach a higher compressive strength. The compressive strength of 7 day hydrated KGA and KGCA are 4.7 MPa and 5.9 MPa, respectively. The compressive strength at 7 days is almost the same irrespective of their curing condition for the heat cured mix designs with KGH achieving 4.7 MPa and KGCH achieving 5.4 MPa.

A more significant difference is seen for the 28-day strength results. KGA and KGCA had 28-day strengths of 7.5 MPa and 9.0 MPa respectively, whereas KGH and KGCH achieved 6.6 MPa and 7.5 MPa, respectively. The results also show the negative impact of heat curing and beneficial effect of cement addition. Despite faster hydration at the early ages, heat curing can retard the hydration at longer ages and develop an uneven distribution of reaction products leading to a comparatively more porous microstructure and consequently a lower strength at later ages (Liu et al., 2022).

Overall, the mortars achieved a strength (>7.5 MPa) that can be considered adequate for low-end applications, such as for wall rendering for replacing lime mortar (Al-Harthy et al., 2003).

3.3.7 X-Ray Diffraction

X-Ray diffraction (XRD) was used in this experiment to identify the chemical phases in the hydrated cementitious samples. Figure 3-7 shows the XRD patterns for KGA, KGH and Figure 3-8 shows the XRD patterns for KGCA, and KGCH a 3, 7, and 28 days. The XRD patterns present several prominent peaks at different 2θ locations. One of the primary differences present in these specimens relative to hydrated OPC, is the presence of Friedel's salt peaks found at 11.3° , 31.2° , and 50.26° . CBPD contains a high concentration of chlorides that react with water and other cementitious phases to precipitate Friedel's salt (Chaunsali and Peethamparan, 2013; Konsta-Gdoutos et al., 2002).

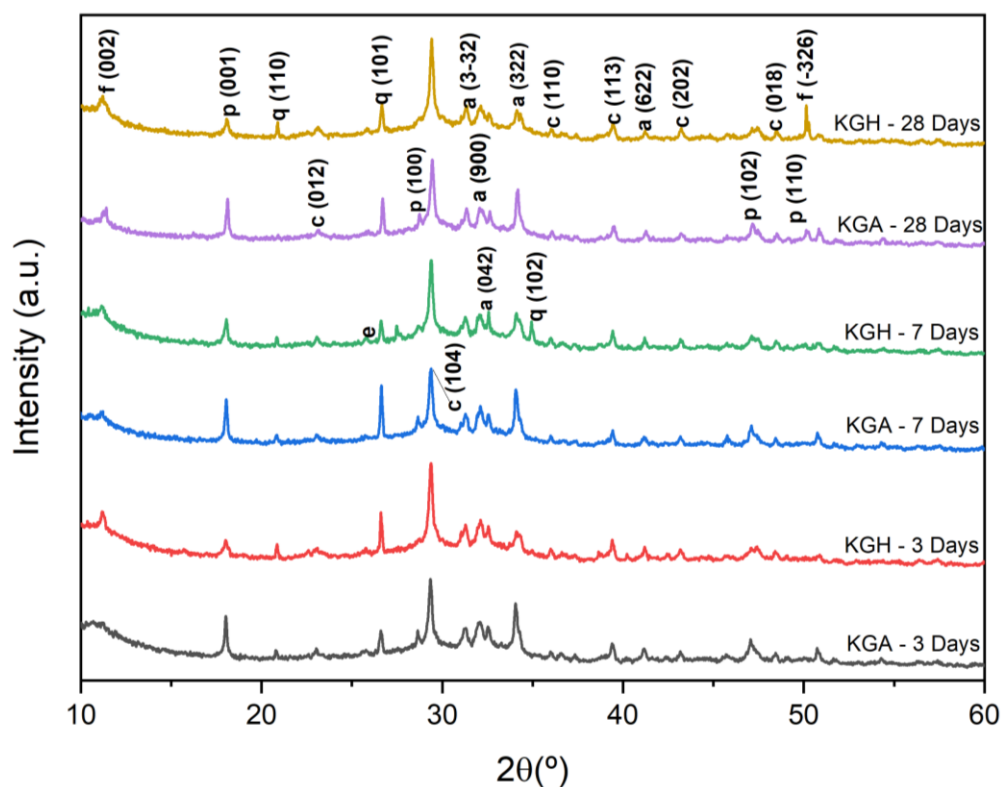


Figure 3-7 – XRD patterns for KGA and KGH

Several portlandite (p) peaks have been detected at $2\theta = 18.07^\circ, 28.7^\circ, 47.1^\circ, 50.8^\circ,$ and 54.3° . The portlandite peaks have a notably higher intensity for ambient cured samples relative to that of the heat cured samples. The peaks located at $2\theta = 31.2^\circ, 32.2^\circ, 32.6^\circ, 34.1^\circ,$ and 41.2° can be attributed to alite (a) (tricalcium silicate). Calcite (c) peaks are observable at $2\theta = 23.1^\circ, 29.4^\circ, 36.1^\circ, 39.4^\circ, 43.2^\circ,$ and 48.5° , which is typically an inert phase. The other prominent peaks due to the presence of quartz (silicon dioxide) are visualised at $2\theta = 20.9^\circ$ and 26.7° . Contrary to observations from other studies (Chaunsali and Peethamparan, 2013; Sadique and Coakley, 2016, Marku et al., 2013), the presence of ettringite (e) is not very prominent in the X-Ray analysis. Only some faint peaks are visible at around $2\theta = 25.8^\circ$. This may be due to the way the specimens were processed to stop the hydration reaction using oven-drying that may have led to the decomposition of the ettringite.

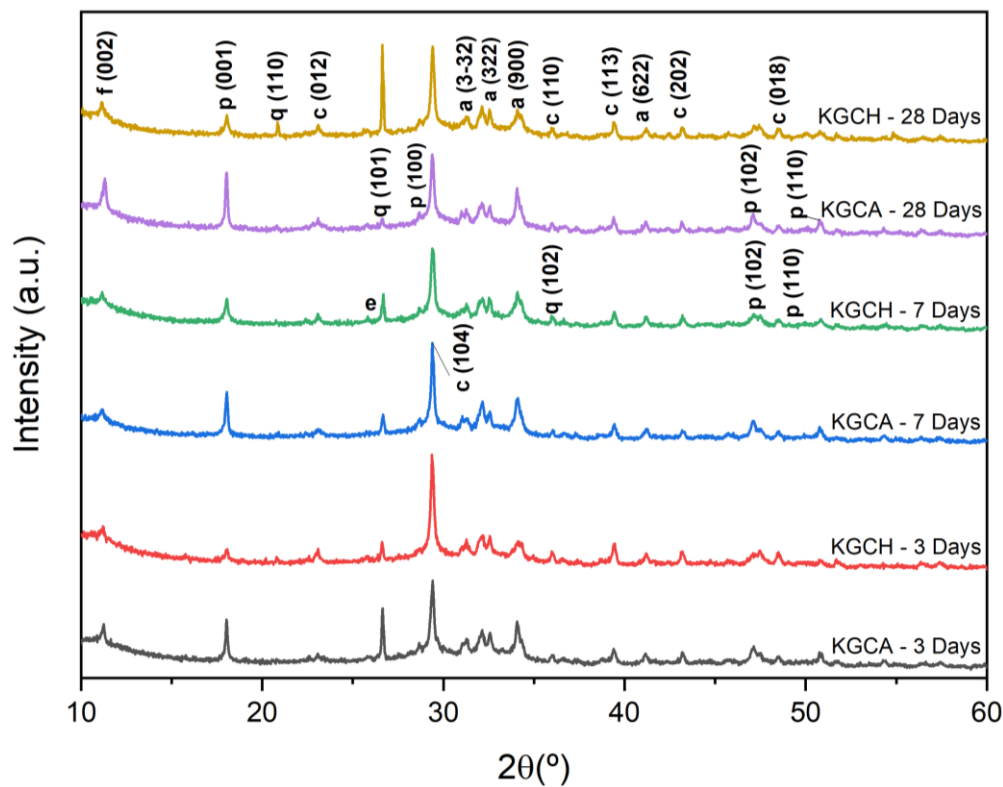


Figure 3-8 - XRD patterns for KGCA and KGCH

As observed in the diffraction patterns, all four mix designs represent the same chemical phases with different intensities. The peak area ratio is used to semi-quantify the degree of hydration by considering the two most prominent peaks that appear in the XRD. Since CSH is amorphous in nature and often located behind a crystalline calcite peak at 29.4° , the portlandite is selected as the main crystalline product of the hydrated CBPD system and its peak located at 18.04° was used for the analysis. Additionally, alite (a) is selected as the reactant, and its most prominent appearance is found at 34.2° (Mollah et al., 1999). The peak area ratio is calculated by taking the ratio between the peak area of portlandite (A_p) and the peak area of alite (A_a). The peak area has been determined through Gaussian fitting of the X-ray diffraction patterns using OriginPro 2021 software as shown in Figure 3-9.

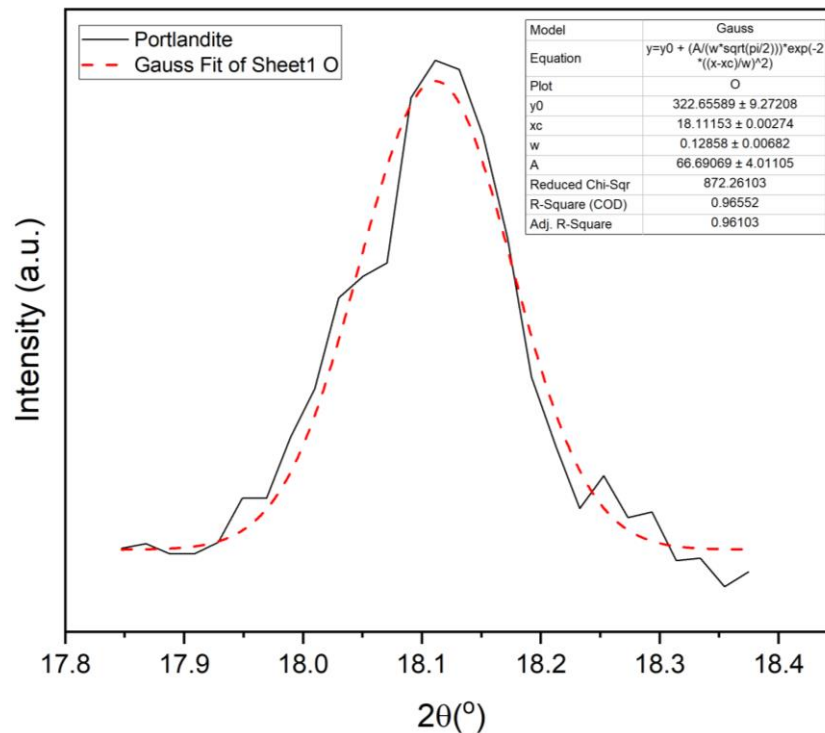


Figure 3-9 – Gaussian fitting of portlandite peak to determine the peak area ratio

Figure 3-10 shows the results, where it is evident that the ambient cured samples presented the largest amount of hydration overall. KGA has peak area ratio values of 0.58, 0.66, and 0.71 at 3, 7, and 28 days, respectively, indicating an increase in hydration over time. On the contrary, KGH has peak area ratio values of 0.57, 0.55, and 0.49 at 3, 7, and 28 days, respectively, demonstrating a slight reduction in the amount of hydration. This clearly indicates the significance of the curing regime for these CBPD binders, where despite the early age benefits of heat curing, long term this has an adverse effect on the hydration and properties of the product.

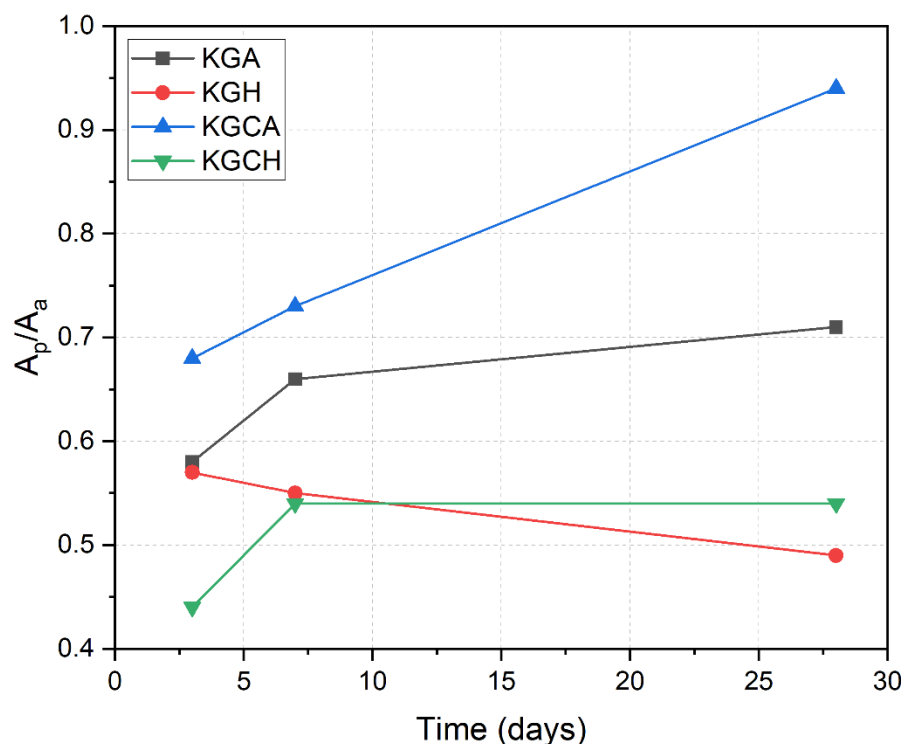


Figure 3-10 – Peak area ratio for CBPD binders

The long-term benefits of ambient curing were further validated by the binders containing cement. KGCA presented peak area ratio results of 0.68, 0.73, and 0.94 at 3, 7, and 28 days, respectively, whereas KGCH presented results of 0.44, 0.54, and 0.54 at 3, 7, and 28 days, respectively. The results indicate that heat curing of CBPD binders leads to a stagnation of hydration, further emphasising that heat curing is mostly effective for early age strength. Overall, these results prove the compatibility of CBPD with GBFS, without the use of cement, however the use of cement has clear benefits in the quality of the binder formed.

3.3.8 Fourier Transform Infrared Spectroscopy

Figure 3-11 presents the FTIR spectra for KGA, KGH, KGCA, and KGCH at 28 days, ranging from 500 cm^{-1} to 4000 cm^{-1} . The results present typical bands that are expected in cementitious materials. All the samples present similar bands and peaks, but with slightly different wavenumbers and intensities. The presence of calcium hydroxide is clear as the peak at $3642\text{--}3645\text{ cm}^{-1}$ represents an absorption peak of portlandite and is attributable to O-H stretching. There are faint peaks visible ranging between $2976\text{--}2980\text{ cm}^{-1}$ and $1794\text{--}1796\text{ cm}^{-1}$ which are due to C-H stretching and the presence of CaCO_3 . Peaks around $1424\text{--}1427\text{ cm}^{-1}$ and $873\text{--}876\text{ cm}^{-1}$ are also due to carbonate phases. A broad shoulder visible at around $1134\text{--}1140\text{ cm}^{-1}$ is

due to the stretching of the S-O functional group, confirming the presence of sulphates in the mixes and consequently ettringite (García Lodeiro et al., 2009).

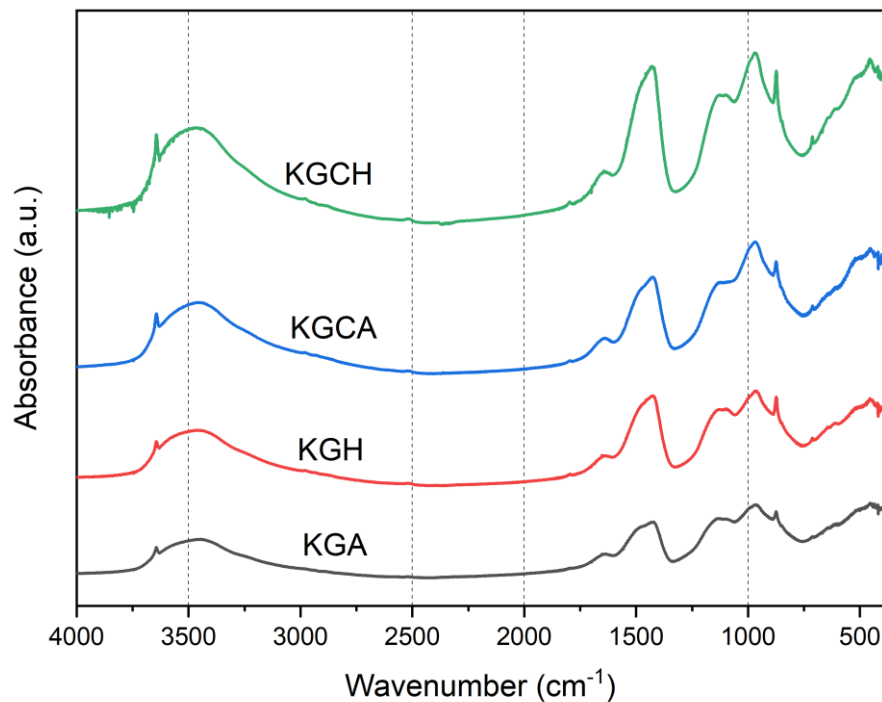


Figure 3-11 - FTIR spectra of CBPD binders at 28 days

CSH peaks are normally found within the range of 1100 cm^{-1} and 950 cm^{-1} (Yu et al., 2004). The presence of CSH was confirmed in the FTIR analysis as a peak was visible between $962\text{--}970\text{ cm}^{-1}$, which can largely be attributable to Si-O stretching as confirmed by past research. Table 3-5 presents the location of all the functional groups. Typically, a shift in the peaks can indicate the degree of polymerisation (Lin et al., 2020), however in the samples tested, the Si-O band was detected in similar locations. These results confirm that the CBPD binders produce similar binders to those expected in cementitious binders, despite the inclusion of chlorides, and different proportions of chemical components.

Table 3-5 – Location of functional groups on the FTIR spectra

Wavenumber (cm ⁻¹)	Functional Group
3642-3645	ν OH (Ca(OH) ₂)
2976-2980	C-H
1794-1796	CaCO ₃
1638-1643	δ OH (H ₂ O)
1424-1427	ν_3 CO CaCO ₃
1134-1140	S-O
962-965	Si-O (CSH)
873-876	C-O ν_2

3.3.9 Differential Scanning Calorimetry

Differential scanning calorimetry (DSC) was used to identify the main products within the CBPD binders at 28 days. Figure 3-12 presents the results from the DSC analysis. The main endothermic peaks were identified at 410-460°C and 660-710°C which can be attributed to the decomposition of portlandite and calcium carbonate, respectively (Stepkowska et al., 2006). The amount of hydrated product can be determined by quantifying the enthalpy change (DH) of portlandite from the DSC graph (Chakraborty et al., 2016). The results overall, corroborate the compressive strength and XRD results, where the ambient cured binders presented a larger amount of hydrated product. KGA and KGH had DH values of 93.7 J/g and 22.7 J/g, respectively, demonstrating a much higher amount of hydration for KGA. The results were very similar for KGCA and KGCH which achieved DH values of 92.1 J/g and 28.1 J/g. Interestingly, KGA had a slightly higher value than that of KGCA, however they are overall almost identical.

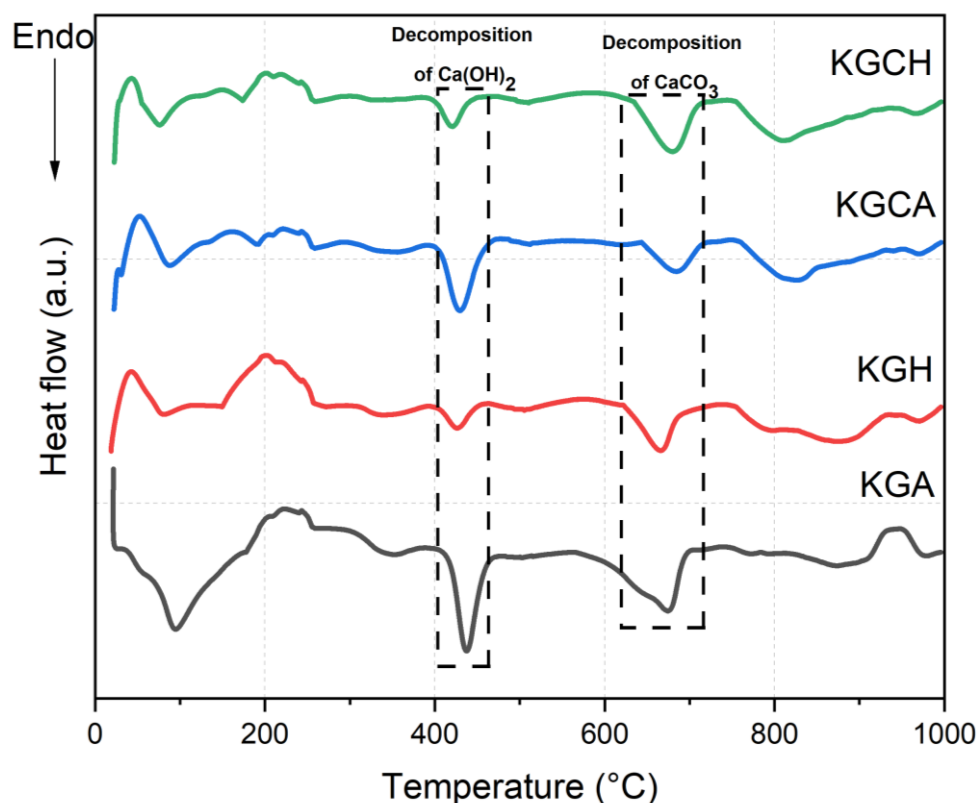


Figure 3-12 - DSC results of CBPD binders at 28 days

3.3.10 Thermogravimetric analysis

Figure 3-13 shows the TGA and DTG curves for KGA, KGH, KGCA, and KGCH after 28 days of hydration. Significant mass loss has been detected initially at 50-200°C. This is due to the evaporation of surface bonded water and the dehydration of hydrated phases such as CSH. This is observed in all pastes. An additional hump can be observed at 100-150 °C which could be attributed to the decomposition of ettringite. The next major mass loss has been located between 290-380°C. This hump, with a peak at around 330°C, is attributable to the decomposition of Friedel's salt (Birnin-Yauri and Glasser, 1998). As observed in the XRD analysis, the chloride salts are abundant in these samples, which undergo a chemical reaction to form Friedel's salt. This hump is visibly reduced in the mixes containing cement due to the reduced content of chloride salts. Another prominent mass loss has been observed at 390-460°C, and it is caused by the decomposition of portlandite.

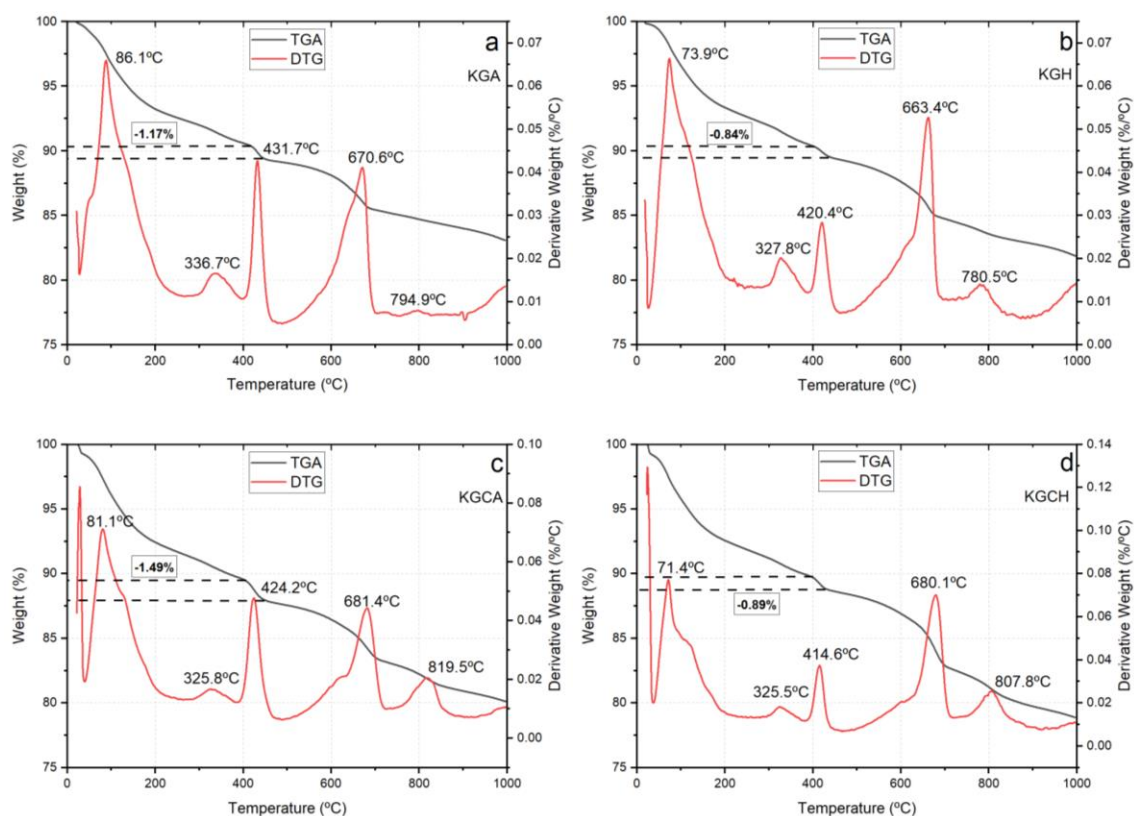


Figure 3-13 – TGA and DTG curves of (a) KGA (b) KGH (c) KGCA (d) KGCH

The mass loss between 600-800°C is due to the decomposition of carbonated phases. At around 615°C, an additional hump is visible in the DTG curves, likely due to the mass loss of OH-groups from the CSH gel formed in the cementitious binders (Gabrovšek et al., 2006). The broadest one of these humps can be seen in the KGCA mix design. The sharpest carbonate peak is seen at 660°C, which is attributable to the mass loss of amorphous carbonate phases. The possible final carbonate peak appears at 780°C due to the decomposition of a more crystallised calcite phase, which requires a higher temperature to decompose (Stepkowska et al., 2006). This peak shifts to the right for KGCA and KGCH (800°C), likely due to the crystalline arrangement in the presence of cement. This hump is not very clear for the KGA mix, possibly due to the sample used not containing a large quantity of ordered CaCO_3 .

The mass losses for portlandite are indicated in Figure 3-13. It is seen that heat cured mixes are characterised by a smaller mass loss due to portlandite decomposition than ambient cured samples, in both binder composition. KGH and KGCH mixes have a mass loss of portlandite of 0.84% and 0.89%, respectively. On the contrary, KGA and KGCA mixes have a portlandite mass loss of 1.17% and 1.49%, respectively.

3.3.11 Mercury Intrusion Porosimetry

Figure 3-14 presents the cumulative mercury intrusion against the pore diameter for the mixes after 28 days of curing. The shapes of the curves are similar to each other; however, it is evident from these results that the use of heat curing for the CBPD paste leads to a more porous microstructure relative to their ambient cured counterparts. The cumulative intrusion value is highest for the KGH sample, followed by the KGCH binder. This increase in porosity due to heat curing is assumed to be due to the increase in stress within individual pores of cementitious paste. These internal stresses can widen the pore and cause micro-cracking, hence increasing the porosity. Consequently, this increased stress may enlarge the pores leading to a more permeable microstructure. The effect of increased porosity is also reflected in the density of the specimens, where the ambient-cured samples are overall denser relative to the heat-cured samples.

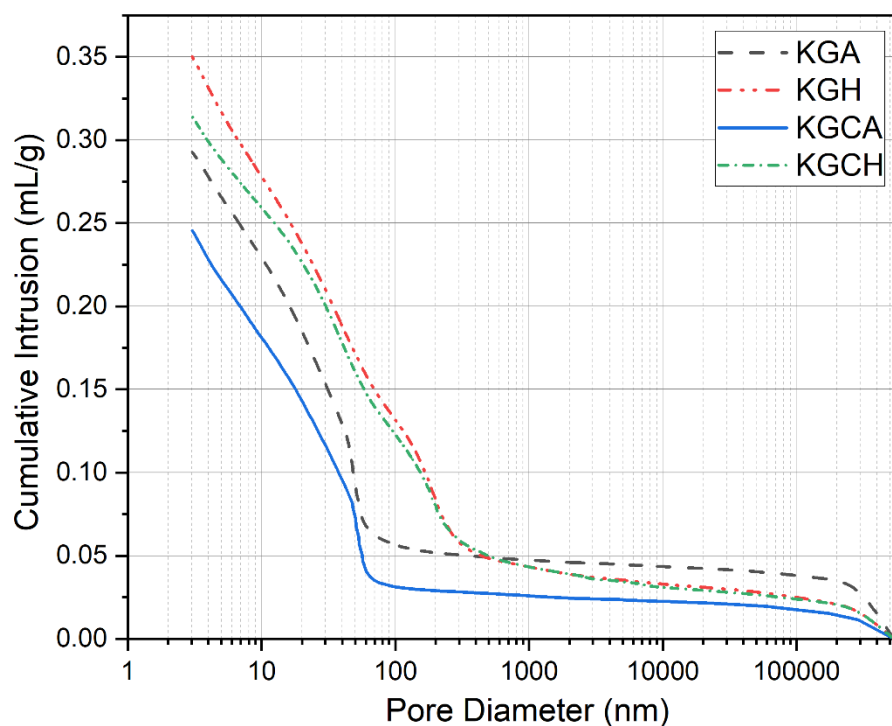


Figure 3-14 - MIP graphs of CBPD binders

Table 3-6 presents the porosity values of these binders. The porosity of these samples can be considered to be quite high. The main reason for this is the particle size of the component used and the water to binder ratio. In general, a higher w/c ratio will lead to separation of cement particles by entrapping air, leading to a more porous and less dense microstructure. High permeability in cementitious binders can lead to detrimental effects on the durability and strength of a cementitious system (Neville, 2012). Furthermore, as observed earlier, the

addition of CBPD can lead to swelling due to the high free CaO content, which subsequently can cause microcracks and increase porosity.

Table 3-6 - Porosity results for CBPD binders

Mix Design	Porosity
KGA	39.5%
KGH	46.0%
KGCA	35.4%
KGCH	42.7%

3.3.12 Scanning Electron Microscopy

The microstructure of the fracture surfaces of CBPD pastes was investigated using a scanning electron microscope (SEM) as shown in Figure 3-15.

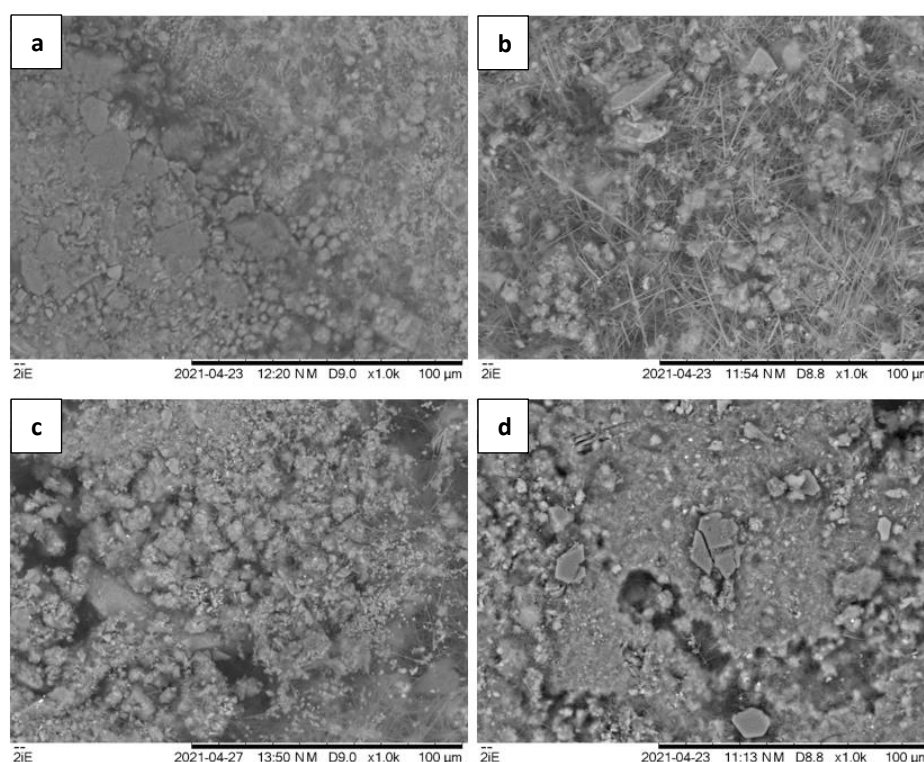


Figure 3-15 – SEM images of (a) KGA (b) KGCA (c) KGH (d) KGCH

From the figure, it is apparent that a large amount of ettringite (strand like crystals) is visible in KGCA (Figure 3-15b). This is due to the higher quantity of sulphates in the CBPD. It has been reported elsewhere that ettringite is largely responsible for the early development of strength of binders containing kiln dusts (Sadique and Coakley, 2016). Additionally, calcium hydroxide crystals are visible in both KGA and KGCA. From Figure 3-15c, some crystals are identified in the microstructure of KGH paste. Compared to the ambient cured samples, the heat cured mixes show similar products but seemingly a more porous microstructure as evidenced by the darker regions in the images. This can indicate that more hydration occurred

in the ambient cured samples, which can explain their enhanced mechanical properties relative to the heat cured mixes. Another possibility is that they had similar hydration, however more expansion occurred in the heat cured samples. The microstructure analysis seems to corroborate the physical and mechanical properties of CBPD based mortar/paste.

3.4 Hydration Reaction

The hydration of CBPD binders is schematically shown in Figure 3-16. Initially, a strong exothermic reaction causes a large change in volume, where a colloidal layer forms around the grains of the binder (Figure 3-16 Step 2) and the free lime is converted into Ca(OH)_2 by reaction with water. As shown by the heat of hydration results, the exothermic reaction is stronger for the CBPD binders than typical OPC binders. GBFS does, however, reduce the overall heat of hydration (Kolani et al., 2012). Hence, a pure OPC binder may have a higher heat of hydration overall. Other products such as ettringite are also formed in this step due to the reaction of sulphate ions with aluminate phases. Aluminium also reacts with the chloride ions in the CBPD to form Friedel's salt, as shown by the XRD results.

Once the colloidal layer has thickened and formed around the grains, water is blocked from the unreacted core, slowing down the reaction and hydration of CaO (Figure 3-16 Step 3). This is defined as a transitional period. Following this step, nucleation and flocculation of the layer continues enabling more water passing through. GBFS hydration is accelerated due to the alkaline environment caused by the portlandite formation. The microstructure will then densify (Figure 3-16 Step 4), and the hydration and formation of reaction products will continue over time. CBPD binders containing cement will result in lower ettringite and Friedel's salt content due to the lower sulphate and chloride content, and an overall denser microstructure.

Evidently, different factors such as the chemical composition of CBPD, GBFS and cement, water to binder ratio, curing regime etc. would lead to changes in the hydration of these binders.

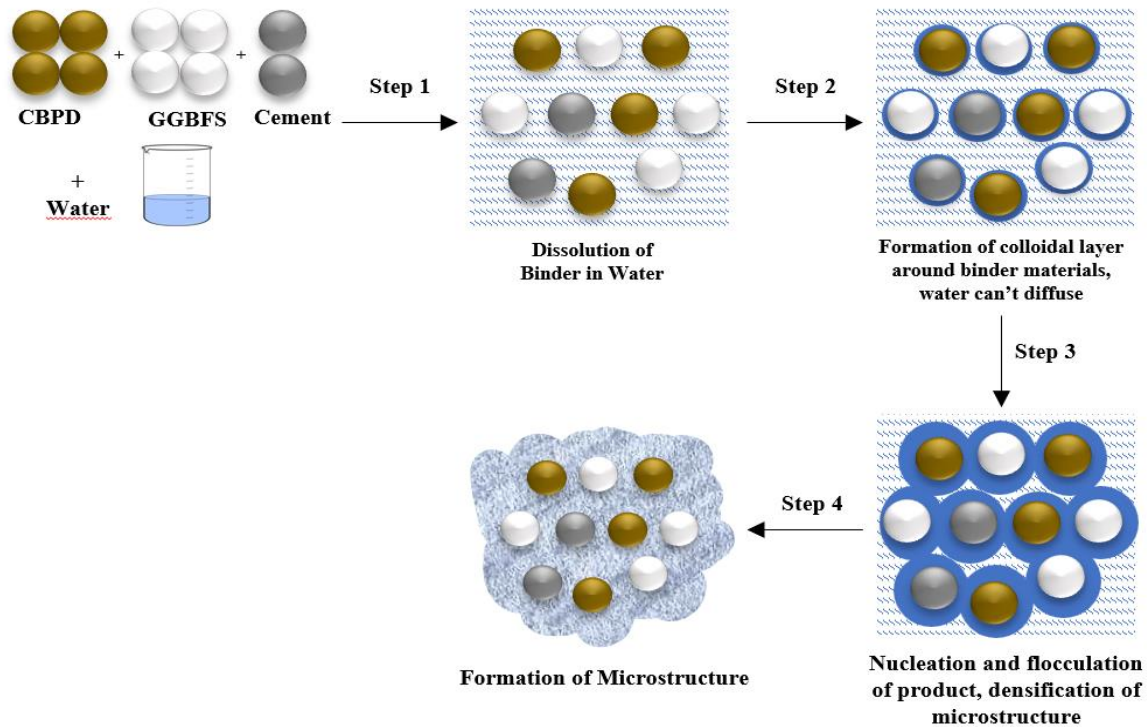


Figure 3-16 – Hydration model of CBPD ternary binders (Chakraborty et al., 2016)

3.5 Life-Cycle Analysis Results

The global warming potential results for all the investigated binders and a representative OPC mix are presented in Figure 3-17a below. As expected, the OPC mix was the highest emitter of all the materials. Relative to OPC, the CBPD binders had significant environmental gains despite the heat curing. OPC had 179.1 kg CO₂ eq, a 47% increase relative to KGCH. Cement was responsible for 92% of emissions of this binder as seen in Figure 3-17b. The adverse effect of cement inclusion is further seen when comparing KGA to KGCA, where KGCA had more than double the total GWP of KGA with only a 20% replacement of cement. Thus, the importance of cement alternatives is stressed in these results.

When comparing the heat and ambient curing results, the benefits of ambient curing are observed. KGA and KGH had 27.9 kg CO₂ eq and 97.5 kg CO₂ eq, respectively. This amounts to a 250% increase in emissions. Heat curing was responsible for 70% of emissions for KGH due to the energy consumption. The total impact from heat curing can be improved if the curing time is reduced or sustainable energy streams are used. Based on these results, heat curing can only be recommended if early age strength is imperative.

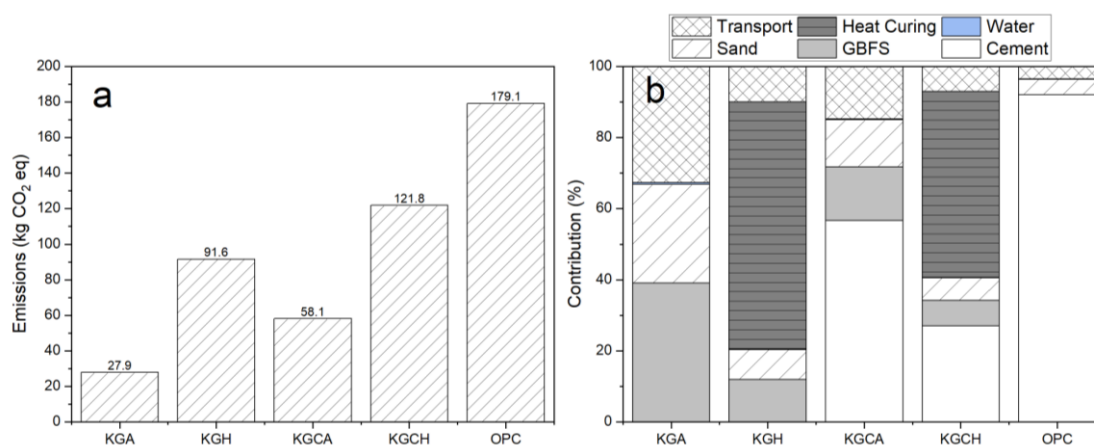


Figure 3-17 - Life cycle analysis results (a) global warming potential (b) contribution analysis

While not covered in this research, the emissions associated with conventional AAM activators can also be quite high. It has been shown that 1.1 kg of CO₂ is emitted for the manufacture 1 kg of sodium hydroxide, and 1.2kg of CO₂ is emitted for 1 kg of sodium silicate (Mellado et al., 2014). In addition, it has also been estimated that 80% of the cost of AAMs is due to the cost of the commercial alkali activator (Luukkonen et al., 2018). Ultimately, the benefits of the reuse of CBPD and waste activators in general are shown from the LCA modelling.

3.6 Technical Feasibility

This investigation was carried out to assess the potential of using CBPD as a cement replacement in combination with GBFS and examine its behaviour in ternary and binary blends composed of CBPD-GBFS-OPC. Hence, the fresh, mechanical, and microstructural properties of these binders were investigated. One of the main drawbacks of using these binders was their high-water demand, consequently leading to a high water to binder ratio. To overcome this, future research will focus on reducing the amount of water either using chemical admixtures, fine aggregates with a lower water absorption, or changing the binder to aggregate ratio. A lower water to cement ratio will likely have positive effects on both mechanical performance and other physical properties, such as porosity. An improvement in these properties would enable the possible uses of these mortars in structural applications.

The long-term performance of these binders is yet to be properly understood. Due to their high chloride content, the use of CBPD mortars would not be suitable for elements reinforced with steel rebars. Steel fibres, however, could be used for the development of structural elements as they have been shown to withstand up to a 5% chloride content (Raupach et al., 2004). Additionally, other types of fibre such as glass, plastic, jute etc. may be tested where they would not be affected by the chloride content.

Furthermore, a factor that makes the reuse of CBPD very feasible is that it is produced at any cement plant which has a bypass installed in its rotary kiln, hence, a circular economy would be promoted as everything produced, including waste, would be reused. This would not only help produce a sustainable and cheap building product but would save on landfilling costs which would be a large incentive for cement plants.

3.7 Conclusions

This paper explored the reuse of CBPD as a cement replacement. The experimental results provided several insights into the behaviour of CBPD based binary (CBPD-GBFS mixture) and ternary (CBPD-GBFS-OPC) binders, and the following conclusions can be drawn:

- 1) CBPD has a high-water demand, and its use leads to stiff mixes. More workable mixes can be obtained by adding 20% of cement to the binder. Consequently, the value of standard consistency is higher for CBPD binders. Due to the required high water to cement ratio, the porosity of the mixes was also found to be relatively high which impacts negatively on the other properties such as strength.
- 2) CBPD is much more reactive at early ages than OPC binders, with a rapid heat evolution and showing no dormant period.
- 3) CBPD-GBFS based binders can be used successfully to develop mortars with suitable 28-day strengths. The inclusion of cement (20% by mass w.r.t binders) was also found to be more beneficial on mechanical properties.
- 4) Heat curing was only found to accelerate early age strength development but did not lead to any additional benefits. On the contrary, the heat-cured samples experienced severe swelling, accompanied with extensive surface cracking, which can negatively affect both short-term and long-term mechanical properties.
- 5) Microstructural analysis showed that the main hydrated phases present in a typical OPC paste are also present in CBPD based paste. A large amount of portlandite was found in the CBPD paste as demonstrated by XRD, TGA, and SEM analysis. While ettringite

was not identified in the XRD analysis, it is clearly identified in the SEM images. Heat curing lead to the formation of less reaction products.

- 6) Life cycle analysis showed that KGA had the lowest CO₂ emissions associated with it, where KGCA had more than double its emissions due to cement content. Heat curing also proved to be detrimental with KGH having 250% higher emissions than KGA.

Overall, it is demonstrated that CBPD can be used as a cement replacement, without the need for heat curing. Sustainable binders like these provide a good option for the reusability of CBPD. The use of this material, for example in the production of mortar for wall plastering, can replace the cement and lime mortar and may lead to promote a circular economy. Given the limitations due to the high-water demand of CBPD, future research should focus on the use of admixtures or different aggregates with CBPD binders to reduce the required water to cement ratio. This would also have a beneficial impact on the performance of such binder in terms of shrinkage, strength development, and durability.

Chapter 4 – The effect of CBPD Composition on the properties of Slag-based Mortars

(Published paper in *Construction and Building Materials* on August 14th, 2024)

Abstract

Research on sustainable alternatives to Ordinary Portland Cement aims to reduce global CO₂ emissions from cement production. Utilizing byproducts or waste materials to create sustainable binders is a promising approach. Cement bypass dust is being investigated as a potential activator of pozzolanic materials, however there is large variability in the composition of this dust and research is necessary to understand the differences for the potential application of the waste material. The objective of this work was to compare two bypass dusts where ternary and binary mortars of bypass dust (50%, 30%, 10%, 0% and by weight), cement (100%, 80%, 40% and by weight), and blast furnace slag (50%, 30%, 10% and 0% by weight), were produced. Mortars were all ambient cured and a water to binder ratio of 0.6 was maintained for all mixes.

The results showed that one bypass dust had a much higher free lime and chloride content, whereas the other had more calcite and sulphates. Compressive strengths of the 1:1 slag and sulphate rich bypass dust were of 18.6 MPa at 90 days, and lime rich bypass dust achieved 15.1 MPa. X-ray diffraction and thermogravimetric analysis revealed that sulphate rich bypass dust formed more ettringite, enhancing strength, while lime rich bypass dust formed more portlandite due to its lime content. Chemical shrinkage results showed volumetric expansion at early ages for both bypass dusts with lime rich bypass dust swelling up to 0.057 ml/g and sulphate rich bypass dust up to 0.015 ml/. Despite this, both bypass dust binders exhibited higher shrinkage strains over a 150-day period compared to cement, where sulphate rich and lime rich bypass dust had strain percentages of 0.225% and 0.228%, respectively. This work found the main differences between the composition of two bypass dusts, and it was found that these materials can be reused to fabricate cementless binders.

Graphical Abstract

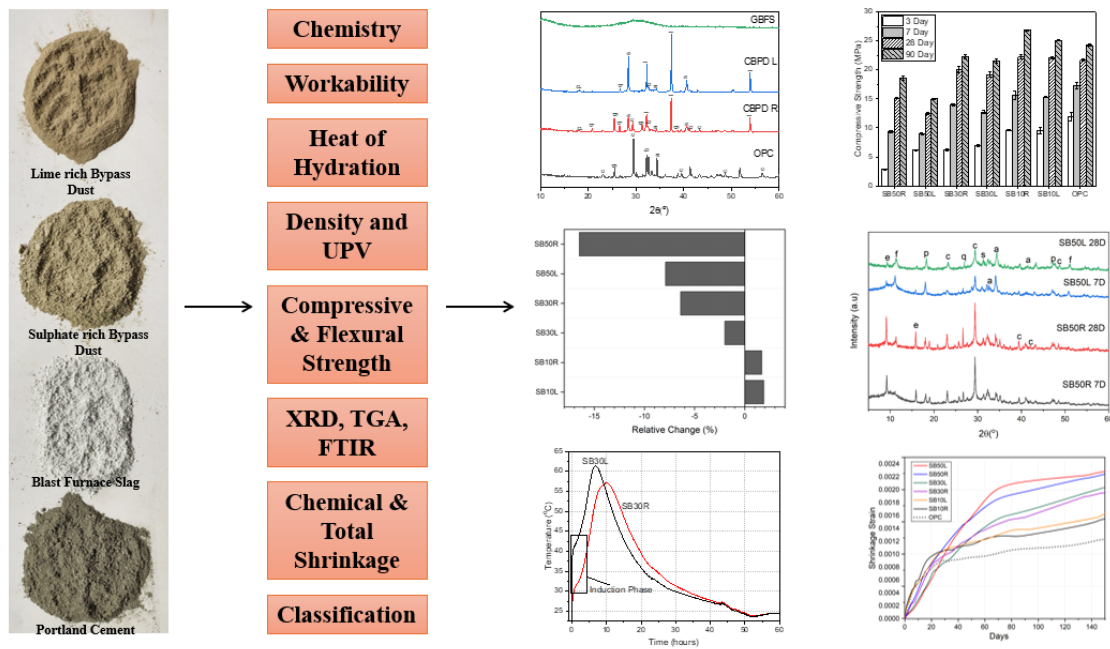


Figure 4-1 – Graphical abstract presented in published journal paper

Keywords: Cement mortar, Bypass dust, Blast furnace slag, Waste utilisation, cement replacement

4.1 Introduction

The production of cement is a very energy intensive process that requires the use of high temperatures (1400°C) to produce clinker (Hewlett, 2019). Due to this, cement manufacture contributes to 8% of global carbon dioxide emissions (Zhang et al., 2023). Hence, the construction industry is facing demand to provide more sustainable solutions to Portland cement (OPC) manufacture.

Many techniques are currently being utilised to reduce the environmental burden of the concrete industry. These include the use of recycled aggregate (Wang et al., 2022), carbon curing of concrete (Kazemian & Shafei, 2023), and the use of supplementary cementitious materials as cement replacements such as granulated blast furnace slag (GBFS) (Lothenbach et al., 2011). GBFS is a foundational element in the formation of alkali-activated materials (AAMs), which offer a cementless alternative for construction applications. Research on GBFS based AAMs has been well established and currently work is being undertaken to further improve the technology through techniques such as the inclusion of titanium dioxide nanoparticles (Coffetti et al., 2023). GBFS has also been shown to combine with waste materials such as glass powders to make AAMs (Derinpinar et al., 2022). Ladle furnace slag

has also been reused at cement levels of 20% showing improvements in compressive strengths (Revilla-Cuesta et al., 2023; Lopez-Ausin et al., 2024).

Additionally, several successful examples of cementless AAMs utilising waste materials have been developed in previous research. Cakmak et al. (2024) developed a binder composed of obsidian and waste glass activated by 12M sodium hydroxide as activator. Their findings showed compressive strengths of up to 52.6 MPa. Use of demolition waste as a precursor in AAMs have also been shown to be very effective (Kravchenko et al., 2024).

Despite all the advances in AAM technology and innovation, challenges such as high global warming potential from chemical activators (sodium silicate), and overhaul in infrastructure, limit their widespread use into sectors like the precast industry (Alnahhal et al., 2021). Exploring sustainable activators from waste streams could address these challenges, offering a more environmentally friendly and cost-effective approach.

Cement bypass dust (CBPD) is a waste material that has been shown to have activating potential of GBFS (Barnat-Hunek et al., 2018). Due to an increase in the use of alternative fuels in the cement kiln has led to the need of implementing a bypass system in most modern kilns (Czapik et al., 2020). CBPD is formed during the manufacturing process of cement clinker. Due to its high alkali, sulphate, free lime and chloride content, this material is largely landfilled and unexploited. Cement Kiln Dust (CKD) and CBPD are often mistaken for being the same material, however they are not and have differences to each other. CKD is typically captured early in the kiln system, where it is captured by exhaust gases and is collected by electrostatic precipitators or baghouses (Adaska & Taubert, 2008). Due to its typically stable condition, CKD is often recycled and returned to the kiln. On the other hand, CBPD is collected from the bypass system at the bottom of the kiln, where the bypass is often used to extract gasses high in chlorides and sulphates. Since CBPD is produced at much higher temperatures (1000°C), it is more calcined than CKD and contains higher levels of free lime. CBPD is much more reactive than CKD and has a higher quantity of chlorides and sulphates. Hence, for this reason CBPD is landfilled. It is important to reuse CBPD as its reuse will promote a circular economy and this is a large incentive for cement companies globally. Furthermore, CBPD has been shown to have the potential of contaminating ground water addressing this would require complicated remediation techniques (Cheng et al., 2023; Hu et al., 2022). Hence better reuse of the material is encouraged.

CBPD accounts for circa 2-5% of the clinker production by weight (Hanein et al., 2020). This indicates that at least 80 million metric tonnes of bypass dust were produced in 2022 based on clinker production statistics (Tkachenko et al., 2023).

The chemical composition of CBPD largely changes based on the cement plant, which has been attributed in the past to the kiln type, fuel type and raw materials utilised (Adaska & Taubert, 2008). Research comparing two types of CBPD is scarce and a large gap in knowledge exists on this subject, however there has been some work comparing two types of CKD. Chaunsali and Peethamparan (2013) investigated two types of CKD on heat-cured mixes and found that the CKD with the higher free lime attained a higher strength in pozzolanic mixes. Sadique and Coakley (2016) also reached the same conclusion, finding that higher sulphate and lime contents lead to stronger concretes, however admitted that due to the range in composition, further investigation was required on this material. Wojtacha-Rychter et al. (2022) replaced cement by up to 30% with CBPD and found strengths up to 51 MPa after 90 days in their concrete blocks. Gdoutos and Shah (2003) compared four types of CKD. They found that the CKD with highest sulphate content formed the most ettringite and had the earliest setting time, and that its formation was also a contributor to strength. CKD has also been used in other building materials such as roof tiles (ElNaggar et al., 2023). Moreover, CKD has been shown to have excellent carbon sequestration potential improving the sustainability of the material (Adekunle, 2024).

Thus, the current state of the research is not enough to fully understand the differences and potential of CBPDs. Proper classification of CBPD is still required if this material is to be standardised and utilised properly in construction. Besides the sustainability potential, one of the primary benefits of using CBPD in mortars and concretes is that it does not change the manufacturing process, where other liquid activators would.

Hence, the main objective of this was to compare two different types of CBPD procured from Eastern and Western Europe by using them as cement replacements in mortars. To the best of the authors knowledge, there is a lack of research on the differences between CBPD compositions and their interactions with GBFS and GBFS-OPC mortars. Additionally there is a gap in knowledge regarding the effect different compositions of CBPD have on cement-like binders. A good understanding on the properties of different CBPDs and what can be expected from this material is lacking. Furthermore, classification of different CBPDs and their potential uses is unavailable currently. To understand the material better, the effects of CBPD composition on fresh and mechanical properties, as well as heat of hydration were investigated.

In addition to this, the microstructure of CBPD-GBFS and CBPD-GBFS-OPC binders were investigated through x-ray diffraction (XRD), thermogravimetric analysis (TGA), and Fourier Transform Infrared Spectroscopy (FTIR). Finally, both the chemical and total shrinkage of these binders were observed in this experiment.

4.2 Experimental Work

4.2.1 Materials

Two types of CBPD were examined, one from a cement plant in Rugby, UK, and another from a plant in Latvia, labelled as CBPD R and CBPD L, respectively. The GBFS used in this experiment was acquired from Scunthorpe, UK. The OPC used was of the CEM II type (containing 35% GBFS), grade 32.5R and was procured from Hope Cement Works, Sheffield. Based on previous work (Chapter 3), CEM II was found to be more comparable to GBFS-CBPD binders due to the content of the OPC and the strength properties.

The mineralogical characterisation of the raw materials was determined using XRD as shown in Figure 4-2. The main crystalline phases present in the CBPDs were free lime (CaO), gypsum ($\text{CaSO}_4 \cdot 2\text{H}_2\text{O}$), sylvite (KCl), quartz (SiO_2), and calcite (CaCO_3).

Table 4-1 – Peak areas of main peaks for CBPD R and CBPD L determined using peak deconvolution

Peak Location (2θ)	CBPD R	CBPD L
Gypsum (25 – 25.9°)	119.8	1.68
Sylvite (27.8 – 29°)	188	349.8
Calcite (28.9 – 29.7°)	100.1	4.3
Gypsum (30.9 – 31.7°)	86.4	24.9
Lime (31.8 – 32.4°)	114.5	195.4
Lime (37.1 - 37.7°)	282.3	441.9
Sylvite (40.1 - 40.9°)	107.6	153

To quantify the chemical composition of the significant phases, gypsum, calcite, sylvite and lime peak areas were calculated using peak deconvolution. The results are shown in table 4-1. While both types of CBPD have similar mineralogical compositions, it is evident that CBPD L has much higher amounts of lime relative to CBPD R. On the other hand, CBPD R has a

higher calcite content and sulphate (gypsum peaks) content. The alkali content in CBPD L is also higher with a pH of 13 relative to pH of 12.6 for CBPD R. OPC, as expected, is mainly composed of alite, belite, and calcite. GBFS, on the other hand, presented a very broad diffuse band indicating that it contained a very large amount of amorphous material.

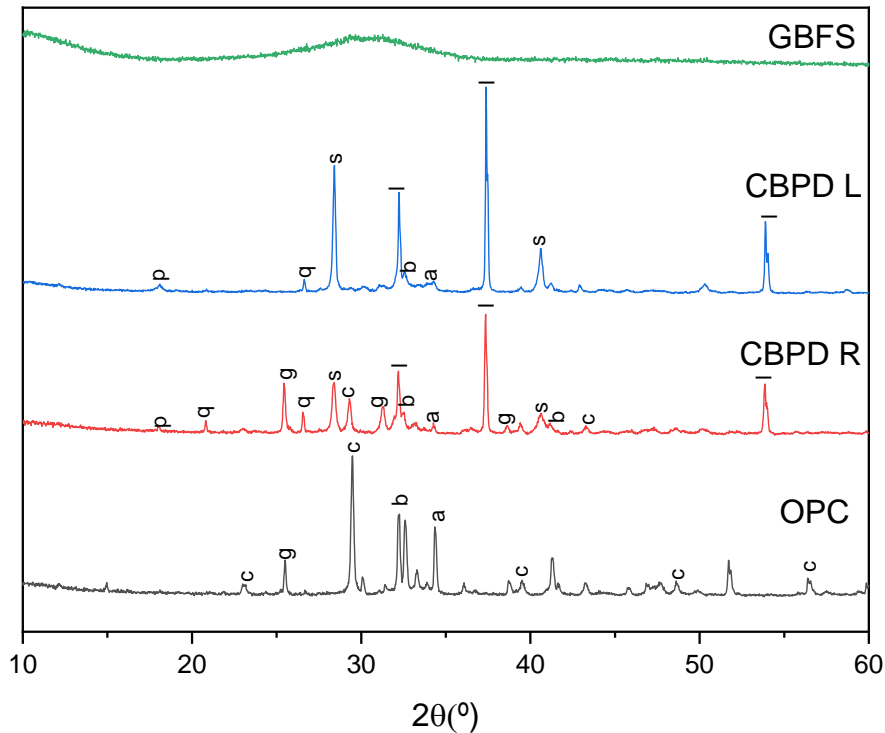


Figure 4-2 – XRD images of OPC, GBFS, CBPD R & CBPD L (l = lime, g = gypsum, s = sylvite, b = belite, a = alite, c = calcite, q = quartz and p = portlandite)

The particle sizes, measured in a laser diffractometer, are shown in Figure 4-3. CBPD L was the finer of the two dusts having a median particle size of 21 microns, whereas CBPD R had a median size of 46.5 microns. The smaller particle size of CBPD L will likely enable it to hydrate further due to a larger surface area. A noticeable difference between the two CBPDs was that CBPD R grains clearly agglomerated more than CBPD L, as balls of dust could easily be seen.

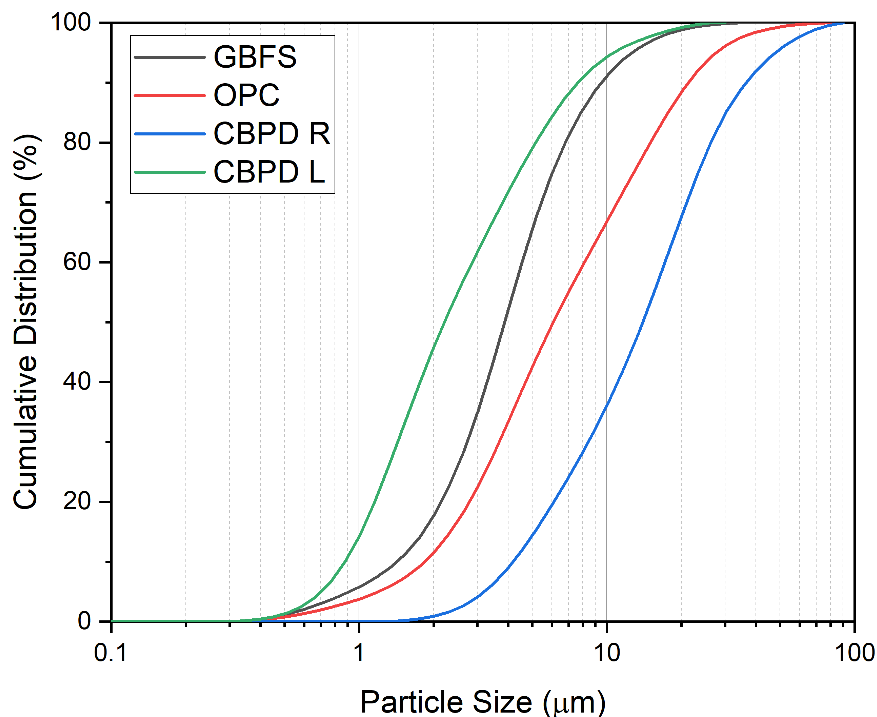


Figure 4-3 – Particle size of GBFS, OPC, CBPD R & CBPD L

4.2.2 Specimen Preparation

The mixes were designed based on the results of pilot studies. During these studies, alternative curing activation techniques such as chemical activation and heat curing were attempted, and it was found that despite a lower early age strength, ambient curing led to the strongest mixes long term. Locally available building sand was used as a fine aggregate for the mortars. The specific gravity and water absorption capacity were measured to be 2.6 and 2.5%, respectively; these conform to the limits specified in BS EN 1097-6:2000. The binder to sand ratio was kept at 1:3. When relevant for comparison purposes, 100% CBPD and OPC pastes at 0.4 w/b ratio were also used. Higher w/b ratios were necessary for the mortars to compensate for the sand absorption.

Seven mixes, with compositions given in table 4-2, were prepared. A ratio of 50:50 of CBPD and GBFS provided the strongest paste mixes in trial tests, hence this ratio was maintained throughout the testing. Cement was then added at 40%, 80% to the GBFS-CBPD binder, to test the potential of cementitious binders with reduced cement content. A control mix containing 100% CEM II OPC was also tested for comparative purposes.

The binders were all mixed in a 9-litre pan-mixer. Powders were initially mixed to ensure a homogenous dry mix. Following this, the water was added, and the material was mixed for 120 seconds. After multiple trials, a water to cement ratio of 0.6 was used and this was kept constant

for all mortar mixes. If dry material remained, the mortar was mixed further. Once properly mixed, the mortar was cast into steel moulds in two layers, and the surface was finished using a flat trowel. The specimens were then covered with a polyethylene sheet for 48 hours and kept in a curing room at 20 ± 2 °C before being demoulded. Once demoulded, the mortar specimens were kept in a water curing tank also at 20 ± 2 °C until the day of testing.

Table 4-2 – Mix Design. Sample ID: S refers to Slag, B refers to Bypass Dust. The number refers to the quantity of each (50 = 50% Slag and 50% Bypass Dust). R and L refer to CBPD from Rugby and Latvia, respectively

Mix ID	CBPD (%)	GBFS (%)	Cement (%)	w/b ratio
SB50 R	50	50	-	0.6
SB50 L	50	50	-	0.6
SB30 R	30	30	40	0.6
SB30 L	30	30	40	0.6
SB10 R	10	10	80	0.6
SB10 L	10	10	80	0.6
OPC	-	-	100	0.6

4.2.3 Test Methods

4.2.3.1 Fresh Properties and Heat of Hydration

The workability of the binders was assessed using a flow table test based on ASTM C1437. Freshly mixed mortar was cast in two layers into a conical mould. The mould was then released, and the mortar was tamped 15 times allowing it to spread out. The diameter of the mix was then measured to quantify the workability of the mix design. To measure the standard consistency, paste is cast into a mould, and different water to cement ratios are tested. The water to cement ratio which allows a Vicat plunger to penetrate a depth of 33-35mm in the cement is the standard consistency.

Heat of hydration measurements were carried out to investigate the heat evolution of CBPD binders. Paste samples were mixed and cast into plastic bags. The total mass of the binder was 200g per mix design. The bags were then pierced with a thermocouple so that it was in contact with the paste. This was then placed in a semi-adiabatic container and the temperature evolution over 60 hours was recorded.

4.2.3.2 Mechanical Properties

For compressive strength 50 mm³ cubes were utilised, whilst for flexural strength 40x 40x160 mm prisms were used. This was following the ASTM C109 standard. To further verify the compressive strength result, the broken prism pieces from the flexural testing were also tested in compression using two 40x40 mm metal plates to spread the load.

Ultrasonic Pulse Velocity (UPV) was measured using two transducers being placed at opposite ends of a prism. The UPV, denoted as V (m/s), was calculated by measuring the time (t) taken for ultrasonic pulses to go through the distance (d) of the two transducers. This is shown in the equation:

$$V = d/t$$

4.2.3.3 Microstructural Analysis

For microstructural analysis, paste samples with a w/b ratio of 0.4 were used. The XRD of the CBPD paste samples was carried out in a Bruker D-2 diffractometer, using X-rays of 1.54 Å generated by a Cu K α target and an Ni filter. The samples were analysed from 5° to 60° at a rate of 0.02° steps per second. The software used for peak identification was Diffrac.EVA by Bruker which has an ICDD library. Origin 2022 was used for peak deconvolution of the main XRD peaks.

Thermogravimetric Analysis (TGA) was carried out using a Perkin Elmer Pyris 1 TGA. Samples were heated from 35°C to 1000°C degrees at a rate of 10°C per minute. In this study, 10 mg of the ground powder samples were used to investigate the thermal behaviour of CBPD paste.

Fourier Transform Infrared Spectroscopy (FTIR) was carried out using a Perkin Elmer Spectrometer. Potassium Bromide (KBr) pellets were formed by mixing and compressing together cementitious powder and KBr powder. The samples were measured from wavelengths 400cm⁻¹ to 4000cm⁻¹.

4.2.3.4 Shrinkage Properties

The chemical shrinkage was determined following Procedure A of ASTM C1608-07. The CBPD pastes were cast into vials and compacted in 5-10 mm layers. The vials were weighed empty and filled with paste to determine the mass of the paste. Following this, they were filled with deaerated water, and sealed with rubber corks that were fitted with capillaries. Readings of the water level were taken every 30 minutes for the first 8 hours after casting, and then every 12 hours for 72 hours. The first measurement was taken 5 minutes after mixing.

Total shrinkage was carried out following ASTM C596-23. Three mortar bars were prepared for each mix design. After demoulding, the samples were water cured for 48 hours. The prisms were then removed and once they were in a saturated surface dry condition, the first length measurement was taken. The shrinkage measurements were carried out using a length comparator to quantify the linear dimension change along the longitudinal axis of the mortar bar. Shrinkage strain measurements were taken for up to 150 days.

4.3 Results and Discussion

4.3.1 Flow Diameter, Standard Consistency and Setting Time

Using the flow table test results, the relative change in flow compared to OPC is shown in Figure 4-4. Large amounts of CBPD (SB50 and SB30 mixes) clearly reduce the workability and led to a stiffer mortar at higher cement replacements. Nonetheless, some flow benefits are observed in SB10 mixes. The control mix had an overall flow diameter of 161mm, whereas SB10R and SB10L achieved 163.1mm and 163.5mm respectively. The same trend is seen in the standard consistency results, shown in table 4-3, where more water was required as CBPD content increased.

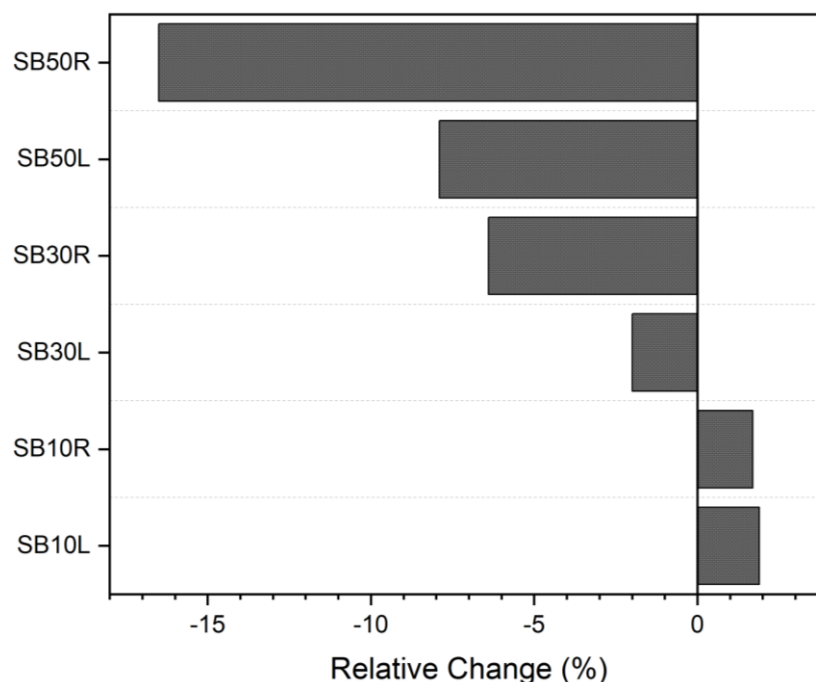


Figure 4-4 – Relative change in flow of mix designs containing CBPD compared to OPC

The reduction in flowability and consistency for large amounts of CBPD is attributed to higher water demand primarily due to the tendency of CBPD particles to agglomerate together (Barnat-Hunek et al., 2018) and the higher alkalinity of CBPD that leads to higher reactivity.

Table 4-3 – Standard consistencies, setting times and flowability of all the investigated mix designs

Mix Design	Standard Consistency (%)	Initial Setting (min)	Final Setting (min)	Flow Diameter (cm)
SB50R	38% ± 2%	38 ± 3 min	140 ± 9 min	134 ± 1 cm
SB50L	35% ± 1%	94 ± 7 min	245 ± 12 min	148 ± 2 cm
SB30R	34% ± 1%	46 ± 3 min	150 ± 8 min	150 ± 1 cm
SB30L	32% ± 1%	76 ± 8 min	250 ± 14 min	157 ± 1 cm
SB10R	28% ± 2%	51 ± 1 min	155 ± 4 min	163 ± 2 cm
SB10L	27% ± 2%	63 ± 2 min	175 ± 10 min	164 ± 3 cm
OPC	28% ± 1%	54 ± 2 min	160 ± 6 min	161 ± 1 cm

When comparing the two CBPD mixes, CBPD L is significantly more workable than CBPD R. This is reflected in the cementless mixes, with SB50L having a flow diameter of 147.8mm and SB50R only achieving 134.0mm. This is likely due to the increased agglomeration in CBPD R relative to CBPD L which increases the water demand. To reduce the effect of agglomeration on rheological particles, repulsive forces, induced by adding extra water, are necessary to separate the particles from each other (Senff et al., 2009).

This is also reflected in the standard consistency results, where SB50R and SB50L had consistencies of 38% and 35% respectively. In fact, SB30R and SB50L almost had identical results for flow and standard consistency, despite the tendency for flow to improve with cement increase. This indicates that CBPD R has a high-water demand.

Setting times are also shown in table 4-3. Overall CBPD R mixes set faster than CBPD L mixes. The slower time of set of CBPD L mixes is likely due to the different chemical reactivity between the dusts.

4.3.2 Heat of Hydration

Heat of hydration curves for CBPD R and CBPD L pastes up to 60 hours are presented in Figure 4-5. The mass of the dry material was maintained at 200g for all the pastes. The time required to reach the maximum temperature is denoted as T_{max} . CBPD L reaches T_{max} faster than CBPD R, at 21 minutes compared to 48 minutes. It must be noted that both values are very fast, indicating a high reactivity. T_{max} of 105°C is significantly higher for CBPD L than CBPD R at 74°C. The speed of reaction and temperature difference is likely largely due to the higher free lime content and fineness of CBPD L that increases the surface area for reactions.

An induction period is not observed for the CBPD pastes and both seem to reach stabilisation at around 15 hours.

Czapic et al. (2020) showed similar results for their CBPD analysis. A rapid heat release was experienced, followed by a rapid decrease, with no induction period. A lack of an induction period may cause difficulties during in situ casting of CBPD mortar/concrete.

Figure 4-5 also includes the results for OPC, which has a small initial temperature increase, a stable induction period of about 5 hours, and a gradual temperature increase where it has a T_{max} of 48°C at around 15 hours, significantly slower than the CBPD pastes.

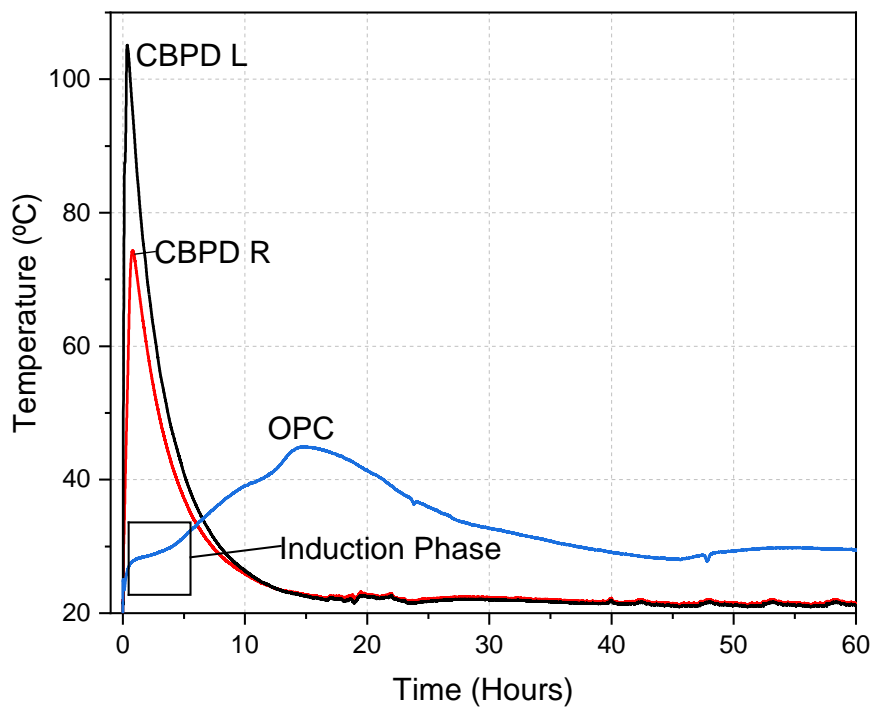


Figure 4-5 – Heat of hydration for CBPD R, CBPD L & OPC pastes

The heat of hydration results for the investigated mortar mixes are shown in figures 4-5 to 4-7. As expected, the T_{max} decreases with an inclusion of GBFS (Khan et al., 2014). SB50L (figure 4-6), SB30L (figure 4-7), and SB10L (figure 4-8) achieved T_{max} of 73°C, 62°C and 56°C, respectively. These values are all higher than their CBPD R counterparts and the control paste. The induction period (phase II) which occurs during cement hydration is observed only when cement is included in the binder and is labelled in the figures when present.

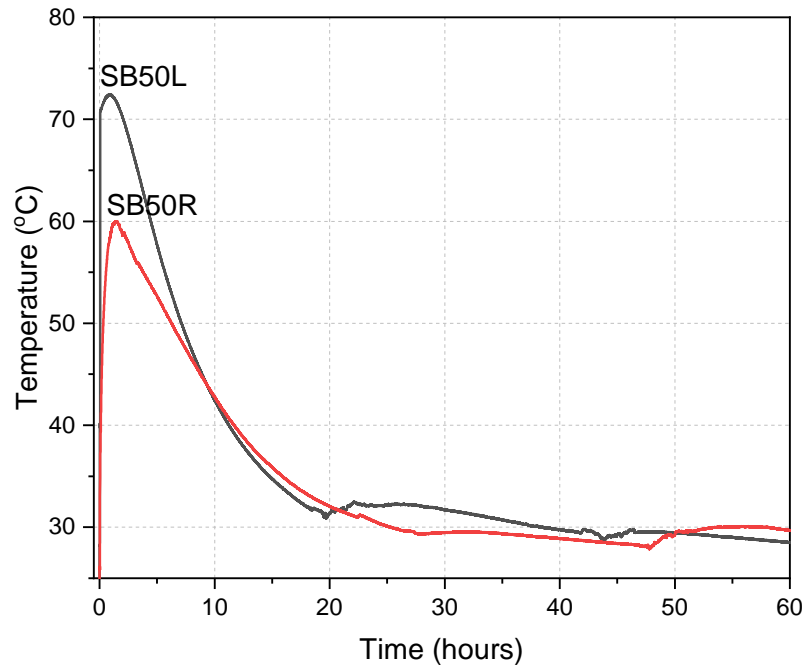


Figure 4-6 - Heat of hydration for SB50R and SB50L

It is evident from the differences in the curves, that free lime hydration is the main factor governing the exothermic reaction for CBPD, whereas OPC is mainly due to C_3S . The heat of hydration of C_3S is circa -12.2 kJ/mol and for lime it is circa -64.4 kJ/mol (Telford, 1997). This explains why as CBPD content increases T_{max} is higher, since the heat emitted from the exothermic reaction of lime is much larger than that of C_3S . This agrees with past research on CBPD heat of hydration by Czopic et al. (2020).

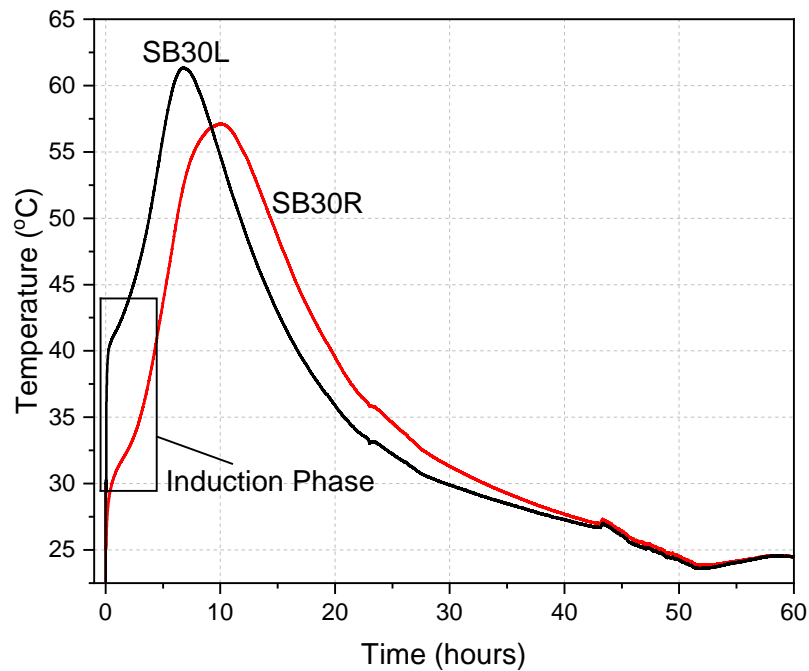


Figure 4-7 - Heat of hydration for SB30R and SB30L

While CBPD L has a slaking reaction due to its lime content, it is important to highlight the difference between free lime and CBPD heat of hydration. Cai et al. (2022) showed that free lime reaction with GBFS leads to a strong exothermic reaction in the first few minutes of hydration with a second peak after 18h. Additionally, they observed rises in heat release as more lime was included in the system, which correlates with these results. Free lime is the critical factor in determining the height of the exothermic peak. In the current results, the second peak can be attributed to the delayed pozzolanic reaction and the slower reaction of free lime and GBFS (Zhu et al., 2023). In some examples, such as SB50R and SB50L, a second peak occurred in this system, however at around the 20–40-hour mark. It can be deduced that a CaO-GBFS system will dissolve GBFS faster than a CBPD-GBFS binder.

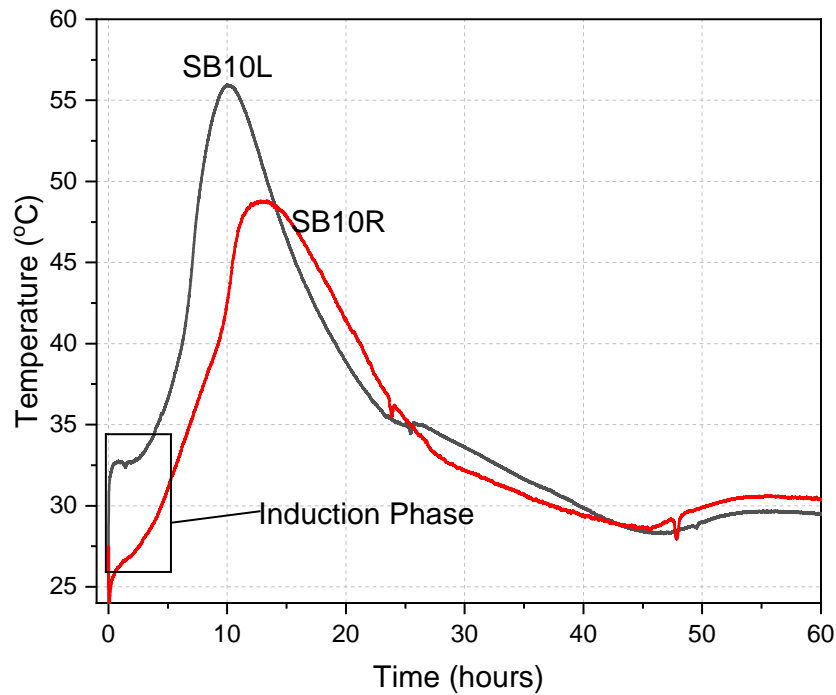


Figure 4-8 – Heat of hydration for SB10R and SB10L

4.3.3 Density and Ultrasonic Pulse Velocity

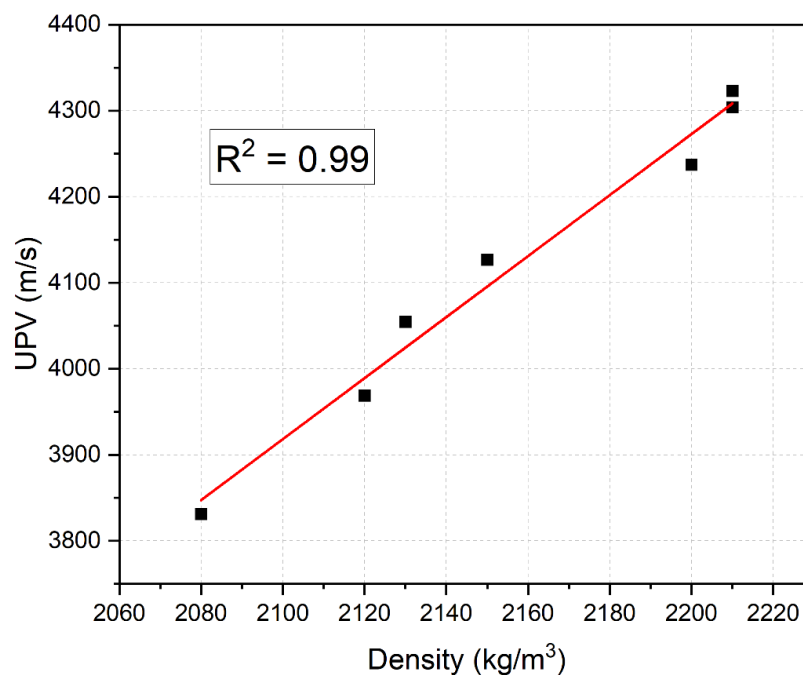
The bulk densities of the mixes after 90 days of curing are shown in table 4-4. The bulk density of the mortar decreases with increasing CBPD content which may lead to a less refined and more porous the microstructure. Additionally, CBPD L leads to less dense mortars than CBPD R, which is likely due to its expansive behaviour at early ages. Expansion was clearly visible in the SB50L binders which showed surface cracks on the prisms. Excessive swelling not only affects density, but it also can increase porosity and reduce the strength of the mortar.

UPV readings (see table 4-4) were taken at 90 days to verify the density results. In general, the UPV results present a similar trend to densities. SB10R shows the highest velocity, but overall, the velocity decreases as CBPD increases. CBPD L mixes show the lowest velocities for the same reasons described above.

Table 4-4 – UPV and Density results of all the investigated binders

Mix	Density (kg/m ³)	UPV (m/s)
SB50R	2110 ± 20	3969
SB50L	2090 ± 15	3831
SB30R	2150 ± 10	4127
SB30L	2140 ± 10	4054
SB10R	2200 ± 20	4323
SB10L	2200 ± 10	4237
OPC	2210 ± 25	4304

The relationship between density at 90 days and UPV is shown in figure 4-9 below. The results show a 0.99 R^2 value showing that there is a very strong correlation between the two properties. This correlative relationship between density and UPV is well documented in research (Ozkan et al., 2016).

**Figure 4-9 – Linear relationship between UPV and density showing a correlation of 99%**

4.3.4 Compressive and Flexural Strength

The average compressive strength of the mortars is shown in figure 4-10. Though CBPD L binders exhibit higher early strength (at 3 days), CBPD R produces stronger mixes over time. This is in line with the temperature vs time results, where CBPD L is shown to be more reactive than CBPD R breaking down the glassy phases of GBFS faster due to its higher exothermic reaction and alkalinity and lime content (Chaunsali & Peethamparan, 2013). Past researchers

utilised this property of CKDs to enhance the early age strength of cementitious products (Sadique & Coakley, 2016)

There are several reasons to explain the improved mechanical properties of SB50R over SB50L with time. Firstly, though it has a finer particle size, higher free lime, and alkali content, CBPD L increases early age strength, however, it appears that there is a limit to this benefit as this causes rapid expansion which can cause an uneven reaction product formation. This leads to a deterioration in the quality of the microstructure (Gallucci, 2013). Expansion was clearly observed on CBPD L binders, hence there was also a reduction in density due to microcrack formation on the surface of the prisms. This consequently can lead to a weaker binder. Another factor contributing to the strength of CBPD binders is ettringite formation (Konsta-Gdoutos & Shah, 2003). Ettringite is a mineral primarily composed of sulphates and aluminates, which CBPD R is abundant in. Ettringite has a long needle shape which has an overlapping effect when formed in excess leading to improvements in the matrix strength due to pore-filling (Gu et al., 2020). Due to the high sulphate content in CBPD, the ettringite formed tends to be quite stable. Chaunsali and Peethamparan (2013) attributed much of the early age strength of their cement kiln dust-fly ash binders to the ettringite formation in their binders. Another factor to consider is the higher quantity of calcite in CBPD R is a factor contributing to the improved strength of the material. Calcite is not only denser, but it also has a larger molar volume than portlandite (von Greve-Dierfeld et al., 2020).

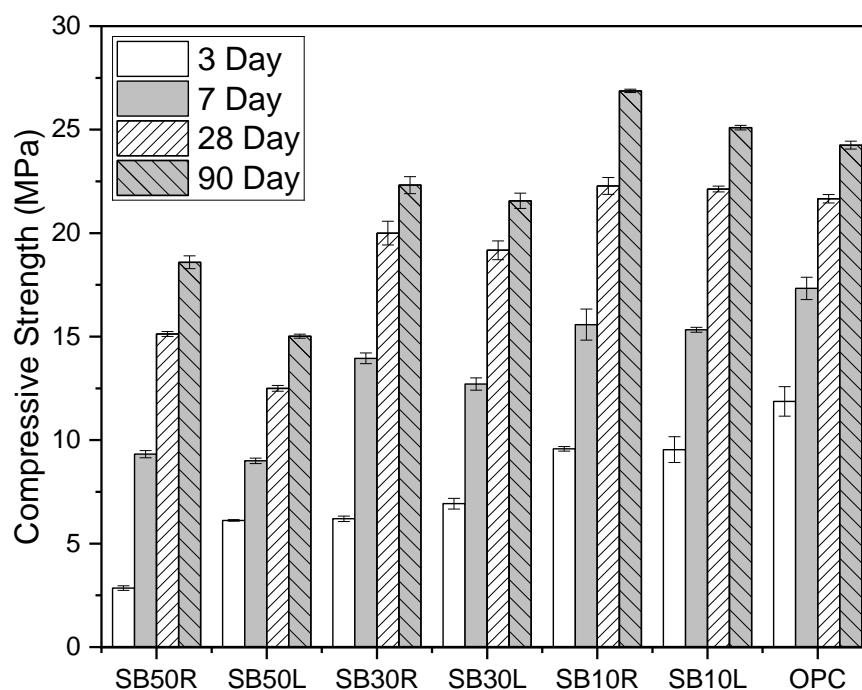


Figure 4-10 – Compressive strength results of all investigated mixes at 3, 7, 28 and 90 days

The highest 90-day compressive strengths were attained by SB10R and SB10L, reaching 26.1 MPa and 25.1 MPa, respectively, representing 11% and 3% improvements over the control mix. Good compressive strengths are achieved for SB30R and SB30L at 22.3 MPa and 21.6 MPa, respectively; these strengths were only 9% and 13% lower than the control mix respectively. The strength results agree with similar previous research, where Marvila et al. (2019) manufactured cement-lime mortars (up to 66% cement replacement) and achieved strengths ranging from 11.4-14.2 MPa at 28 days with similar w/b and binder to sand ratios as this research. Hence, these results confirm that CBPD can replace up to 10% of typical OPC binders and still result in higher compressive strength concrete/mortar. Nonetheless, it can also be used at higher cement replacement levels up to 100% for lower strength concrete/mortar applications.

Flexural strength obtained from three-point bending tests are shown in figure 4-11. In general, the strength develops in a similar trend to the compressive strength. SB50L was stronger in flexure at 3 days achieving 1.12MPa whereas SB50R achieved 0.4 MPa. By 90 days, however, SB50R had exceeded SB50L's strength of 2.2 MPa achieving a flexural strength of 2.5MPa. As is typically expected, the flexural strength at 90 days for all mixes ranged from around 10-15% of the total compressive strength. The flexural strength decreased with an increase in CBPD content.

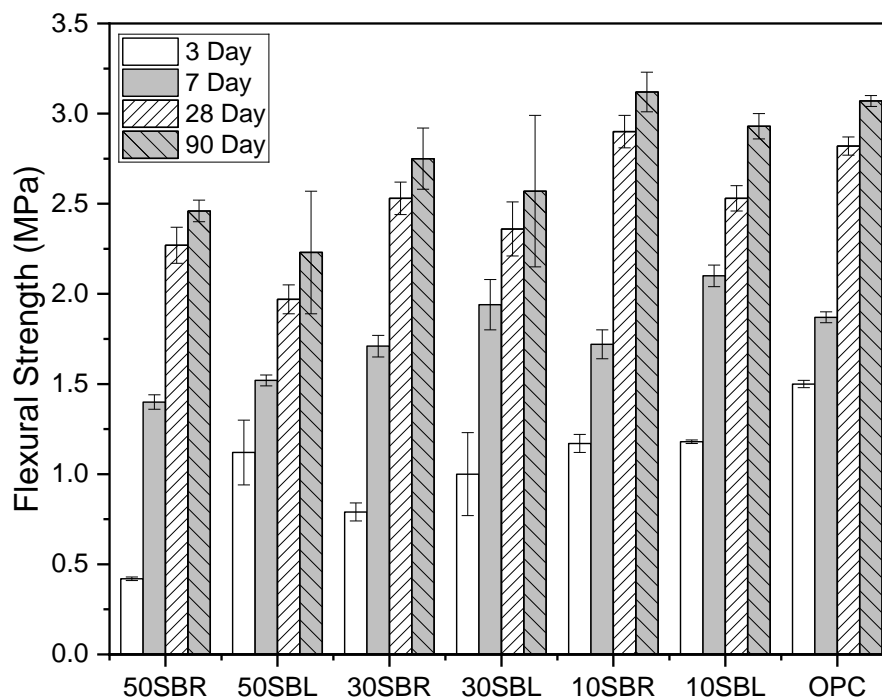


Figure 4-11 – Flexural strength results of all investigated mixes at 3, 7, 28 and 90 days

4.3.5 XRD Analysis

XRD is used to identify the chemical phases formed during the hydration of the pastes. Figure 4-12 presents the XRD pattern for SB50R and SB50L at 7 and 28 days. At 7 days, a broad band in the range of 5-15°, attributed to the amorphous nature of CBPD, was evident, with SB50L displaying greater amorphousness than SB50R. This characteristic band diminishes by 28 days. With an increase in cement content, the amorphousness is reduced, resulting in less noise in the diffractograms, as seen in figures 4-12 and 4-13. While CSH typically forms broad diffusion peaks around 29°, these peaks are often obscured on XRD due to overlap with the major crystalline calcite peak at 29.4° (Chakraborty et al., 2016).

Overall, both CBPDs exhibited similar phases, albeit at varying intensities due to their distinct chemical compositions. Ettringite was prominently present in these binders, with CBPD L binders showing less intense peaks, indicative of a lower quantity formed. This aligns with the strength results, where SB50R binders demonstrated greater strength than SB50L binders, underscoring the significant role of ettringite formation in strength development. CBPD R mixes produced more ettringite due to their higher sulphate content, as sulphate concentration influences ettringite formation (Ghorab, 2004). It should be noted that the stability of ettringite is contingent on sulphate quantity; reduced amounts can lead to depletion and conversion into monosulphate (AFm) (Havlica & Sahu, 1992). The sulphate content is sufficient as is evident in the XRD, with ettringite peaks intensifying at 28 days.

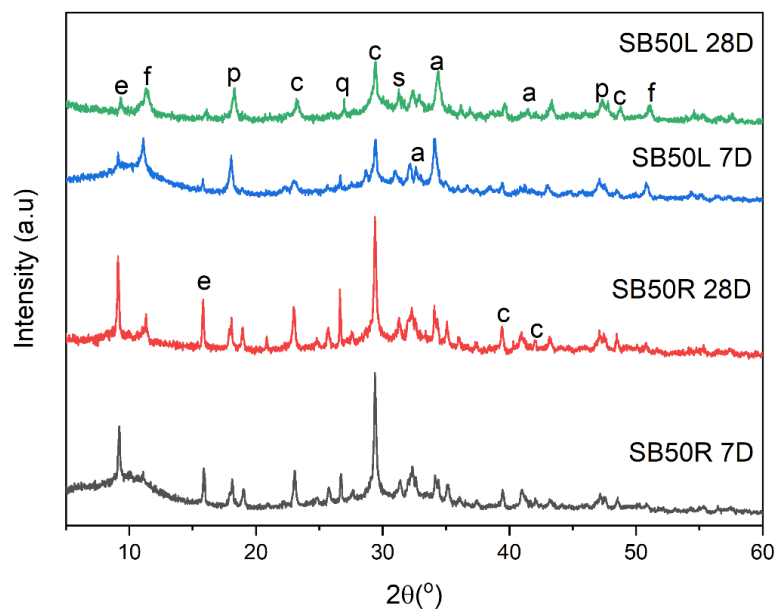


Figure 4-12 – XRD results of SB50R and SB50L (p = portlandite, c = calcite, e = ettringite, f = friedel's salt, a = alite, q = quartz and s = syngenite)

Another noticeable difference between the control and the CBPD mixes is the presence of syngenite (at 31.3°). Syngenite peaks form due to the potassium and sulphate content in the CBPD and are mostly visible in the SB50 mixes. Over time, sulphate ions from the syngenite are released and benefit the development of further ettringite (Konsta-Gdoutos & Shah, 2003). The intensity of these peaks decreased as the CBPD content was reduced in the binder.

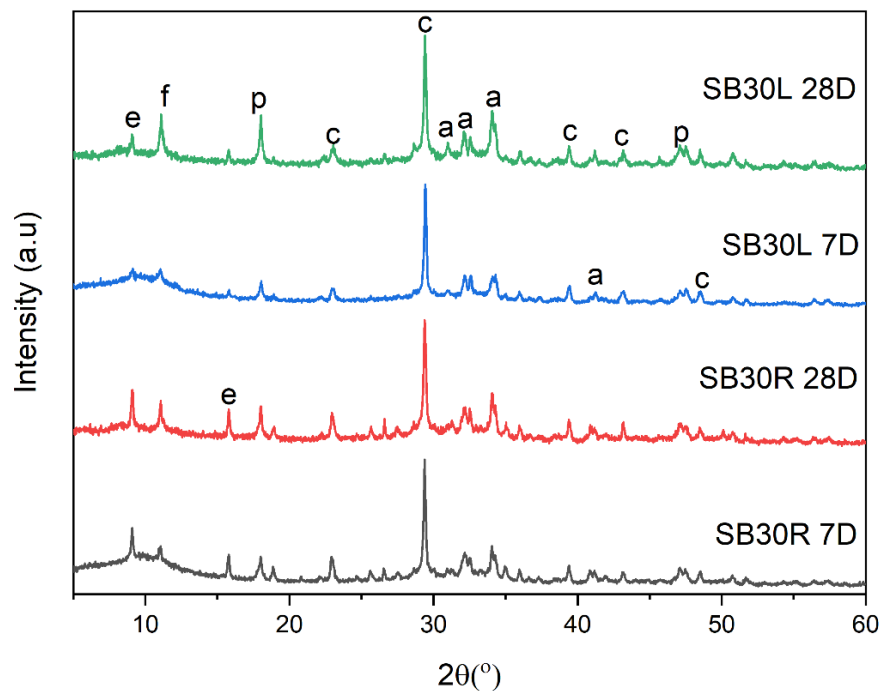


Figure 4-13 - XRD results of SB30R and SB30L (p = portlandite, c = calcite, e = ettringite, f = friedel's salt and a = alite)

Calcite peaks remained largely constant at all ages, indicating that the phase was mostly inert. On the other hand, portlandite was found in much higher concentrations in SB50L at both ages, which can be attributed to the increased free lime content in this bypass dust. Hence, it can be deduced that most of the portlandite in CBPD binders comes from the hydration of free lime. The reactivity of CBPD, dependent on free lime, sulphate, and alkali content, suggests CBPD L is more reactive. However, more reactivity and a higher portlandite content do not necessarily mean a stronger or denser product as seen from the strength results. Based on the XRD results, the ettringite content is a large determinant of overall strength. As mentioned previously, the increased calcite content is also a factor to consider due to its filling and densification effect in the binder. It is observed that at 28 days, the portlandite peak for SB50L loses intensity. This may be due to a secondary reaction between GBFS and portlandite.

The compressive strength results indicate an overall increase in strength with cement content. It is also clear from the diffractogram that the amorphous content diminishes with increasing cement content due to the orderly crystalline structure in cement. Quartz peaks were not observed in the control mix, which may be due to the lack of GBFS that contains silica. It is also possible that the samples used in the XRD did not have a high composition of quartz. SB10R and SB10L binders exhibited both enhanced fresh and mechanical properties. These mixes are characterised by higher calcite peaks (see figure 4-14) than the SB30 and SB50 mixes, consistent with the higher cement content. When observing the ettringite peaks, it is clear from the intensity that CBPD R produces the most. The inclusion of 10% CBPD R in OPC mixes aids the quantity developed and ultimately may enhance the final compressive strength. From the diffractogram, SB10R has a higher ettringite content than OPC. The tendency of the SB10L quartz peak to decrease over time could be attributed to the formation of other cementitious gels such as CSH and CASH (Bernard et al., 2018). It can be assumed that the improved strength for SB10 mixes is due to the enhanced pozzolanic reaction of slag due to the alkalinity of CBPD.

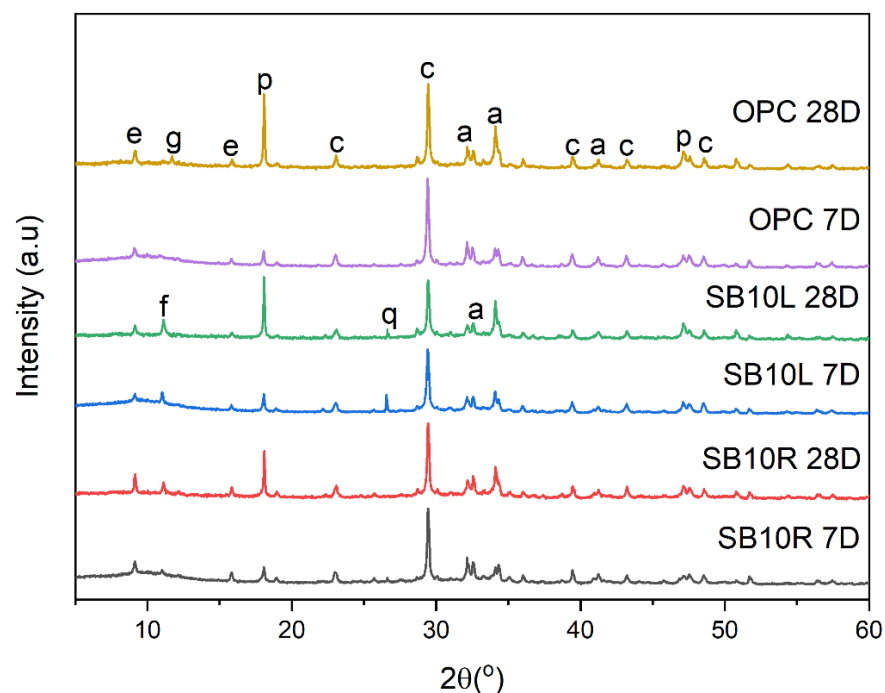


Figure 4-14 - XRD results of SB10R, SB10L and OPC (p = portlandite, c = calcite, e = ettringite, f = friedel's salt, a = alite, g = gypsum and q = quartz)

The peak areas shown in table 4-5 are obtained from semi quantitative peak quantification of the main calcite (29.4°), ettringite (9.8°), and portlandite (18.4°) peaks. OPC produces the most

calcite, and there is a steady decrease in this peak as OPC content decreases, however it is also clear that calcite content is higher in CBPD R than in CBPD L, when comparing SB50R and SB50L peaks for this phase.

Table 4-5 – Main peak area ratio for all investigated mix designs at 28 days determined using peak deconvolution of main peaks

Mix	Ettringite	Portlandite	Calcite
SB50R	162.4	106.4	290.8
SB50L	38.7	176.9	197.8
SB30R	100.8	120.5	464.6
SB30L	41.3	138.3	442.9
SB10R	93.1	148.1	693.8
SB10L	77.3	171.2	625.5
OPC	87.6	160.1	844.8

CBPD L binders exhibit higher portlandite production than CBPD R, primarily due to their substantial free lime content. SB50L has the highest portlandite content among all mixes at 28 days.

CBPD R mixes show the highest ettringite content, possibly a significant factor contributing to their improved strength results compared to CBPD L mixes. SB50R has notably higher ettringite content than the control mix, highlighting differences in hydration between pure OPC and CBPD-GBFS binders.

Based on the hydration results, a simplified hydration model was developed based on the XRD results as seen on figure 4-15. Water is added to the binder materials, and they begin to dissolve (figure 4-15 Step 1 and Step 2). An exothermic reaction results in the formation of a colloidal layer around the binder grains and free lime begins to be converted into portlandite (figure 4-15 Step 3). Ettringite also begins to form due to the reaction of sulphate ions with aluminate phases. Following this the colloidal layer thickens around the grain blocking water from the unreacted core of the grain (figure 4-15 Step 4). The binder begins to flocculate and nucleate which enables more water to pass through. Hydration continues and the microstructure will densify forming a dense binder (figure 4-15 Step 5). Hydration continues over time forming more reaction product and further densifying the microstructure of the material.

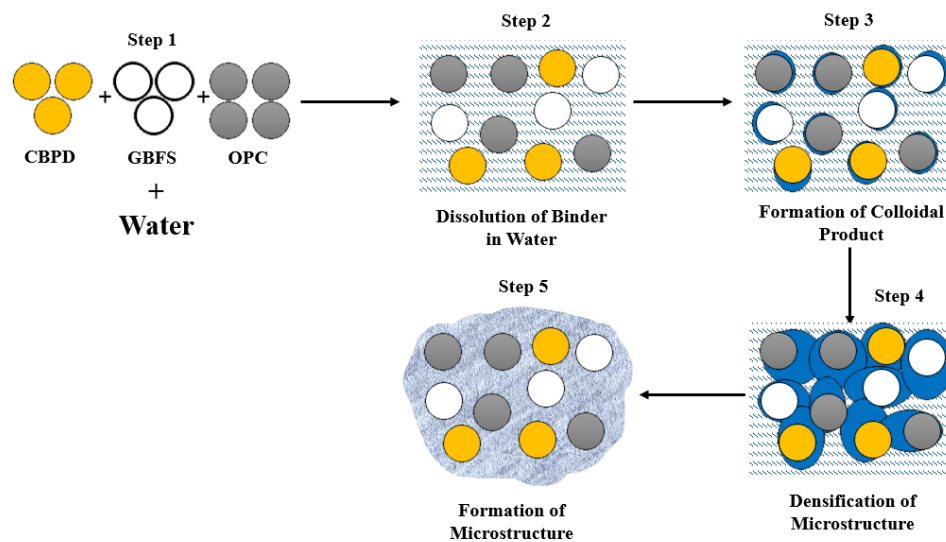


Figure 4-15 – Simplified hydration model of CBPD-GBFS-OPC Binders (Jo et al., 2017)

4.3.6 FTIR Analysis

Chemical phases that are difficult to locate using techniques such as XRD are easier to identify with the help of FTIR. Table 4-6 presents the identified IR bands and their functional groups.

Table 4-6 - Functional groups classification for the FTIR results for all mix designs

Wavenumber (cm ⁻¹)	Functional Group
3642-3645	ν OH (Ca(OH) ₂)
2976-2980	C-H
1791796	CaCO ₃
1638-1643	δ OH (H ₂ O)
1421427	ν_3 CO CaCO ₃
1131140	S-O
962-965	Si-O (CSH), Aft
873-876	C-O ν_2

The FTIR spectra of the investigated mix designs are presented in figures 4-16, 4-17 and 4-18. The results show several distinct peaks typically expected in cementitious products, however, in some cases they are slightly shifted and have different intensities. The peaks located around the wavelength of 800 cm⁻¹ and 965 cm⁻¹ are due to Si-O asymmetric stretching, which occur due to the generation of CSH. This confirms that this gel forms in CBPD binders (Chakraborty et al., 2016). The Si-O stretching band consistently shifts to a lower wavelength in all cases, especially as cement content increases. This has been reported in the past due to the progressive

depolymerisation of the silicate Si-O chains. This band tends to shift to a lower frequency as the calcium/silica ratio increases in the mix (Yu et al., 1999).

CSH forms in CBPD-GBFS binders when the release of OH⁻ ions (from the portlandite content in CBPD) in the solution break the Si-O and Al-O bonds of GBFS, forming SiO₄ and AlO₄ and releasing Ca²⁺ ions. The free calcium ions then react with the active SiO₄ and AlO₄ leading to the formation of CSH and CASH (Yan et al., 2022). The peak around 965 cm⁻¹ can also indicate the presence of an ettringite and monosulphate phase that increases as CBPD content increases.

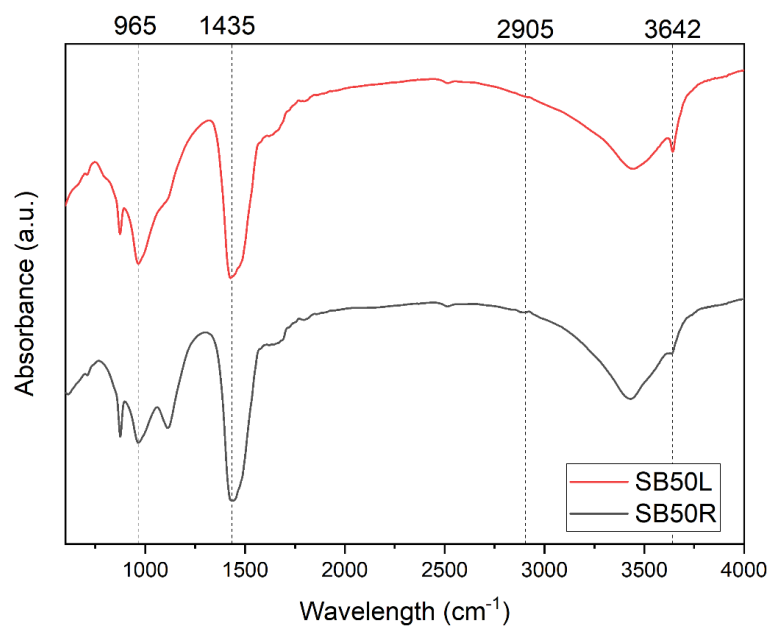


Figure 4-16 – FTIR results for SB50R and SB50L

Ettringite formation can also be analysed by observing the band around 1120 cm⁻¹ (Scholtzova et al., 2015). This peak is the most intense for the mixes containing CBPD R binders, indicating more ettringite formation due to this bypass dust.

The bands located at around 1644 cm⁻¹ and 3425 cm⁻¹ occur due to the bending and stretching of bound water molecules (Shi et al., 2019). From the results, the difference in intensities between CBPD R and CBPD L mixes are not apparent except for the SB50 mixes as seen from figure 4-16.

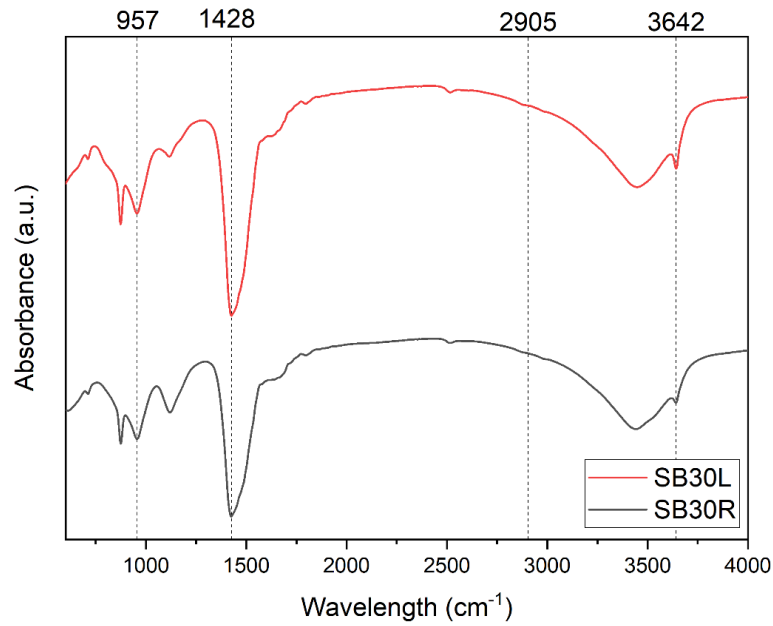


Figure 4-17 – FTIR results for SB30R and SB30L

The band at 3642 cm^{-1} represents an absorption peak of portlandite and is attributable to O-H stretching. The mixes containing CBPD L had higher and sharper peaks at this band relative to CBPD R, indicating more portlandite content, which confirms the XRD results. Broad bands were also observed between $3200 - 3400\text{ cm}^{-1}$ for all mixes. This band gets broader and less sharp as the cement content increases, indicating again a lower degree of polymerisation (Basri et al., 2021).

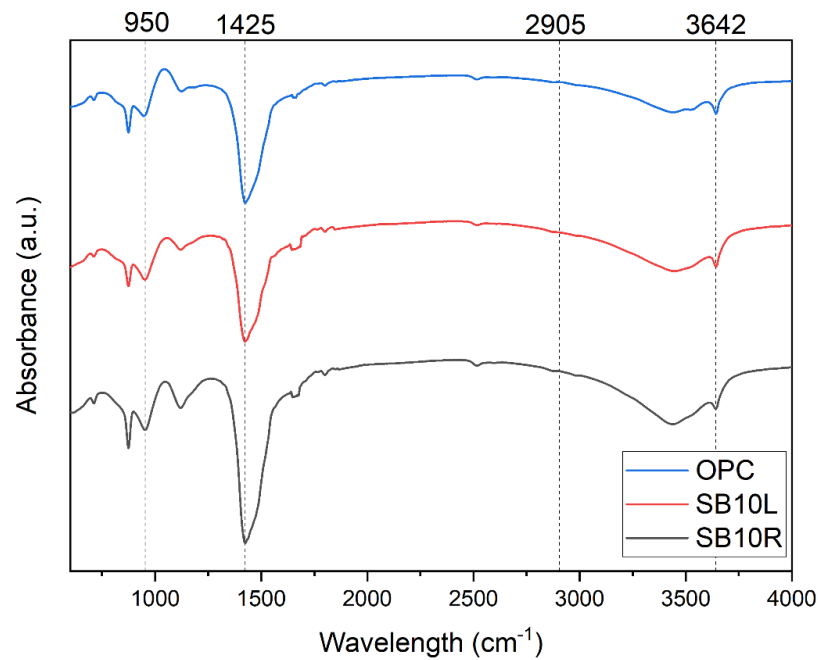


Figure 4-18 – FTIR results for SB10R, SB10L and OPC

At around 1430 cm^{-1} a band due to the C-stretching of carbonate molecules is observed. These molecules are formed through the reaction of calcium hydroxide and carbon dioxide from the air (Huntzinger et al., 2009). As observed, as the cement content increases the bands slightly shift towards a lower wavelength. This indicates a higher degree of reaction in the OPC relative to the bypass dusts for calcite formation.

4.3.7 TGA/DTG Analysis

Figure 4-19 presents the TGA curves of the mixes (at 28 days) from 35°C to 1000°C . The main temperature ranges that need to be considered are between $35\text{-}220^{\circ}\text{C}$, $220\text{-}400^{\circ}\text{C}$, $400\text{-}600^{\circ}\text{C}$, and $600\text{-}800^{\circ}\text{C}$ which correspond to the loss of water and ettringite, the loss of Friedel's salt and monosulphate, the decomposition of portlandite, and the decomposition of calcium carbonate, respectively (Czapik et al., 2020).

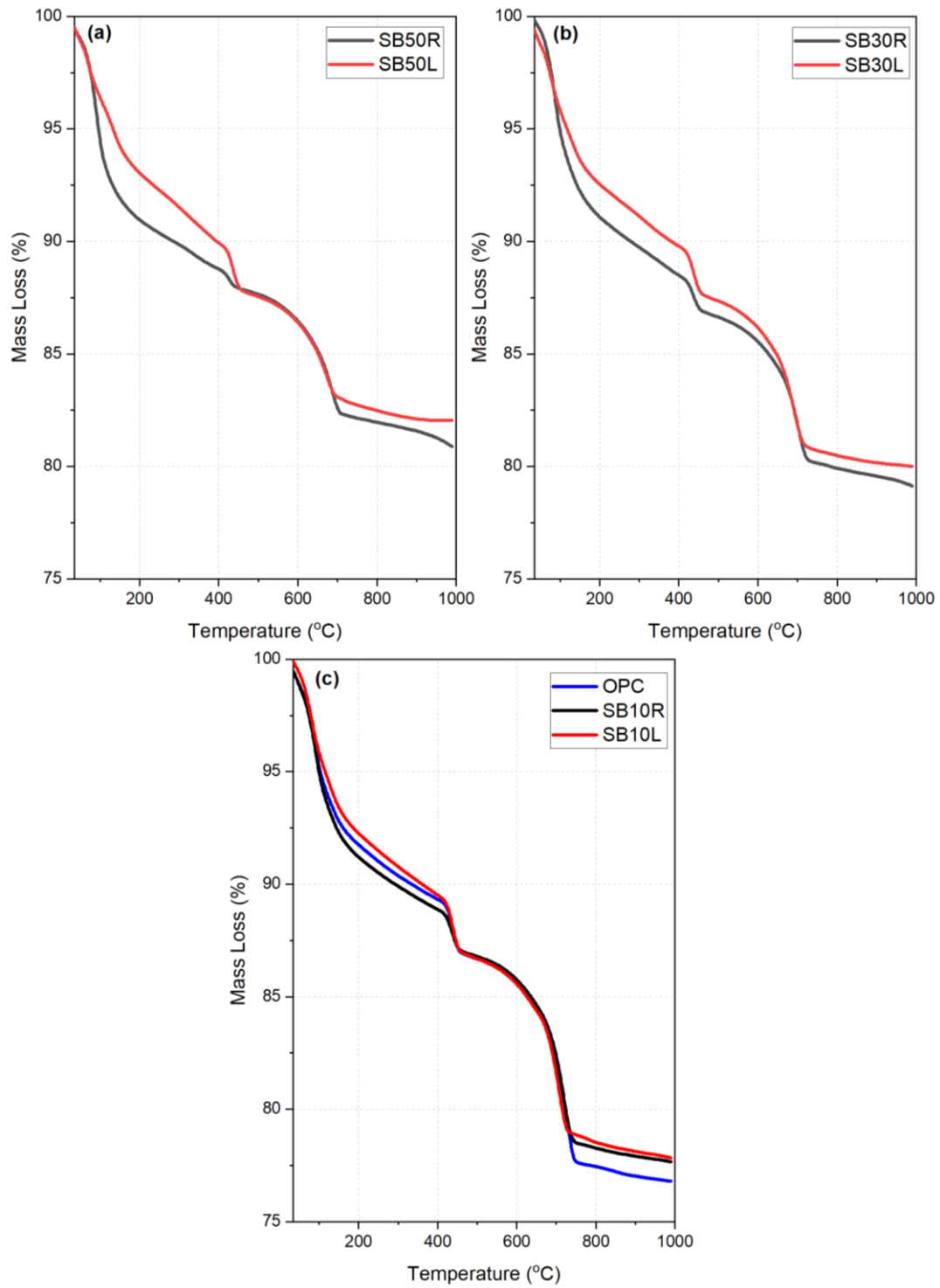


Figure 4-19 - TGA results for the investigated mix designs (a) SB50R and SB50L (b) SB30R and SB30L (c) SB10R, SB10L and OPC

The results show that the final weight loss decreases as the CBPD content increases. The control mix experienced the greatest mass loss (23.2%) followed closely by SB10R (22.5%), showing that a 10% addition of CBPD R does not significantly reduce overall reaction product formation. This mass loss is mostly the result of calcite decomposition. SB50L, had the least mass loss of 17.6%, showing the lowest hydration products overall. Overall, CBPD L mixes show less mass loss than CBPD R mixes, confirming that they resulted in fewer hydration products. Fewer hydration products lead to a less dense matrix, weakening the binder due to less pore-filling.

Mass loss can be better understood when observing the different stages of decomposition of the mixes. The DTG results (figure 4-20) indicate that there were three distinct peaks and a weak broad peak observed in the samples, except for CBPD L samples which had four distinct peaks.

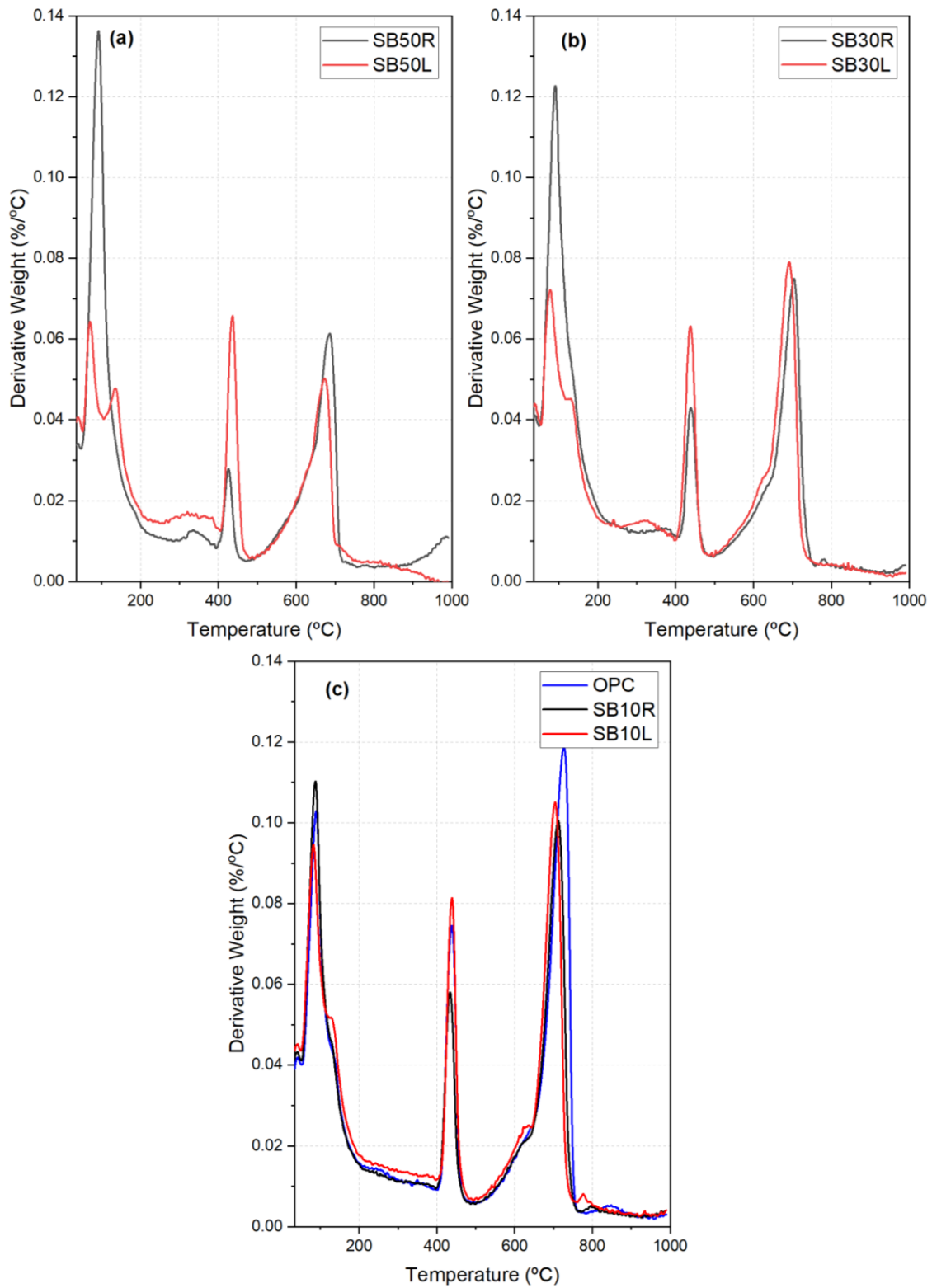


Figure 4-20 – DTG results for the investigated mix designs (a) SB50R and SB50L (b) SB30R and SB30L (c) SB10R, SB10L and OPC

In the first phase (35-220°C), CBPD R mixes consistently exhibit the largest mass loss, indicating a higher formation of hydration products, such as ettringite and CSH. This trend holds even when compared to the control mix, emphasizing the impact of CBPD R's high sulphate content on ettringite formation, in agreement with XRD and FTIR results. From the DTG, the order of peak intensity in this phase is highest for SB50R, followed by SB30R and SB10R.

The broad band (220-400°C) corresponds to the decomposition of monosulphate and Friedel's salt. The greatest mass loss in this phase is seen in SB50L, with the mass loss reducing as the CBPD content decreased. This is because of two main factors: the presence of Friedel's salt due to the chloride content and the conversion of ettringite to monosulphate. As is evidenced from the XRD and the thermal decomposition, CBPD L mixes contain less ettringite likely due to the lower sulphate content of the dust. The Al/S ratio is imperative in the stability of ettringite, hence the reduction of sulphates in CBPD L relative to CBPD R led to the formation of monosulphate. This is also the case for the mixes containing less CBPD R which would also lead to a reduction in monosulphate phases.

When assessing the decomposition of portlandite (400-600°C) or de-hydroxylation, CBPD R mixes show the lowest mass loss where SB50R only decreased by 2.3%. On the contrary, SB50L had a mass loss of 3.5% with a comparable value to the overall mass loss of 3.6% for the control mix. When considering that only 50% of the mix was composed of bypass dust for SB50 mixes, a large amount of portlandite has been formed. This was also confirmed by the XRD results which show a larger amount of portlandite for CBPD L mixes.

The final phase corresponds to the decomposition of calcium carbonate. From the results, the control mix had the largest amount of mass loss with a decrease of 8.3%. Furthermore, CBPD R binders exhibited greater loss relative than CBPD L in each mix indicating a higher carbonate content. A significant aspect to consider is that the CaCO_3 decomposition of the control mix occurs at a higher temperature than mixes containing CBPD. Peaks occurring at a higher temperature indicate a more ordered CaCO_3 (Zhou et al., 2019).

These results show the high variability in CBPD content, as CBPD R contained more CaCO_3 and ettringite and CBPD L contained more free lime. While increased free lime is associated with an accelerated reaction and more hydration products, excessive free lime can detrimentally impact compressive strength and structural integrity due to uneven hydration product

distribution. The presence of stable and inert calcium carbonate is also identified as a significant factor in the strength of CBPD binders.

4.3.8 Chemical Shrinkage

Figure 4-21 presents volume change versus time during the first 24 hours of CBPD and OPC pastes. CBPD L caused significant expansion and experienced the greatest overall volume change, followed by CBPD R and OPC. The expansion of CBPD L was fastest during the first five hours of curing, stabilising after that. Czapic et al. (2020) also observed similar results where their 100% CBPD mix achieved a 55% volume expansion mostly within the first 10 hours.

Swelling of up to 0.091 ml/g was experienced in CBPD L. This large expansion is due to the CaO hydration that is highly exothermic enabling thermal expansion. The ratio of volume change of a CaO particle to a Ca(OH)₂ particle is circa 17/33 (Kurdowski et al., 1981). Excessive ettringite formation also causes expansion and likely the coupled effect of free lime hydration and ettringite formation lead to this swelling.

Though both CBPDs experienced eventual swelling, they did in a different manner. As observed from figure 4-22, CBPD R experienced shrinkage during the first 90 minutes before expanding. This indicates that there may be two factors that affect volume change in CBPD: ettringite formation and free lime hydration. It is possible that initially, CBPD R is shrinking, however as ettringite begins forming at early ages, it begins to expand. Overall, due to the compensating effect of shrinkage and swelling the volume change was the least with swelling of 0.018 ml/g by the end of testing. OPC only experienced shrinkage and had a result of -0.043 ml/g by the end of testing.

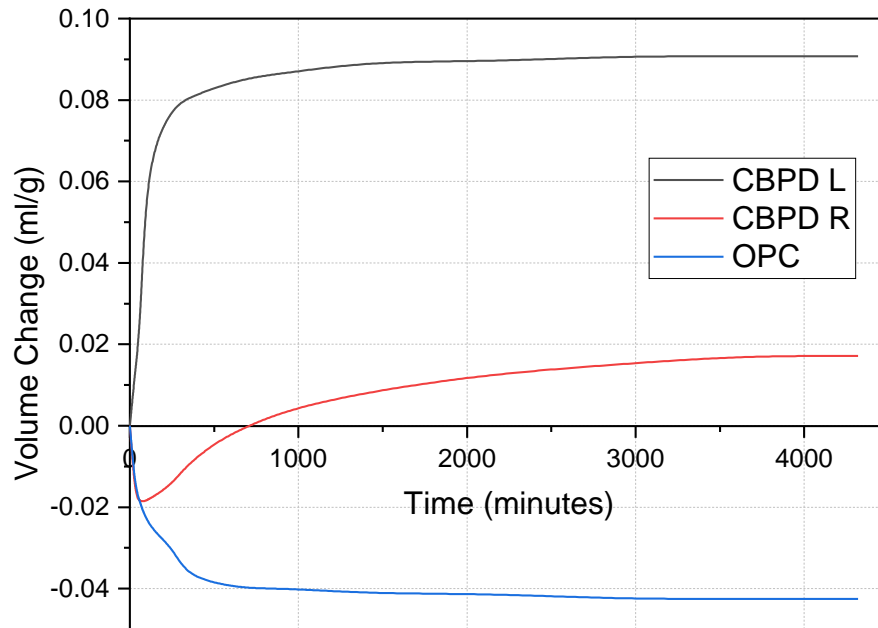


Figure 4-21 – CBPD R, CBPD L and OPC chemical shrinkage results

The chemical shrinkage results for the mixes containing GBFS are shown figures 4-22, 4-23 and 4-24. For SB50 mixes (figure 4-22) the expansion largely follows the trend of the CBPD pastes, however, to a lesser degree. They both experience swelling where SB50R and SB50L experienced swelling of 0.015 ml/g and 0.057 ml/g, respectively after 3 days. Clearly the inclusion of GBFS inhibits the volume change, largely due to the slower reaction as seen in the heat of hydration results.

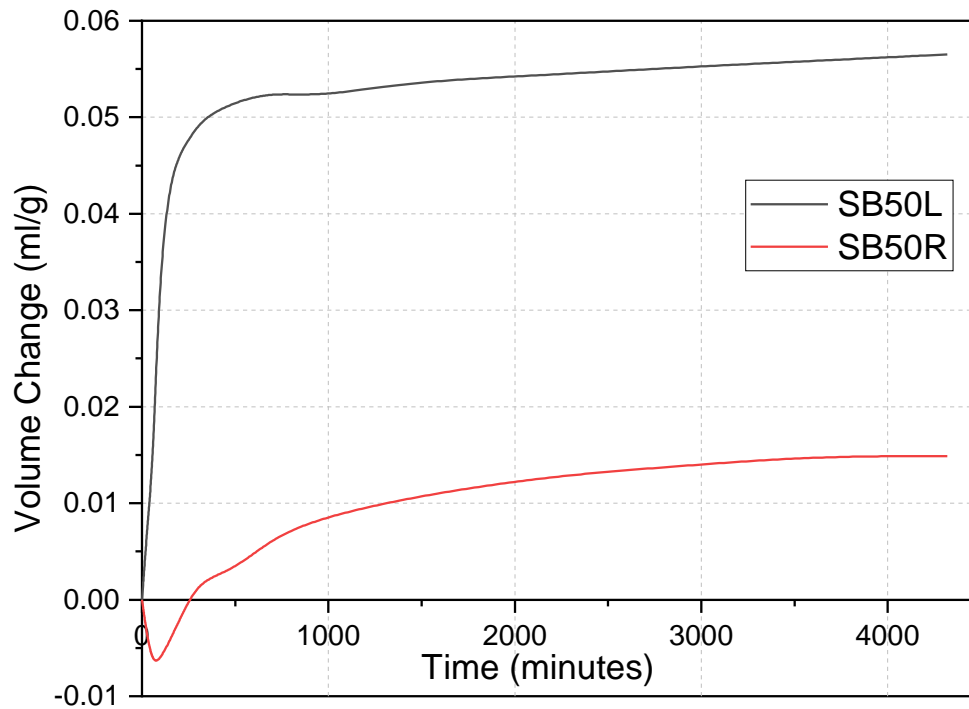


Figure 4-22 – SB50R and SB50L chemical shrinkage results

SB30R (figure 4-21) showed even lower volume change and it is evident that the expansion from the CBPD and the shrinkage from the cement are counteracting each other leading to an overall volume change -0.011 ml/g. SB30L also experienced swelling, however to a lesser extent than before, clearly due to the reduced CBPD and increased cement content. Interestingly, after 48 hours, the paste started to shrink. This indicates that the CBPD L reacts

at a much faster pace than cement. As the cement hydrates further, it induces shrinkage on the binder. SB30R experienced a similar effect, however to a lesser extent.

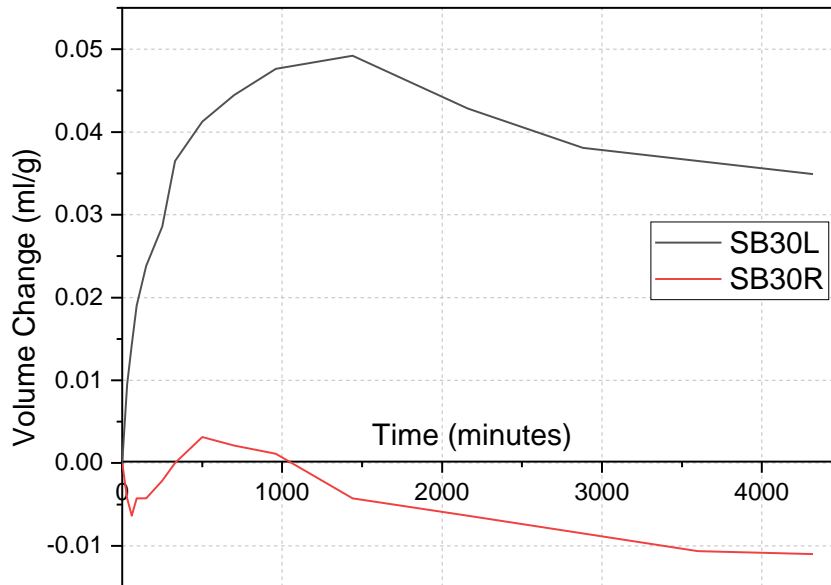


Figure 4-23 – SB30R and SB30L chemical shrinkage results

SB10 mixes showed shrinkage due to the high cement content (80%), however SB10L showed a reduction in overall early age shrinkage relative to OPC. This is an interesting outcome that shows that CBPD has the potential to inhibit early age chemical shrinkage of cementitious binders.

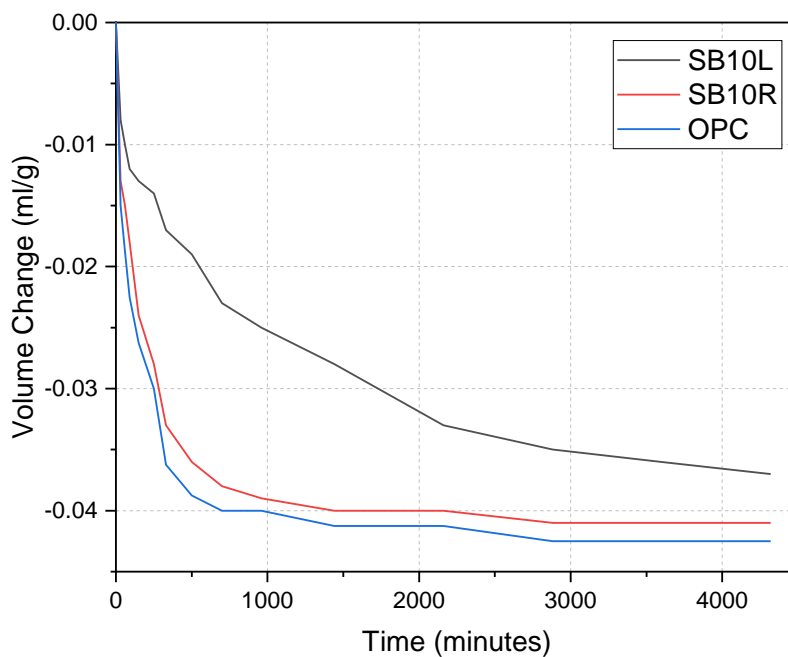


Figure 4-24 - SB10R, SB10L and OPC chemical shrinkage results

4.3.9 Total Shrinkage

Figure 4-25 shows the total shrinkage for all samples up to 150 days. Final total shrinkage increases with increasing content of CBPD.

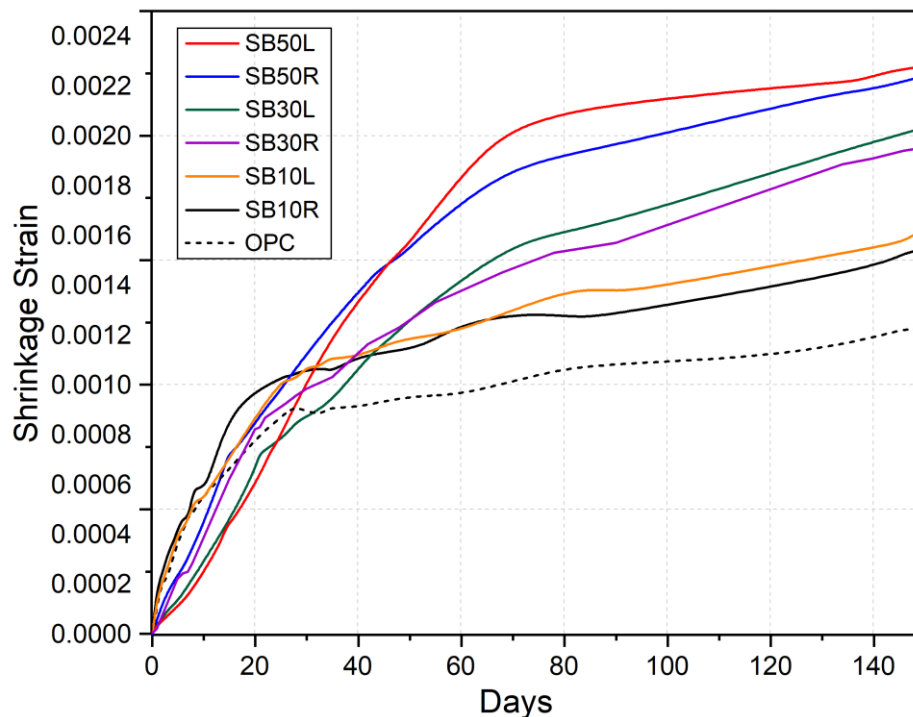


Figure 4-25 - Total shrinkage strains for all investigated mix designs

At early ages up to 10 days, the shrinkage of both SB10 mixes and OPC is practically the same, due to the high OPC content. CBPD L binders somehow exhibits the capability to reduce early age-shrinkage, most notably observed in SB30L and SB50L with the lowest shrinkage up to 30 days. This indicates a direct effect of the initial chemical expansive behaviour on total drying shrinkage. This is likely due to the expansion during the formation of ettringite and the hydration of free lime which slowed down the overall shrinkage of these mixes. As this expansion slows down, CBPD mixes eventually exhibit higher shrinkage, surpassing that of OPC at later ages. This phenomenon was also observed in the chemical shrinkage, where SB30 binders expanded and then began shrinking after a few days. Future work should focus on the use of admixtures to reduce overall shrinkage. Shrinkage reducing admixtures have been effective in reducing drying shrinkage of GBFS based AAMs in previous research (Coppola et al., 2020).

Another factor to consider is that the prisms were stored in ambient curing conditions. It has been found that expansion due to ettringite formation is greatly enhanced when cured in water and can take up to several months to complete. However, this is significantly reduced when

stored in air, due to less access to water, and an increase in restraint (Ghorab, 2004). It is likely that if water immersion shrinkage/expansion was monitored or the samples were cured for longer in water, the results would be very different and CBPD mixes would shrink less.

The type of CBPD clearly influences overall shrinkage, with CBPD R mixes consistently exhibiting lower shrinkage than their CBPD L counterparts by 90 days. However, mixes with the same CBPD quantity show similar trends, regardless of CBPD type. While the total shrinkage was highest by 150 days for SB50L, it should be noted that swelling did occur prior to the hardening of the paste with visible effect on the prisms. This may indicate that overall, the paste material expanded more than it shrunk. Total shrinkage values at 7, 28, 90, and 150 days are detailed in table 4-7.

Table 4-7 – Total shrinkage at 7, 28, 90 and 150 days for all the investigated mix designs

Mix	7 Days	28 Days	90 Days	150 days
SB50R	0.031%	0.108%	0.197%	0.225%
SB50L	0.016%	0.093%	0.213%	0.228%
SB30R	0.025%	0.096%	0.156%	0.195%
SB30L	0.019%	0.085%	0.165%	0.203%
SB10R	0.048%	0.105%	0.129%	0.155%
SB10L	0.046%	0.102%	0.137%	0.163%
OPC	0.048%	0.091%	0.109%	0.123%

4.3.10 CBPD Classification

From the results, the differences between the two types of CBPD investigated are clear. CBPD L has a higher free lime and chloride content as evidenced by the XRD diffractograms. This enabled it to have different properties such as expansive behaviour, high exothermic behaviour, and weaker binders overall due to reduced density and uneven hydration. A CBPD as such may be classified as lime rich and based on the strength results, should be limited to low controlled strength applications. As example of a low strength material CBPD L can be reused as would be as a backfilling material. Li et al., (Li et al., 2022) developed a backfilling material composed of fly ash, gypsum and GBFS with strengths up to 6.5 MPa. CBPD L binders can also be reused in soil stabilisation. Low strength GBFS AAMs have been utilised in the past to stabilise hazardous arsenic-bearing tailings as an example (Jiang et al., 2024).

CBPD R binders gained strengths largely due to their sulphate content, which facilitated the formation of ettringite, and the higher quantity of calcite. Thus, this CBPD can be classified as sulphate rich. The balance between sulphates and free lime in this binder allows it to be more appropriate for reuse in more structural applications due to its suitable strength. Further optimisation of the material, through milling and other methods could lead to a much stronger binder.

It must be noted that while this research covered two types of CBPD that significantly varied in composition, future work needs to be carried out on further types. CBPD may be procured from different parts of the world and compared similarly as in this research, as this will help standardise and classify the material further. Future work may also focus on treatment methods to reduce the variability of the material. An example of this could be the reduction of chloride content through leaching techniques. This method was used by Seo et al. (2019) where they managed to reduce chloride contents in the CBPD by up to 90%.

4.4 Conclusions

This paper compared two types of bypass dust as activators of CBPD and discussed their differences. The results provided information on the effect the composition of CBPD has in GBFS-based mortars. Two types of CBPD were analysed, a sulphate-rich CBPD (CBPD-R) and a lime-rich CBPD (CBPD L). The following conclusions can be drawn:

1. CBPD R binders have a higher water demand than CBPD L, and produce stiffer mixes relative to CBPD L. Hence, the binders also set faster. The reduction of GBFS and CBPD content lead to a better flowability.
2. CBPD L is much more reactive and has a higher heat of hydration relative to CBPD R. This is attributed to the highly exothermic reaction between lime and water.
3. CBPD R binders are denser than CBPD L binders, and lead to stronger binders. Inclusion of cement is overall beneficial for the strength, however the 20% replacement of OPC with CBPD-GBFS provided the strongest binders both in flexure and compression.
4. Chemical shrinkage results show initial expansion for both CBPD L and R binders, however for different reasons. It is hypothesised that CBPD L expands due to the free lime reaction with water, whereas CBPD R expands due to ettringite formation. This expansion also leads to lower total shrinkage at early ages, however by 90 days CBPD binders show higher total shrinkage than OPC.

5. Microstructural analysis shows that CBPD L produces a much larger amount of portlandite than CBPD R, however CBPD R produces more ettringite due to its higher sulphate content. Ultimately, both hydration reactions are dominated by these phases. CBPD R also had a higher calcite content.

Overall, this research explained the reason for the differences in hydration with different types of CBPD, and what may be expected when dealing with these materials. Based on these results, it can be concluded that a CBPD that is lower in free lime content can be more favourable due to less overall expansion, leading to stronger binders and likely more durable mortar/concrete. At the end the CBPD was classified as sulphate or lime rich, and the potential uses of each type was highlighted. Future work should focus more on durability studies on CBPD binders as well as the use of admixtures to aid in workability and shrinkage of these binders.

Chapter 5 – Carbon Curing of Cement Bypass Dust

5.1 Introduction

Carbon curing of cementitious binders has been experimented upon since the beginning of the 1970s (Klemm & Berger, 1972). Only recently, however, has this technique begun to gain prominence. Figure 5-1 shows the yearly increase of publications (key words: carbon curing concrete, carbon curing cement, carbon curing mortar, CO₂ curing) related to carbon curing of cementitious materials since 2015 (Scopus, 2023). This is due to the urgent need to reduce CO₂ emissions associated with cement manufacturing process. CO₂ sequestration and utilisation are alternatives that can play a very important role in the mitigation of emissions worldwide (Cuellar-Franca & Azapagic, 2015).

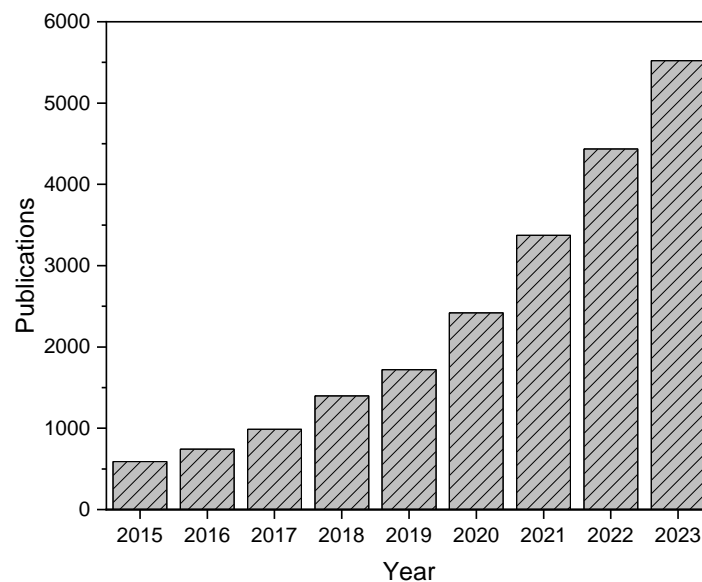
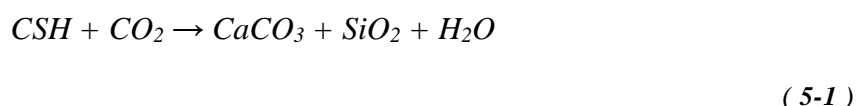
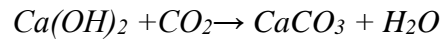


Figure 5-1 - Publications related to carbon curing of cement since 2015

A practical application includes curing of precast concrete/mortar specimens inside an enclosed chamber, which is subsequently filled with pure CO₂ gas. Following this, CSH, free lime, and portlandite react with the CO₂ and form calcium carbonate as seen in the equations below (Zhang et al., 2017):





(5-3)

The difference between atmospheric carbonation and carbonation curing is that the CO₂ in carbon curing directly reacts with the binding matrix during critical hydration periods. The CO₂ will act as a reactant, and not a catalyst like in atmospheric carbonation, allowing different reaction products to be formed (Zhang et al., 2017). Atmospheric carbonation is detrimental to concrete due to a reduction in pH of the pore solution causing rebar corrosion (Mi et al., 2023).

Research involving carbon curing of cement has shown very positive results regarding strength and durability. The main reasons for strength increase are attributed to the unhydrated cement minerals reacting with carbon dioxide, accelerating the hardening process leading to improved mechanical and durability properties (Li et al., 2019). Following carbon curing, CSH and calcium carbonate are the most important products formed (Zhang et al., 2023). Additionally, research has also shown environmental advantages of using this technology to cure concrete (Mahoutian & Shao, 2016; Kashef-Hagigi et al., 2015).

Rostami et al. (2012), compared carbon cured concrete to conventional steam curing. They found a reduction in total portlandite due to its conversion to calcium carbonate. The strength of their binders was enhanced at early ages and reached comparable values to steam curing by 28 days. They found improved sulphate and freeze-thaw resistance, as well as an increased surface resistivity in carbon cured concretes. Similar results were obtained by He et al. (2016) which had a stronger CO₂ cured binder at 28 days relative to an ambient cured binder. Early age strength was enhanced and decreased porosity was achieved due to densification of the binder. Hassan et al. (2014) also showed large increases in their carbon cured concrete relative to steam cured concrete at both early and late ages.

Research on the carbon curing of CBPD is very scarce, however there is some literature on the reuse of cement kiln dust (CKD). Since the materials are similar in nature, the research is quite relevant. The increased alkalinity and availability of alkaline cations can be beneficial and can enhance the rate of carbon uptake of CKD relative to OPC (Sharma and Goyal, 2018). Furthermore, the environmental benefits of CO₂ capture coupled with the reduction in landfilling, can lead to a very sustainable cement binder. There are several reaction pathways in CKD that can capture CO₂ as seen from the equations below (Huntzinger et al., 2009):



Lutnyski and Pierzyna (2017) investigated the possible reuse of CKD for carbonation and as a backfilling material. They concluded that CKD was satisfactory in carbon capture and the rate of capture was determined by the free lime content. Gunning et al. (2010) investigated the accelerated carbonation of several industrial wastes, including CKD and CBPD, and found that wastes mainly composed of lime absorbed the most CO₂ due to the formation of calcite. CKD and CBPD were the most reactive wastes they found. Finally, Alimi et al. (2022) compared the carbonation potential of two CKDs replacing cement at high percentages. They found that the finer CKD had an increased carbon capture potential and concluded that the relative CO₂ uptake was higher for increased CKD replacement. Contrary to these results, Biava et al. (2023) investigated the direct carbonation of different wastes including electric arc furnace slag and CKD. CO₂ gas was directly pumped into a vacuum sealed chamber that contained the wastes. The results showed that CKD had the worst CO₂ performance relative to the slags, however it still showed a relatively strong sequestration capacity.

This chapter aims to investigate the potential of CBPD in carbon curing technologies. Previously two CBPDs were investigated, where one had a much higher quantity of free lime. Due to this, the reaction between lime and water caused severe expansion and, consequently, reduced compressive strengths. The primary target of this research is to find a potential use for this CBPD and investigate the main differences between the carbon curing of two CBPDs. The CBPDs will be in binary and ternary blends composed of GBFS and cement and will undergo carbon curing for 5 hours in a pressurised container.

5.2 Methodology

5.2.1 Materials

Two types of CBPD are examined: CBPD R, sourced from a CEMEX plant in Rugby UK; and CBPD L, from a cement plant in Latvia. Additionally, 32.5R Cement Type II (OPC) and GBFS were used. The particle size distribution of these materials is presented in figure 5-2 below, which shows that CBPD R is the coarsest of the binders, whilst CBPD L is the finest.

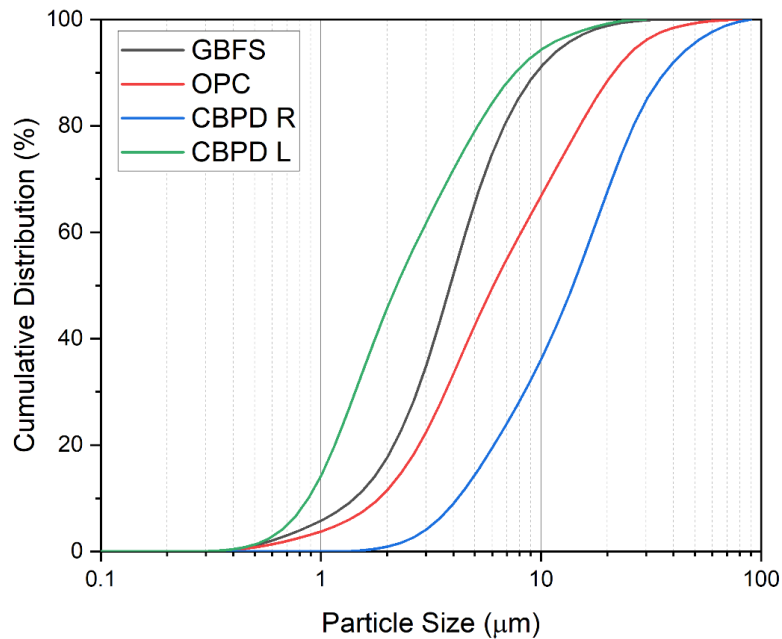


Figure 5-2 – Particle size of raw materials

The XRD patterns of the materials are shown in figure 5-3. The OPC contains all phases typically expected of cement. As expected, GBFS is high in calcium and is largely amorphous. The primary difference between the two types of CBPD is in the lime and sulphate contents, with CBPD L having much higher lime contents and CBPD R having much more sulphate, reflected by the gypsum peaks. Additionally, CBPD L shows more prominent sylvite peaks which is a potassium chloride mineral.

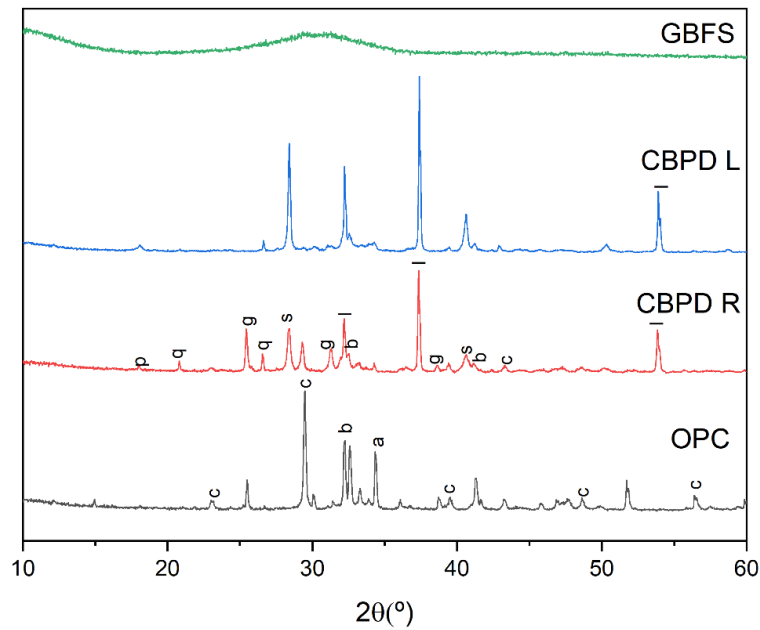


Figure 5-3 - XRD patterns of raw materials (p=portlandite, q = quartz, g = gypsum, b = belite, l = lime, a = alite, s = sylvite, c = calcite)

5.2.2 Curing and Casting Procedure

Due to the small size of the carbonation chamber the samples used in this experiment were 20 mm paste cubes. The water to binder ratio was 0.4, however, two more water to cement ratios (0.3, 0.5 etc.) were examined on CBPD L during trials. These trials are shown in section 5.3.1. The mixes used in this experiment are listed in table 5-1.

Table 5-1 – Mix designs investigated

Mix Design	CBPD R (%)	CBPD L (%)	OPC (%)	GBFS (%)	Curing Type (W/C)
OPC	0	0	100	0	W
OPC-C	0	0	100	0	C
SB50R	50	0	0	50	W
SB50R-C	50	0	0	50	C
SB50L	0	50	0	50	W
SB50L-C	0	50	0	50	C
SB30R	30	0	40	30	W
SB30R-C	30	0	40	30	C
SB30L	0	30	40	30	W
SB30L-C	0	30	40	30	C

The dry material was mixed first and the water was then added. Mixing continued until the paste was consistent, with no dry material or lumps. The paste was then cast into the mould and vibrated to release any entrapped air. A polyethylene sheet was used to cover the paste to prevent excessive water evaporation.

After 24 hours, the cubes were demoulded and preconditioned for 3 hours in an environmental chamber at 50% relative humidity and a temperature of 23°C. Preconditioning was used to reduce free water and facilitate the penetration of CO₂. After preconditioning, two curing techniques were applied:

1. Carbon-Curing – Samples were placed in an airtight carbonation chamber for 5 hours (see figure 5-4). The chamber supplied CO₂ gas of 99% purity and pressure of 1 atm. Following carbon curing, the cubes were wrapped in moist hessian and placed in plastic bags, to ensure a moist environment until the testing age. This curing method was derived from the research conducted by Sharma and Goyal (2018), whose findings demonstrated that this curing technique was more effective in promoting the strength development of carbon-cured mortar.

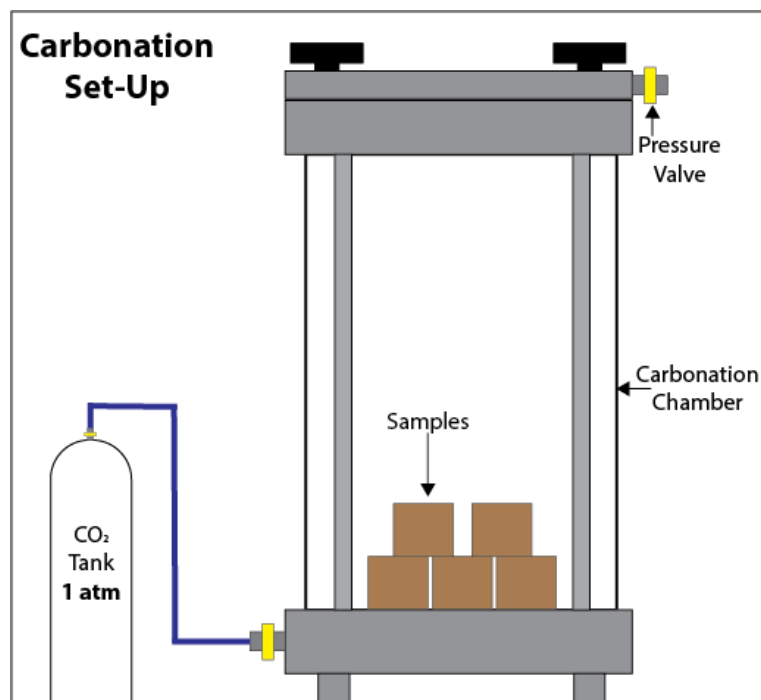


Figure 5-4 - Carbonation curing set-up

2. Water-Curing – Water curing was carried out right after demoulding, where the paste cubes were placed in a water tank at $21 \pm 2^\circ\text{C}$ until the testing age.

5.2.3 Analytical Techniques

5.2.3.1 Mass Change

As a measure of CO₂ uptake, the mass change between the surface dry cubes prior to carbonation and after carbonation was measured. Nine cubes were carbonated for each mix design and the average mass change of all nine was taken.

$$CO_2 = \frac{Mass_{afterCO_2} - Mass_{beforeCO_2}}{Mass_{drybinder}} \quad (5-7)$$

5.2.3.2 Water absorption and Bulk Density

Water absorption was determined in accordance with ASTM C 642. Bulk density was measured by weighing the dry weight of the cubes and the submerged weight. The following equation was then used:

$$Bulk\ Density = \frac{Dry\ Weight}{(Dry\ Weight - Submerged\ Weight)} \quad (5-8)$$

5.2.3.3 Compressive Strength Testing

Compressive strength tests were carried out at the age of 3, 7 and 28 days on a universal testing machine with a maximum load capacity of 10kN. The loading rate used was of 0.5 N/mm²/sec.

5.2.3.4 Microstructural Analysis

Microstructural analysis was only performed for SB50R, SB50L and OPC mixes as these were deemed to be sufficient to understand the effect of carbonation curing.

5.2.3.4.1 X-Ray Diffraction

X-Ray diffraction (XRD), used to analyse the microstructural analysis of each mix, was performed at 28 days with a Bruker D2 Phaser. The 2θ range was of 5-60° with a step size of 0.02°.

5.2.3.4.2 Thermogravimetric Analysis

Thermogravimetric Analysis (TGA) was carried out using a Perkin Elmer Pyris 1 TGA. Samples were heated from 40°C to 1000°C degrees at a rate of 10 °C per minute. 10 mg of the ground powder samples were used to investigate the thermal behaviour of CBPD paste.

5.2.3.4.3 Scanning Electron Imaging

The fractured surface of the CBPD based paste was observed using a FEI Inspect F field emission scanning electron (FE-SEM) microscope. The microstructure was analysed at a voltage of 15 kV using a backscattering electron mode.

5.3 Results

5.3.1 Mass Gain

5.3.1.1 Trials

Water is a very important factor when carbonating a material and it needs to be proportioned correctly. A high w/c ratio can block the diffusion of CO₂ in the system, and a too low w/c ratio can halt the reaction (Shi et al., 2012). Thus, prior to testing a suitable w/c ratio was selected based on most CO₂ absorption. Trials took place on SB50L. Initial preconditioning entailed 3 hours in an environmental chamber at a temperature of 23°C and a relative humidity of 50%. The results are shown in table 5-2 below. The w/c ratio selected was 0.4.

Table 5-2 - Mass gain of SB50L with different W/C ratios

w/c Ratio	Mass Gain (%)
0.3	5.1
0.35	5.9
0.4	6.9
0.45	6.7
0.5	6.6

The appropriate time of carbonation was also selected based on trials. This is shown in figure 5-5, where 5 hours of curing provided the largest mass gain. Due to laboratory constraints, longer periods of time could not be attempted, however, most of the mass gain occurs during the first hour of carbon curing and a notable decrease in the rate of mass gain can be observed after about 4 hours.

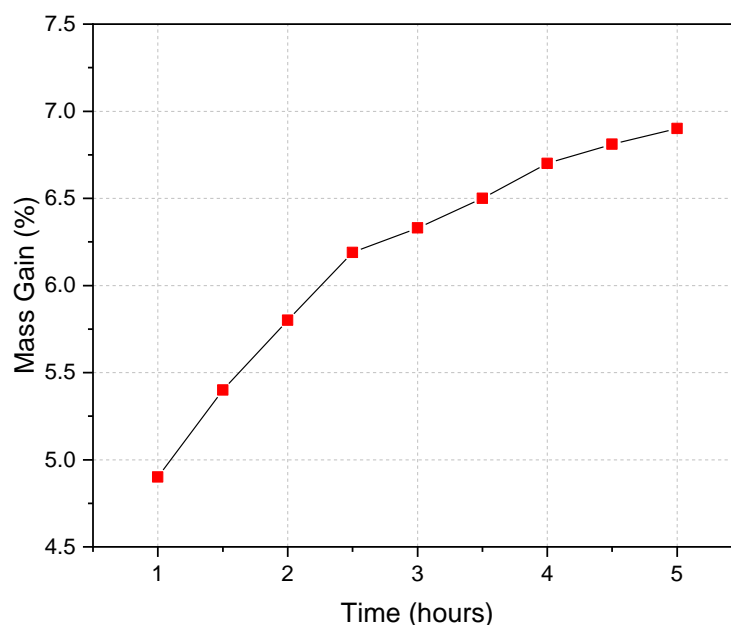


Figure 5-5 - Mass gain over time of SB50L

5.3.1.2 Mass Change

From the mass change results shown in table 5-3, SB50L-C shows the largest mass gain following carbon curing, with a mass increase of 6.9%. This gain can be largely attributed to formation of CaCO_3 as a result of the absorption of CO_2 by lime that was present in higher volume in CBPD L. CBPD R, having a significantly lower free lime content, showed a reduced mass gain. The mass gain reduced as the CBPD content decreased as seen in SB30 mixes. While the mass gain technique method underestimates the total CO_2 uptake, since not all water evaporated during carbonation can be collected, as a comparative method it is shown to be effective (Shao and Morshed, 2013).

Table 5-3 – Mass gain of each mix design after CO_2 mass gain

Mix Design	Mass Gain (%)
SB50R	1.9
SB50L	6.9
SB30R	1.2
SB30L	4.7
OPC	0.6

It must be noted that lime content is not the only factor in mass uptake of CBPD binders. Alimi et al. (2022), tested the carbon uptake of CKD-OPC binders with OPC binders replaced by up to 60% with CKD. Their results showed that the higher-lime CKD in fact had a lower carbon

dioxide uptake, which was attributed to the coarseness of the CKD. In this study, CBPD L is much finer than CBPD R, which likely enhances CO₂ uptake.

Another factor to consider is the calcite content present in CBPD R binders relative to CBPD L. As research by Biava et al. (2023) has shown, the large presence of calcite as a phase reduces the CO₂ sequestration potential, due to the low solubility of this phase in water. Additionally, calcite does not react with CO₂. This also explains the behaviour of the control mix.

5.3.2 Density and Water Absorption

Figure 5-6 shows the water absorption results at 3, 7, and 28 days, whilst figure 5-7 shows the 28-day density. Carbon curing has a positive effect on both density and absorption. The largest improvements are observed in SB50L-C where there is a reduction in water absorption of up to 14% at 7 days and 10% at 28 days relative to SB50L. There is also a significant increase in density when comparing SB50L-C to SB50L. Regarding SB50R and OPC, the results also indicate an improvement, albeit to a lesser extent.

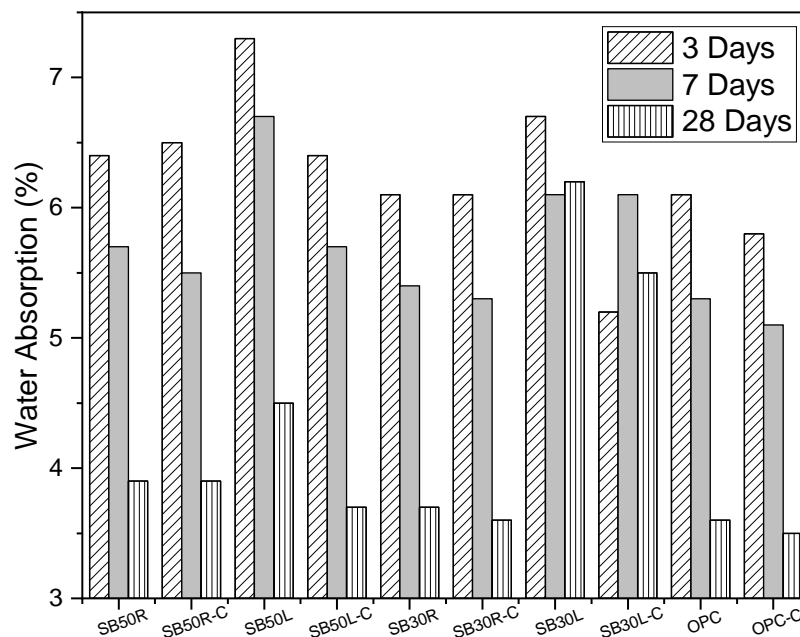


Figure 5-6 - Water absorption over time of the specimens

The density at 28 days is shown below, with the density of the carbonated mixes vs the non-carbonated mixes. Mass gain is expected to increase density as more hydration products are formed leading to a denser structure. It should be noted that the main hydration product from carbon curing is CaCO₃ that has a significantly higher density and molar volume than portlandite (von Greve-Dierfeld et al., 2020).

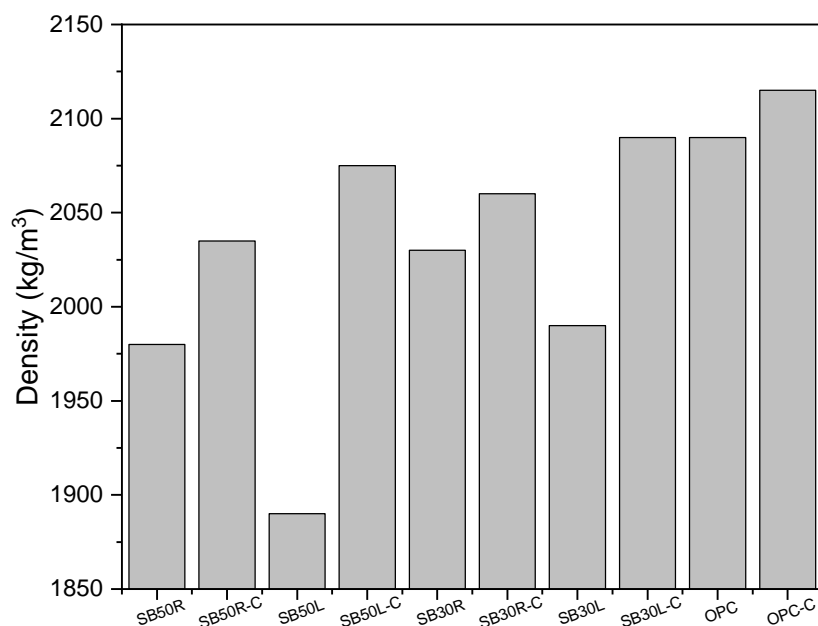


Figure 5-7 - Density results for CBPD and control mix at 28 days

The mass gain does not fully follow the density gain percentage as seen from table 5-4. This is likely due to the mass gain measurement being measured at early ages, hydration over time may have increased the relative density further. This may also be indicative of a change in volume or other factors beyond the scope of this research.

Table 5-4 – Density increase of the CO₂ cured mixes relative to non-CO₂ cured mixes

Mix	Density increase (%)
SB50R-C	2.8
SB50L-C	9.8
SB30R-C	1.5
SB30L-C	5.0
OPC	1.1

5.3.3 Compressive Strength

The average compressive strengths for the pastes at 3, 7 and 28 days are shown in figure 5-8. When examining the strength development in the OPC control mixes, the benefits of carbon curing are not evident as the water cured specimens were slightly stronger than carbon cured ones. The low mass gain may indicate that the amount of calcite formed did not supplement the loss in hydration products due to lack of water curing during initial curing of the paste.

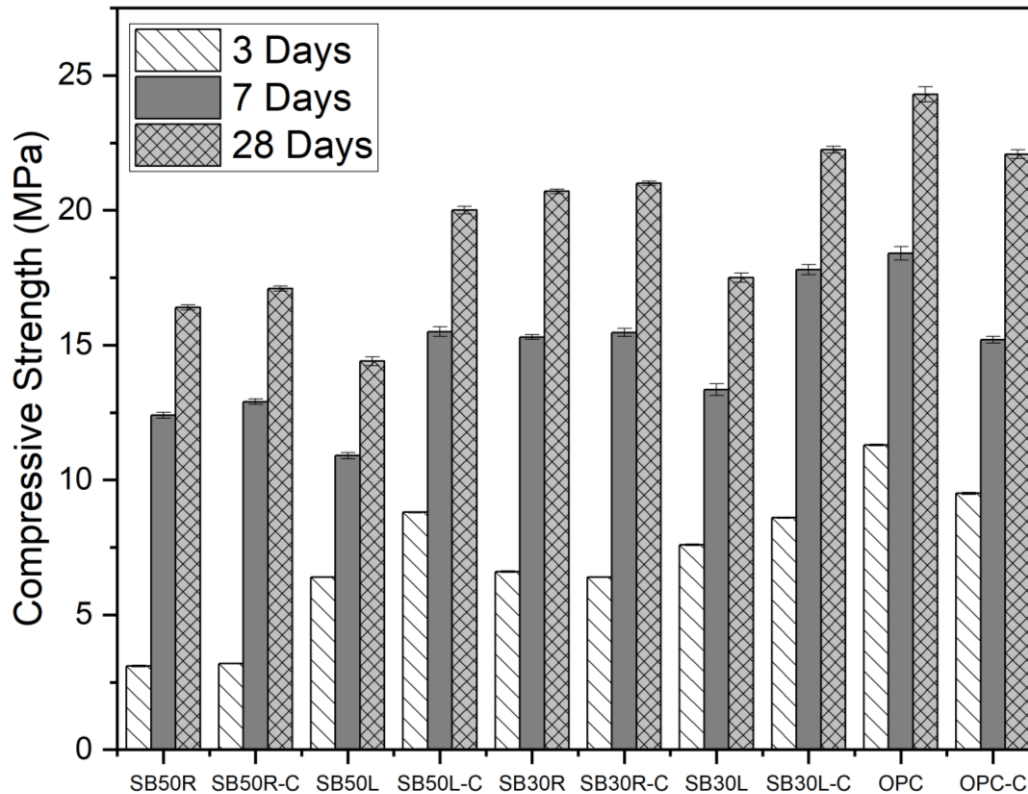


Figure 5-8 - Compressive strength results

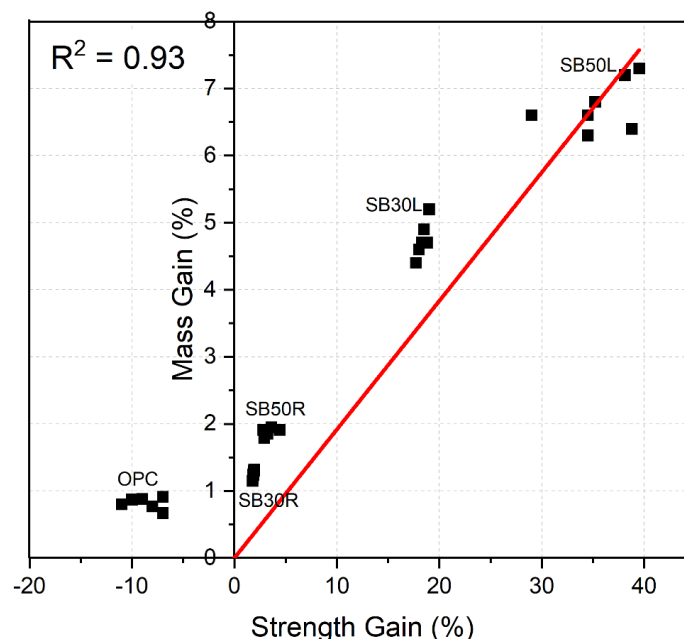
SB50 mixes performed better after carbonation curing relative to their water-cured counterparts. The relative strength increases between the mixes remained similar during the testing period. SB50L-C benefitted the most from carbon curing and by 28 days had a compressive strength of 20MPa, an increase of 38.8% compared to SB50L which achieved 14.4MPa. This increase also means that SB50L-C exceeded the strength of SB50R at all ages, which is not the case without carbon curing. This confirms that high lime contents in CBPD can be exploited using carbon curing to make stronger binders. SB30 mixes also achieved strength gains, however more moderate, which is likely due to the lower quantity of CBPD. The strength gain due to carbonation enabled SB30L-C to achieve a strength only 9% weaker than the uncarbonated control sample. The strength gain percentage due to carbon curing at 28 days is presented in table 5-5.

Table 5-5 – Strength increase of the CO₂ cured mixes relative to non-CO₂ cured mixes

Mix	Strength increase (%)
SB50R-C	4.2
SB50L-C	38.8
SB30R-C	1.0
SB30L-C	27.1
OPC	-9.2

Sharma et al. (2018) tested the compressive strength of mortars containing OPC replaced by CKD up to 50% by weight and found that carbon curing can increase strength by up to 30%, with strength increasing with an increase in CKD content. They concluded that this strength increase was due to the CaCO₃ and CSH gel formation.

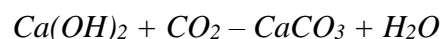
There is a very strong linear correlation between mass and strength gain as seen in figure 5-9. This indicates that the mass gain due to the intake of carbon dioxide was largely responsible for the strength gains of the carbonated specimens and hence the benefits of carbon curing are clear in CBPD mixes.

**Figure 5-9 - Correlation between mass and strength gain (%)**

It must also be considered that, due to laboratory restraints, the carbon curing was only carried out for 5 hours, where research in the past has shown the benefits of carbon curing for extended periods of time (Zhang et al., 2017). This indicates that CBPD binders may have even more potential for strength increase if carbonated for longer.

5.3.4 XRD

Figure 5-10 shows the XRD pattern for SB50L and SB50L-C. The most significant peaks to consider are the portlandite peaks at 18.04°, 28.68° and 47.1°, and the calcite peaks at 23.02°, 29.4°, 39.5, and 43.15°. The XRD patterns for the carbon cured CBPD pastes all show strong calcium carbonate peaks, indicating carbonation at a microstructural level. What is also apparent is the reduction in portlandite peaks, indicating that these were likely converted into calcium carbonate, which also explains the densification of the specimens. This is the primary reaction that occurs due to carbonation in cementitious products (Zhang et al., 2017):



(5-9)

Unreacted free lime may also react with CO₂ and form CaCO₃. The largest increase in the carbonate peak was observed for SB50L-C. The work presented in Chapter 4 showed that CBPD L-GBFS binders did not have a large amount of calcite, and this is confirmed in the SB50L XRD pattern. Due to its free lime content, it produces a very large amount of portlandite that can even exceed that formed by hydrated OPC. Hence, this is clearly the reason for the increase in carbonation. The significance of lime and portlandite formation is also evidenced when observing the portlandite peak at 18.04° which practically disappears due to carbonation.

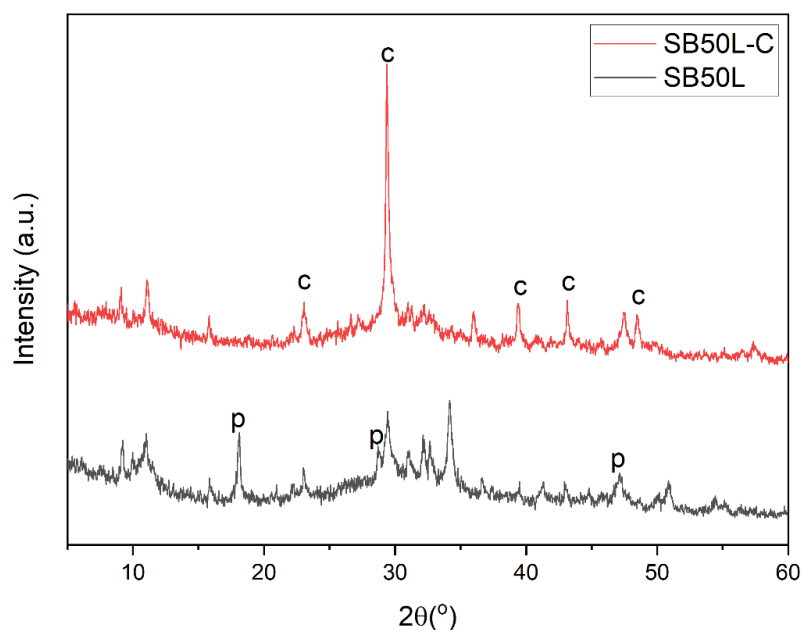


Figure 5-10 - XRD patterns for SB50L and SB50L-C (c = calcite, p = portlandite)

Similar behaviour is observed for SB50R-C, as seen in figure 5-11. This CBPD also exhibited a significant increase in CaCO_3 , albeit to a lesser extent. The previous chapter shows that CBPD R-GBFS binders are calcite-rich and produce far less portlandite than CBPD L mixes, hence the benefits of carbon curing may be hindered by this. The fact that CBPD L is more alkaline and finer is also a factor to consider. Nevertheless, SB50R-C clearly shows evidence of increased calcite due to carbonation. Despite not having a large strength increase, the benefits are not solely mechanical but also environmental.

Potassium phases also seem affected, as a prominent syngenite (potassium calcium sulphate) typically located at $31.3^\circ 2\theta$ has a reduced intensity post carbonation. Previous work on these binders has shown a reduction of this syngenite peak over time, likely due to the release of sulphate ions in the pore solution leading to the formation of ettringite. It is possible the K^+ ions in the pore solution were carbonated as well, however this was not reflected in the XRD as K_2CO_3 was not located.

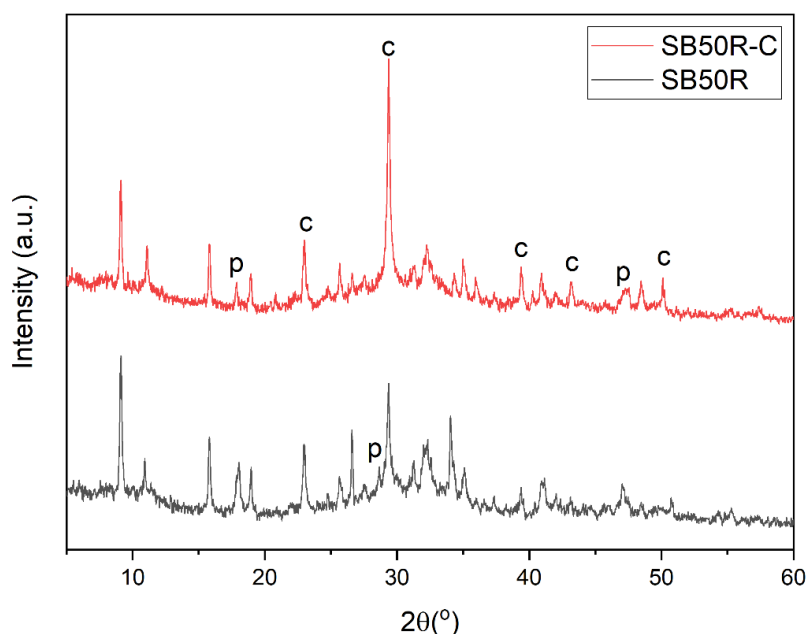


Figure 5-11 - XRD patterns for SB50R and SB50R-C (c = calcite, p = portlandite)

The OPC control mix (figure 5-12) shows the least change, as the carbonate and portlandite peaks remained mostly similar post carbonation. Past results have shown that carbon curing has positive effects on OPC binders (Rostami et al., 2012), but for longer carbon curing periods. Hence it is anticipated that further carbonation would happen with longer curing periods. Nonetheless, there is the possibility that the lack of carbonation could be due to the binder being saturated with calcite in which case it cannot produce more.

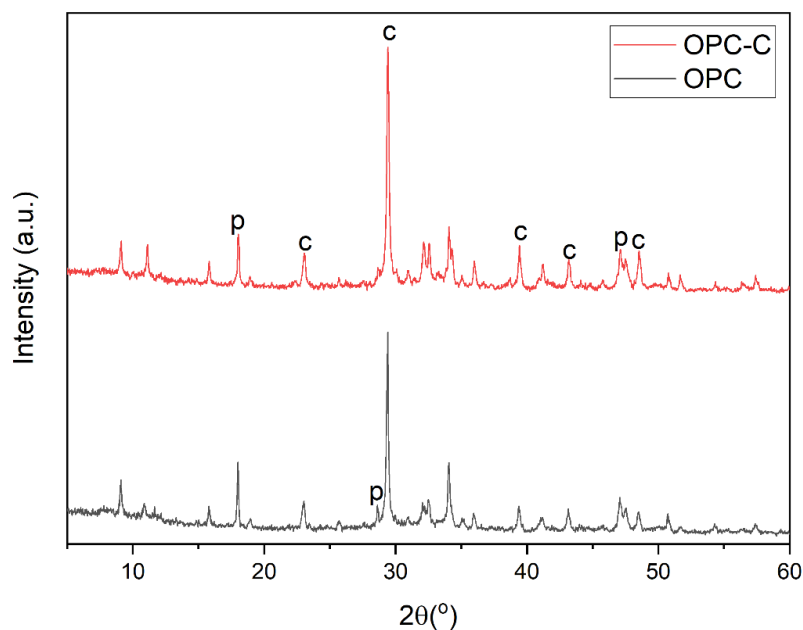


Figure 5-12 - XRD patterns of OPC and OPC-C (c = calcite, p = portlandite)

Peak quantification was carried out through deconvolution of the main portlandite (18.4°) and calcite (29.4°) peaks. The area of the peaks is presented in table 5-6 below. These results verify the visual observations. Calcite increases circa 4 times and 2 times for SB50L and SB50R, respectively. Interestingly, both SB50R-C and SB50L-C have a very similar amount of calcite which might indicate that there is a limit to the amount of carbonation for CBPD. Hence, it is possible that SB50L cannot absorb much more CO_2 as the portlandite was nearly fully converted to calcite, unlike for the case of SB50R. Considering SB50L contained the more reactive and alkaline CBPD, portlandite consumption is not necessarily the sole phase contributing to CO_2 absorption. Other alkaline phases can also factor into this.

Table 5-6 – Peak quantification of calcite and portlandite

Mix Design	Portlandite	Calcite
SB50R	47.4	106.9
SB50R-C	24.8	244.4
SB50L	71.3	69.3
SB50L-C	5.1	278.6
OPC	68.8	246.8
OPC-C	54.2	305.4

5.3.5 Thermogravimetric Analysis

The TGA curves for 28 day cured specimens are shown in figures 5-13 to 5-15 below, while the mass loss results are summarised in table 5-7. The main decomposition mass losses to

observe are for portlandite (380-500°C) and calcite (600-740°). SB50L shows a mass loss of calcite and portlandite of 1.7% and 2.8%, respectively. Comparatively, SB50L-C has mass losses of 7.9% for calcite and 1.2% for portlandite, clearly corroborating the XRD results showing the significant increase in calcite due to carbon curing. Consequently, the portlandite had a sharp decrease for SB50L-C where it had been mostly consumed. The TGA also highlights the benefits of carbon curing SB50L-C when observing the overall mass loss, as SB50L-C has a mass loss of 18.5% and SB50L of 29%, however, this loss is largely in the range between 35-105°C which is typically attributed to the loss of hygroscopic water (Unluer and Tabbaa, 2013). It must be noted that this mass loss was quite variable from the results, hence the most significant losses to consider should be between 380-800°C.

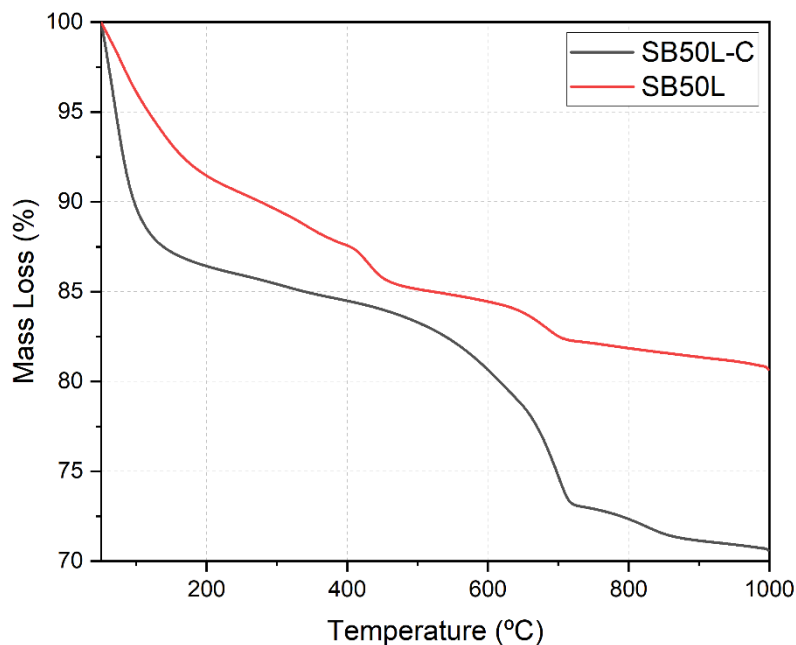


Figure 5-13 – TGA results of SB50L and SB50L-C

The results for SB50R-C show a clear increase in the calcite weight loss due to carbon curing. SB50R and SB50R-C had mass losses of 1.9% and 3.5% respectively. In contrast, the portlandite quantity for SB50R and SB50R-C were 1.9% and 1.1%, respectively. Much like with the XRD, potassium carbonate phases were not identified in the TGA.

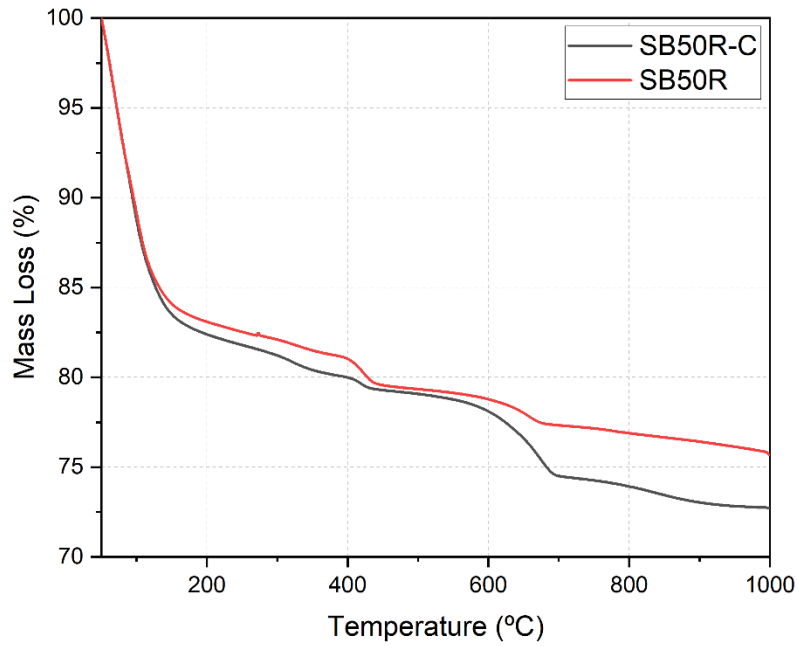


Figure 5-14 – TGA results of SB50R and SB50R-C

The results for the OPC (figure 15-5) control also show little change in both the carbonated and non-carbonated mix. It can be inferred that the reason for the strength drop due to carbonation was due to the lack of water curing. Hence, the beneficial effect of carbon curing on strength is only evident when large amounts of CO₂ are absorbed. Similarly, to the SB50 results, the mass loss in the hygroscopic temperature range was variable.

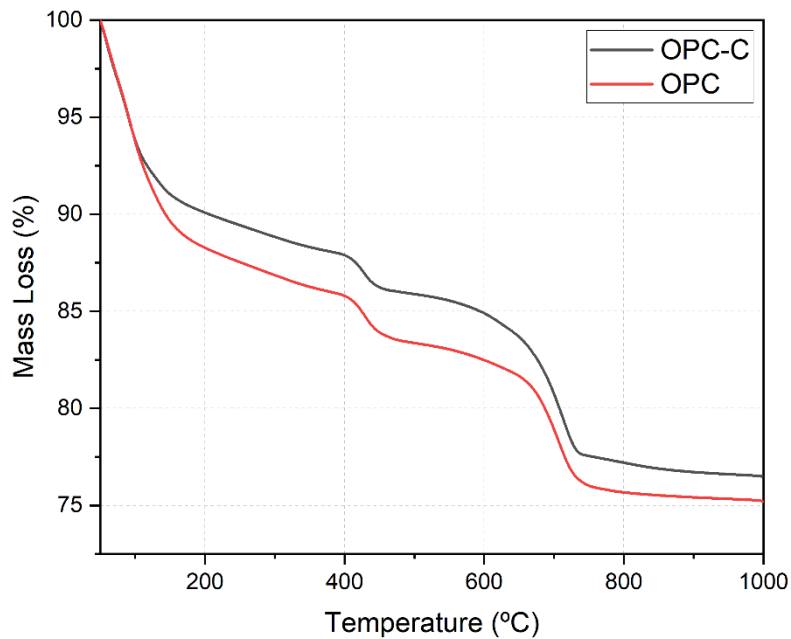


Figure 5-15 – TGA results of OPC and OPC-C

The loss results are presented in table 5-7.

Table 5-7 - TGA mass loss results

Mix Design	Portlandite Mass Loss (%) (380°-500°)	Calcite Mass Loss (%) (600°-740°)
SB50R	1.9	1.9
SB50R-C	1.1	3.5
SB50L	2.8	1.7
SB50L-C	1.2	7.9
OPC	2.6	6.3
OPC-C	2.2	7.1

Carbon uptake will not always result in calcite formation as CO₂ may react with other alkali cations. This was not evident, however, from the TGA hence the calcite mass loss can be deemed as a rough estimate of carbon uptake. As seen from the table, SB50L-C gained the most calcite and had virtually no portlandite due to its consumption. On the other hand, for SB50R-C longer carbonation times may be required. The reduced CO₂ intake may be attributed to coarser particles of CBPD R that lead to a reduced surface area and fewer reaction points, possibly leaving large unhydrated CBPD particles with a coating of the reaction product (Abidoeye and Das, 2021). Another reason for this can be due to the reduced alkalinity of CBPD R compared to CBPD L. CO₂ reacts with alkali cations to produce carbonate minerals, hence the significance of alkalinity (Kirchofer et al., 2023). Carbonation in alkaline wastes has been widely investigated (Gunning, 2010). While OPC has high alkalinity, several of the alkaline cations in CBPD are present in much lower levels in OPC except for calcium.

The DTG images are presented in figure 5-16, 5-17 and 5-18 below. The results generally provide the same results to the TGA; however, they highlight certain peaks and mass losses that are not clearly distinguishable in the TGA.

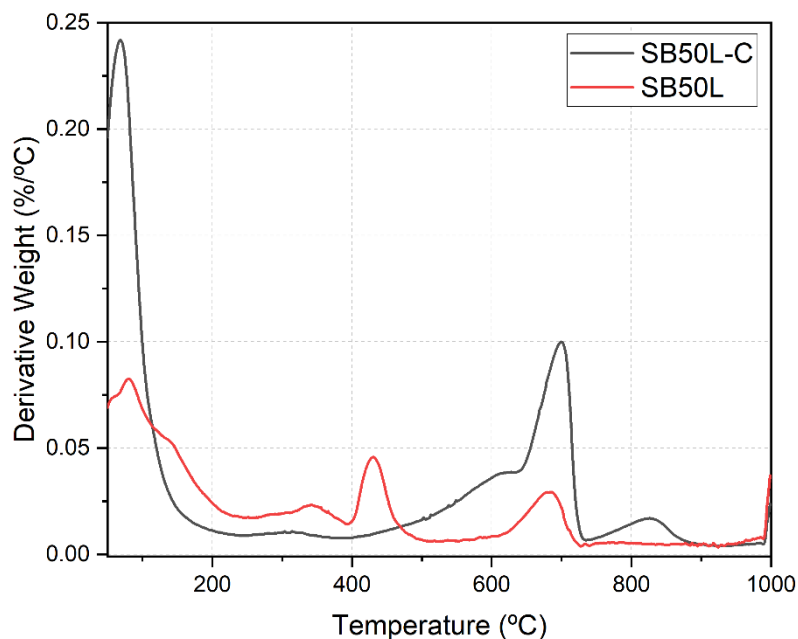


Figure 5-16 – DTG results of SB50L and SB50L-C

The main difference between carbonated and non-carbonated results, besides the calcite and portlandite peaks, occurs at 800°C where a peak occurs only for carbonated mixes, primarily SB50L-C. A similar peak was observed for Huntzinger et al. (2009) for carbonated CKD. They could not identify its origin, however, they argued that it may be anhydrite. Nonetheless, it is possible that this is a second calcite peak. Stepkowska et al. (2005), identified carbonate peaks that decomposed at temperatures above 750°C and attributed this to the larger size of the calcite crystals relative to other calcite. Hence, this mass loss could be due to the larger calcite crystals.

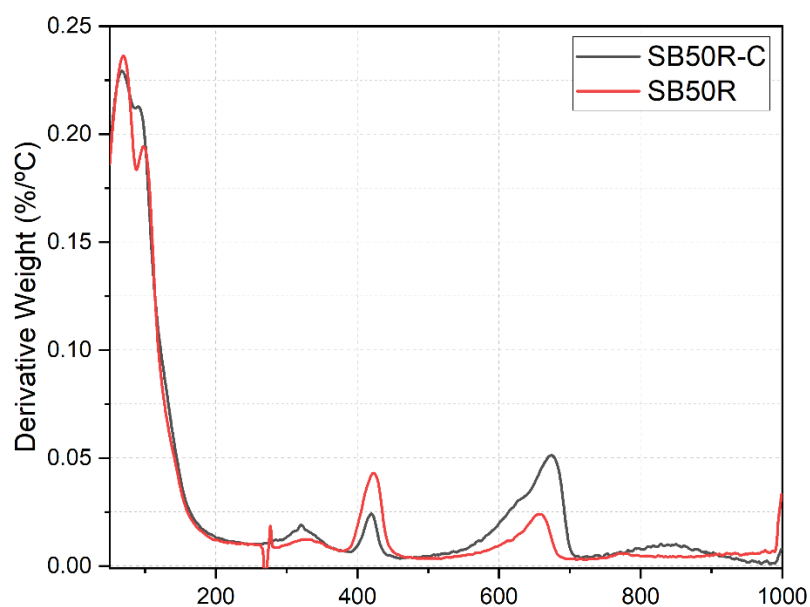


Figure 5-17 – DTG results of SB50R and SB50R-C

Additionally, SB50L-C produces a large shoulder between 600°C and 650°C which is visible in all mixes to a lesser extent. This may indicate the decomposition of smaller and weaker calcite crystals. Thus, the effects of carbonation are more clearly seen through the TGA/DTG analysis.

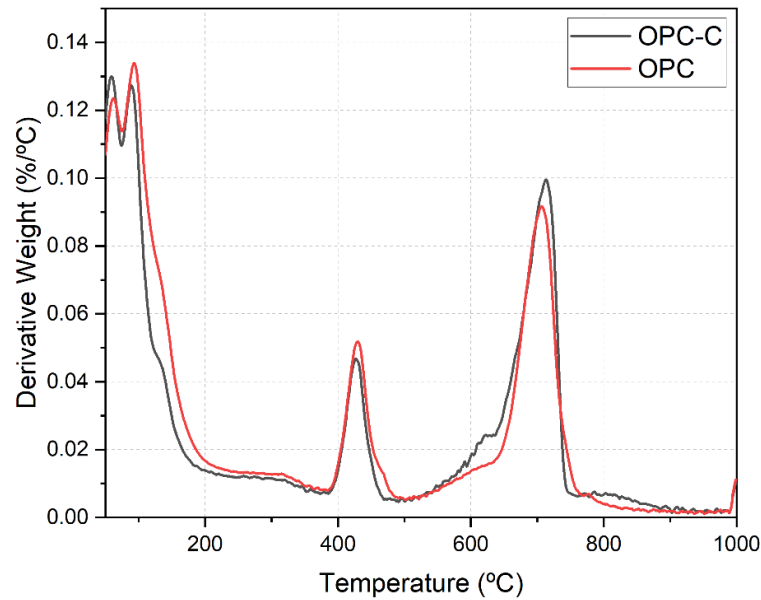


Figure 5-18 – DTG results of OPC and OPC-C

5.3.6 Scanning Electron Imagery

SEM images for SB50L and SB50L-C are shown in figure 5-19. The main microstructure of the binder clearly undergoes a large change through carbonation where several CaCO_3 cubes are seen abundantly in SB50L relative to SB50L-C. From the images it can be inferred that the SB50L-C also has the denser microstructure due to the lesser dark spots that show voids. Lesser voids are observed due to the pore filling qualities of the CaCO_3 .

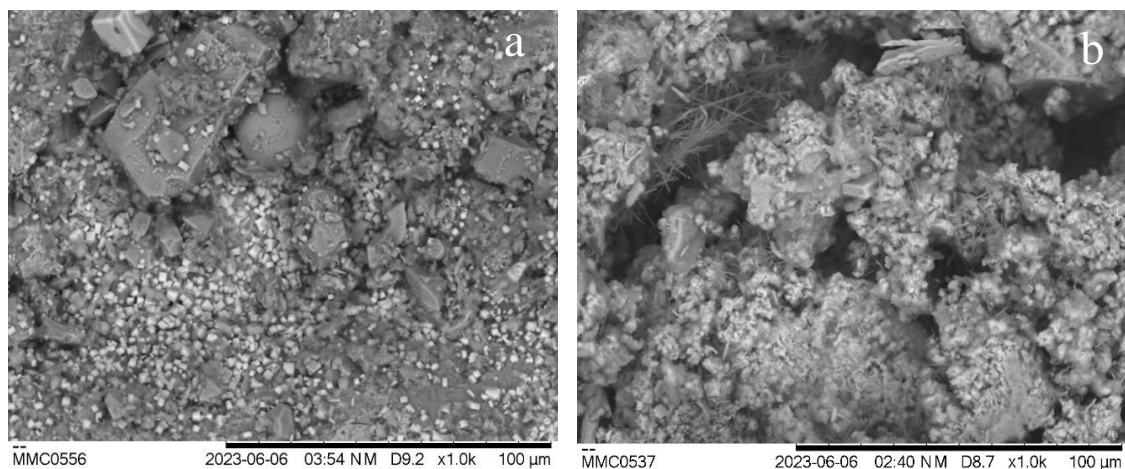


Figure 5-19 - SEM images (a) SB50L (b) SB50L-C

The reduced number of voids explains the lower water absorption and the higher density and strength of SB50L-C binders relative to SB50L.

Larger calcite crystals are evident in figure 5-19 (a), and a closer look at a larger calcite crystal is shown in figure 5-20. This supports the hypothesis that the DTG peaks around 750°C+ can be attributed to such large calcite crystals.

Similar results were seen in the TGA-DTG where calcite of different size ranges was formed. Higher decomposition temperatures in the TGA results were attributable to larger calcite crystals.

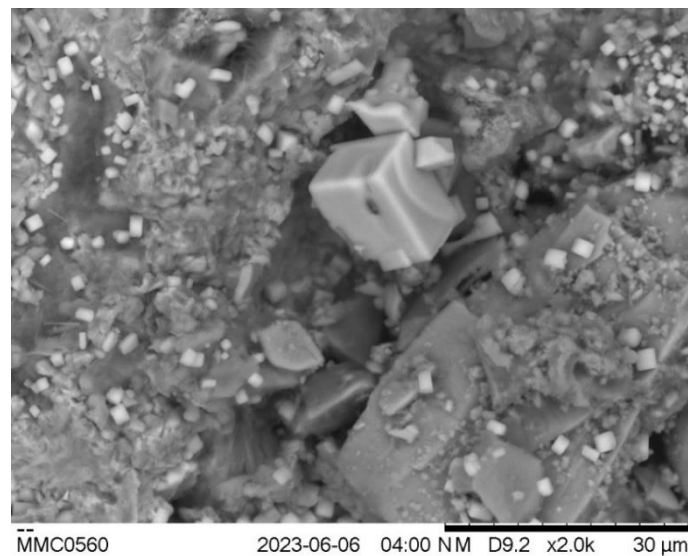


Figure 5-20 – Large calcite crystal for SB50L-C

5.3.7 Technical Feasibility

Carbon curing has shown clear mechanical benefits for CBPD binders, especially if they are lime rich. The previous chapter comparing the two binders found CBPD R superior due to its higher ettringite and calcite content when mixed with slag. However, when carbon cured CBPD L had a much higher strength and density than CBPD R pastes. It can be inferred that these gains may also help durability, however, due to technical limitations, larger scale carbon curing could not be attempted.

Carbon curing technology is already commercialised and will only grow over time (Hanifa et al., 2023). Carbon8 is a company set up in 2006 that has commercialised Accelerated Carbonation technology. Through their patented method they have successfully carbonised over two tonnes of waste that otherwise would have been used in landfill in the UK. This

number is forecasted to grow. CarbonCure is another company that produces strong concretes in Canada using carbon curing technology. They have already been part of large commercial projects such as in the Calgary Airport. They have estimated to have saved up to 900 million tonnes of CO₂ through their technology. Finally, Carbstone is a company responsible for the carbonation of slag in Belgium, having already several patents. Many other companies involved in carbon curing exist. Despite this, implementation of this technology in factories can also prove to be very costly due to transportation and upgrading of the factory.

The largest hindrance on the uptake of this technology occurs due to operational and economic reasons (Hassan et al., 2021). One of the costs to consider is the carbon dioxide itself, which is estimated to cost between 42-84€ per tonne (Normann et al., 2019). Nevertheless, this is much cheaper when considering waste CO₂ and, furthermore, CO₂ gas pricing is expected to reduce as the need for sustainable technologies is further necessitated (China carbon pricing, 2016). The use of this technology will only keep increasing in the future. Additionally further research is needed to fully understand its effects on OPC. Carbonation curing is still a growing technology and research still must be made on the long-term impact of this type of curing on the potential pH reduction and subsequent damaging of the passive layer formed on the rebar.

The main benefit of CBPD is that it is a solid waste material; hence it would not require any different treatment than other raw materials used in mortar/concrete such as fly ash or GBFS. Waste products such as CBPD can produce much stronger binders when this technology is implemented, hence it is largely feasible and manageable to perform large scale carbon curing.

5.3.8 Sustainability

Besides the improvement in mechanical and durability performance, the clear advantage of carbon curing of CBPD is the environmental benefit. Cement based products are already considered to be CO₂ sinks where a recent study has shown that 43% of CO₂ emissions can be offset due to atmospheric carbonation (Xi et al., 2016). Carbon curing can cut down the carbonation process from years and decades to potentially hours and days. Based on research by Hassan and Shao (2014) in the US, concrete blocks with 13% OPC content can uptake up to 24% CO₂ in 4 hours. This indicates an expected CO₂ storage of up to 2 million tonnes per annum in the US, which accounts to a 2.5% reduction in CO₂ footprint.

Few papers exist on the life cycle analysis of CO₂ cured concrete/mortar. Huang et al. (2019), performed a life cycle assessment on seven different concrete blocks and assessed the global warming potential (GWP) of these blocks. The blocks were carbon cured and were compared

to steam-cured blocks. Their results indicated a range between 292-454 kg CO₂-eq for the carbon cured samples, showing that there could be up to a 30% reduction in emissions. The environmental benefit of this curing technique was also estimated by Xuan et al. (2015). Their results estimated the CO₂ capture and storage to be circa 9-18% depending on the mass of cement which meant that annual CO₂ uptake could be up to 4.9x10⁶ kg/year. Mahoutian & Shao (2016) compared the performance of carbonated steel slag concrete vs a commercial concrete block. Their results showed that production for each cement block emitted 1.56kg of CO₂ in the atmosphere, however through carbonation, 0.23 kg of carbon dioxide was captured in the carbonated steel block.

Considering the CBPD used in this research is an unprocessed waste product, there would be zero emissions associated with the material. When factoring in that it is absorbing CO₂, it has the potential to have negative CO₂ emissions associated with the binder, where the only emissions that need to be considered would be transport and GBFS.

5.4 Conclusion

The effect of carbon curing on CBPD binders was investigated in this chapter. The results showed that CBPD has very high potential in carbon cured mortars and concretes. The main findings are summarised below:

1. Lime-Rich CBPDs have much higher CO₂ absorption potential than sulphate and calcite rich CBPDs. This is largely due to the increased formation of portlandite and unreacted lime in the system which forms calcite when reacting with CO₂.
2. Carbon curing increases both density and strength of CBPD binders with observed compressive strength increases of up to 39% in the lime rich CBPD. There is a direct correlation between the mass gained due to carbonation and the increase in strength of the binder.
3. XRD and TGA analysis showed large increases in calcite content for CBPD binders and reductions in portlandite. This evidences the successful reaction between carbon dioxide and portlandite to form calcite. CBPD L binders had the largest increases in calcite due to the increased free lime content. Slight decreases in syngenite were observed, however reactions of other alkaline phases and carbon dioxide were not observed.

4. Formation of calcite was observed using SEM analysis, both large and small crystals were formed showing large pore-filling capabilities. This is the main reason for the increase in density.

Overall, the results show that CBPD, which is currently deemed to be a waste, is a viable option for use in several applications due to its large potential of CO₂ absorption and overall strength increase when carbon curing. Further research needs to be carried out on carbon curing of CBPD binders, particularly on large scale carbonation and long-term durability of carbon cured CBPD blocks.

Chapter 6 – Mechanical and Durability Properties of Ternary Blends of Milled CBPD-GBFS-Metakaolin

(Draft ready to be submitted in Cement and Concrete Research)

Abstract

Given the world's pressing climate change concerns, it has become evident that alternative binders are needed due to the high CO₂ emissions caused during the manufacturing of cement. Currently, several by-products and waste materials are being researched as potential cement replacements. Cement bypass dust (CBPD) is a waste material that is characterised by its high alkalinity and free lime and sulphate content. It is a material that has been investigated as a potential activator of pozzolans such as granulated blast furnace slag (GBFS) and fly ash in the past. Research has shown, however, that its binders are significantly weaker than OPC binders or other alkali-activated materials. This study attempts to maximise the potential of CBPD by milling it to increase its fineness. Ternary blends composed of milled CBPD, GBFS and 10% or 20% metakaolin were developed and their short- and long-term mechanical performance was examined, including alkali-silica reaction (ASR) and corrosion potential of steel fibres reinforced CBPD binders. Results showed that milling CBPD for just 150 seconds led to a reduction in particle diameter from 46.5 microns to 13.2 microns. Milling caused a significant improvement in flowability due to less particle agglomerations. Furthermore, milled binders showed large increases in strength and more total shrinkage. Some evidence of mechanical activation was seen; however, it was deemed that physical changes in the particle led to most of the enhancement of properties. Inclusion of metakaolin proved to be even more beneficial, with the mix composed of 10% metakaolin, 45% GBFS and 45% milled CBPD achieving a strength of 32.7 MPa, a 9.7% increase relative to OPC. The property improvement was attributed to both chemical and physical changes due to metakaolin replacement. ASR tests showed that CBPD binders performed significantly better than OPC, with their expansions being almost half of the OPC expansion and metakaolin content increase having an inverse correlation with expansion. Steel fibres were also shown to be compatible with CBPD-metakaolin binders, and mechanical property improvements were observed where no significant deterioration was found after 8 months of corrosion simulation.

Keywords: Cement mortar, Bypass dust, Blast furnace slag, GBFS, Waste utilisation, Microstructure, Metakaolin

6.1 Introduction and Background

The construction industry has an urgent need to develop environmentally friendly solutions to address the significant amount of emissions associated with the manufacture of cement. Currently, 8% of global anthropogenic carbon dioxide (CO₂) emissions are due to the cement manufacturing process (J.G.J Olivier et al., 2017). The use of supplementary cementitious materials (SCMs) and waste materials has now become widespread due to their environmental and, at times, performance benefits. Cement Bypass Dust (CBPD) is a waste material, largely composed of sulphates, free lime, and chlorides, that is currently largely landfilled due to its composition (Adaska & Taubert, 2008). Circa, 2% of CBPD is produced per ton of clinker by mass (Hanein et al., 2020). In certain plants, this can reach up to 6% depending on the efficiency of the kiln bypass system (Stevulova et al., 2020). Considering it is a largely unexploited material, reuse of CBPD as a cement replacement can help reduce total CO₂ emissions and additionally lead to a circular economy where all waste in the cement manufacturing process can be reused.

The use of CBPD as a cement replacement will lead to large environmental benefits. Research has shown, however, that in terms of performance, high volume replacements of cement with CBPD leads to a worse performance relative to OPC binders in terms of fresh and mechanical properties (Siddique, 2009). In fact, typically only substitutions of cement by circa 5% show any benefits (Barnat-Hunek et al., 2018). This will undoubtedly lead to limitations in the use of high-volume CBPD binders for structural applications. Furthermore, the durability of concretes including CBPD and their compatibility with steel reinforcement has not been properly investigated. As will be explained in the literature review, CBPD typically has a high chloride content which has adverse effects on rebar due to corrosion inhibition. To begin using a waste material in cement products, further research is required to ensure that the material is safe to use and to understand its potential.

Hence, the purpose of this research is to maximise the potential of CBPD through the incorporation of metakaolin in ternary CBPD-Metakaolin-GBFS blends and through the mechanical activation of CBPD. A thorough review of literature has been performed to understand the state of research regarding durability aspects of CBPD binders, milling of CBPD and the benefits of the use of metakaolin in cementitious binders.

6.1.1 Effect of Milling on CBPD

To the best of the author's knowledge, studies on milled CBPD have not been reported in the literature and only limited research is available on the effect of milling on cement kiln dust (CKD). Wang et al. (2007) investigated the effects of mechanical activation on CKD-fly ash blends using a Bruno 50-90 ball mill. They found that within the first two hours of milling, particles were rapidly broken down, with no particles being retained in the 45-micron sieve after 6 hours. This reduction in particle size led to enhanced hydration rates due to increased surface area exposure. However, while the samples ground for 6 and 12 hours exhibited higher early-age compressive strength, their 28-day compressive strength was lower. This decrease is attributed to the rapid hydration generating excessive products that coated the unreacted binder grains.

In another study, Bondar and Coakley (2016) explored grinding ternary blends of fly ash, OPC, and CKD. They found that grinding these blends beyond one hour was not effective as particles tended to agglomerate. Additionally, when focusing on grinding only the activator components (OPC and CKD), there was minimal improvement in the overall blend's fineness.

Muhammed et al. (2021), investigated the use of CKD as a nano material by milling it for 4 hours, where its particle size reduced to below 20nm from an original size ranging from 200-100nm. The nano-CKD replaced cement by up to 20% and the properties of the binder were analysed. They found that strength increased at all CKD replacement intervals, and this was attributed to the denser microstructure of the material due to the increased fineness.

6.1.2 CBPD-Metakaolin Binders

CBPD and metakaolin binders have not been researched in concretes and mortar in literature, however there is some scarce research on CKD and metakaolin binders. Oriola et al. (2015), studied ternary blends of CKD-metakaolin-OPC with up to 50% cement replacement. Their results indicated that, while high replacements of cement had adverse effects on compressive strength and workability, lower replacements (10%) gave similar results to the control. Attah et al. (2022), tested the effect of CKD-metakaolin on soil strength and found that this blend aided in forming more compact soils with improved geotechnical properties.

Recently, there has been an increase in research on CKD-metakaolin geopolymers. Ahmed et al. (2023) carried out research on a geopolymer comprised of metakaolin and CKD activated by sodium silicate. The results showed a positive influence on the mechanical properties of the CKD on metakaolin based geopolymers, largely due to the free lime content leading to a faster

dissolution of metakaolin. Abbas et al. (2021), carried out research on metakaolin-CKD geopolymers activated by potassium hydroxide and potassium metasilicate. Their binders showed reduced setting times and increased strengths relative to their CKD-GBFS geopolymers. Zawrah et al. (2022), also created a metakaolin-CKD geopolymer activated with sodium hydroxide and sodium silicate. They had metakaolin at different ratios and found that a metakaolin content of above 30% had an adverse effect on the compressive strength of the binders. Contrarily, the CKD-metakaolin geopolymer binder developed by Kassem et al. (2021), found the highest strengths at metakaolin-CKD ratios of 80-20.

6.1.3 Corrosion due to CBPD

Due to the high chloride content of CBPD (Borek et al., 2022), its compatibility with steel reinforcement or fibres is still generally unknown. Very limited research exists on the effect of kiln and bypass dusts on corrosion of rebar, and none exists on the corrosion effect of them on steel fibre reinforcement. Limited work exists on CKD compatibility with fibre reinforcement (Ashteyat et al., 2019). Batis et al. (2002) studied the corrosion effect of OPC mortar replaced by different amounts of slag and CKD, with up to 15% by mass of CKD in the mortar. From the results, 15% replacement of CKD presented a high probability of corrosion, however CKD did not have a very adverse effect on corrosion at 5% replacement. Similar results were reported by El-Sayed et al. (1991), where they reported that a 5% substitution of cement with CKD did not have an adverse effect on reinforcement passivity. Maslehuddin et al. (2009) replaced cement with CKD by up to 15% and studied the electrical resistivity of these concretes, amongst other tests. Their results showed a decrease in concrete electrical resistivity at higher cement replacements, indicating a higher risk of corrosion.

Standards indicate that any chloride content above 1% will induce rust in steel reinforcement (BS 8110., 1997). Research has shown, however, that steel fibres have a higher corrosion resistance than that of rebars. Janotka & Krajci (2004) found that the necessary chloride content to corrode steel fibres was three times higher than that of steel bars. Dauberschmidt (2004) concluded that steel fibres do not corrode with a chloride content below 5.2%. This seems to indicate that certain types of CBPD can indeed be compatible with steel fibres. Figure 6-1 below presents the typical chloride content in CBPD and kiln dusts that has been found in literature. While there are certain outliers that have a chloride content above 5.2%, most of the reported results fall within the allowable chloride content threshold.

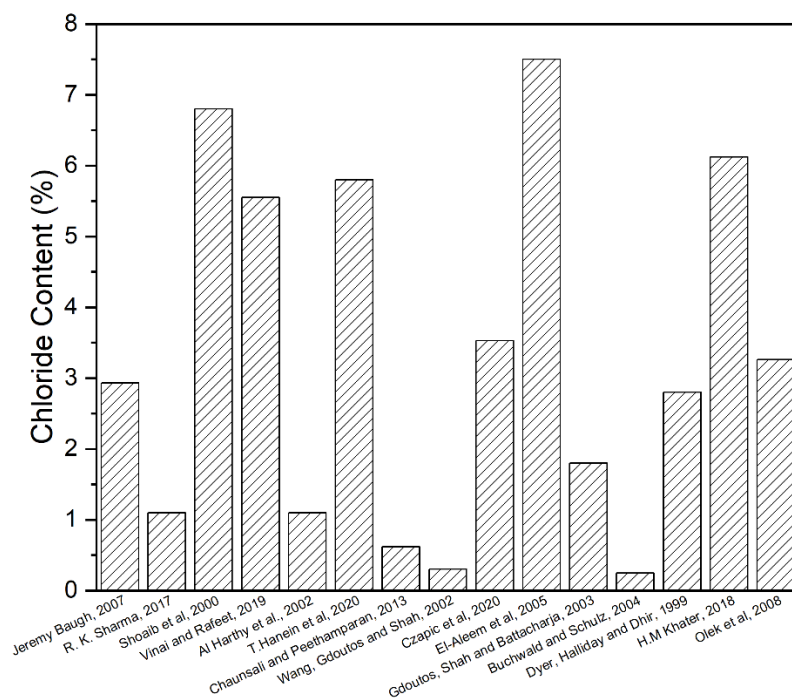


Figure 6-1 - Chloride content in CBPD from different sources of literature

6.1.4 Effect of Metakaolin on Corrosion Resistance

Metakaolin has been researched for its ability to reduce corrosion risk in cement-based materials. Various studies highlight its positive impact, mainly attributed to pore structure densification, which immobilizes chloride ions. Batis et al. (2005) observed a 10% metakaolin replacement of OPC to improve corrosion behaviour in mortar, however, for higher replacements, corrosion resistance decreased due to pH reduction and excess portlandite consumption. Despite this, the mixes with higher replacements still performed better than the control mix. Similarly, Guneyisi et al. (2013) found up to a 50% improvement in corrosion resistance when replacing up to 15% cement with metakaolin. Kelestemur and Demirel (2015) also reported improved corrosion resistance up to 15%, emphasizing pore size distribution reduction and enhanced microstructural diffusion properties.

Studies on geopolymer and alkali activated binders exhibit mixed results in terms of corrosion resistance due to varying precursor compositions, however, metakaolin-based geopolymers generally show enhanced resistance. Lyu et al. (2023) indicated a 15% reduction in corrosion rate in metakaolin-replaced geopolymers, and Azar et al. (2023) found no corrosion products in metakaolin-based alkali activated materials even after two years of exposure.

6.1.5 ASR in CBPD binders

In addition to corrosion, limited research has been carried out on alkali silica reaction (ASR) and CBPD and kiln dusts, however results seem to be positive. Ashteyat et al. (2019), investigated the effect of ASR on self-compacting concrete with cement replaced between 5-25% by white CBPD, a waste produced from white cement manufacture. The results were very positive and showed a reduction of up to 46% in expansion at higher replacements of cements. This was attributed to the pozzolanicity of the bypass dust which lead to a large amount of CSH forming, limiting the formation of expansive silica-gel. Al-Rezaiqi et al. (2018), studied ASR on concretes with CKD contents up to 40% replacing cement. Interestingly their results showed no ASR expansion, but contraction. All CKD binders, with exception of the 40% replacement, returned close to their original length by 90 days of immersion in Sodium Hydroxide. Chaunsali and Peethamparan (2013) investigated ASR on their heat and limewater cured kiln dust-slag binders. Their results showed that the control mix expanded beyond the threshold value of 0.2% at 14 days, whereas the CKD mix performed better. The improvement in expansion was mainly attributed to the presence of slag in the binder. Furthermore, the consumption of portlandite due to the pozzolanic reaction has also been shown to inhibit the ASR mechanism. While overall the literature has shown positive results with regards to CBPD/CKD and ASR expansion, there is still very limited research and this area needs to be further investigated, particularly when the composition of CBPD can be very variable.

6.1.6 ASR in Metakaolin Binders

The effect of metakaolin on ASR has been examined in several studies. Sinngu et al. (2023), tested durability properties of cement binders replaced by metakaolin by 5-15%. Their results indicated that at higher replacements metakaolin was very effective at lowering expansion. Slaweta (2017), tested metakaolin mortar replacing cement 5-20% by mass. The results showed a reduction of ASR expansion of 92% and 98% for 15% and 20% metakaolin-cement binary binders, respectively. The reason for this improvement was attributed to the compact microstructure of the metakaolin binders as this compactness binds the alkali and calcium hydroxide in the system, which leads to a reduction in the aggressive hydroxyl ions acting on the aggregate. Moser et al. (2010) investigated ASR on cement-metakaolin and cement-metakaolin-fly ash binders. The results indicated that metakaolin was much more effective than fly ash at reducing overall ASR. This was due to the smaller particle size and the higher contents of alumina and silica in the metakaolin which increased the reactivity and the

consumption of portlandite. Additionally, a lower permeability in the metakaolin mixes increased alkali binding which also helped mitigate ASR.

6.2 Research Significance

From the review of current literature, it appears that research on CBPD and metakaolin binders is very scarce, and very little information is available on the effects of milling on CBPD. This research aims to investigate the effects of milling and metakaolin inclusion in CBPD-GBFS binders with the objective of achieving a cementless mix that can perform similarly to a typical cement binder. Durability and mechanical properties will be observed, as well as a microstructural investigation exploring the hydration reaction of these binders.

6.3 Materials and Methodology

6.3.1 Material Properties

The mineralogical compositions of CBPD, metakaolin, GBFS, and OPC used in this study are shown in the XRD diffractogram in figure 6-2 below. Metakaolin is a largely amorphous material with a broad hump in the range of 15-35° (see figure 6-2). This hump is a result of the calcination process of kaolinite (Scrivener et al., 2018). The main crystalline peaks identified show that metakaolin is largely composed of quartz, kaolin, anatase, muscovite and illite (Marsh et al., 2018). Both illite and muscovite are similar in structure, however illite tends to have slightly more silica, and less alumina and potassium relative to muscovite. As is expected from a clay material, the main chemical components of metakaolin are silica and alumina.

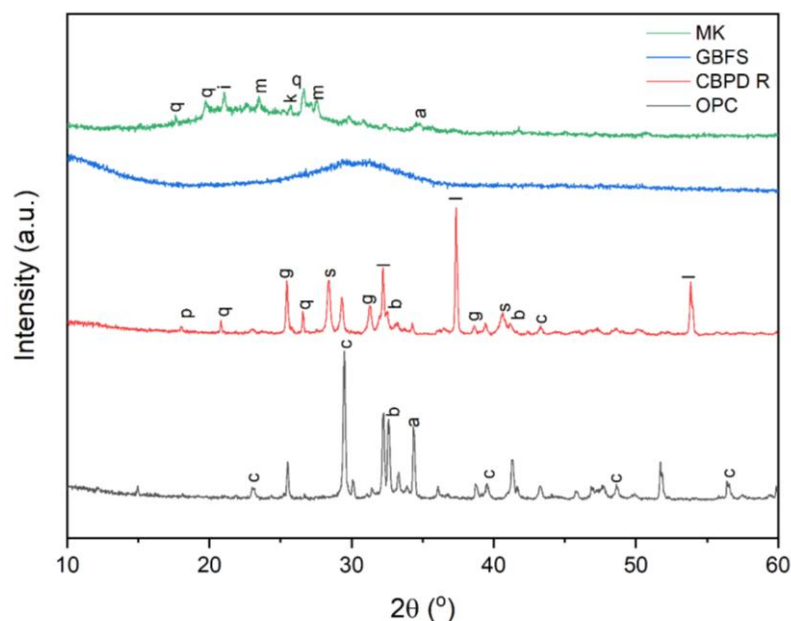


Figure 6-2 – XRD of CBPD, metakaolin, GBFS, and OPC (p = portlandite, q = quartz, g = gypsum, s = sylvite, l = lime, c = calcite, b = belite, a = alite, i = illite, m = muscovite, k – kaolinite)

The main crystalline phases present in the CBPD are free lime (CaO), gypsum, sylvite (KCl), quartz (SiO₂), and calcite (CaCO₃). The sylvite peak is indicative of the chloride content of the CBPD. The GBFS is high calcium and the diffractogram shows an amorphous wave that is mainly anhydrite. OPC is primarily calcite, belite and alite. The median particle size of the OPC, GBFS and metakaolin were determined to be 20 µm, 15.3 µm and 5µm. The particle size of the CBPD will be discussed in detail in section 6.4.1.

6.3.2 Mix Designs and Preparation

CBPD and GBFS were mixed in different proportions (10-90, 30-70, 50-50 etc.). The best performance was obtained from 50-50 CBPD-GBFS blends, albeit typically performing not nearly as well as pure OPC binders. To enhance the strength and durability properties of the binders, milling of CBPD and the use of metakaolin were considered in this study. The mixes examined are shown in table 6-1. In the mix ID, SB50 indicates a 50:50 ratio of GBFS and CBPD, the letter M indicates milling and XMK indicates the use of metakaolin at X% replacement. For example, SB50M 20MK contains milled CBPD at a 50:50 ratio with GBFS in a mix with 20% metakaolin replacement. Only replacements up to 20% were used as this was an ideal proportion for mitigating ASR based on literature and in other cases 10% replacement was shown to be optimal. Ultimately, a replacement in the range of 10-20% was deemed sufficient to exploit the benefits of metakaolin. The 50:50 ratio between GBFS and CBPD was chosen based on the results in chapter 4. Hence, all the mixes used in this research are cementless except for the control mix, which was 100% OPC.

Table 6-1 – Mix designs investigated

Mix ID	CBPD (%)	GBFS (%)	Metakaolin (%)	OPC (%)
SB50	50	50	0	0
SB50M	50	50	0	0
SB50 10MK	45	45	10	0
SB50M 10MK	45	45	10	0
SB50 20MK	40	40	20	0
SB50M 20MK	40	40	20	0
OPC	0	0	0	100

Locally available building sand was used as a fine aggregate for the mortars. The binder to sand ratio was kept at 1:3.

Milling was carried out using a standard TEMA mill, where the CBPD was ground for a range between 60-240 seconds. This is further discussed in section 6.4.1. The mixes were prepared in a 9-litre planetary mixer, with the powders being mixed first to ensure a homogenous dry mix. After adding water at a w/c ratio of 0.52, the material was mixed for 120 seconds. The mortar was then cast into steel moulds in two layers, and the surface finished using a flat trowel. The specimens were then covered with a polyethylene sheet for 24 hours before being demoulded. Once demoulded, the mortar specimens were kept in a water curing tank at room temperature (21 ± 2 °C) until the day of testing.

6.3.3 Experimental Methodology

6.3.3.1 Particle Size Analysis

Particle size was determined utilising a laser diffractometer. Milling took place using a TEMA mill. The analysis was based on trials where the CBPD was milled for intervals of 30 seconds and measured, until the particle size did not change significantly. The results for the CBPD particle size will be shown in section 6.4.1.

6.3.3.2 Fresh Properties

The workability of the binders was measured using a flow table based on ASTM C1437. Freshly mixed mortar was cast in two layers into a conical mould. The mould was then released, and the mortar was tamped 15 times allowing it to spread out. The diameter of the mortar was then measured to quantify the workability of the mix.

6.3.3.3 Mechanical Properties

The compressive strength was determined on 50mm cubes according to ASTM C109 using a 300kN universal testing machine.

6.3.3.4 Total Shrinkage

Total shrinkage was carried out following ASTM C596-23. Three mortar bars (40x40x160mm) were prepared for each mix. After demoulding, the samples were water cured for 48 hours. The prisms were then removed and once they were in a saturated surface dry condition, the first length measurement was taken. The shrinkage measurements were carried out using a length comparator as seen in figure 6-3 below. Length measurements were taken for up to 140 days.

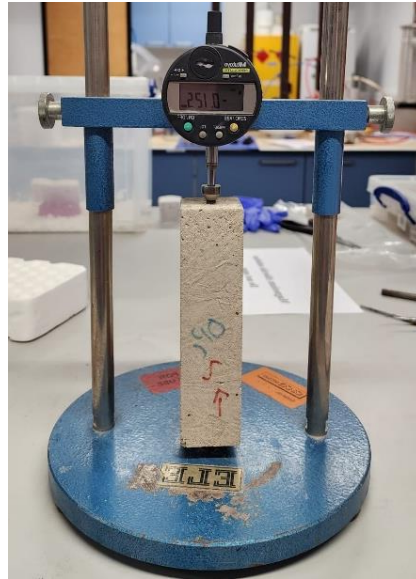


Figure 6-3 - Total shrinkage testing using a length comparator

6.3.3.5 XRD and TGA Analysis

X-ray diffraction was carried out in a Bruker D-2 diffractometer, using X-rays of 1.54 Å generated by a Cu K α target and an Ni filter. The samples were analysed from 5° to 60° at a rate of 0.02° steps per second. The software used for peak identification was Diffrac.EVA by Bruker, which has an ICDD library.

Thermogravimetric Analysis (TGA) was carried out using a Perkin Elmer Pyris 1 TGA. Samples were heated from 35°C to 1000°C degrees at a rate of 10°C per minute.

6.3.3.6 ASR Testing

The Alkali-Silica Reaction (ASR) test was carried out using the accelerated mortar bar test according to ASTM C 1260. For ASR, SB50, SB50 10MK and SB50 20MK will not be tested. Three mortar bars with dimensions 25x25x280mm were cast for each mix (Figure 6-4). Stainless steel studs were embedded on each end of the prisms to allow the expansion using a length comparator. The bars were demoulded after 24 hours, and the zero reading was measured on the length comparator. The bars were then stored in water at 80°C for another 24 hours, before exposure to sodium hydroxide.



Figure 6-4 - Bars cast for ASR testing

NaOH of 1 Normality was prepared for this experiment by mixing water and 40g of sodium hydroxide pellets in a fume cupboard. Graded sharp sand was utilised as the aggregate to comply with the standard at a cement to aggregate ratio of 1:2.25. The gradation used is shown in table 6-2, based on ASTM C1260.

Table 6-2 – Gradation of the aggregate used for durability tests

Passing	Retained On	Mass (%)
4.75 mm	2.36 mm	10
2.36 mm	1.18 mm	25
1.18 mm	600 μ m	25
600 μ m	300 μ m	25
300 μ m	150 μ m	15

The bars were placed in the hydroxide solution at 80°C to accelerate the ASR and expansion. Expansion was measured up to 28 days. The standard states that an expansion of above 0.2% at 14 days is classified as deleterious expansion, while anything below 0.1% is deemed as non-reactive. An intermediate result is classified as possibly prone to ASR damage but requires further investigation. In addition to the expansion, mass loss and XRD testing were also carried out.

6.3.3.7 Corrosion Testing

Corrosion testing was carried out for all the mixes shown in table 6-1. The aggregate grading and composition were the same as used for ASR tests, however 3% steel fibre by weight of binder were added to the mixes subjected to corrosion tests. The mortar was also cast in 40x40x160mm moulds. 9 prisms were cast for each mix design, where 6 would be tested for corrosion potential (3 specimens at 4 months and 3 specimens at 8 months) and 3 would be cured in water for 8 months and used as non-corroded control samples. Corrosion testing began

after 28 days of water curing. Corrosion testing entailed wet-dry cycles where the reinforced prisms would be submerged in 3% NaCl solution for 4 days and dried for 3 days. This process took place for 8 months.

The effect of corrosion was investigated through visual analysis and by measuring the flexural and compressive strengths of the corroded samples against non-corroded controls.

The flexural strength was determined through this equation:

$$\text{Flexural Strength} = 3Pl/2bh^2 \quad (6-1)$$

where P = applied load, l = span length, b = width of prism and h = depth of prism.

The broken pieces of the prisms were later tested for compressive strength, with the load being applied via two 40x40mm square metal plates placed on opposite sides of the specimens. Residual strength was also measured to assess the effect of corrosion on the steel fibres.

6.4 Results

6.4.1 Effects on Milling on CBPD

6.4.1.1 Particle Size

Milling was carried out at different intervals up to 240 seconds. It was found that no significant decreases in particle size were achieved after milling for 150 seconds. Previous literature has shown that the effect of prolonged milling can lead to large agglomerations of fine particles, and that increased grinding does not necessarily have a positive effect (Bondar and Coakley, 2017). It must be noted that in previous literature, milling was carried out for much longer periods of time. This can be attributed to the use of different milling equipment, and to the use of coarser CBPD/CKD.

Particle size distribution plots are shown in figure 6-5 for the unmilled, 60 seconds, 150 seconds and 240 seconds milled CBPD. From the figure it is evident that the 150 and 240 second milled CPBD are largely the same size. Past research has shown this stagnation in particle size reduction can be overcome with prolonged milling (Mucsi et al., 2013). This was not attempted to not further reduce the sustainability of the material.

The median particle size for no milling and milling at 60, 150 and 240 seconds were 46.5µm, 21.8µm, 13.3µm and 13.1µm, respectively. To achieve a balance between fineness and economy, the 150 second milled CBPD was selected for the remainder of the experiments.

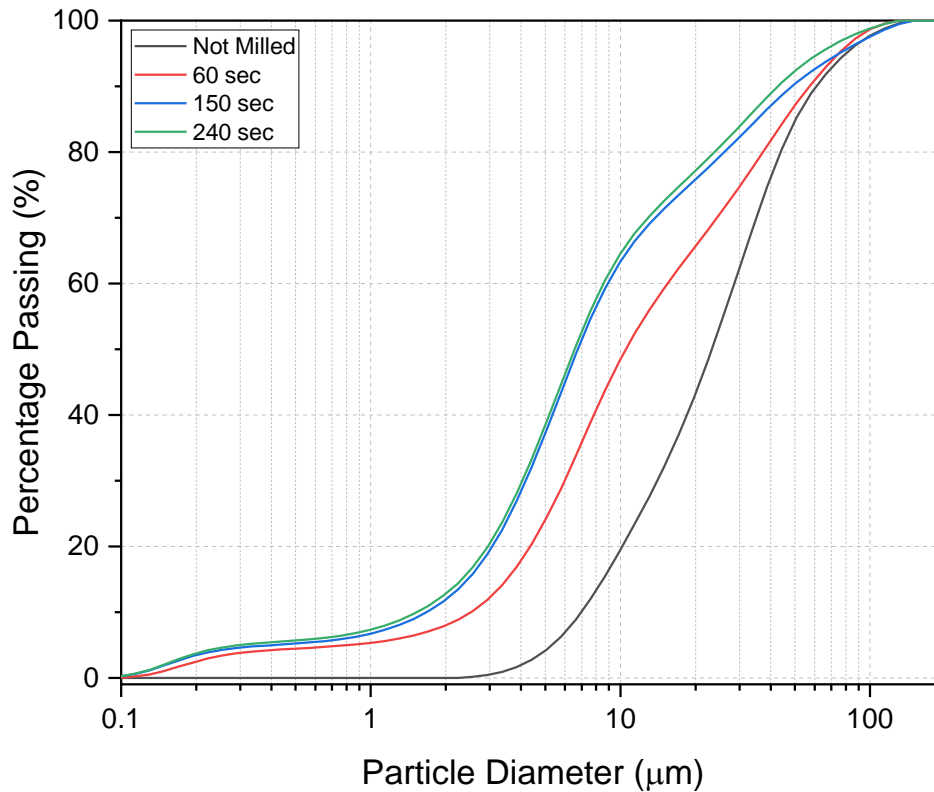


Figure 6-5 – Particle size distribution of CBPD at different milling times

6.4.1.2 Chemical Changes

Figure 6-6 shows the diffractogram of the milled (150 seconds) and unmilled CBPD. The peaks of gypsum, sylvite, calcite, and quartz have a reduced intensity after milling. This indicates that some mechanical activation has taken place, as the crystalline structure of these phases has become more disordered/amorphous after milling. Mejdoub et al. (2017) also found significant reductions in peak intensity of milled cement, until peak broadening and amorphization was fully achieved. Full peak broadening would indicate the disappearance of that phase from that diffractogram and is indicative of mechanical activation (Hamzaoui et al., 2016).

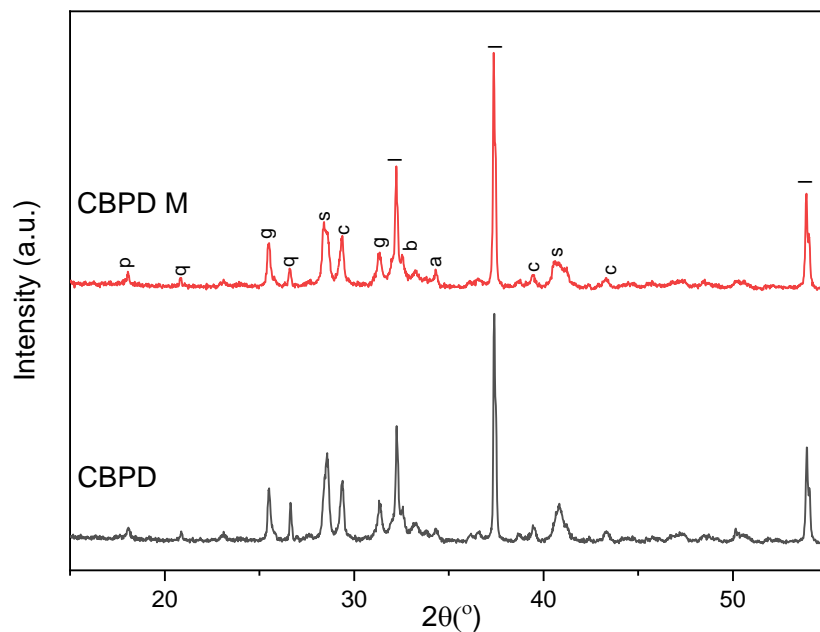


Figure 6-6 - X-Ray diffraction of milled CBPD and unmilled CBPD

Figure 6-7 (a) and (b) show the reduced intensity after milling of the calcite and gypsum peaks, respectively. While some amorphization did take place, the peak reduction is not very large and hence the chemical changes in CBPD are not expected to be significant, but the reduced particle sizes may still help enhance packing.

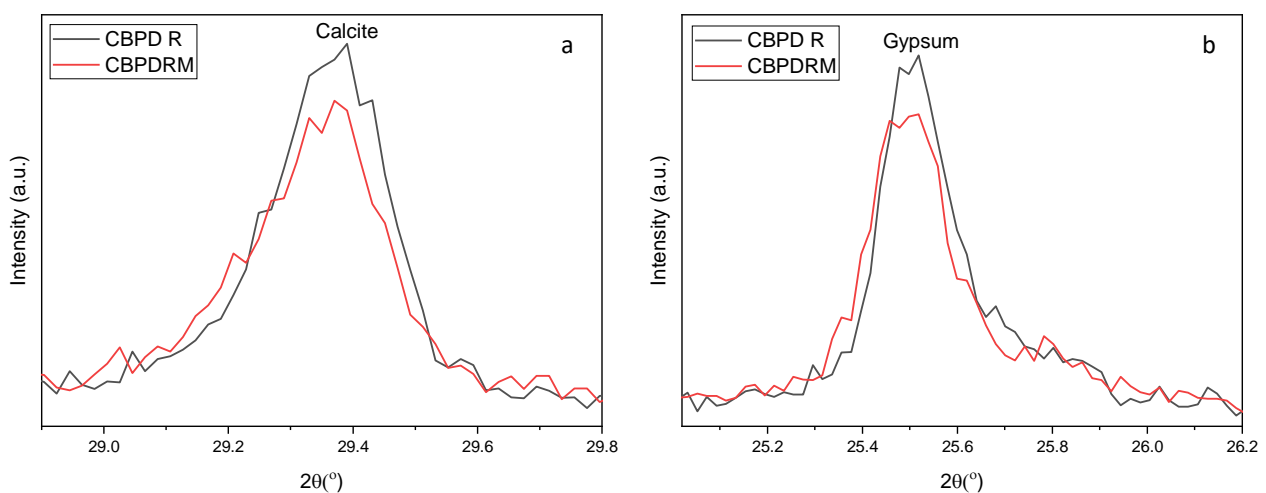


Figure 6-7 - Diffractograms showing peak reduction after milling (A) calcite (B) gypsum

Extended grinding would likely induce more mechanical activation; however, it would have an adverse effect on sustainability benefits of CBPD due to the required higher energy input.

6.4.2 Workability

6.4.2.1 Effect of Milling

In terms of workability, milling had a very beneficial effect on the overall flowability of CBPD binders as seen in table 6-3. When comparing the flow of mixes containing SB50 (un-milled) and SB50M (milled), there is an 18% improvement in overall flow. This is also evident in the standard consistency, which for mixes containing milled material is 16% lower than that of mixes with un-milled CBPD. While past research (Luo et al., 2013) indicates that an increased fineness leads to a higher water demand due to the increase in surface area, this is not always the case. As explained in Wang et al. (2002), the coarseness of CBPD increases the viscosity of the binder. This is due to coarse particles behaving independently to colloidal particles in concentrated suspension systems. As mentioned earlier, CBPD particles tend to group and agglomerate together, however milling aids in breaking them apart allowing for a more flowable mix. The agglomeration clearly has a more adverse effect on CBPD flowability than the fineness of the milled CBPD. If techniques can be developed to reduce CBPD agglomeration without milling, the unmilled mix would likely have a much better flow.

Table 6-3 - Flow diameter, standard consistency, and density of investigated mix designs

Mix Design	Flow Diameter (mm)	Standard Consistency	Density (kg/m ³)
SB50	132 ± 12	38% ± 1	2120 ± 25
SB50M	155 ± 5	32% ± 0	2195 ± 10
SB50 10MK	130 ± 3	38% ± 2	2210 ± 25
SB50M 10MK	151 ± 6	32% ± 1	2285 ± 15
SB50 20MK	125 ± 7	40% ± 3	2200 ± 10
SB50M 20MK	145 ± 10	34% ± 1	2290 ± 20
OPC	159 ± 11	28% ± 0	2270 ± 15

6.4.2.2 Effect of Metakaolin Inclusion

Metakaolin leads to a stiffer mix overall as seen by the 10% and 20% replacements in table 6-3. These results are evident in the standard consistency, which showed a moderate increase as metakaolin content increased. Past research (Chen et al., 2020) also confirms that the inclusion of metakaolin leads to a reduced workability. The chemical reactivity of metakaolin can be an important factor when considering this due to the increased water consumption (El-Diadamony et al., 2018). While milling was shown to be effective, this is largely dependent on the material, and its agglomeration rather than just the fineness. Hence, despite the opposite occurring with milled CBPD, the fineness of milled metakaolin also plays a big role due to its higher surface area leading to an increased water demand (Batis et al., 2005).

6.4.3 Heat of Hydration

6.4.3.1 Effect of Milling

Figure 6-8 presents the heat of hydration results of SB50 and SB50M. As expected in CBPD binders, there is a rapid increase in temperature followed by a gradual drop in temperature (Czopic et al., 2020). When comparing the results, it is apparent that milling enhances the exothermic reaction. Not only is the peak temperature higher for SB50M, but also the reaction occurs faster than for the unmilled counterpart. This is observed by the more rapid drop in temperature of the milled binder. The main reason for this temperature increase is likely the larger specific surface area of the CBPD, allowing for more contact points with water and further hydration. Fluctuations in the data are likely due to external factors rather than the behaviour of the material.

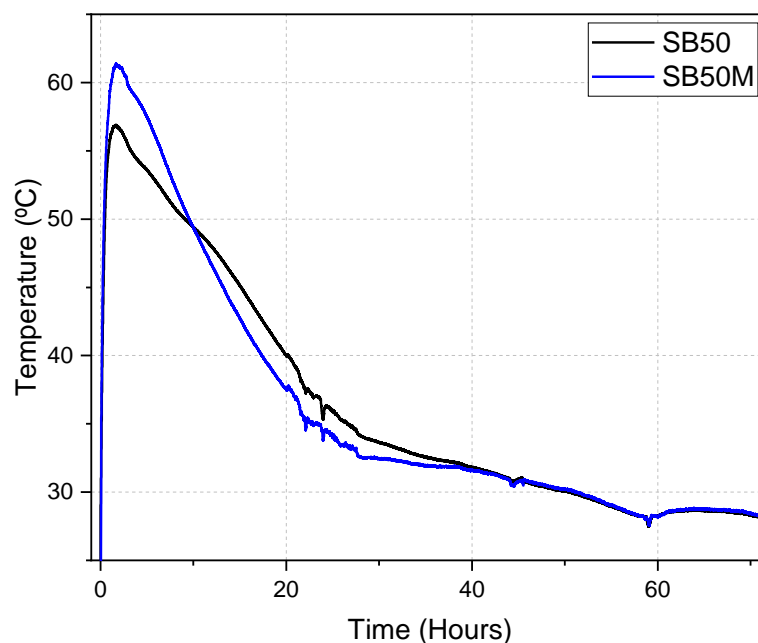


Figure 6-8 - Heat of hydration for SB50 vs SB50M

6.4.3.2 Effect of Metakaolin

The temperature rise vs time for SB50M, SB50M 10MK, SB50M 20MK, and OPC are shown in figure 6-9. The mixes with metakaolin both show similar behaviour with a rapid temperature increase, like that observed for the CBPD-GBFS binders. Nonetheless, this is followed by a brief stabilisation phase much like the induction phase for OPC as shown in figure 6-9. Following this phase there is a further temperature increase, with the SB50M 10MK and SB50M 20MK achieving peak temperatures of 64°C and 57°C, respectively. This increase in temperature likely signifies the dissolution of metakaolin in the CBPD binder. As the inclusion

of 10% metakaolin shows higher temperature, it is likely the amount of CBPD still dominates the level of overall exothermic reaction, however metakaolin plays an important contribution to the reaction. These results also signify that there is a chemical effect due to metakaolin inclusion and not just a physical filler effect.

Past research has shown an increase in heat of hydration when metakaolin has replaced OPC due to the pozzolanic reaction and the increased consumption of portlandite (Frias and Cabrera, 2000). Portlandite has been shown to be a common phase in CBPD binders due to its lime content.

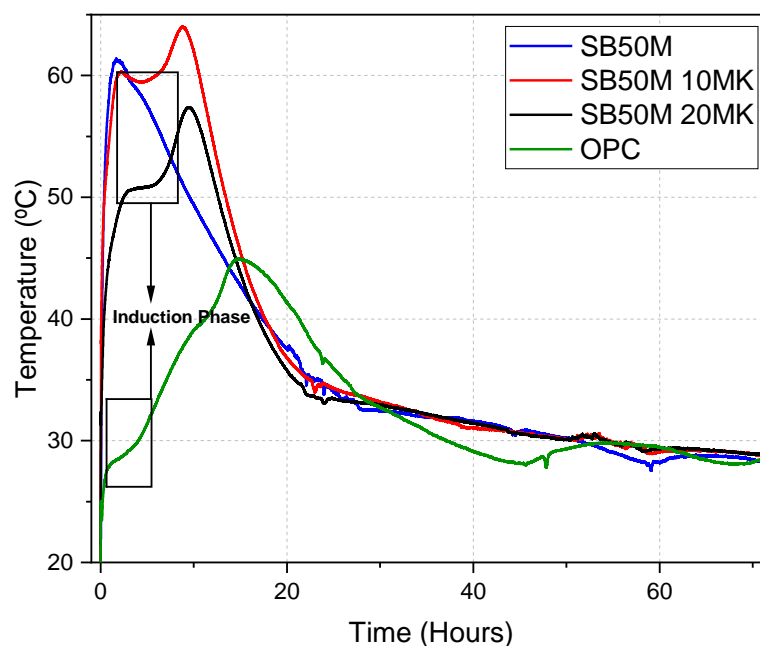


Figure 6-9 - Heat of hydration for metakaolin CBPD binders

6.4.4 Density

The effect of milling and metakaolin on density is largely similar in these binders as can be seen in table 6-3. Replacement by 10% and 20% metakaolin lead to density improvements, with SB50M 10MK and SB50M 20MK both exceeding the control, however just moderately. Overall milling lead to a 5% density improvement of SB50M over SB50.

Past research has also shown that CBPD binders have higher water absorption and lower density relative to OPC. The inclusion of metakaolin has a positive effect on density, and it is likely that the filler effect, due to the fineness of metakaolin, and the refined pore structure due to the pozzolanic reactions are the main factors that enhance density.

6.4.5 Compressive Strength

6.4.5.1 Effect of Milling

As seen from the results in table 6-4, there is a clear strength gain due to milling of CBPD that may be attributed to several factors. Firstly, an increase in CBPD fineness has led to a denser product as evidenced from the density results. Furthermore, large agglomerates in unmilled CBPD are detrimental not only to flow but also strength, as more particles could remain unhydrated due to lack of contact with water. Milling aids in breaking them apart and leads to a higher surface area and more contact points with water, leading to improved hydration.

6.4.5.2 Effect of Metakaolin

It is evident that the inclusion of metakaolin leads to a significant increase in overall compressive strength at all ages. Relative to SB50M, the strength gains are 50% for SB50M 10MK and 44% for SB50M 20MK at 28 days.

Table 6-4 – Compressive strength of investigated binders

Mix ID	7 Day Strength (MPa)	28 Day Strength (MPa)
SB50	10.3 ± 0.08	16.8 ± 0.26
SB50M	13.8 ± 0.16	21.5 ± 0.27
SB50 10MK	18.5 ± 0.15	22.3 ± 0.25
SB50M 10MK	26.4 ± 0.05	32.7 ± 0.36
SB50 20MK	16.9 ± 0.09	21.4 ± 0.10
SB50M 20MK	24.9 ± 0.16	26.5 ± 0.26
OPC	19.2 ± 0.22	26.4 ± 0.18

As seen by table 6-4, the best cementless binder is SB50M 10MK with a strength of 32.7 MPa, exceeding that of OPC at 29.8 MPa.

It is also evident that the inclusion of metakaolin is most beneficial at early ages, as there is a less significant increase in strength from 7 to 28 days in mixes containing metakaolin. This is seen in figure 6-10. This improvement of early age strength was also observed by others. For example, Justice and Kurtis (2007) found that metakaolin binders almost fully react within the first week after curing. Bai et al. (2004) carried out compressive strength tests on mixes containing cement and metakaolin at 1-5% replacements and found strength increases at all these replacement levels with the mix containing 5% metakaolin exceeding the control mixes strength by 92%.

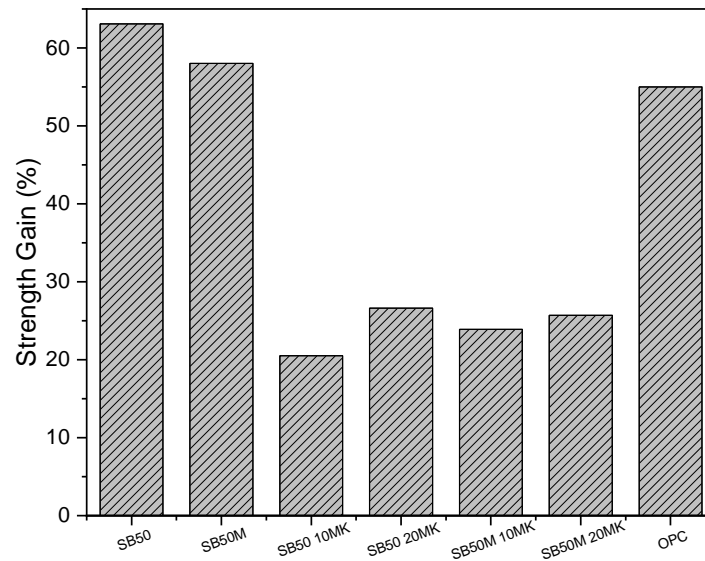


Figure 6-10 - Percentage strength increase of mix designs between 7 and 28 days

The filler effect is another factor to consider when dealing with strength and density. While the inclusion of metakaolin is known to reduce the quantity of hydration products such as portlandite (Sabir et al., 2001), as its particle size is much finer relative to the other materials, the filler effect also plays a large factor in the strength and density. The filler effect is beneficial, even for inert materials, as it leads to more efficient packing allowing an overall denser and more compact product.

The relationship between density and compressive strength is shown in figure 6-11. The trend does indicate overall that strength increases with density. However, beyond the 10% replacement, metakaolin substitution has led to a decrease in overall strength, possibly due to the dilution of the hydration products formed. That is the main reason why the use of high quantities of metakaolin replacing cement is uncommon.

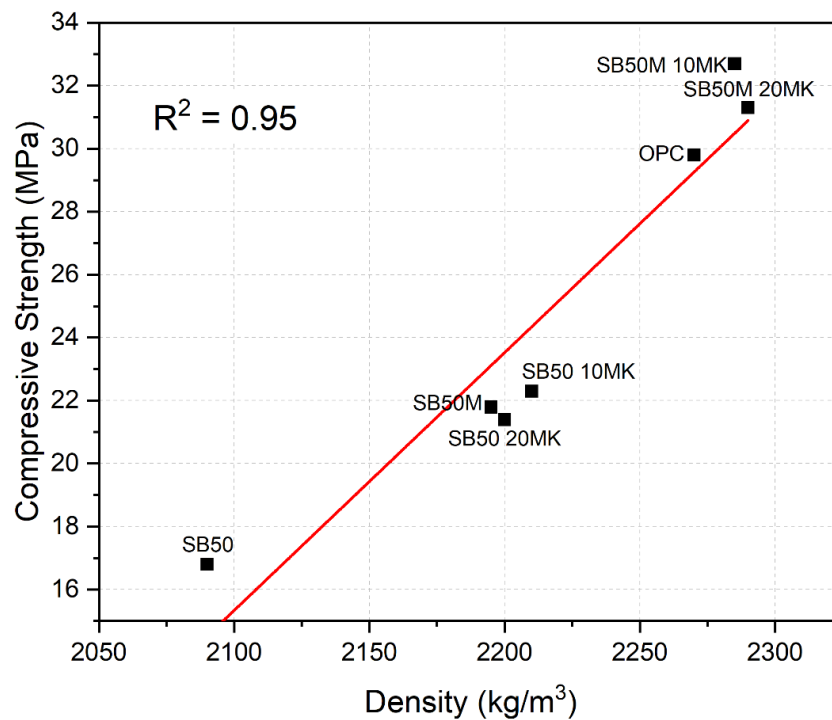


Figure 6-11 - Relationship between density and compressive strength

6.4.6 X-Ray Diffraction

6.4.6.1 Effect of Milling

The diffractogram comparing SB50M and SB50 shows little difference in the chemical composition of these mixes as seen in figure 6-12. The same phases are present in both mixes with almost identical intensities. The main differences are seen between 6° - 12.5° where a broader hump occurs in the milled mix, which is likely due to the increased amorphousness of the CBPD due to milling (Hamzaoui et al., 2016). There also seems to be more noise in the diffractogram of the milled mix, which also indicates amorphousness, however this is not quantifiable. Slight increases in ettringite and portlandite can also be seen, which indicates the formation of more of these hydration products. This is expected as milling increases the surface area leading to more contact points for hydration.

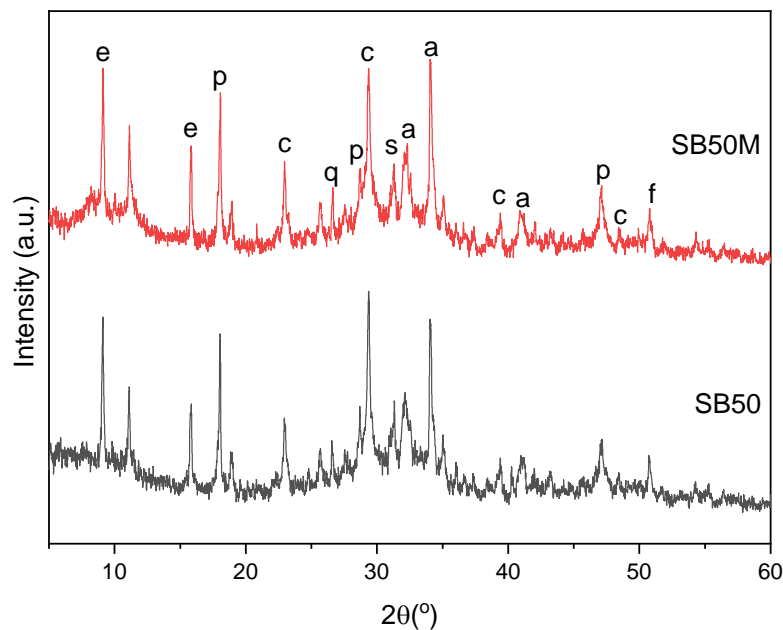


Figure 6-12 - Diffractogram for SB50 and SB50M (e = ettringite, p = portlandite, a = alite, q = quartz, s = syngenite, f = friedel's salt and c = calcite)

Ultimately, while significant differences are seen in the fresh and mechanical properties, these appear to be mostly due to physical changes rather than chemical changes.

6.4.6.2 Effect of Metakaolin

The mineralogical compositions of SB50M, SB50M 10MK, and SB50M 20MK after 7 days of curing are shown in figure 6-13 (a). The main crystalline phases for these binders consist of calcite, portlandite, alite, ettringite, and quartz, at different intensities. The changes in the peak intensity of crystalline phases such as quartz and portlandite are largely attributable to the compositions of the precursors used. Metakaolin, being largely composed of SiO_2 , seemingly has more silica peaks in the system. This can be seen by the main quartz peak, at 26.6° , which is more intense for the SB50M MK10 and SB50M MK20. A very clear result is the reduction of portlandite in the system as the metakaolin content increases (figure 6-13 (b)). The most

evident portlandite peaks are at 18.1° , 28.7° and 47° 2θ , and each peak visibly decreases as metakaolin content increases.

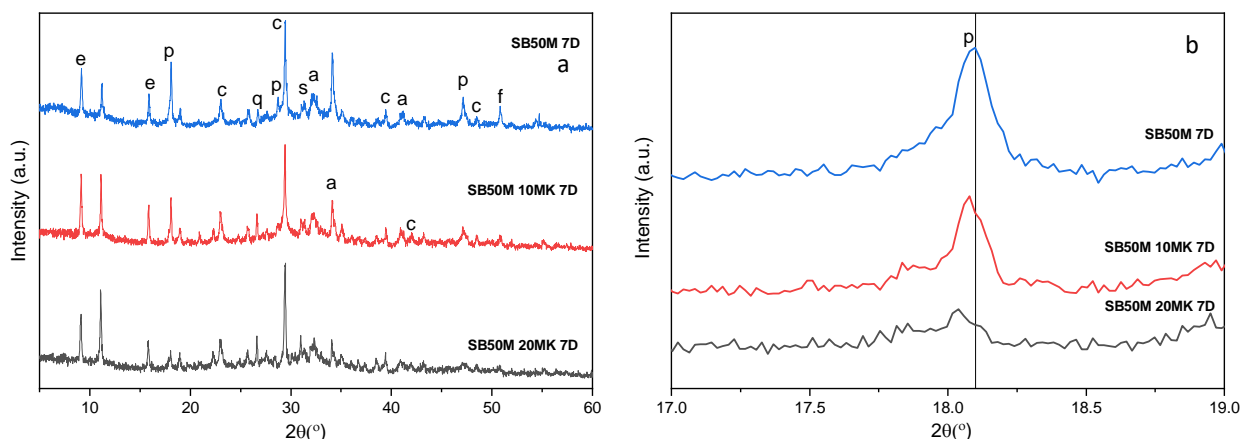


Figure 6-13 – XRD patterns SB50M, SB50M 10MK & SB50M 20MK at 7 days (a) 5-60° (b) 17-19° (e = ettringite, p = portlandite, a = alite, q = quartz, s = syngenite, f = friedel's salt and c = calcite)

Portlandite peak reduction can be attributed to the pozzolanicity and the reactivity of the metakaolin. Typically, the portlandite peak in a cement paste highlights the degree of hydration, however the portlandite consumption in an aluminosilicate-cement paste is due to the pozzolanic reaction (Poon et al., 2001). Portlandite reduces due to the pozzolanic reaction being faster than the hydration of OPC (Wild and Khatib, 1997). Due to the high content of alumina and silica in the metakaolin, as verified by the XRD in the materials characterisation section, the reaction between metakaolin and portlandite likely leads to CSH products and alumina phases, such as CASH (Wild et al., 1998). These gels contribute significantly to strength, hence this can explain the significant strength improvement of the binders containing metakaolin, however this gel cannot be located with the XRD as its peak is typically blocked by the calcite peak (29.4°). Ultimately, as portlandite decreases, it can be inferred that the CSH will subsequently increase. Additionally, the availability of alkali cations in the CBPD can accelerate the reaction due to alkali activation and improve the strength at early ages (Alonso and Palomo, 2001). Past research has shown the formation of other aluminate phases such as hydrogarnet (Morsy, 2005), however, these were not visible on the XRD diffractograms.

The 28 day XRD results are presented in figure 6-14. Similar results are observed, where the portlandite peaks have reduced even further. In fact SB50M MK20 showed no distinct portlandite peak, indicating that it had possibly fully reacted by 90 days. The calcite peaks appeared to remain at the same intensity due to the inertness of the phase (Matschei et al., 2007).

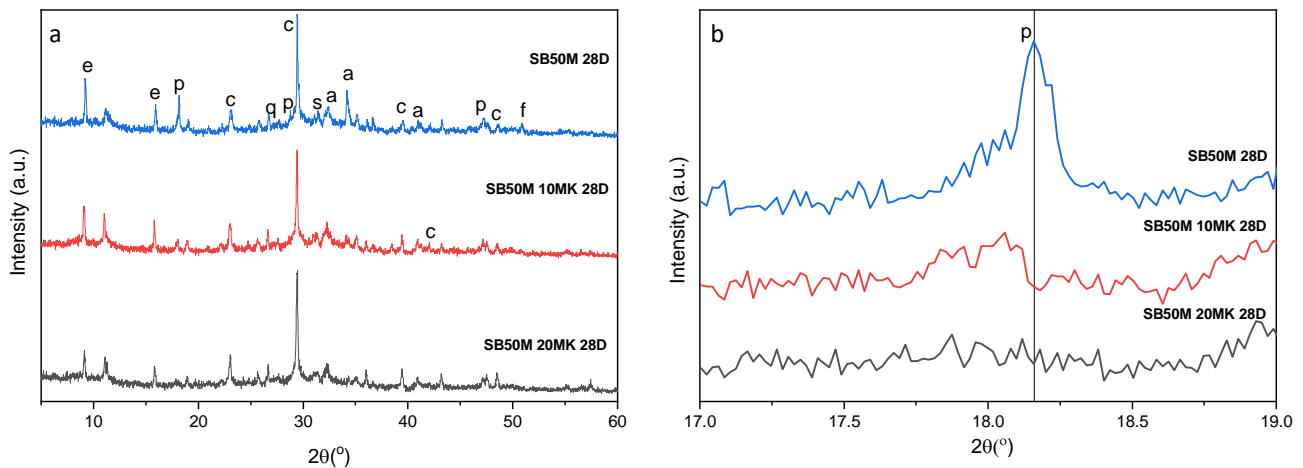


Figure 6-14 – XRD patterns SB50M, SB50M 10MK & SB50M 20MK at 28 days (a) 5-60° (b) 17-19° (e = ettringite, p = portlandite, a = alite, q = quartz, s = syngenite, f = friedel's salt and c = calcite)

Ettringite, a large factor in strength gain in CBPD binders, is not seen to be reduced by metakaolin inclusion. In fact, SB50M MK10 showed an increased ettringite content, which could be due to the increased content of Al_2O_3 (alumina) in the pore solution from the metakaolin (Bohac et al., 2014). However, there is a decrease in SB50M MK20, which may be due to the consequential reduction in sulphates in the system due to the reduced CBPD quantity. This also can explain the strength reduction relative to SB50M MK10.

Active pozzolans, such as metakaolin, are known to react rapidly with portlandite and remove it from the system, leading to an acceleration of OPC hydration (Wild et al., 1998). As is seen in the following section, CBPD R binders produce less portlandite content than OPC binders, hence it can be inferred that beyond 10% replacement in CBPD mixes, metakaolin is no longer contributing to forming hydration products and the ‘filler effect’ is not enough to compensate for the strength loss due to the dilution of the hydration products. Clearly there is an optimal replacement level of cement with metakaolin and with this CBPD it likely falls between 10-20% replacement level.

6.4.7 CBPD-Metakaolin Thermogravimetric Analysis

The hydration of CBPD-metakaolin blends was also investigated using thermogravimetric analysis as seen in figure 6-15. The mass loss due to CSH or CASH can be typically seen

between 109°C and 220°C (Antoni et al., 2012). The CSH phase forms after the consumption of portlandite (Madadi and Wei, 2022), however, as also reported in literature, due to the increased alumina content from the metakaolin, it is likely that CASH is also formed.

The mixes containing metakaolin show a significant reduction in the amount of portlandite relative to the SB50M. As was also shown from the XRD results, the higher the substitution rate, the stronger the relative decrease of portlandite content. In fact, by 28 days, SB50M 20MK had almost full consumption of portlandite, where it only had a mass loss of 0.67%. This is seen between the temperatures of 400 and 600°C. While this is beneficial at early ages, later age strength might be affected by metakaolin inclusion. Portlandite is largely responsible for long term age development of cement binders, however the benefits from portlandite are likely supplemented by other products forming such as CSH and CASH gels. The reduction in portlandite is more clearly demonstrated when examining the DTG results in figure 6-16 (b).

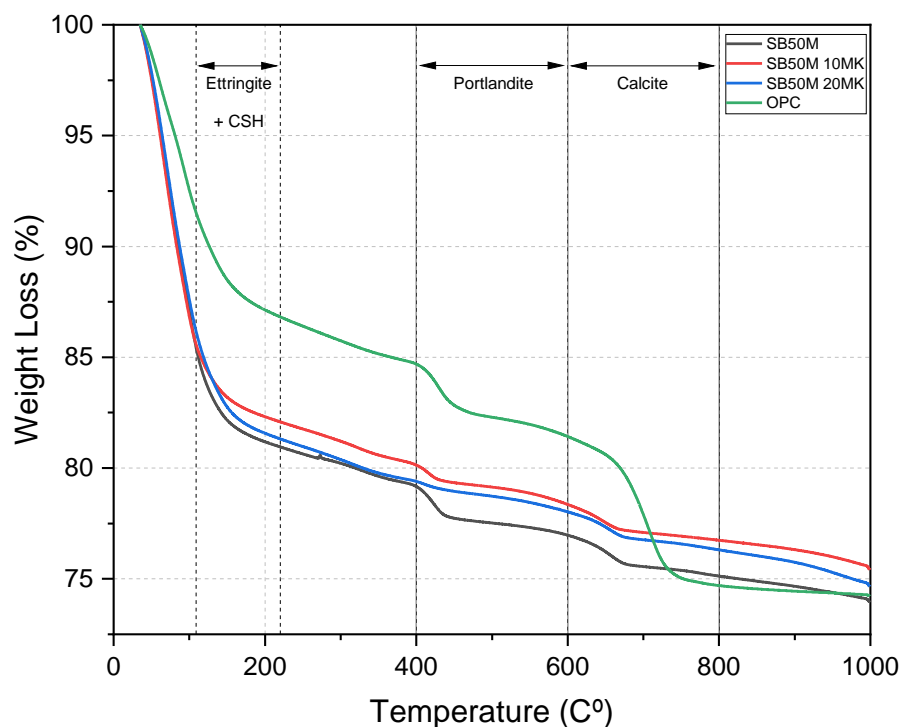


Figure 6-15 - TGA of the investigated mix designs

An increased amount of CASH likely forms due to the pozzolanic reaction. This typically results in a more dense and durable binder. SB50M had the highest mass loss between 109°C and 220°C followed by SB50M 20MK, SB50M 10MK and the control. SB50M likely had a higher mass loss in this temperature range than the metakaolin binders as this temperature range would also include ettringite decomposition, a phase CBPD R binders are abundant in. More

portlandite consumption likely means more CASH, explaining why the mass loss increases for SB50M 20MK.

A noticeable difference between the control and the CBPD binders is the mass loss between 35-100°C which represents the loss of combined water. This is clearly observed in figure 6-16. This mass loss increases with CBPD and metakaolin inclusion. This could be attributed to the increased standard consistency and the increased surface area of metakaolin and milled CBPD.

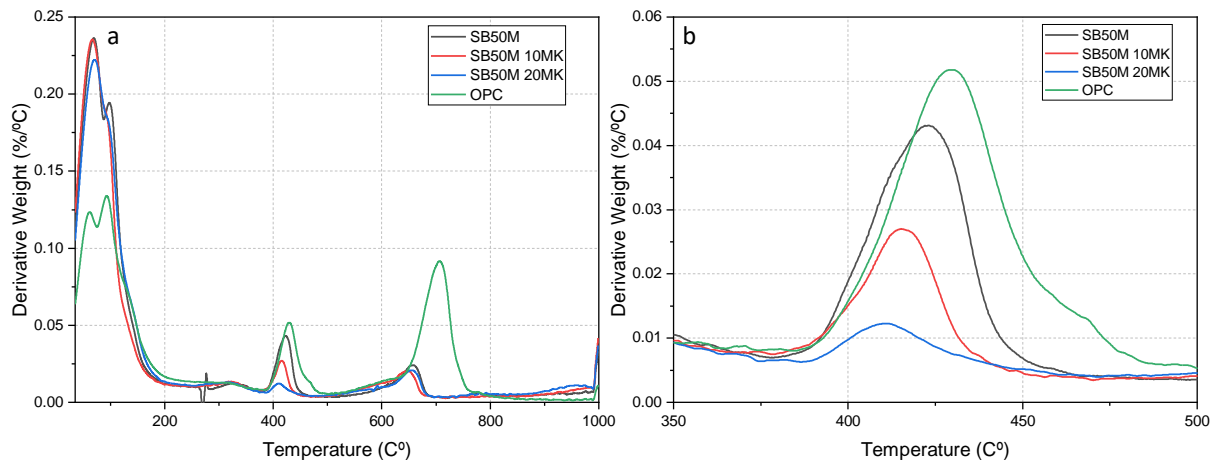


Figure 6-16 - DTG results for investigated mix designs (a) 35-1000°C (b) 350-500°C

6.4.8 Total Shrinkage

6.4.8.1 Effect of Milling

Figure 6-17 shows the total shrinkage strain development vs time measured on unsealed milled and non-milled mortar bars. The overall shrinkage development trend for both mixes is very similar, nonetheless, milling leads to a slight increase in drying shrinkage for milled CBPD mixes. At 140 days this results in a 3% increase in final shrinkage for SB50M.

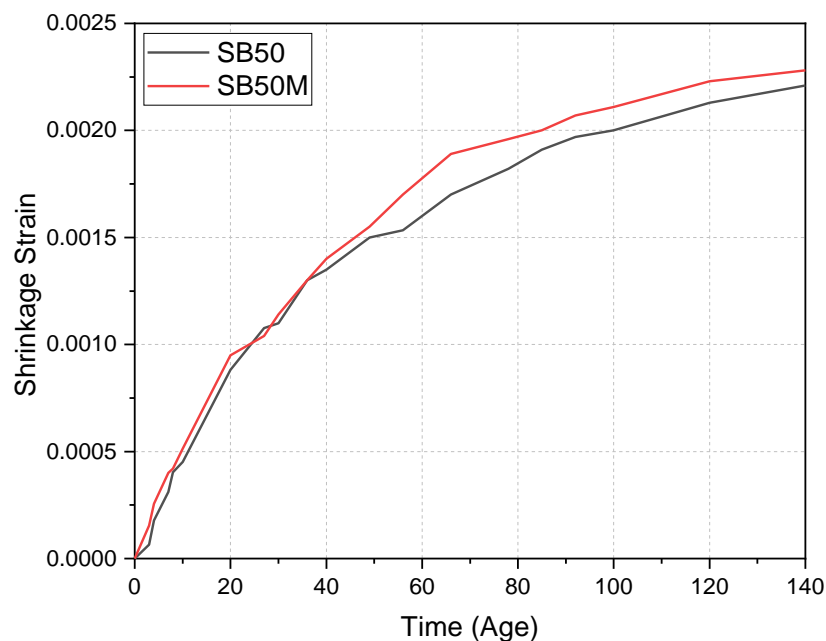


Figure 6-17 – Drying shrinkage of SB50 and SB50M binders

The increase in shrinkage can be explained by the faster hydration of milled powder that can lead to a reduced volume stability (Maruyama et al., 2022; Hammat et al., 2021).

6.4.8.2 Effect of Metakaolin

As seen in figure 6-18, metakaolin reduces the total shrinkage with increasing replacement levels with SB50 20MK showing the most improvement overall. The shrinkage reduction may be also due to the reduction of CBPD in the mix.

While metakaolin itself is finer than the milled CBPD, there are several reasons to explain the reduction in shrinkage. Due to the pozzolanic reaction induced by metakaolin in the system, a significant amount of the free water in the CBPD blends is used up. CBPD-metakaolin binders also have a lower water absorption rate, which implies that they are overall less porous than both the OPC and CBPD binders investigated. Additionally, water loss due to self-desiccation instead of diffusion to the outside environment has been previously observed in metakaolin-OPC binders (Guneyisi et al., 2007). Water loss due to diffusion is also reduced due to the pore-filling of the metakaolin.

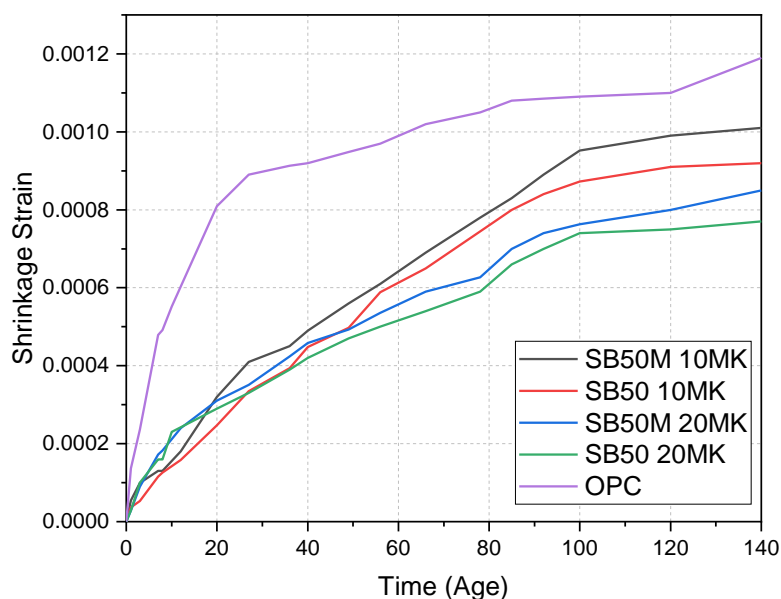


Figure 6-18 – Drying shrinkage of CBPD-GBFS-metakaolin binders and OPC

Brooks and Johari (2001) reached the same conclusions when investigating their metakaolin binders with up to 15% cement replacement. They found that total shrinkage reduced with increasing cement replacement, reaching an overall reduction of up to 50%. Again, this was attributed to the loss of water through self-desiccation.

Overall, the use of metakaolin with CBPD is shown to be very effective in reducing overall shrinkage as shrinkage of SB50M 10MK and SB50M 20MK was 15% and 29% lower than that of the OPC control mix, respectively.

6.4.9 Alkali-Silica Reaction

6.4.9.1 Expansion Results

Expansion measurements were taken up to 28 days and the evolution of ASR expansion is shown in figure 6-19. According to the specifications of ASTM C1260, it can be seen that none of the binders exhibited deleterious expansion ($>0.2\%$) after 28 days of curing, however OPC was closest to moderate expansion ($>0.1\%$). ASR expansion decreased for SB50M which showed a reduction of 41% by 28 days relative to OPC. ASR expansion was further reduced with increasing metakaolin content with reductions of 50% and 73% at 10% and 20% replacement, respectively. This indicates that both the use of GBFS and metakaolin have a positive effect on the mitigation of ASR.

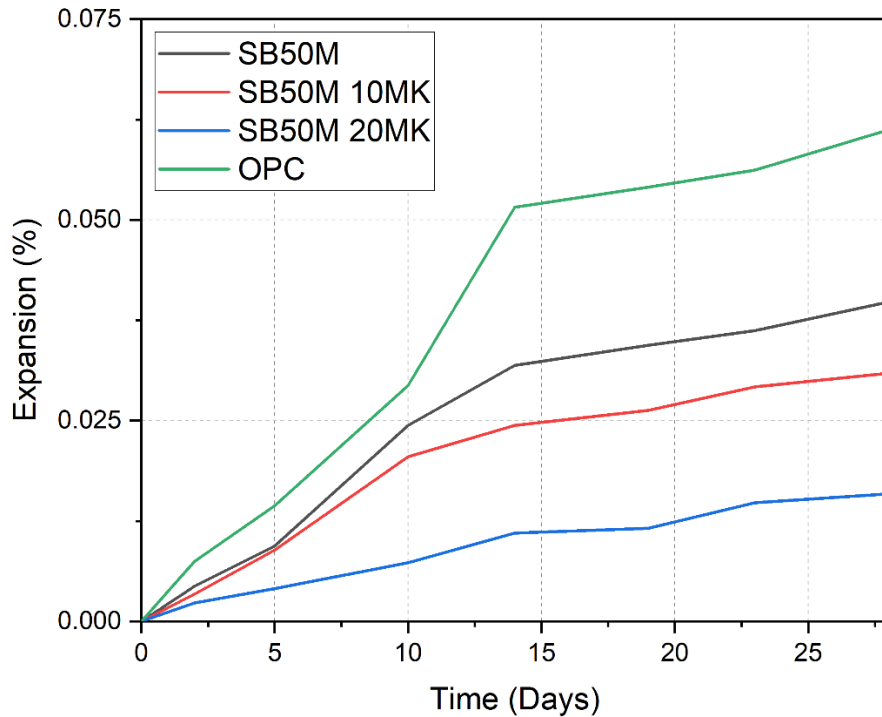


Figure 6-19 - ASR expansion of OPC, SB50M, SB50M 10MK, and SB50M 20MK

These results were to be expected, as it is known that suppression of ASR is related to the alkali dilution effect and the immobilisation of alkali cations in the pore solution, due to increased metakaolin content (Bakera et al., 2019). The presence of GBFS has also been shown to reduce pore solution alkalinity, due to increased alkali binding, which in turn can suppress ASR (Chaunsali & Peethampan, 2013). Other reasons for reduced ASR include metakaolin's greater fineness and its alumino-silicate composition that enhance reactivity. Increased fineness also enables immobilisation of alkali cations in the pore solution. Furthermore, the increased consumption of portlandite by metakaolin decreases the availability of Ca^{2+} ions in the pore solution and likely leads to a reduction in permeability (Moser et al., 2010).

6.4.9.2 XRD Analysis

XRD analysis was carried out on paste samples after 28 days to measure the formed products due to ASR. Figure 6-20 shows the diffractograms of SB50M 10MK (c) and SB50M 20MK (d). It is apparent that the main difference is the significant decrease in ettringite and gypsum peaks after exposure to NaOH. This has also been observed previously, as the formation of ettringite requires an appropriate alkalinity level and the inclusion of sodium hydroxide can retard its formation (Way and Shayan, 1993). Furthermore, Brown and Bothe (1993) found a large reduction of ettringite peaks when observing its stability in potassium hydroxide solution at elevated temperatures. They found that the hydroxides accelerate the hydration of alite and retard ettringite, hence CSH formation is more extensive. This large reduction is also observed in figure 6-20 for SB50M and the control OPC mix.

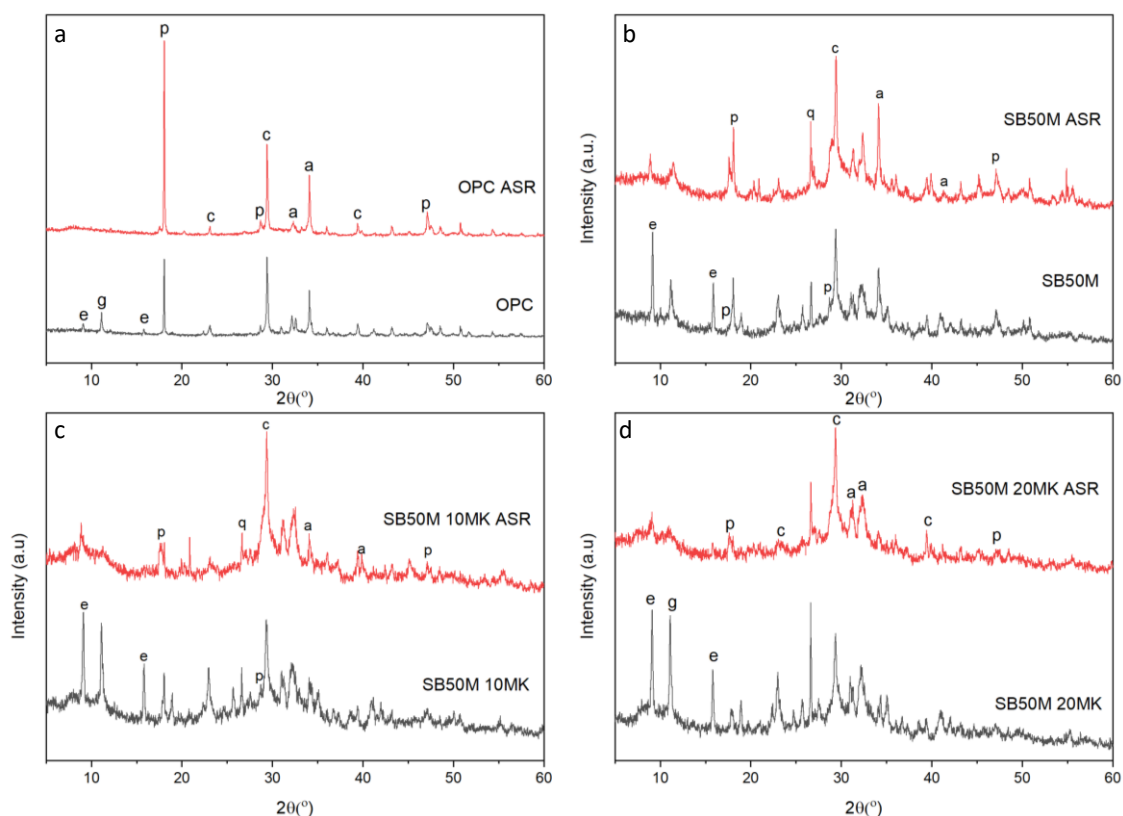


Figure 6-20 - XRD of pastes submerged in NaOH and water (a) OPC (b) SB50M (c) SB50M 10MK (d) SB50M 20MK

The very apparent effect of NaOH exposure can be observed for the control with the major portlandite peak at 18.09° where a drastic increase is seen. While portlandite increase is beneficial for strength increase, oftentimes the formation of this product also induces expansion (Xu et al., 2007). It can be inferred from this that the higher expansion of OPC relative to the

other mixes may be due to this. Wei et al. (2019), also observed this increase and attributed it to the calcium in the OPC reacting rapidly with the hydroxide ions in the alkali solution. Furthermore, they found that when replacing cement with 10% metakaolin there were large decreases in the portlandite produced. This is also observed in the XRD of the cementless mixes. Clearly the inclusion of GBFS and metakaolin have a positive effect on the reduction of ASR expansion.

Other peak differences are observable, however no distinct trend is observed and changes are most likely due to the specific samples tested rather than chemical changes.

6.4.10 Corrosion Resistance

6.4.10.1 Visual Analysis

6.4.10.1.1 Prior to Corrosion Acceleration

Prior to corrosion acceleration there were some visible signs of rust on the mixes as seen in figure 6-21. This was mainly due to some fibres being exposed on the surface of the prisms. Overall, though, there is no indication that the chlorides from the CBPD had any effect on the fibres.



Figure 6-21 - Minor corrosion due to water curing

6.4.10.1.2 Four Months of Corrosion

After 4 months of corrosion simulation, a large amount of external rust can be observed on the specimens (see figure 6-22) that completely changes the colour of the specimens. It must be noted, in most cases the bottom of the prisms was more affected by this. This is likely due to the fibres moving to the bottom surface of the prism during vibration. Besides the colour change, it is not evident immediately how detrimental the effect of rust is on the concrete performance.



Figure 6-22 – View of the external corrosion of the prisms

When observing the prisms internally, it became clear that most of the rust was on the outer surface of the prisms, which indicates that there was not a large amount of chloride penetration. This is seen in figure 6-23 where (a) presents the rust near the surface and (b) shows a typical sample cross-section and provides evidence that there is no apparent corrosion in the central part of the specimen.

From visual analysis, the OPC samples showed lower signs of corrosion relatively to the mixes containing CBPD. This is to be expected due to the lower chloride content in cement. Overall, however, both mixes do not seem to have excessive corrosion damage.



Figure 6-23 - Corrosion of prisms (a) near surface corrosion of fibres (b) cross-sectional view

6.4.10.1.3 Eight Months of Corrosion

Figures 6-24 and 6-25 show samples after 8 months of accelerated corrosion. The surface corrosion has increased and the colour of the rust is darker. However, as before, the extent of internal damage is not easy to discern.



Figure 6-24 - SB50M following 8 months of corrosion



Figure 6-25 - Fibres exposed likely due to chloride acceleration

Internally there are signs of rust on the fibres closer to the centre of the prisms for SB50 and SB50M, indicating that there was some penetration of chlorides. This can be seen in figure 6-26, which shows rust patterns around the centre of the prism. Other samples show that only fibres close to the surface had corrosion. However, there is no clear distinction between the effects of metakaolin and milling on the total corrosion based on visual analysis.



Figure 6-25 - SB50M showing signs of rust in the centre of the prism

6.4.10.2 Compressive Strength Results

The results for compressive strength after 4 and 8 months of corrosion testing are shown in figure 6-27. The control labelled ‘No Corrosion’ on the legend of the graphs, were water cured for 8 months, and did not undergo any accelerated corrosion. Curing in salt water seems to have had a positive effect on the strength overall, as in every case they exceed the control mix. Previous studies have shown that salt water can have positive effects on curing of cement. Wang et al. (2020), investigated the effect of curing cement paste in salt water, and found compressive strength increases up to 60%. Increases in compressive strength due to corrosion of steel fibres have also been observed before, where the corrosion has been shown to cause improved bonding with the cement matrix (Anandan et al., 2014).

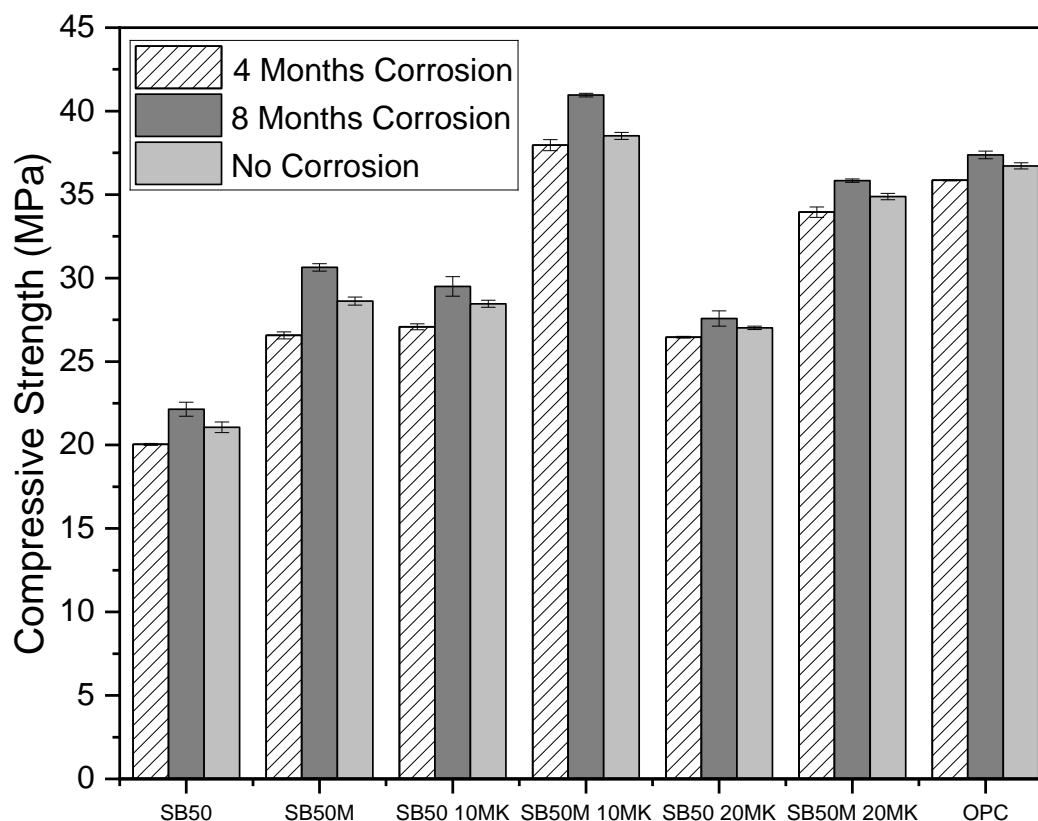


Figure 6-26 - Compressive strength of mixes following corrosion simulation at 4 and 8 months

After 8 months of corrosion, the relative strength is not much higher, which indicates that most of the hydration was completed by around 4 months. As observed previously, SB50M 10MK and SB50M 20MK were the strongest mixes followed by the OPC control.

6.4.10.3 Flexural Strength Results

The flexural behaviour of samples exposed to salt solution at 4 months and 8 months, and the control samples are presented in figure 6-28. The results show that specimens exposed to salt solution were stronger than the control samples after 8 months, once again showing the positive effect of salt water curing on strength. Similar results have been observed in previous studies, where the effect of accelerated corrosion up to circa 8 months had a negligible effect on the loss of mechanical properties (Marcos-Meson et al., 2018).

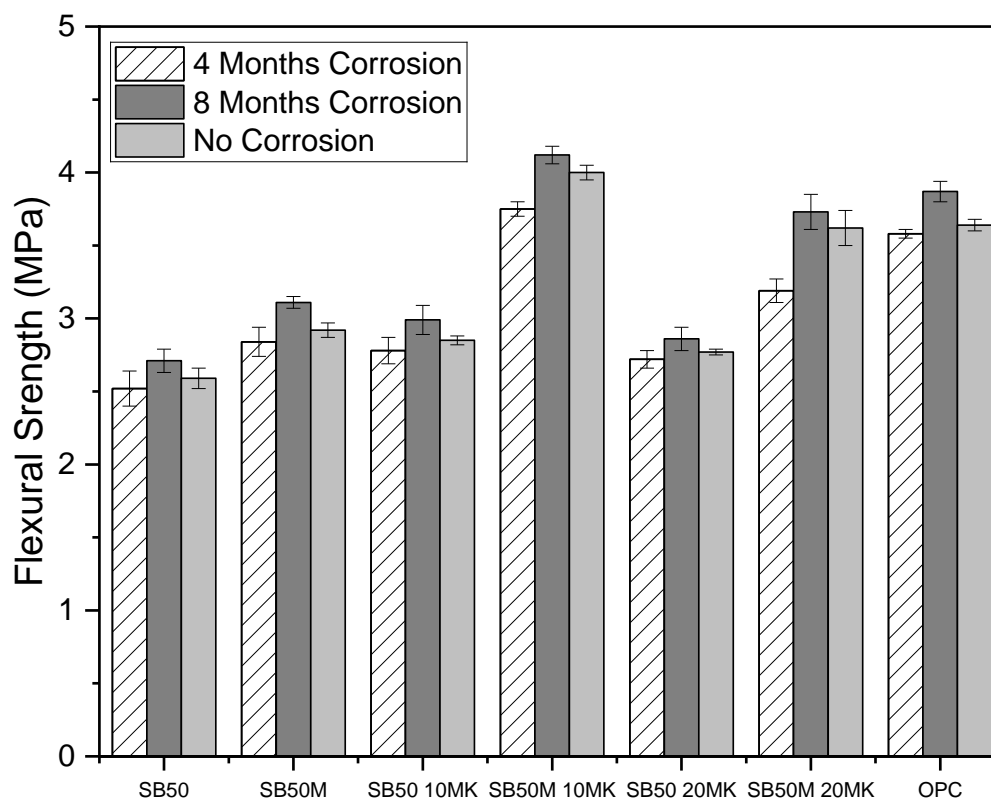


Figure 6-27 - Flexural strength of mixes following corrosion simulation at 4 and 8 months

6.4.10.4 Residual Flexural Strength Results

Figure 6-29 presents the residual flexural strength up to a central displacement of 0.6 mm. The effect of corrosion is a bit clearer in these graphs, however there are only small changes between corroded and control samples. All the mixes shown below seem to also be characterised by similar residual strengths, with no significant difference. Overall it is seen that the non-corroded samples have slightly higher residual strengths. There also is a small increase in residual strength at 8 months corrosion relatively to 4 months of corrosion.

From these results it can be concluded that fibre corrosion is not only superficial and it does affect the mechanical characteristics of these binders, however not in any significant manner at 8 months.

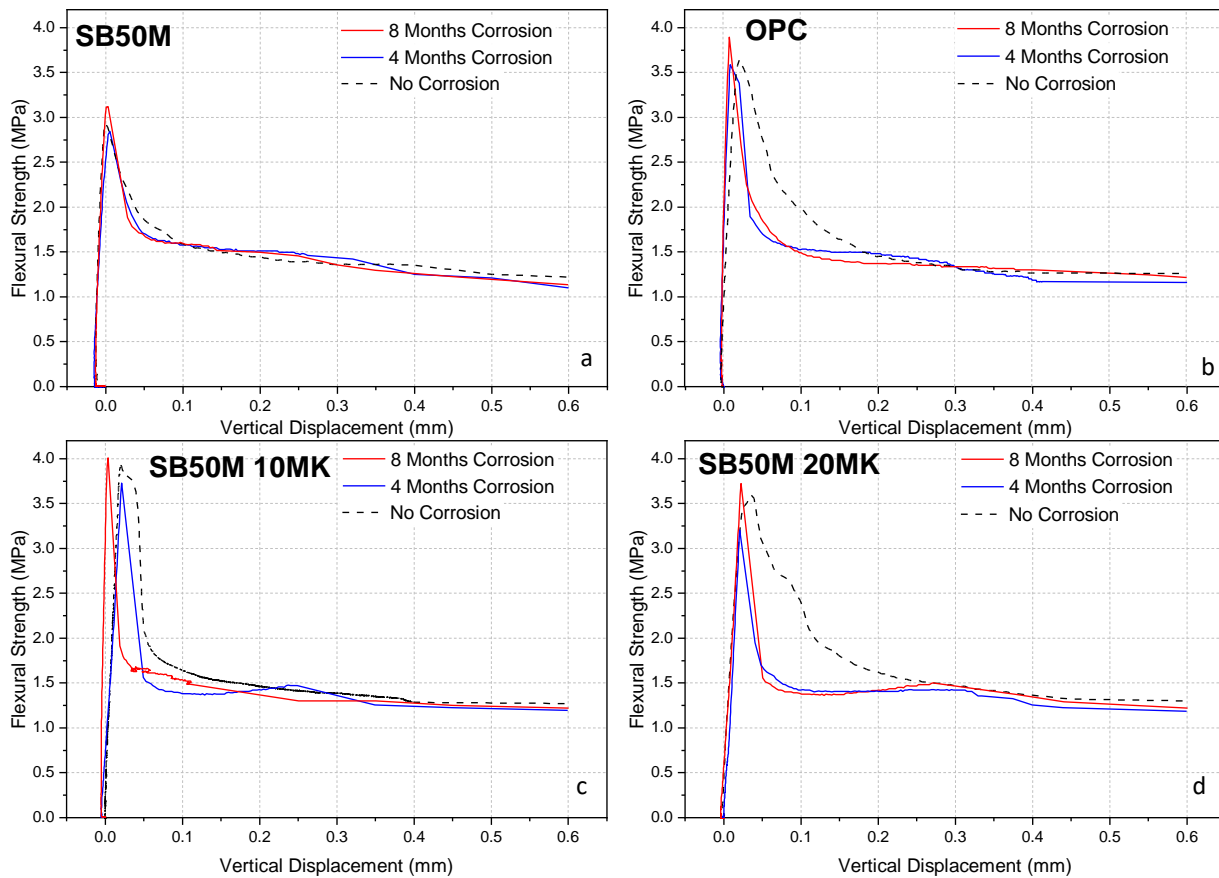


Figure 6-28 - Residual strength of main mixes following corrosion simulation at 4 and 8 months (a) SB50M (b) OPC (c) SB50M 10MK (d) SB50M 20MK

6.4.10.5 Influence of Water Absorption and Density on Corrosion

Water absorption and density were measured at the same ages to assess the effect of exposure to salt solution. The results are shown in table 6-5. Overall, the mortars showed a decrease in water absorption and an increase in density when subjected to accelerated corrosion. Steel fibres have been previously shown to improve transport properties of mortars and concrete, where the fibre-matrix interface prevents microcracks from forming leading to a denser microstructure (Graeff, 2011).

Table 6-5 - Density and water absorption following corrosion simulation

	Density (kg/m ³)		Water Absorption (%)	
	No Corrosion	8 Month Corrosion	No Corrosion	8 Month Corrosion
SB50	2115 ± 75	2140 ± 45	5.9% ± 0.1	5.7% ± 0.5
SB50M	2210 ± 55	2230 ± 45	5.4% ± 0.2	5.2% ± 0.3
SB50 10MK	2215 ± 30	2220 ± 10	4.9% ± 0.2	4.5% ± 0.1
SB50M 10MK	2300 ± 85	2315 ± 90	4.3% ± 0.1	4.2% ± 0.2
SB50 20MK	2225 ± 30	2235 ± 50	4.7% ± 0.3	4.5% ± 0.2
SB50M 20MK	2305 ± 45	2330 ± 25	4.3% ± 0.2	4.1% ± 0.0
OPC	2290 ± 60	2300 ± 70	4.6% ± 0.1	4.6% ± 0.3

In summary, no significant detrimental effects were identified due to corrosion of fibres and, in fact, mechanical properties were mostly enhanced. There is no clear indication that the chloride content from the CBPD caused any further corrosion as the CBPD-GBFS mixes did not seem to perform worse relatively to the other binders. There are also some visual signs of further corrosion when comparing the 4 month corrosion images to the 8 month images. It must be noted that longer term testing may be necessary to truly assess the effect of CBPD binders on steel fibre corrosion.

6.5 Conclusions

This paper investigated the effect of milling on CBPD and replacement of metakaolin in GBFS-CBPD binders. The results evidenced the benefits of these two materials and proved that the reuse of CBPD in OPC-free binders is viable and can produce strong and durable mortars. The following conclusions can be drawn:

1. Grinding CBPD using a TEMA mill for just 150 seconds was sufficient to reduce its particle size from 46.5 microns down to 13.3 microns (median size). The effect of grinding also seemed to have induced mechanical activation, indicated by the increased amorphousness from the XRD pattern of the milled CBPD.
2. Milling led to a much more flowable mix, due to the break up of agglomerates allowing a more even flow, also showing a large improvement in standard consistency. The inclusion of metakaolin led to a moderate decrease in flow properties. An increase in heat of hydration was observed when using milled material and a 10% replacement of GBFS-CBPD with metakaolin.
3. Strength and density results show enhanced properties with milling, where there was a 30% increase in compressive strength of milled CBPD-GBFS binder relatively to an unmilled CBPD-GBFS binder. The coupled effect of metakaolin and milling showed

strengths up to 90% higher than the unmilled CBPD-GBFS binder, even outperforming the control OPC mix.

4. XRD analysis showed higher peaks for the milled CBPD-GBFS mix, indicating more hydrated product is formed, likely due to further hydration due to a larger surface area. The XRD patterns showed that the inclusion of metakaolin led to a decrease in portlandite peaks, which is indicative of a pozzolanic reaction taking place and the formation of CSH/CASH gel. This, and the filler effect, contributed to the strength gain of the CBPD-GBFS-metakaolin mixes. This was further verified through TGA analysis.
5. Shrinkage results showed vast improvements for the CBPD-metakaolin-GBFS binders relatively to the control binder, with total shrinkage strains almost half of those of the control mortars. On the other hand, the effect of milling showed a slight worsening effect overall on the total shrinkage results.
6. ASR results show large improvements for all the binders relative to the OPC control, with reductions up to 70%. This is due to the coupled effect of GBFS and metakaolin refining the pore structure and the immobilisation of alkali cations.
7. In terms of corrosion, there were no significant adverse effects after 8 months exposure to a salt solution. Visually the appearance of the corrosion worsened, and there were signs of internal corrosion by eight months, which were not observed at four months. The wet-dry cycles in salt water still enhanced the flexural and compressive strength of the binders over time, however slight reductions in residual flexural strength were observed relative to the control samples

Overall, this research has showed that CBPD binders can be optimised when combined with 10% metakaolin. Not only does this mix improve upon the OPC control mortar in terms of mechanical properties, but it is also shown to have excellent durability properties. Future work could focus on longer term durability testing, and the investigation of the effect of CBPD binders on steel reinforcing bars. Large-scale applications need also to be investigated to prove the viability of the use of these binders outside of a laboratory setting.

Chapter 7 – Life Cycle Assessment of CBPD Binders

7.1 Introduction

7.1.1 Background

Sustainable alternatives to cement (OPC) are in high demand due to the large emissions associated with the manufacture of the material. The main sustainable alternative to OPC currently are alkali activated materials (AAMs) and extensive research on these has been undertaken regarding their life cycle assessment (Habert & Oullet, 2015).

The results of the carbon dioxide emissions, as well as the environmental impact, have been shown to vary tremendously across literature for AAMs. The results generally indicate a reduction in global warming potential of AAMs relative to OPC. As an example, Weil et al. (2009) showed a 70% reduction of AAMs compared to OPC concrete. Yang et al. (2013) calculated that alkali activated binders emitted between 110-187 kg/m³ of carbon dioxide. However, the upper threshold is largely based on the type of curing method used. For example, solely fly ash or metakaolin based AAMs would have a higher carbon dioxide emission due to heat curing or calcination (Yang et al., 2013). The overall variation in results is likely due to the different approaches that have been taken into consideration during the life cycle assessment. Additionally, AAMs have been found to have a negative impact on the other environmental aspects such as abiotic depletion, ozone layer depletion, human toxicity, and eutrophication (Habert and Oullet, 2016).

Habert et al. (2015) used the Ecoinvent v2 database to analyse the global warming potential of AAMs. They stated that alkali activated mixes could hardly be identified as ground-breaking techniques since they rarely reach 75% savings largely due to the reliance on sodium silicate as a primary activator. This was shown to have the largest environmental footprint in alkali activated cements (up to 90%), especially if produced using the Solvay process. The global warming potential of sodium silicate solution was 1.14 kg CO₂ eq and sodium metasilicate powder reaching 1.24 kg CO₂ eq, which exceeds the emission from the production of OPC (0.844 kg CO₂ eq). McLellan et al. (2011) also highlighted the need to find alternatives for sodium hydroxide reporting that the chemical was the key source of emissions for geopolymer mixes.

7.1.2 Research Gap

Although not a great deal of work has been carried out on CBPD-based binders, Estokova & Holosova et al. (2023) found that replacing 20% of a cement binder with CBPD led to a 17.6%

reduction in total global warming potential, thus providing some initial evidence of the potential environmental benefits that such a waste stream can offer.

Based on the outcome of the work presented in previous sections, a comprehensive Life-Cycle Assessment of representative CBPD mixes is presented in this chapter, and their environmental performance is compared to that of a control mix and a GBFS alkali activated binder.

7.2 Methodology

7.2.1 Mortar Mix Description

This study comprises of a total of 9 mortar mixes: 7 containing CBPD, 1 AAM and 1 OPC mortar. The AAM mix was taken from literature and is deemed to be generally representative of AAMs (Yang et al., 2013). It is composed of GBFS and activated utilising sodium hydroxide and sodium silicate. The mortars and their composition are presented in table 7-1 below. The w/c ratio was kept at 0.52 for all mixes and a cement to aggregate ratio of 1:3 was maintained.

Table 7-1 – Investigated mix designs

Mix Design	GBFS (%)	CBPD (%)	Metakaolin (%)	OPC (%)	Milling (yes/no)
SB50	50	50	0	0	no
SB50M	50	50	0	0	yes
SB30	30	30	0	40	no
SB50 10MK	45	45	10	0	no
SB50 20MK	40	40	20	0	no
SB50M 10MK	45	45	10	0	yes
SB50M 20MK	40	40	20	0	yes
AAM	100	0	0	0	no
OPC	0	0	0	100	no

7.2.2 Life Cycle Assessment

A life cycle assessment (LCA) has been carried out to evaluate the sustainability of the binders in table 7-1. The purpose of this LCA is to assess the environmental benefits of the mixes developed as part of this work and compare them with more traditional cementitious materials.

The LCA has four main phases (ISO 14040, 2006):

1. Scope and Goal
2. Life Cycle Inventory
3. Life Cycle Impact Assessment
4. Interpretation

7.2.2.1 Scope and Goal Definition

This LCA follows the standard ISO 14040 (2006), and the modelling was carried out in OpenLCA 2.0 (2022), an open source LCA software. The functional unit used in this work is 1000kg of mortar and the system boundary used will be cradle to gate. This method is more typically used for cementitious products (PAS 2050). This is chosen over a cradle to grave analysis since concrete can be included in end products having different lifecycles (Habert et al., 2015). An example of a CBPD-GBFS-OPC binder analysed using a cradle to gate system boundary is shown in figure 7-1 below.

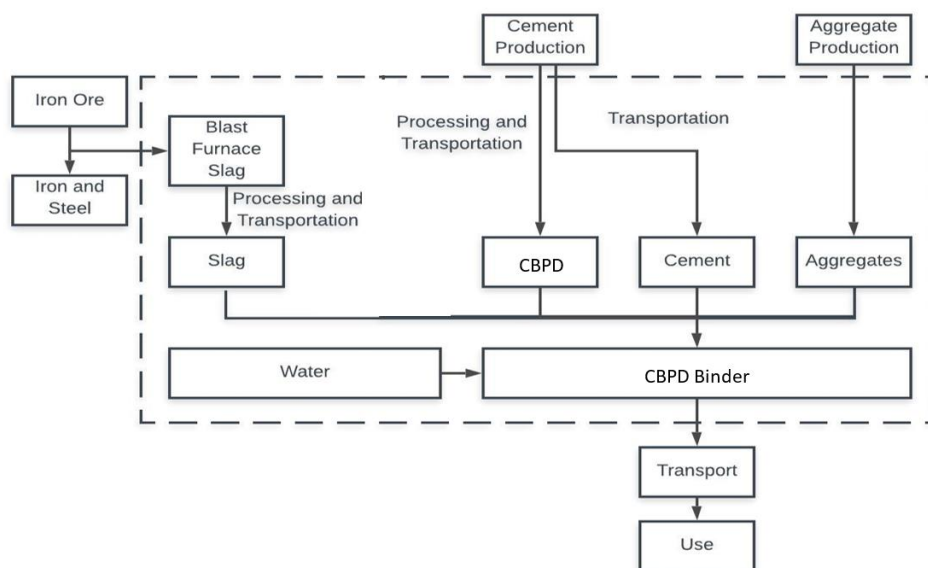


Figure 7-1 – Cradle to gate system boundary of CBPD-GBFS-OPC mix

7.2.2.2 Life Cycle Inventory

Following the scope determination, the inventory analysis is carried out. The inputs and outputs, including the emissions due to milling, were collected from the Ecoinvent 3.8 database following the UK processes available. The Global Warming Potential (GWP) of the raw materials is presented in table 7-2. The cost of all the raw materials were based on the commercial rates in the UK (lime-mortars.co.uk).

Table 7-2 – GWP and transport data of the raw materials investigated

Raw Material	GWP (kg CO₂ eq)	Cost (£/kg)	Distance (km)
CBPD	/	/	100
OPC	0.730	0.28	18
GBFS	0.083	0.65	77
Metakaolin	0.230	2.6	50
Sand	0.005	0.204	50
Tap Water	0.0001	0.0031	/
Sodium Silicate	0.803	/	/
Sodium Hydroxide	0.820	/	/

No emission data was associated with CBPD as this material is deemed as a waste. Based on the EU waste management law (2018), CBPD can be categorised as a waste rather than byproduct. As for milling of CBPD, the only emissions associated with the material is the energy required for grinding the material. The environmental burden to produce milled CBPD as a precursor attributed the same electricity as that for clinker grinding which is of 110 kWh/ton (Hosten and Fidan, 2012). This is a conservative estimate as the size of clinker particles are typically much larger than unprocessed CBPD. The cost associated with milling were based on UK electricity prices (energyguide, 2023).

The total emissions associated with alkali activators is highly variable in literature with several different results being presented (Nikravan et al., 2023). Due to this reason a value considered to be in the middle-ground was selected for GWP of the alkali activators from the Ecoinvent database.

As seen from table 7-2, metakaolin emissions are relatively high compared to GBFS, which is due to the calcination of kaolinite at 800-900°C. It is worth noting that GWP values in literature and databases can vary significantly, largely due to the origin of the metakaolin, the efficiency of the process and the heating source (Habert and Ouellet, 2016). The total impact of metakaolin, however, is always lower than that of cement as limestone calcination is the main driver of emissions for cement production (Tasiopoulou et al., 2023).

Transport data was based on the distance to the consumer in Sheffield. When the transport data was not easily determined, a standard 50km distance was utilised. A freight lorry weighing 16-32 metric tonnes, from the Ecoinvent database, was assumed as the transporter of raw materials. This transport data will be generally applicable to users in the UK.

7.2.2.3 Impact Assessment

The impact assessment method used was EN15804 2020 for the impact evaluation. The impact categories measured were acidification potential, GWP, marine eutrophication potential, terrestrial eutrophication potential, and ozone depletion.

7.2.2.4 Interpretation and Efficiency Study

To compare the materials to each other, an efficiency study has been carried out analysing cost, global warming potential and compressive strength of the binders (Isa et al., 2020). The binders are all evaluated against the control OPC mix. Essentially, if a value is less than 1 (OPC normalised value) then it is less efficient than OPC in that category.

7.2.2.4.1 Environmental Efficiency

The environmental efficiency will be determined based on:

$$En = GWP/GWP_{con} \quad (7-1)$$

Where:

GWP = is the GWP of the investigated mix

GWP_{con} = is the GWP of the control mix

7.2.2.4.2 Mechanical Efficiency

The mechanical efficiency was determined by dividing the 28-day compressive strength of each mix with the 28-day compressive strength of the control mix:

$$Me = fc/fc_{con} \quad (7-2)$$

Where:

fc (MPa) - 28-day compressive strength

fc_{con} (MPa) - 28-day compressive strength of the control mix

7.2.2.4.3 Economic Efficiency

The cost of the binders was determined to be the sum cost of the raw materials and the electricity cost for the milling of CBPD. Following this, the economic efficiency was carried out for each material by dividing the cost of the mix with the control OPC mix:

$$Ec = Cost_{con}/Cost \quad (7-3)$$

Where:

Cost_{con} = Cost of the Control mix

Cost = Cost of the investigated mix

7.2.2.4.4 Total Efficiency

Finally, the total efficiency of the mortar mix was calculated with the following equation:

$$E = E_c . E_n . E_m$$

(7-4)

7.3 Results

7.3.1 Compressive Strength of Binders

The compressive strength of the binders is presented in Table 7-3 below. The AAM was not considered as it was only used for environmental comparison. The results indicate that the SB50 is the weakest binder, however replacing it with 10% metakaolin and milling of the CBPD (SB50M 10MK) enables it to exceed the strength of the OPC control. Milling is proven to be very effective with SB50M exceeding SB50 by 30%. The inclusion of 10% and 20% metakaolin also lead to 33% and 27% increases, respectively, relative to SB50. Hence the coupled effect of these two factors proved to be beneficial overall.

Table 7-3 – Compressive strength results

Mix Design	Compressive Strength (MPa)
SB50	16.8
SB50M	21.5
SB30	24.9
SB50 10MK	22.3
SB50 20MK	21.4
SB50M 10MK	32.7
SB50M 20MK	31.3
OPC	29.8

The mechanical efficiency results shown in figure 7-2 indicate that the SB50M 10MK is the most efficient binder followed by SB50M 20MK and then OPC. As previously discussed, only SB50M 10MK and SB50M 20MK outperform the OPC control in terms of mechanical strength.

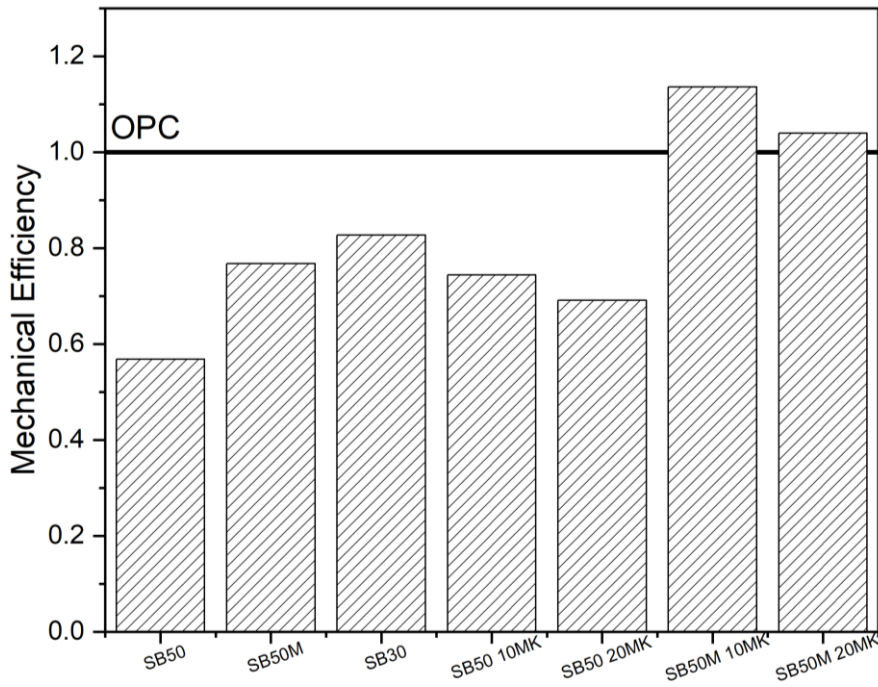


Figure 7-2 - Mechanical efficiency scores

7.3.2 LCA Results

Presented below are the LCA results for the investigated mixes. Two figures are presented for each comparison where (a) shows the total GWP and (b) shows the contribution of each component to the GWP. At the end the environmental efficiency is assessed.

7.3.2.1 Performance of OPC and AAM

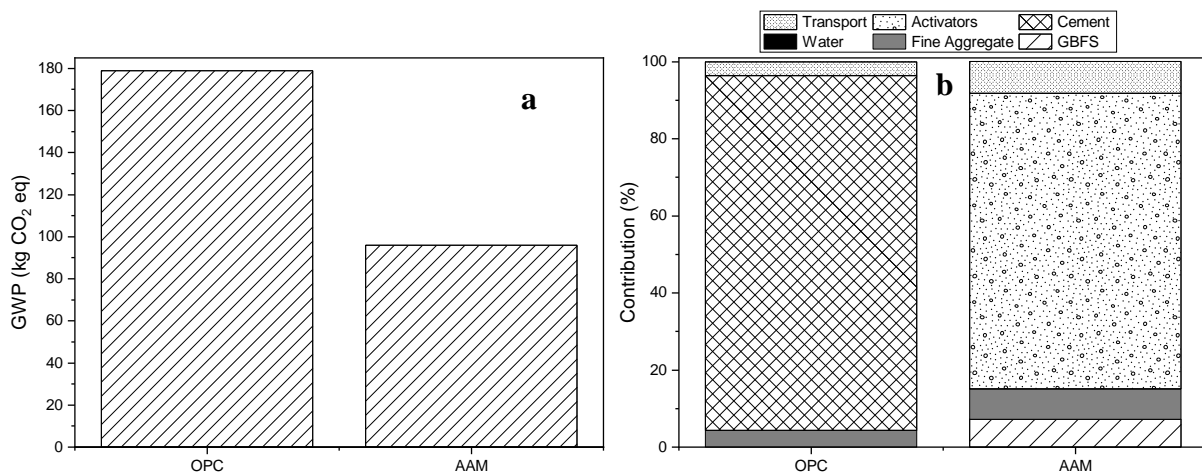


Figure 7-3 (a) GWP of OPC and AAM (b) contribution of inputs

As can be seen from figure 7-3 (a), the main contributor to the GWP of these binders is that of cement and the alkali activators used for the AAMs. 92% of the OPC control GWP was due to the production of cement (figure 7-3 (b)). Clearly the AAM performs better in GWP, as it had

almost half the kg CO₂ eq, however the use of commercial alkaline activators is the main CO₂ emitter for AAMs.

7.3.2.2 Performance of SB50, SB30 and SB50M

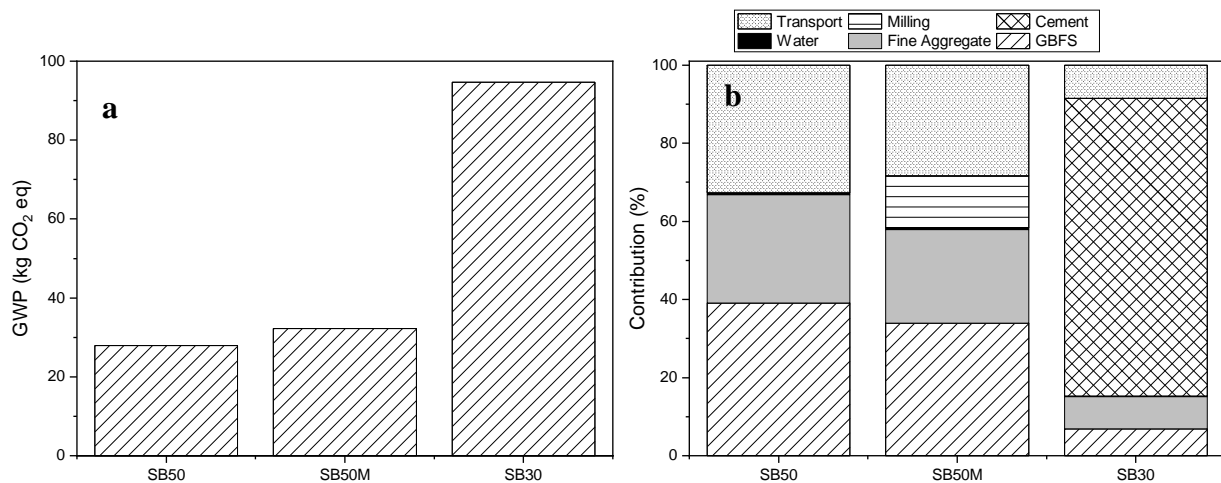


Figure 7-4 - (a) GWP of CBPD-GBFS, CBPD-GBFS and milled CBPD mixes (b) Contribution of inputs

As would be expected, figure 7-4 (a) shows that SB50 had the lowest emissions overall, largely due to the lack of cement and the low emissions associated with GBFS. The largest contributions in these binders were due to transport and GBFS as seen by figure 7-4 (b). It is also evident when comparing SB50 to SB30, how much the inclusion of cement adversely affects the GWP and other impact categories. While milling leads to a worse overall environmental performance where SB50M emits 14% more CO₂ than SB50, this is still significantly less than the AAM and the control. In fact, when observing other impact categories, the use of milling does not significantly affect the results. It must be noted that the inventory data for milling energy output was determined to be the same as that of clinker grinding, which is a conservative estimate. Due to the size of the product in its raw form, grinding of clinker is a much more energy intensive process. In fact, it is responsible for about 10-12% of total emissions associated with OPC (Moeini and Akono, 2011). The emissions due to milling CBPD would likely be lower.

7.3.2.3 Effect of Metakaolin Inclusion

Based on figure 7-5 (a) the inclusion of metakaolin worsens the environmental performance, due to the calcination of kaolinite during its production which reaches temperatures between 800-900°C (Bumanis et al., 2022).

SB50 20MK had a GWP of 36.8 kg CO₂ eq which is a 13% increase relative to SB50M. As seen from the figure below, the main contributor of the binders containing 20% metakaolin was

due to the metakaolin. Milling also shows an increase, however when observing the difference in GWP of SB50 10MK and SB50M 10MK, it is only a change of 11%.

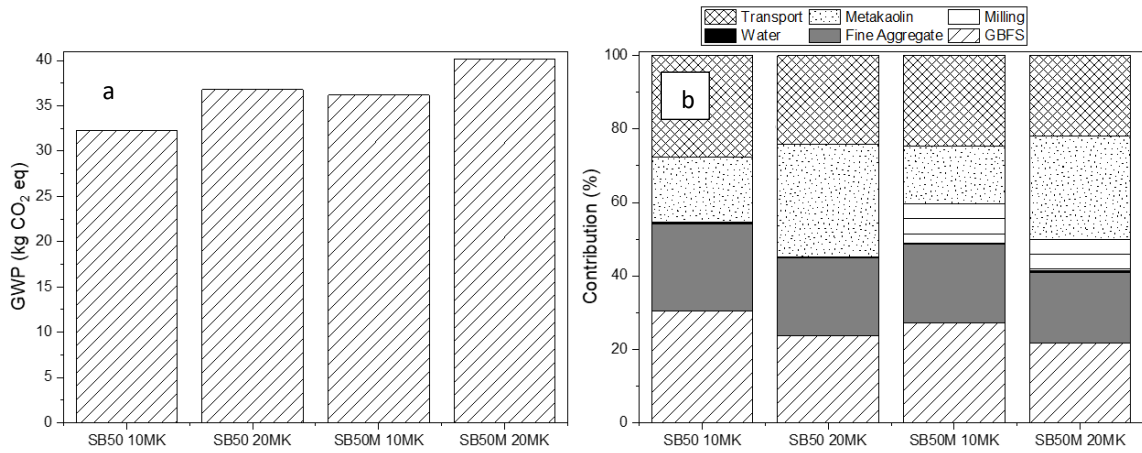


Figure 7-5- (a) GWP of CBPD-metakaolin mixes (b) Contribution of inputs

7.3.2.4 Environmental Efficiency

The total GWP (figure 7-6 (a)) and the relative improvement in GWP potential of the CBPD binders compared to OPC (figure 7-6 (a)) are shown below. SB50M 20MK had just 23% of the total GWP of OPC, despite being the highest emitter of the CBPD binders. While the emissions of metakaolin are relatively high compared to other by products such as GBFS, the quantity used is relatively low. Overall, complete replacement of OPC with CBPD and other supplementary cementitious materials (SCMs) proved to be very beneficial. From these results it can clearly be concluded that CBPD binders are significantly more sustainable than OPC binders and typical AAMs.

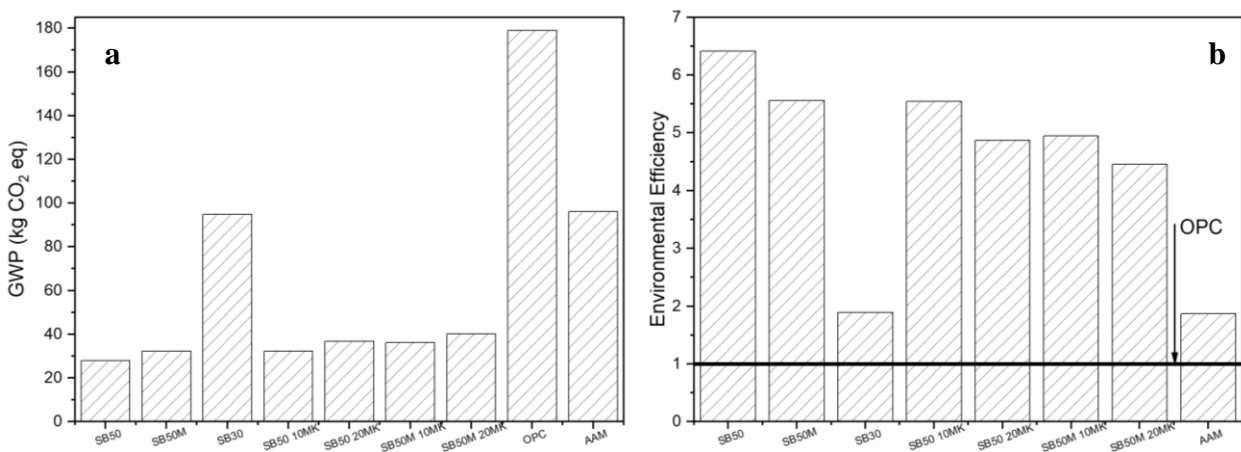


Figure 7-6 – (a) GWP of the studied binders (b) Efficiency of CBPD binders vs OPC

7.3.2.5 Other Impact Categories

A comparison of the different binders regarding other impact categories is shown in figure 7-7 below. The results show as a percentage the difference other binders achieved in impact categories relative to OPC. In general, the trend follows that of the GWP. As the cement content increases, the impact category is more adversely affected. In fact, the only comparable results in other impact categories were that of the AAM. AAM has reasonably close results to OPC regarding both eutrophication categories and exceeds it regarding Ozone Depletion and Acidification. Ozone depletion and acidification burden mostly occurs during the chlor-alkali process (sodium hydroxide production) (Salas et al., 2018). Contrastingly, CBPD binders had much reduced values in other impact categories, highlighting the negative effect of commercial alkali activators. Metakaolin does, however, also lead to an increase in ozone depletion.

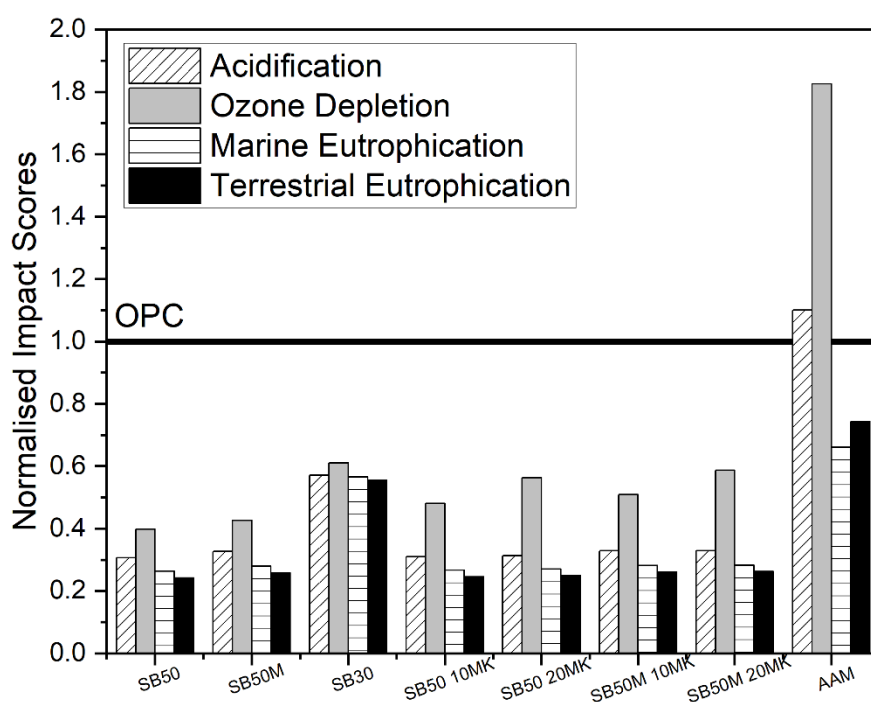


Figure 7-7 - Normalised impact scores of CBPD binders relative to OPC

While not presented in this work, another factor to consider is the high embodied energy associated with the manufacture of alkali activators. Nematollahi et al. (2017), found a significant reduction in overall CO₂ emissions of their one-part and two-part geopolymers relative to OPC. The results for embodied energy, however, showed lesser improvements due to the large energy required to manufacture commercial alkali activators.

7.3.3 Cost Analysis

To consider the viability of the CBPD binders, a financial cost comparison is also required. A simplified cost of materials was used, where three main assumptions were made:

1. Milling was performed for 15 minutes assuming 110 kWh.
2. No costs were associated with CBPD as this is a waste.
3. No transport costs were considered.

The total cost of the mixes is shown in table 7-4 below.

Table 7-4 – Cost of the investigated binders

Mix Design	Cost (£ per tonne)
SB50	204.5
SB50M	236.4
SB30	200.5
SB50 10MK	254.6
SB50 20MK	304.6
SB50M 10MK	286.5
SB50M 20MK	336.5
OPC	194.6

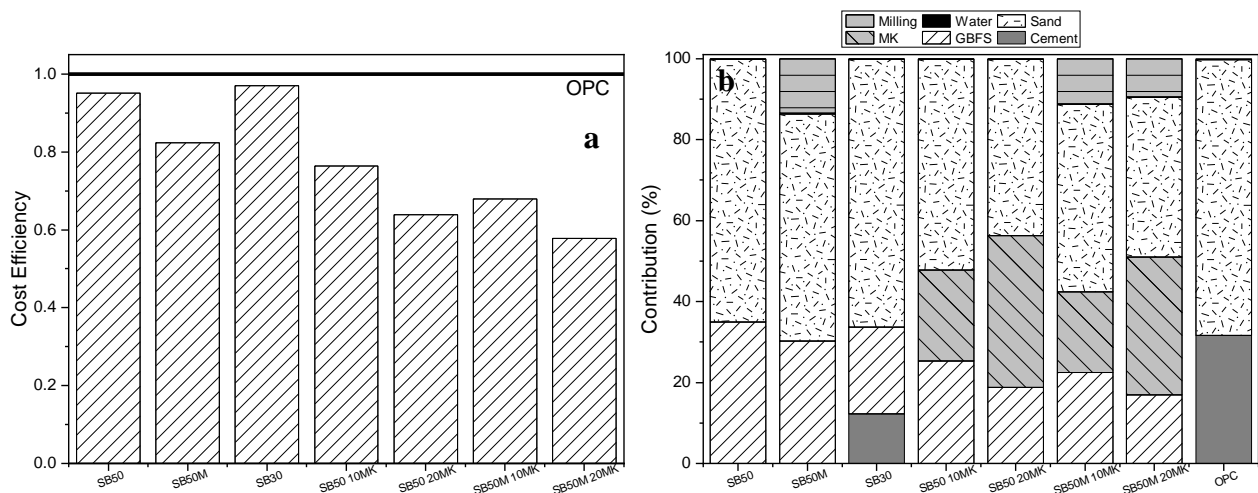


Figure 7-8 - (a) Cost efficiency (b) Contribution of inputs to cost

The results indicate that the control binder has the least amount of cost associated with it. This is due to the fact that, besides CBPD having no cost associated with it, cement is the cheapest binder material. From the research, metakaolin is significantly more expensive than OPC in the UK. When observing the contribution of the various inputs to overall cost (figure 7-8 (b)),

metakaolin and milling led to a more expensive solution than OPC. Looking at the overall efficiency results (figure 7-8 (a)), the CBPD-GBFS binders approach the efficiency of OPC, however, there is a clear decline with metakaolin inclusion despite only using a limited amount.

While these results show the negative impact SCMs have on binder cost, carbon price estimates need to be considered. In fact, carbon price forecasts predict that there could be up to a five time increase in cost by 2050 (Luckow et al., 2015). Being the highest emitter of all materials evaluated the cost of using cement will undoubtedly increase over time. Building companies are incentivised to use more sustainable binders and within a short period of time, the overall cost of solely using cement will likely be higher than what these results have shown.

7.3.4 Total Efficiency

Figure 7-9 presents the total efficiency of all the binders relative to OPC. Overall, the analysis shows that SB50M 10MK is the best performing mix as, despite having a higher cost, it outperformed the OPC mix in both strength and GWP. SB50 was also shown to be quite efficient, however it must be noted that this is due to the large improvement in environmental efficiency. The binder is shown to be significantly weaker than OPC and its use should be reserved for lower strength applications. Its milled counterpart proved to be more efficient, due to the large strength gain following grinding. Clearly what these results show is that as the cement content decreases, the total efficiency increases largely due to the environmental performance. The analysis ultimately shows that ternary binder composed of metakaolin, milled CBPD, and slag is a more sustainable and an economically competitive alternative to the investigated OPC binder.

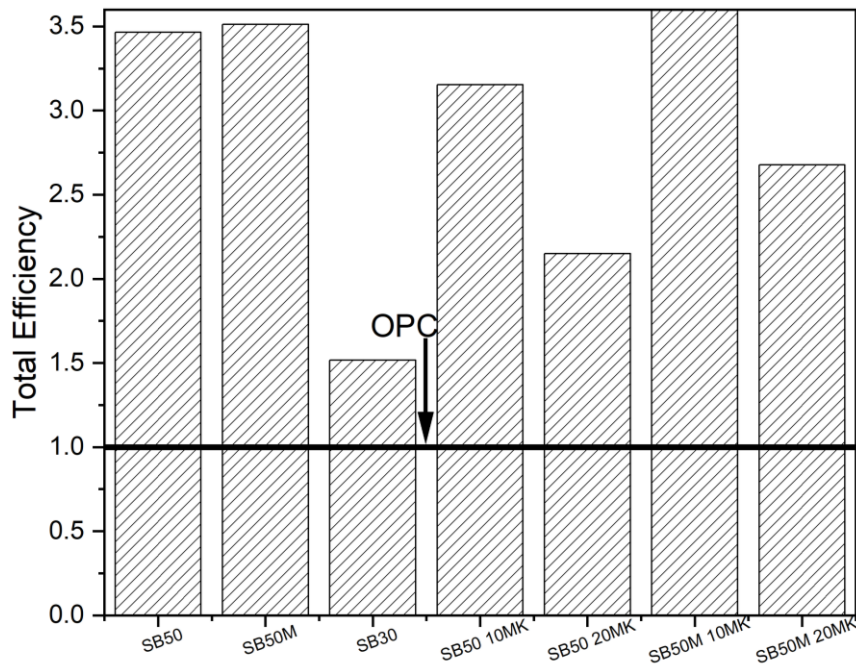


Figure 7-9 - Total efficiency of CBPD binders relative to OPC

7.4 Conclusion

An environmental evaluation was carried out analysing the performance of an OPC binder against CBPD binders containing SCMs such as metakaolin and GBFS. The results indicate:

1. OPC was superior in terms of compressive strength except for the milled CBPD binders containing metakaolin.
2. Metakaolin has a higher cost associated with it relative to other binder products, hence it had the most expensive binders, with OPC being the cheapest binder overall. This was also due to the higher GBFS cost. The trend of increasing carbon and emission prices over time will likely benefit this factor in the future.
3. The AAM performed better than OPC in terms of GWP and marine and terrestrial eutrophication, however it was significantly worse in terms of ozone depletion and acidification. These emissions were due to commercial alkali activators such as sodium silicate and sodium hydroxide.
4. When investigating the CBPD binders, they outperformed both the AAM and the OPC in all impact factors. The milled CBPD-GBFS binder containing 10% metakaolin had less than half the GWP of the AAM showing the benefits of using binder materials from SCMs and waste streams.

5. In terms of efficiency, SB50M 10MK was proven to be the most efficient as it was the strongest binder and had much superior environmental performance relative to OPC. Ultimately, due to its high emissions, OPC was shown to be the least efficient.

This research shows that manufacturing waste cementitious binders is a viable alternative to typical OPC. To curb CO₂ emissions, several different solutions need to be put in place in the construction industry, and the reuse of CBPD, a highly unexploited waste, is just one of those many solutions. Future research can focus on the behaviour of CBPD with fly ash or different types of calcined clay, materials that are often shown to have lower emissions than GBFS.

Chapter 8 - Conclusion and Recommendations

8.1 Introduction

The objectives of this study were to investigate and classify Cement Bypass Dust to determine its potential in cementless and low-cement content binders through its combination with supplementary cementitious materials. Several properties of the material were investigated at both fresh and hardened state, including mechanical performance and durability indicators. Different curing techniques were researched such as heat-curing, ambient temperature curing and carbonation curing. Finally, mechanical activation and the combination of the material with metakaolin were researched.

This final chapter presents the conclusions reached regarding the potential of CBPD and its possible uses in the future. Additionally it suggests some recommendations for future research.

8.2 Main Conclusions

8.2.1 Effectiveness of Cement Bypass Dust in Heat and Ambient Temperature Cured Slag-Based Mortars

This initial work focused on exploring the viability of CBPD as a cement replacement. As mentioned in the methodology section, different proportions of CBPD and GBFS were trialled (10:90, 25:75: 40:60 etc.) where the laboratory trials showed that 50:50 CBPD and GBFS ratio provided the strongest binder after 28 days of curing. Perhaps higher quantities of CBPD would have led to even stronger binders; however, this was not possible to test due to limited amount of material.

A binary (GBFS:CBPD) and a ternary (GBFS:CBPD:OPC) blend were investigated, where heat curing, and ambient temperature curing were examined. This research proved to be very useful to gather insights on the potential of CBPD and laid the groundwork for the work carried out as part of this project.

Fresh property results showed that CBPD had a high-water demand leading to high standard consistency values as well as stiffer flow. This was shown to have an adverse effect on the binary mix and led to increased porosity. Consequently, the mixes achieved relatively low strengths. It was shown that in every case, the use of 20% cement led to stronger binders.

Heat curing was compared to ambient curing. It was found that heat curing is only beneficial up to 7 days and did not lead to any long-term benefits. Ambient cured samples had equalled

or exceeded the heat cured binders in terms of strength by 7 days. Heat curing also led to adverse swelling, leading to surface cracks. The microstructural investigation also revealed more hydration products for ambient cured binders.

This initial phase of the study confirmed the potential of using CBPD as a cement replacement and create cementless binders without the need of any heat curing, which may have offset any environmental benefits.

8.2.2 The Effect of CBPD Composition on the Properties of GBFS-based mortars

Two types of CBPD were researched in this study to understand the significance of their composition. They were named CBPD L and CBPD R. Chemical investigation showed that CBPD L had a higher free lime and chloride content, whereas CBPD R had a higher gypsum, calcite and sulphate content. Several binders were investigated that had different proportions of cement (40%, 80% and 100%).

It was found that the performance of CBPD L was governed by its high lime content, whereas CBPD R's behaviour was based on both its sulphate, calcite and lime content. CBPD R had a higher water demand than L, and this was attributed to the higher agglomeration in CBPD R. Consequently, this led to worse flow properties and higher standard consistencies. Because of its high free lime content, CBPD L was also a much more reactive material. Free lime has a strong exothermic slaking reaction when it contacts water, this was reflected in the heat of hydration results, which were highly exothermic for CBPD L binders. It was found that as the cement content increased, the heat of hydration reduced.

CBPD R did provide stronger and denser binders relative to CBPD L binders. Chemically this was attributable to the formation of ettringite and the higher presence of calcite which has excellent pore filling properties. Physically this was also likely due to the rapid expansion of CBPD L binders lowering its strength, which was due to the reaction of free lime and water. This expansion was quantified with a chemical shrinkage test showing that, while both CBPD types led to expansion, CBPD L had the highest expansion in all cases. In terms of strength, lower CBPD replacements of cement (10%), proved to be beneficial and stronger than the 100% cement control. This is due to cement ultimately having improved hydration properties relative to CBPD. Thus, small replacements are recommended, however they will likely not have significant improvements on sustainability.

In terms of hydration, CBPD R binders had a much higher formation of ettringite and CBPD L binders had a large formation of portlandite, even exceeding that of the cement control. The reason for this is largely due to the sulphate and lime contents in CBPD R and CBPD L, respectively. Thus, it can be stated that CBPDs can be classified as sulphate or lime rich CBPDs. Other classifications such as high/low calcium is also viable, much like classifications of fly ash. What is clear from this work, is that excessive lime content severely affects the use of CBPD as a cement replacement and may need to be limited to other uses such as soil stabilisation.

8.2.3 Carbon Curing of CBPD-Slag Binders

A minor carbon curing study was carried out as it was speculated that the free lime content of CBPD L could be exploited to react with CO₂. CBPD binders were placed in a sealed chamber and pumped with 99% purity CO₂ gas for 5 hours. Small paste samples were made due to laboratory constraints.

The findings showed that SB50L, which was a mix of 50% CBPD L and 50% GBFS, absorbed a large amount of CO₂, increasing in mass by 7%. It also had a strength increase of 39% by 28 days, which allowed it to exceed that of SB50R (50% CBPD R and 50% GBFS). Due to their high free lime content, CBPD L binders formed a very high amount of portlandite which consequently could be exploited through its reaction with CO₂ to form calcite. Binders from SB50R showed increases too, however to a much lesser degree. This was due to the lower free lime and portlandite in the binders, as well as the higher calcite content. The lower portlandite content would limit the reaction of CBPD R binders with CO₂.

Microstructural changes from XRD and TGA analysis also showed very large increases in calcite content, primarily in CBPD L binders. There was also a significant reduction of portlandite which signified the reaction of this phase with CO₂. SEM images showed the change in microstructure with a very large quantity of calcite crystals forming in SB50L explaining the increase in strength due to the pore filling properties of calcite.

This study showed that there is a very high potential for the use of carbon curing on CBPD binders, primarily the lime rich binders. In the previous work, CBPD L binders had a significantly lower strength than CBPD R binders. This means that lime-rich CBPD may find uses in construction when carbon-cured, however further research is required.

8.2.4 Mechanical and Durability Properties of Ternary Blends of Milled CBPD-GBFS-Metakaolin

Though cementless binders containing CBPD and GBFS were shown to be viable, they did not perform nearly as well as pure OPC binders when comparing strength and shrinkage. This study set to enhance the properties of CBPD:GBFS binders through the milling of CBPD and including metakaolin to make ternary CBPD:GBFS:metakaolin binders. Binders were fabricated using 40% CBPD, 40% GBFS and 20% metakaolin (SB50 20MK) and 45% CBPD, 45% GBFS and 10% metakaolin (SB50 10MK). A binder composed of 50% GBFS and 50% CBPD (SB50) was also used as well as a control mix composed of 100% OPC. Milled and unmilled CBPD were also compared in all the binders, and this was represented in the notation with an 'M' symbol. For example, a binder containing 50% GBFS and 50% milled CBPD was classified as SB50M.

Durability properties such as ASR were investigated as well as the compatibility of CBPD binders with steel fibres with corrosion testing. Due to the content of chlorides and sulphates in CBPD, this was necessary to understand. Steel fibres were chosen as past research has shown that their corrosion potential is much lower relative to steel rebar.

Milling was attempted at different time intervals, and it was found that 150 seconds of grinding was sufficient to achieve a fineness of 13.1 μm , which is a large reduction to the unmilled 46.5 μm . Milling proved to be very beneficial. In terms of fresh properties, the CBPD binder was much more flowable following the milling and had an improvement in standard consistency. This was likely due to the breakup of the CBPD agglomerates in unmilled CBPD. The heat of hydration also showed an increase, likely due to the further contact points in the increased surface area of the milled CBPD.

Regarding strength, there was a 30% increase in the SB50M relative to SB50. While mechanical activation did occur to a small degree, evidenced from the XRD of the material, small changes were found in the XRD diffractogram of the binder. Thus, the strength benefits are likely due to physical aspects such as improved pore filling capabilities from the milled CBPD and the more refined microstructure.

Metakaolin inclusion coupled with the effect of milling of CBPD proved to be very beneficial. The strength values of SB50M 10MK exceeded those of control OPC, which showed that a purely cementless binder can be a viable option. Significant improvements were also found due to metakaolin inclusion, where the metakaolin binders had almost half the shrinkage of

OPC. The strength increases were due to both physical and chemical aspects. Physically the binder components utilised were much finer than unmilled CBPD binders ensuring a denser binder. Chemically the strength increases of binders containing metakaolin can be attributed to the pozzolanic reaction of metakaolin. It was in the XRD diffractograms that portlandite was being consumed as the metakaolin content increased, confirming the pozzolanic reaction which has been shown to improve strength and binder properties in past research.

Durability results were also quite positive, with all CBPD binders outperforming the control OPC in terms of ASR. SB50M, despite having no metakaolin, performed better than the control likely due to the 50% GBFS content. The results showed that as the metakaolin content increased, the ASR results improved. In terms of corrosion, the results showed no significant detriments on the fibre due to the use of CBPD. There were some slight reductions in residual flexural strength at 8 months, however longer-term research is required to truly see the effects of corrosion on reinforcement of CBPD binders.

8.2.5 Life-Cycle Assessment of CBPD Binders

Finally, as sustainability is the key factor when identifying OPC alternatives, life cycle analysis (LCA) was performed for the main CBPD binders examined in this research. Prior to this, research on any LCA or sustainability analysis was not available for CBPD binders. In this chapter, global warming potential, other impact factors, cost and mechanical efficiency were analysed.

In terms of mechanical efficiency, SB50M 10MK (45% GBFS, 45% milled CBPD and 10% metakaolin) proved to be the most efficient binder and thus the best performing, with OPC being the second strongest.

In terms of cost, metakaolin proved to be quite an expensive material and, therefore, performed worse than OPC binders, costing almost 50% more than OPC (a total of £286.5 per tonne relative to OPC's £194.6). While this is a significant increase in price, it was speculated that the future cost of carbon emissions in the form of taxation will offset this increase in cost. Ultimately, companies are being encouraged to find and use sustainable alternatives and heavy penalties will likely fall on excessive carbon emissions. It must be noted, however, that no cost was associated with CBPD due to its categorisation as a waste. It will likely have a value associated with it when the material becomes standardised and used more widely.

Regarding sustainability, clearly the most detrimental material was OPC. When observing global warming potential, OPC had a GWP of circa 180 and SB30 (40% OPC content) achieved

almost 100 GWP. This was followed by the representative AAM value, which was used for sustainability comparison. It was found that, due to calcination, metakaolin had a relatively high CO₂ emission, however since only small amounts were utilised (maximum of 20% by weight of the binder) there were no significant impacts. Additionally, milling was shown to increase the GWP, however not significantly with SB50 and SB50M achieving 29 and 31 GWP, respectively. It must also be noted that this was a conservative estimate. While the AAM performed better in the GWP impact category, it had much worse results regarding other impact categories. This was due to its chemical activator, which suggests that it is necessary to source activators from waste streams.

Finally, when discussing the efficiency value, it was found that SB50M 10MK was the most efficient due to its mechanical and sustainability results. This research showed that the optimal mix design from this work was SB50M 10MK and it is recommended to study this mix further in future research.

8.3 Recommendations for Future Research

Following the research and experience gained from this study, presented below are some recommendations for future research on CBPD binders:

1. Create concrete mixes based on the insights gained from this work and examine the potential of CBPD in concrete. Furthermore investigate the development of CBPD pastes.
2. Study the compatibility of these mixes with different admixtures and superplasticisers to verify whether this material is compatible with the conventional types.
3. Use superplasticisers to maintain the standard consistency and w/b ratios at constant values in future research. This ensures better comparability.
4. Study blending of different materials with CBPD, such as fly ash, calcined clay, biomass ash etc. Other wastes, such as ceramic and quarry dust, could also be blended as CBPD would likely act as a suitable activator for these materials.
5. Attempt intergrinding of CBPD and other raw materials in its binders. This has been shown to be very beneficial in previous research (Bondar et al., 2016) and will likely enhance the properties of CBPD mixes.
6. Perform a more in depth study on carbon curing involving mortar and concrete CBPD mixes. While carbon curing was performed and proven to be a viable option, the CBPD binders were only cured for 5 hours and were limited in size. A larger chamber with no

laboratory constraints is necessary. Different carbonation times and increased CO₂ pressures can be tested out. Further durability and shrinkage studies are also required on carbon-cured CBPD binders, particularly when dealing with lime-rich CBPD binders.

7. Attempt other curing techniques such as steam curing and autoclaved curing as this will clarify the potential of these binders in the precast industry.
8. Test additional types of CBPD using the techniques utilised in this research as this may further aid in fully classifying the material. Additionally perform Rietveld analysis or XRF analysis to fully characterise the composition of the materials investigated.
9. Investigate CBPD binders in a field study to understand the viability of these binders for real life applications. Both in-situ and precasting should be investigated to understand where the best use of the material lies.
10. Thoroughly research the durability properties of the CBPD binders.. Vulnerability to sulphate attack freeze-thaw and natural carbonation are good areas to explore. Finally, while corrosion was investigated, the compatibility of this material with steel rebar is yet to be assessed.

References

1. 'Effect of mechanochemical activation on reactivity of cement kiln dust-fly ash systems' (2003) *ACI Materials Journal*, 100(1). doi:10.14359/12463.
2. *70,000 tonnes geopolymers concrete for airport* (2014) *Geopolymer Institute*. Available at: <https://www.geopolymer.org/news/70000-tonnes-geopolymer-concrete-airport/> (Accessed: 25 September 2022).
3. Abbas, R. A. H., Shehata, N., Elrahman, E. A., Salah, H., & Abdelzahera, M. A. (2021). Environmental safe disposal of cement kiln dust for the production of geopolymers. *Egyptian Journal of Chemistry*, 64(12), 7429–7437. <https://doi.org/10.21608/EJCHEM.2021.89060.4276>
4. Abd Razak, S. N., Shafiq, N., Hasan Nikbakht, E., Mohammed, B. S., Guillaumat, L., & Farhan, S. A. (2022). Fire performance of fly-ash-based geopolymer concrete: Effect of burning temperature on mechanical and microstructural properties. *Materials Today: Proceedings*, 66, 2665–2669. <https://doi.org/10.1016/j.matpr.2022.06.491>
5. Abdelfatah, A.S., Tabsh, S.W., 2011. Review of Research on and Implementation of Recycled Concrete Aggregate in the GCC. *Advances in Civil Engineering* 2011. <https://doi.org/10.1155/2011/567924>
6. Abdollahnejad, Z., Mastali, · M, Falah, · M, Shaad, · K Mohammad, Luukkonen, · T, Illikainen, · M, 2021. Durability of the Reinforced One-Part Alkali-Activated Slag Mortars with Different Fibers 12, 487–501. <https://doi.org/10.1007/s12649-020-00958-x>
7. Abidoye, L.K. and Das, D.B. (2021) 'Carbon Storage in Portland Cement Mortar: Influences of hydration stage, carbonation time and aggregate characteristics', *Clean Technologies*, 3(3), pp. 563–580. doi:10.3390/cleantechnol3030034.
8. Abo-El-Enein, S.A., Heikal, M., Amin, M.S., Negm, H.H., 2013. Reactivity of dealuminated kaolin and burnt kaolin using cement kiln dust or hydrated lime as activators. *Construction and Building Materials* 47, 1451–1460. <https://doi.org/10.1016/J.CONBUILDMAT.2013.06.078>
9. Abukhashaba, M., Mostafa, M. and Adam, I., 2014. Behavior of self-compacting fiber reinforced concrete containing cement kiln dust. *Alexandria Engineering Journal*, 53(2), pp.341-354. <https://doi.org/10.1016/j.aej.2014.03.006>
10. Adaska, W. and Taubert, D., 2008. Beneficial Uses Of Cement Kiln Dust. IEEE-IAS Cement Industry Committee, Miami, Florida
11. Adesanya, E., Perumal, P., Luukkonen, T., Yliniemi, J., Ohenoja, K., Kinnunen, P., & Illikainen, M. (2021). Opportunities to improve sustainability of alkali-activated

- materials: A review of side-stream based activators. In *Journal of Cleaner Production* (Vol. 286). Elsevier Ltd. <https://doi.org/10.1016/j.jclepro.2020.125558>
12. Aggarwal, J., Goyal, S. and Kumar, M. (2023) ‘Sustainable utilization of industrial by-products spent foundry sand and cement kiln dust in controlled low strength materials (CLSM)’, *Construction and Building Materials*, 404, p. 133315. doi:10.1016/j.conbuildmat.2023.133315.
 13. Ahmad, S., Assaggaf, R. A., Maslehuddin, M., Al-Amoudi, O. S. B., Adekunle, S. K., & Ali, S. I. (2017). Effects of carbonation pressure and duration on strength evolution of concrete subjected to accelerated carbonation curing. *Construction and Building Materials*, 136, 565–573. <https://doi.org/10.1016/j.conbuildmat.2017.01.069>
 14. Ahmed, D.A. et al. (2023) ‘Green synthesis of the effectively environmentally safe Metakaolin-based geopolymer for the removal of hazardous industrial wastes using two different methods’, *Polymers*, 15(13), p. 2865. doi:10.3390/polym15132865.
 15. Al-Harthy, A., Taha, R. and Al-Maamary, F., 2003. Effect of cement kiln dust (CKD) on mortar and concrete mixtures. *Construction and Building Materials*, 17(5), pp.353-360. [https://doi.org/10.1016/S0950-0618\(02\)00120-4](https://doi.org/10.1016/S0950-0618(02)00120-4)
 16. Alnahhal, M. F., Kim, T., & Hajimohammadi, A. (2021). Waste-derived activators for alkali-activated materials: A review. *Cement and Concrete Composites*, 118. <https://doi.org/10.1016/j.cemconcomp.2021.103980>
 17. Alonso, M.M. et al. (2019) ‘Olive biomass ash as an alternative activator in Geopolymer Formation: A study of strength, radiology and leaching behaviour’, *Cement and Concrete Composites*, 104, p. 103384. doi:10.1016/j.cemconcomp.2019.103384.
 18. Alonso, S. and Palomo, A. (2001) ‘Calorimetric study of alkaline activation of calcium hydroxide–metakaolin solid mixtures’, *Cement and Concrete Research*, 31(1), pp. 25–30. doi:10.1016/s0008-8846(00)00435-x.
 19. Al-Rezaiqi, J., Alnuaimi, A. and Hago, A.W. (2018) ‘Efficiency factors of burnt clay and cement kiln dust and their effects on properties of blended concrete’, *Applied Clay Science*, 157, pp. 51–64. doi:10.1016/j.clay.2018.01.040.
 20. *Annual CO₂ emissions from cement* (2023) *Our World in Data*. Available at: <https://ourworldindata.org/grapher/annual-co2-cement> (Accessed: 29 October 2023).
 21. Antoni, M., Rossen, J., Martirena, F., & Scrivener, K. (2012). Cement substitution by a combination of metakaolin and limestone. *Cement and Concrete Research*, 42(12), 1579–1589. <https://doi.org/10.1016/j.cemconres.2012.09.006>

22. Ashraf, W. (2016) 'Carbonation of cement-based materials: Challenges and opportunities', *Construction and Building Materials*, 120, pp. 558–570. doi:10.1016/j.conbuildmat.2016.05.080.
23. Ashteyat, A.M., Haddad, R.H. and Obaidat, Y.T. (2018) 'Case study on production of self compacting concrete using white cement by pass dust', *Case Studies in Construction Materials*, 9. doi:10.1016/j.cscm.2018.e00190.
24. Askarian, M., Tao, Z., Adam, G. and Samali, B., 2018. Mechanical properties of ambient cured one-part hybrid OPC-geopolymer concrete. *Construction and Building Materials*, 186, pp.330-337. <https://doi.org/10.1016/j.conbuildmat.2018.07.160>
25. Askarian, M., Tao, Z., Samali, B., Adam, G., & Shuaibu, R. (2019). Mix composition and characterisation of one-part geopolymers with different activators. *Construction and Building Materials*, 225, 526–537. <https://doi.org/10.1016/j.conbuildmat.2019.07.083>
26. ASTM (2012) ASTM C1608-07: *Standard Test Method for Chemical Shrinkage of Hydraulic Cement Paste*
27. ASTM (2020) ASTM C1437-20: *Standard Test Method for Flow of Hydraulic Cement Mortar*
28. ASTM (2021) ASTM C109/C109M-21: *Standard Test Method for Compressive Strength of Hydraulic Cement Mortars (Using 2-in. or [50mm] Cube Specimens)*
29. ASTM (2023) ASTM C1260-23: *Standard Test Method for Potential Alkali Reactivity of Aggregates (Mortar-Bar Method)*
30. ASTM (2023) ASTM C596-23: *Standard Test Method for Drying Shrinkage of Mortar Containing Hydraulic Cement*
31. Attah, I. C., Etim, R. K., Ekpo, D. U., & Usanga, I. N. (2022). Effectiveness of cement kiln dustsilicate based mixtures on plasticity and compaction performance of an expansive soil. *Epitoanyag - Journal of Silicate Based and Composite Materials*, 74(4), 144–149. <https://doi.org/10.14382/epitoanyag-jsbcm.2022.22>
32. Azar, P., Samson, G., Deby, F., Trincal, V., Lahalle, H., Benavent, V., & Cyr, M. (2023). Transfer properties and chloride-induced corrosion resistance of GGBS and metakaolin alkali-activated materials. *Cement and Concrete Composites*, 142. <https://doi.org/10.1016/j.cemconcomp.2023.105182>
33. Baghdadi, Z., Fatani, M. and Sabban, N., 1995. Soil Modification by Cement Kiln Dust. *Journal of Materials in Civil Engineering*, (218). [https://doi.org/10.1061/\(ASCE\)0899-1561\(1995\)7:4\(218\)](https://doi.org/10.1061/(ASCE)0899-1561(1995)7:4(218))

34. Bakera, A.T. and Alexander, M.G. (2019) 'Use of Metakaolin as supplementary cementitious material in concrete, with focus on durability properties', RILEM Technical Letters, 4, pp. 89–102. doi:10.21809/rilemtechlett.2019.94.
35. Bandara, N., Hettiarachchi, H., Jensen, E., & Binoy, T. H. (2020). Upcycling potential of industrial waste in soil stabilization: Use of kiln dust and fly ash to improve weak pavement subgrades encountered in Michigan, USA. Sustainability (Switzerland), 12(17). <https://doi.org/10.3390/su12177226>
36. Barnat-Hunek, D., Góra, J., Suchorab, Z., Łagód, G., 2018. Cement kiln dust, in: Waste and Supplementary Cementitious Materials in Concrete: Characterisation, Properties and Applications. Elsevier, pp. 149–180. <https://doi.org/10.1016/B978-0-08-102156-9.00005-5>
37. Batis, G. et al. (2005) 'The effect of Metakaolin on the corrosion behavior of cement mortars', Cement and Concrete Composites, 27(1), pp. 125–130. doi:10.1016/j.cemconcomp.2004.02.041.
38. Batis, G., Rakanta, E., Sideri, E., Chaniotakis, E., Papageorgiou, A., 2002. ADVANTAGES OF SIMULTANEOUS USE OF CEMENT KILN DUST AND BLAST FURNACE SLAG. Challenges of Concrete Construction: Volume 5, Sustainable Concrete Construction 205–212. <https://doi.org/10.1680/SCC.31777.0021>
39. Baugh, J. and Edil, T.B. (2007) 'Suitability of Cement Kiln Dust for Reconstruction of Roads'.
40. Berger, R.L. and Klemm, W.A. (1972) 'Accelerated curing of cementitious systems by carbon dioxide', Cement and Concrete Research, 2(6), pp. 647–652. doi:10.1016/0008-8846(72)90002-6.
41. Bernard, E., Lothenbach, B., Cau-Dit-Coumes, C., Chlique, C., Dauzères, A., & Pochard, I. (2018). Magnesium and calcium silicate hydrates, Part I: Investigation of the possible magnesium incorporation in calcium silicate hydrate (C-S-H) and of the calcium in magnesium silicate hydrate (M-S-H). Applied Geochemistry, 89, 229–242. <https://doi.org/10.1016/j.apgeochem.2017.12.005>
42. Berrocal, C., Lundgren, K. and Löfgren, I., 2016. Corrosion of steel bars embedded in fibre reinforced concrete under chloride attack: State of the art. Cement and Concrete Research, 80, pp.69-85. <https://doi.org/10.1016/j.cemconres.2015.10.006>
43. Bhatti, J., Bhattacharja, S. and Todres, H., 1996. Use of Cement Kiln Dust in Stabilizing Clay Soils. *Research & Development Bull, Portland Cement Association.*,
44. Biava, G., Zacco, A., Zanoletti, A., Sorrentino, G. P., Capone, C., Princigallo, A., Depero, L. E., & Bontempi, E. (2023). Accelerated Direct Carbonation of Steel Slag

- and Cement Kiln Dust: An Industrial Symbiosis Strategy Applied in the Bergamo–Brescia Area. *Materials*, 16(11). <https://doi.org/10.3390/ma16114055>
45. Bilek, V., Bilek, V., Kalina, L., Khestl, F., Palovcik, J., & Simonova, H. (2021). Durability of alkali-Activated concretes containing cement kiln by-pass dust. *IOP Conference Series: Materials Science and Engineering*, 1039(1). <https://doi.org/10.1088/1757-899X/1039/1/012012>
46. Boháč, M., Palou, M., Novotný, R., Másilko, J., Všianský, D., & Staněk, T. (2014). Investigation on early hydration of ternary Portland cement-blast-furnace slag-metakaolin blends. *Construction and Building Materials*, 64, 333–341. <https://doi.org/10.1016/j.conbuildmat.2014.04.018>
47. Bondar, D., Coakley, E., 2014. Use of gypsum and CKD to enhance early age strength of High Volume Fly Ash (HVFA) pastes. *Construction and Building Materials* 71, 93–108. <https://doi.org/10.1016/j.conbuildmat.2014.08.015>
48. Bondar, D., Coakley, E., 2017. Effect of grinding on early age performance of high volume fly ash ternary blended pastes with CKD & OPC. *Construction and Building Materials* 136, 153–163. <https://doi.org/10.1016/j.conbuildmat.2017.01.044>
49. Borek, K., Czapiak, P. and Dachowski, R. (2022) ‘Cement bypass dust as an ecological binder substitute in autoclaved silica–lime products’, *Materials*, 16(1), p. 316. doi:10.3390/ma16010316.
50. Bredy, P., Chabannet, M. and Pera, J. (1988) ‘Microstructure and porosity of Metakaolin blended cements’, *MRS Proceedings*, 137. doi:10.1557/proc-137-431.
51. British Standard 8110: Part 1, Structural use of concrete – code of practice for design and construction, British Standards Institute, London UK, 1985
52. British Standard: EN 15804:2012+A2:2020 – *Sustainability of construction works - Environmental product declarations - Core rules for the product category of construction products*, British Standards Institute, London UK, 2020
53. British Standard: PAS 2050 – Specification for the assessment of the life cycle greenhouse gas emissions of goods and services, British Standards Institute, London UK, 2008
54. British Standards Institution (2000). *BS EN 1097-6:2000: Tests For Mechanical And Physical Properties Of Aggregates. Determination Of Particle Density And Water Absorption*. London: British Standards Institution
55. Brooks, J.J. and Megat Johari, M.A. (2001) ‘Effect of metakaolin on creep and shrinkage of concrete’, *Cement and Concrete Composites*, 23(6), pp. 495–502. doi:10.1016/s0958-9465(00)00095-0.

56. Brown, P.W. and Bothe, J.V. (1993) 'The stability of Ettringite', *Advances in Cement Research*, 5(18), pp. 47–63. doi:10.1680/adcr.1993.5.18.47.
57. BSI (1978) BS EN 4550-3-3.5:1978: Methods of testing cement. Physical tests – Determination of standard consistence. BSI, London, UK.
58. BSI (1999) BS EN 1015-3:1999: Methods of test for mortar for masonry. Determination of consistence of fresh mortar (by flow table). BSI, London, UK.
59. BSI (2000) BS EN 1097-6:2000: Tests For Mechanical And Physical Properties Of Aggregates. Determination Of Particle Density And Water Absorption. BSI, London, UK
60. BSI (2009) BS EN 480-2: Admixtures for concrete, mortar and grout. Test methods. Determination of setting time. BSI, London, UK.
61. BSI (2016) BS EN 998-1:2016: Specification for mortar and masonry – Rendering and plastering mortar. BSI, London, UK.
62. Buchwald, A. and Schulz, M., 2005. Alkali-activated binders by use of industrial by-products. *Cement and Concrete Research*, 35(5), pp.968-973. <https://doi.org/10.1016/j.cemconres.2004.06.019>
63. Bumanis, G. and Vaičiukynienė, D. (2022) 'Alkali activation of milled red brick waste and calcined illite clay with silica gel addition', *Materials*, 15(9), p. 3195. doi:10.3390/ma15093195.
64. Bye, G., Livesey, P. and Struble, L., 2011. *Portland cement*.
65. Cai, G. H., Zhou, Y. F., Li, J. S., Han, L. J., & Poon, C. S. (2022). Deep insight into mechanical behavior and microstructure mechanism of quicklime-activated ground granulated blast-furnace slag pastes. *Cement and Concrete Composites*, 134. p. 104767. doi:10.1016/j.cemconcomp.2022.104767.
66. Cakmak, T., Ustabas, I., Kurt, Z., & Yilmaz, E. (2024). Geopolymer mortars having glassy materials considering mechanical and microstructural features. *Journal of Building Engineering*, 91.
67. *Carbon8* (2023). Available at: <https://www.carbon8.co.uk/> (Accessed: 11 January 2024).
68. *Carboncure's Sustainable Concrete Solution* (2023) *CarbonCure Technologies Inc.* Available at: <https://www.carboncure.com/> (Accessed: 11 January 2024).
69. *Carbstone* (2023) *VITO*. Available at: <https://vito.be/en/carbstone> (Accessed: 11 January 2024).

70. *CCC Insights Briefing 1 the UK climate change act* (2019) *Climate Change Act Committee*. Available at: <https://www.theccc.org.uk/wp-content/uploads/2020/10/CCC-Insights-Briefing-1-The-UK-Climate-Change-Act.pdf> (Accessed: 15 April 2023).
71. *Cement carbon dioxide emissions quietly double in 20 years* (2022) *WTTW News*. Available at: <https://news.wttw.com/2022/06/22/cement-carbon-dioxide-emissions-quietly-double-20-years> (Accessed: 30 January 2023).
72. Cement Kiln Dust Wastes EPA. Available at: <https://archive.epa.gov/epawaste/nonhaz/industrial/special/web/html/index-2.html> (Accessed: 17 February 2022).
73. *Cement technology roadmap plots path to cutting CO₂ emissions 24% by 2050 - news* (2018) *International Energy Agency*. Available at: <https://www.iea.org/news/cement-technology-roadmap-plots-path-to-cutting-co2-emissions-24-by-2050> (Accessed: 09 February 2021).
74. Cement.mineralproducts.org. 2020. *Mineral Products Association (MPA) Cement - Representing The UK Cement Industry*. [online] Available at: https://cement.mineralproducts.org/downloads/industry_statistics.php [Accessed 27 April 2020].
75. Cement-co2-protocol.org. 2020. *Cement CO₂ Protocol*. [online] Available at: <https://cement-co2-protocol.org/en/> [Accessed 27 September 2020].
76. Cement-co2-protocol.org. 2020. *Mass Balance Of A Kiln System*. [online] Available at: https://www.cement-co2-protocol.org/en/Content/Internet_Manual/tasks/mass_balance_of_kiln_system.htm [Accessed 30 August 2021].
77. Chakraborty, S. et al. (2017) 'Effectiveness of sewage sludge ash combined with waste pozzolanic minerals in developing sustainable construction material: An alternative approach for waste management', *Journal of Cleaner Production*, 153, pp. 253–263. doi:10.1016/j.jclepro.2017.03.059.
78. Chakraborty, S., Jo, B.W. and Sikandar, M.A. (2016) 'Hydration mechanism of the hydrogen-rich water based cement paste', *The Journal of Physical Chemistry C*, 120(15), pp. 8198–8209. doi:10.1021/acs.jpcc.6b01444.

79. Chatterjee, A.K. (2018) 'Clinker grinding and cement making', *Cement Production Technology*, pp. 175–212. doi:10.1201/9780203703335-6.
80. Chaunsali, P. and Peethamparan, S. (2011) 'Evolution of strength, microstructure and mineralogical composition of a CKD–GGBFS binder', *Cement and Concrete Research*, 41(2), pp. 197–208. doi:10.1016/j.cemconres.2010.11.010.
81. Chaunsali, P., & Peethamparan, S. (2013a). Influence of the composition of cement kiln dust on its interaction with fly ash and slag. *Cement and Concrete Research*, 54, 106–113. <https://doi.org/10.1016/j.cemconres.2013.09.001>
82. Chaunsali, P., & Peethamparan, S. (2013b). Novel cementitious binder incorporating cement kiln dust: Strength and durability. *ACI Materials Journal*, 110(3), 297–304. doi.org/10.14359/51685663
83. Chen, C., Habert, G., Bouzidi, Y., Jullien, A. and Ventura, A., 2010. LCA allocation procedure used as an incitative method for waste recycling: An application to mineral additions in concrete. *Resources, Conservation and Recycling*, 54(12), pp.1231-1240. <https://doi.org/10.1016/j.resconrec.2010.04.001>
84. Chen, J.J. *et al.* (2020) 'Cement equivalence of Metakaolin for workability, cohesiveness, strength and Sorptivity of concrete', *Materials*, 13(7), p. 1646. doi:10.3390/ma13071646.
85. Choo, H. *et al.* (2016) 'Compressive strength of one-part alkali activated fly ash using red mud as alkali supplier', *Construction and Building Materials*, 125, pp. 21–28. doi:10.1016/j.conbuildmat.2016.08.015.
86. Colangelo, F., Forcina, A., Farina, I. and Petrillo, A., 2018. Life Cycle Assessment (LCA) of Different Kinds of Concrete Containing Waste for Sustainable Construction. *Buildings*, 8(5), p.70. DOI: 10.3390/buildings8050070
87. Collins, R, J., and Emery, J. J. (1983). "Kiln Dust-Fly Ash System for Highway Bases and Subbases," Federal Highway Administration Report FHWA/RD-82/167, U.S Department of Transportation, Washington D.C
88. Committee on Climate Change, Climate Change Act 2008, Clause 27. Available at: <https://www.legislation.gov.uk/ukpga/2008/27/part/1/crossheading/the-target-for-2050>
89. Coppola, L., Coffetti, D., Crotti, E., Candamano, S., Crea, F., Gazzaniga, G., & Pastore, T. (2020). The combined use of admixtures for shrinkage reduction in one-

- part alkali activated slag-based mortars and pastes. *Construction and Building Materials*, 248.
90. Cristelo, N., Fernández-Jiménez, A., Castro, F., Fernandes, L., & Tavares, P. (2019). Sustainable alkaline activation of fly ash, aluminium anodising sludge and glass powder blends with a recycled alkaline cleaning solution. *Construction and Building Materials*, 204, 609–620. <https://doi.org/10.1016/j.conbuildmat.2019.01.226>
91. Cristelo, N., Miranda, T., Oliveira, D., Rosa, I., Soares, E., Coelho, P. and Fernandes, L., 2015. Assessing the production of jet mix columns using alkali activated waste based on mechanical and financial performance and CO₂ (eq) emissions. *Journal of Cleaner Production*, 102, pp.447-460. <https://doi.org/10.1016/j.jclepro.2015.04.102>
92. Cuéllar-Franca, R.M. and Azapagic, A. (2015) ‘Carbon capture, storage and Utilisation Technologies: A critical analysis and comparison of their life cycle environmental impacts’, *Journal of CO₂ Utilization*, 9, pp. 82–102. doi:10.1016/j.jcou.2014.12.001.
93. Czapik, P., Zapała-Sławeta, J., Owskiak, Z., Stępień, P., 2020. Hydration of cement by-pass dust. *Construction and Building Materials* 231. <https://doi.org/10.1016/j.conbuildmat.2019.117139>
94. Dauberschmidt, C., and M. Raupach. 2005. “Passivity and depassivation of steel fibres and cold-drawn steel wires in artificial pore solution and concrete containing chlorides.” In *Proc., EUROCORR 2005*. Brussels, Belgium: European Federation of Corrosion
95. Department of Environment, Food and Rural Affairs, 2015. *Rapid Evidence Assessment: Cement Kiln Dust And By-Pass Dust From Cement Kilns*. Warrington: Amec Foster Wheeler Environment & Infrastructure UK Limited, pp.27-32.
96. *Directive (EU) 2018/851 of the European Parliament and of the Council of 30 May 2018 Amending directive 2008/98/EC on waste (2020) European Environment Agency*. Available at: <https://www.eea.europa.eu/policy-documents/directive-eu-2018-851-of> (Accessed: 05 July 2022)
97. Du, S., Wu, J., AlShareedah, O. and Shi, X., 2019. Nanotechnology in Cement-Based Materials: A Review of Durability, Modeling, and Advanced Characterization. *Nanomaterials*, 9(9), p.1213. <https://doi.org/10.1680/scc.31777.0021>
98. Ecoinvent, 2020. Version 3 Database. <https://www.ecoinvent.org>

99. El-Awney, Saleh & Abd-El-Aziz, Magdy & Heikal, Mohamed & Didamony, H. (2005). Effect of Cement Kiln Dust Substitution on Chemical and Physical Properties and Compressive Strength of Portland and Slag Cements. *Arabian Journal for Science and Engineering*. 30. 263-274.
100. El-Diadamony, H., Amer, A. A., Sokkary, T. M., & El-Hoseny, S. (2018). Hydration and characteristics of metakaolin pozzolanic cement pastes. *HBRC Journal*, 14(2), 150–158. <https://doi.org/10.1016/j.hbrcj.2015.05.005>
101. El-Hassan, H. (2021) ‘Accelerated carbonation curing as a means of reducing carbon dioxide emissions’, *Cement Industry - Optimization, Characterization and Sustainable Application* [Preprint]. doi:10.5772/intechopen.93929.
102. El-Hassan, H. and Shao, Y. (2014) ‘Carbon storage through concrete block carbonation’, *Journal of Clean Energy Technologies*, pp. 287–291. doi:10.7763/jocet.2014.v2.141.
103. Elkhadiri, Imad & Elkhadiri, M. & Puertas, F.. (2009). Effect of curing temperature on cement hydration. *Ceramics - Silikaty*. 53. 65-75.
104. El-Mohsen, M.A., Anwar, A.M., Adam, I.A., 2015. Mechanical properties of Self-Consolidating Concrete incorporating Cement Kiln Dust. *HBRC Journal* 11, 1–6. <https://doi.org/10.1016/J.HBRCJ.2014.02.007>
105. ElNaggar, K.A. et al. (2023) ‘Recycling of Bypass Cement Kiln Dust in the production of eco-friendly roof tiles’, *Materials Research Express*, 10(6), p. 065505. doi:10.1088/2053-1591/acddb9.
106. EL-SAYED, H.A. et al. (1991) ‘Re-utilization of by-pass kiln dust in cement manufacture’, *Blended Cements in Construction*, pp. 84–94. doi:10.1201/9781482296631-7.
107. Eštoková, A. and Holosova, M. (2023) ‘Study of pozzolanic activity of selected waste materials’, 4th International Conference on Advances in Environmental Engineering [Preprint]. doi:10.4028/p-vv7w3i.
108. Fernández-Jiménez, A. et al. (2017) ‘Sustainable alkali activated materials: Precursor and activator derived from Industrial Wastes’, *Journal of Cleaner Production*, 162, pp. 1200–1209. doi:10.1016/j.jclepro.2017.06.151.
109. Finance Act 2020, Section 42. Available at: <https://www.legislation.gov.uk/ukpga/2020/14/contents/enacted/data.htm>
110. Font, A., Soriano, L., Moraes, J. C. B., Tashima, M. M., Monzó, J., Borrachero, M. V., & Payá, J. (2017). A 100% waste-based alkali-activated material by using olive-

- stone biomass ash (OBA) and blast furnace slag (BFS). *Materials Letters*, 203, 46–49. <https://doi.org/10.1016/j.matlet.2017.05.129>
111. Frías, M. and Cabrera, J. (2000) ‘Pore size distribution and degree of hydration of metakaolin–cement pastes’, *Cement and Concrete Research*, 30(4), pp. 561–569. doi:10.1016/s0008-8846(00)00203-9.
112. Gabrovšek, Roman & Vuk, Tomaž & Kaučič, Venčeslav. (2006). Evaluation of the Hydration of Portland Cement Containing Various Carbonates by Means of Thermal Analysis. *Acta Chimica Slovenica*. 53.
113. Gallucci, E., Zhang, X. and Scrivener, K.L. (2013) ‘Effect of temperature on the microstructure of calcium silicate hydrate (C-S-H)’, *Cement and Concrete Research*, 53, pp. 185–195. doi:10.1016/j.cemconres.2013.06.008.
114. Gayathri, P. and Rajasekhar, D., 2017. Behaviour of High Strength Concrete Using Cement Kiln Dust and Silica Fume. *IOSR Journal of Mechanical and Civil Engineering*, 14(02), pp.23-26. <https://doi.org/10.9790/1684-1402072326>
115. Ghorab, H.Y. (2004) ‘On the chemistry of delayed ettringite formation’, *International RILEM Workshop on Internal Sulfate Attack and Delayed Ettringite Formation [Preprint]*. doi:10.1617/2912143802.005.
116. Gok, S.G. and Sengul, O. (2021) ‘The use of waste glass as an activator in alkali-activated slag mortars’, *Proceedings of the Institution of Civil Engineers - Engineering Sustainability*, 174(3), pp. 120–130. doi:10.1680/jensu.19.00070.
117. Gołaszewska, M., Giergiczny, Z., 2021. Study of the Properties of Blended Cements Containing Various Types of Slag Cements and Limestone Powder. *Materials (Basel)* 14. <https://doi.org/10.3390/MA14206072>
118. Graeff, A.G. (2011) Long-term performance of recycled steel fibre reinforced concrete for pavement applications. PhD thesis. University of Sheffield.
119. Gu, Y., Omikrine Metalssi, O., Martin, R. P., Fen-Chong, T., & Dangla, P. (2020). Locating ettringite due to DEF at the pore scale of cement paste by heat-based dissolution tests. *Construction and Building Materials*, 258. <https://doi.org/10.1016/j.conbuildmat.2020.120000>
120. Güneysi, E. et al. (2013) ‘Corrosion behavior of reinforcing steel embedded in chloride contaminated concretes with and without metakaolin’, *Composites Part B: Engineering*, 45(1), pp. 1288–1295. doi:10.1016/j.compositesb.2012.09.085.

121. Güneyisi, E., Gesoğlu, M. and Mermerdaş, K. (2007) 'Improving strength, drying shrinkage, and pore structure of concrete using metakaolin', *Materials and Structures*, 41(5), pp. 937–949. doi:10.1617/s11527-007-9296-z.
122. Güneyisi, E., Özturan, T. and Gesoğlu, M. (2005) 'A study on reinforcement corrosion and related properties of plain and blended cement concretes under different curing conditions', *Cement and Concrete Composites*, 27(4), pp. 449–461. doi:10.1016/j.cemconcomp.2004.05.006.
123. Gunning, P.J., Hills, C.D. and Carey, P.J. (2010) 'Accelerated carbonation treatment of industrial wastes', *Waste Management*, 30(6), pp. 1081–1090. doi:10.1016/j.wasman.2010.01.005.
124. Gursel, A.P., Maryman, H. and Ostertag, C. (2016) 'A life-cycle approach to environmental, mechanical, and durability properties of "green" concrete mixes with rice husk ash', *Journal of Cleaner Production*, 112, pp. 823–836. doi:10.1016/j.jclepro.2015.06.029.
125. Habert, G., D'Espinoze De Lacaillerie, J.B., Roussel, N., 2011. An environmental evaluation of geopolymer based concrete production: Reviewing current research trends. *Journal of Cleaner Production* 19, 1229–1238. <https://doi.org/10.1016/j.jclepro.2011.03.012>
126. Habert, G., Miller, S.A., John, V.M., Provis, J.L., Favier, A., Horvath, A., Scrivener, K.L., 2020. Environmental impacts and decarbonization strategies in the cement and concrete industries. *Nature Reviews Earth & Environment* 2020 1:11 1, 559–573. <https://doi.org/10.1038/s43017-020-0093-3>
127. Habert, G., Ouellet-Plamondon, C., 2016. Recent update on the environmental impact of geopolymers. *RILEM Technical Letters* 1, 17–23. <https://doi.org/10.21809/RILEMTECHLETT.2016.6>
128. Hakkomaz, H., Yorulmaz, H., Durak, U., İlkentapar, S., Karahan, O., & Atiş, C. D. (2022). The influence of cement kiln dust on strength and durability properties of cement-based systems. *Environmental Science and Pollution Research*, 29(50), 76166–76175. <https://doi.org/10.1007/s11356-022-21281-z>
129. HAMMAT, S., MENADI, B., KENAI, S., THOMAS, C., KIRGIZ, M. S., & SOUSA GALDINO, A. G. de. (2021). The effect of content and fineness of natural pozzolana on the rheological, mechanical, and durability properties of self-compacting mortar. *Journal of Building Engineering*, 44. <https://doi.org/10.1016/j.jobbe.2021.103276>
130. Hamzaoui, R., Bouchenafa, O., Guessasma, S., Leklou, N., & Bouaziz, A. (2016). The sequel of modified fly ashes using high energy ball milling on mechanical

- performance of substituted past cement. *Materials and Design*, 90, 29–37.
<https://doi.org/10.1016/j.matdes.2015.10.109>
131. Hanein, T., Hayashi, Y., Utton, C., Nyberg, M., Martinez, J.C., Quintero-Mora, N.I., Kinoshita, H., 2020. Pyro processing cement kiln bypass dust: Enhancing clinker phase formation. *Construction and Building Materials* 259.
<https://doi.org/10.1016/j.conbuildmat.2020.120420>
132. Hanifa, M., Agarwal, R., Sharma, U., Thapliyal, P. C., & Singh, L. P. (2023). A review on CO₂ capture and sequestration in the construction industry: Emerging approaches and commercialised technologies. In *Journal of CO₂ Utilization* (Vol. 67). Elsevier Ltd. <https://doi.org/10.1016/j.jcou.2022.102292>
133. Hatfield, A. (2022) *Mineral Commodity Summaries 2022 - cement - USGS publications warehouse*, U.S. Geological Survey. Available at:
<https://pubs.usgs.gov/periodicals/mcs2022/mcs2022-cement.pdf> (Accessed: 12 May 2023).
134. Havlica, J. and Sahu, S. (1992) ‘Mechanism of ettringite and monosulphate formation’, *Cement and Concrete Research*, 22(4), pp. 671–677. doi:10.1016/0008-8846(92)90019-r.
135. Haynes, W.B., and Kramer, G.W. 1982. Characterization of U.S. Cement Kiln Dust, Information Circular #8885, U.S Bureau of Mines, U.S. Department of the Interior
136. He, P., Shi, C., Tu, Z., Poon, C. S., & Zhang, J. (2016). Effect of further water curing on compressive strength and microstructure of CO₂-cured concrete. *Cement and Concrete Composites*, 72, 80–88. <https://doi.org/10.1016/j.cemconcomp.2016.05.026>
137. Heath, A., Paine, K. and McManus, M. (2014) ‘Minimising the global warming potential of clay based geopolymers’, *Journal of Cleaner Production*, 78, pp. 75–83. doi:10.1016/j.jclepro.2014.04.046.
138. Heikal, M., Zaki, M.E.A. and Ibrahim, S.M. (2020) ‘Preparation, physico-mechanical characteristics and durability of eco-alkali-activated binder from blast-furnace slag, cement kiln-by-pass dust and microsilica ternary system’, *Construction and Building Materials*, 260, p. 119947. doi:10.1016/j.conbuildmat.2020.119947.
139. Hewlett, P.C. (2019) *Lea’s chemistry of cement and concrete*. San Diego: Elsevier Science.
140. Hosten, C. and Fidan, B. (2012) ‘An industrial comparative study of cement clinker grinding systems regarding the specific energy consumption and cement properties’, *Powder Technology*, 221, pp. 183–188. doi:10.1016/j.powtec.2011.12.065.

141. Hu, W., Cheng, W. C., Wang, Y., & Wen, S. (2023). Feasibility study of applying a graphene oxide-alginate composite hydrogel to electrokinetic remediation of Cu(II)-contaminated loess as electrodes. *Separation and Purification Technology*, 322.
142. Hu, W., Cheng, W. C., Wen, S., & Kang, N. (2022). Revealing underlying mechanisms affecting electrokinetic remediation of an artificially Cu- and Pb-contaminated loess using the external regulatory system with adsorbent. *Frontiers in Materials*, 9.
143. Huang, H., Wang, T., Kolosz, B., Andresen, J., Garcia, S., Fang, M., & Maroto-Valer, M. M. (2019). Life-cycle assessment of emerging CO₂ mineral carbonation-cured concrete blocks: Comparative analysis of CO₂ reduction potential and optimization of environmental impacts. *Journal of Cleaner Production*, 241. <https://doi.org/10.1016/j.jclepro.2019.118359>
144. Huntzinger, D. N., Gierke, J. S., Kawatra, S. K., Eisele, T. C., & Sutter, L. L. (2009). Carbon dioxide sequestration in cement kiln dust through mineral carbonation. *Environmental Science and Technology*, 43(6), 1986–1992. <https://doi.org/10.1021/es802910z>
145. IEA (2009) *Technology roadmap - low-carbon transition in the cement industry – analysis*, IEA. Available at: <https://www.iea.org/reports/technology-roadmap-low-carbon-transition-in-the-cement-industry> (Accessed: 30 January 2023).
146. Isa, M. N., Pilakoutas, K., Guadagnini, M., & Angelakopoulos, H. (2020). Mechanical performance of affordable and eco-efficient ultra-high performance concrete (UHPC) containing recycled tyre steel fibres. *Construction and Building Materials*, 255. <https://doi.org/10.1016/j.conbuildmat.2020.119272>
147. ISO 14040:2006 (en) – Environmental Management – Life Cycle Assessment – Principles and Framework. International Organization for Standardization, Geneva, Switzerland, 2006
148. Janotka, I. and Krajci, L. (2004) ‘La Efectividad del método de la Resistencia Eléctrica del Acero en la evaluación de la corrosión de armaduras en sistemas cementantes’, *Materiales de Construcción*, 54(274), pp. 17–32. [doi:10.3989/mc.2004.v54.i274.230](https://doi.org/10.3989/mc.2004.v54.i274.230).
149. Jiang, H., Zheng, J., Fu, Y., Wang, Z., Yilmaz, E., & Cui, L. (2024). Slag-based stabilization/solidification of hazardous arsenic-bearing tailings as cemented paste backfill: Strength and arsenic immobilization assessment. *Case Studies in Construction Materials*, 20.

150. Jo, B. wan, Chakraborty, S. and Jo, J.H. (2017) 'Effectiveness of a hydrothermally produced alternative cementitious material on the physical and mechanical performance of concrete', *Journal of Cleaner Production*, 142, pp. 3269–3280. doi:10.1016/j.jclepro.2016.10.142.
151. Justice, J.M. and Kurtis, K.E. (2007) 'Influence of metakaolin surface area on properties of cement-based materials', *Journal of Materials in Civil Engineering*, 19(9), pp. 762–771. doi:10.1061/(asce)0899-1561(2007)19:9(762).
152. Kalina, L., Bílek, V., Kiripolský, T., Novotný, R. and Másilko, J., 2018. Cement Kiln By-Pass Dust: An Effective Alkaline Activator for Pozzolanic Materials. *Materials*, 11(9), p.1770.
153. Kamon, M. and Nontananandh, S., 1991. Combining Industrial Wastes with Lime for Soil Stabilization. *Journal of Geotechnical Engineering*, 117(1), pp.1-17.
154. Kamseu, E., Beleuk à Moungam, L. M., Cannio, M., Billong, N., Chaysuwan, D., Melo, U. C., & Leonelli, C. (2017). Substitution of sodium silicate with rice husk ash-NaOH solution in metakaolin based geopolymer cement concerning reduction in global warming. *Journal of Cleaner Production*, 142, 3050–3060. <https://doi.org/10.1016/j.jclepro.2016.10.164>
155. Kashef-Haghighi, S., Shao, Y. and Ghoshal, S. (2015) 'Mathematical Modeling of CO₂ uptake by concrete during accelerated carbonation curing', *Cement and Concrete Research*, 67, pp. 1–10. doi:10.1016/j.cemconres.2014.07.020.
156. Kassem, N., Ahmed, D. and Kishar, E. (2021) 'Effect of elevated temperatures on the performance of Metakaolin geopolymer pastes incorporated by cement Kiln Dust', *Egyptian Journal of Chemistry*, 0(0), pp. 0–0. doi:10.21608/ejchem.2021.50848.3041.
157. Kazemian, M., & Shafei, B. (2023). Carbon sequestration and storage in concrete: A state-of-the-art review of compositions, methods, and developments. In *Journal of CO₂ Utilization* (Vol. 70). Elsevier Ltd. <https://doi.org/10.1016/j.jcou.2023.102443>
158. Ke, X., Bernal S.A. (2014) 'One-part geopolymers based on thermally treated Red Mud/NaOH blends', *Journal of the American Ceramic Society*, 98(1), pp. 5–11. doi:10.1111/jace.13231.
159. Keleştemur, O. and Demirel, B. (2015) 'Effect of metakaolin on the corrosion resistance of structural lightweight concrete', *Construction and Building Materials*, 81, pp. 172–178. doi:10.1016/j.conbuildmat.2015.02.049.

160. Kessler, G.R. (1995) 'Cement kiln dust (CKD) methods for reduction and control', *IEEE Transactions on Industry Applications*, 31(2), pp. 407–412.
doi:10.1109/28.370292.
161. Khan, S. U., Nuruddin, M. F., Ayub, T., & Shafiq, N. (2014). Effects of different mineral admixtures on the properties of fresh concrete. In *The Scientific World Journal* (Vol. 2014). ScientificWorld Ltd.
162. Kirchofer, A., Becker, A., Brandt, A., Wilcox, J. (2013) 'CO₂ mitigation potential of mineral carbonation with industrial alkalinity sources in the United States', *Environmental Science & Technology*, 47(13), pp. 7548–7554.
doi:10.1021/es4003982.
163. Kolani, B., Buffo-Lacarrière, L., Sellier, A., Escadeillas, G., Boutillon, L. and Linger, L., 2012. Hydration of slag-blended cements. *Cement and Concrete Composites*, 34(9), pp.1009-1018.
164. Konsta-Gdoutos, M.S., Shah, S.P., 2003. Hydration and properties of novel blended cements based on cement kiln dust and blast furnace slag. *Cement and Concrete Research* 33, 1269–1276. [https://doi.org/10.1016/S0008-8846\(03\)00061-9](https://doi.org/10.1016/S0008-8846(03)00061-9)
165. Kounadis, A., Badogiannis, E., Sideris, K., Antiohos, S., & Marinos, I. (2024). Rheology, Mechanical Properties and Shrinkage of Self-Compacting Concrete Containing Cement Kiln and By-Pass Filter Dust. *Sustainability (Switzerland)*, 16(1). <https://doi.org/10.3390/su16010320>
166. Kul, A., Ozel, B. F., Ozcelikci, E., Gunal, M. F., Ulugol, H., Yildirim, G., & Sahmaran, M. (2023). Characterization and life cycle assessment of geopolymer mortars with masonry units and recycled concrete aggregates assorted from construction and demolition waste. *Journal of Building Engineering*, 78. <https://doi.org/10.1016/j.jobe.2023.107546>
167. Kunal, Siddique, R., Rajor, A., 2012. Use of cement kiln dust in cement concrete and its leachate characteristics. *Resources, Conservation Recycling*, 61, pp.59-68.
<https://doi.org/10.1016/j.resconrec.2012.01.006>
168. Kurdowski, W. and Thiel, A. (1981) 'On the role of free calcium oxide in expansive cements', *Cement and Concrete Research*, 11(1), pp. 29–40. doi:10.1016/0008-8846(81)90006-5.
169. Lannegrand, R., Ramos, G. and Talero, R. (2001) 'Estado del Conocimiento sobre la sal de friedel', *Materiales de Construcción*, 51(262), pp. 63–71.
doi:10.3989/mc.2001.v51.i262.372.

170. Lanzerstorfer, C., 2016. Residue from the chloride bypass de-dusting of cement kilns: Reduction of the chloride content by air classification for improved utilisation. *Process Safety and Environmental Protection*, 104, pp.444-450.
<https://doi.org/10.1016/j.psep.2016.06.010>
171. Lee, M.H., Lee, J.C., 2009. Study on the cause of pop-out defects on the concrete wall and repair method. *Construction and Building Materials* 23, 482–490.
<https://doi.org/10.1016/J.CONBUILDMAT.2007.10.017>
172. *Lex - 02008L0098-20180705 - en - EUR-Lex* (2022) *EUR*. Available at: <https://eur-lex.europa.eu/legal-content/EN/TXT/?uri=CELEX%3A02008L0098-20180705> (Accessed: 24 October 2021).
173. Li, J., Cao, S., & Yilmaz, E. (2022). Characterization of macro mechanical properties and microstructures of cement-based composites prepared from fly ash, gypsum and steel slag. *Minerals*, 12(1). <https://doi.org/10.3390/min12010006>
174. Li, P., Tang, J., Bai, Y., Chen, X., Chen, J., 2046. Experimental study on the pH for activating ground granulated blast-furnace slag activity at different temperatures.
<https://doi.org/10.1007/s12046-019-1204-zS>
175. Li, P., Tang, J., Chen, X., Bai, Y. and Li, Q., 2019. Effect of Temperature and pH on Early Hydration Rate and Apparent Activation Energy of Alkali-Activated Slag. *Advances in Materials Science and Engineering*, 2019, pp.1-13.
DOI:10.1155/2019/3531543
176. Li, Z., He, Z. and Chen, X. (2019) ‘The performance of carbonation-cured concrete’, *Materials*, 12(22), p. 3729. doi:10.3390/ma12223729.
177. Lin, W.Y., Prabhakar, A.K., Mohan, B.C., Wang, C.H., 2020. A factorial experimental analysis of using wood fly ash as an alkaline activator along with coal fly ash for production of geopolymer-cementitious hybrids. *Science of The Total Environment* 718, 135289. <https://doi.org/10.1016/J.SCITOTENV.2019.135289>
178. Liu, C., Yang, L., Li, Z., Nie, S., Hu, C., Wang, F., 2022. Improve the long-term property of heat-cured mortars blended with fly ash by internal curing. *Journal of Building Engineering* 54, 104624. <https://doi.org/10.1016/j.jobe.2022.104624>
179. López-Ausín, V., Revilla-Cuesta, V., Skaf, M., & Ortega-López, V. (2024). Mechanical properties of sustainable concrete containing powdery ladle furnace slag from different sources. *Powder Technology*, 434.
<https://doi.org/10.1016/j.powtec.2024.119396>

180. Lothenbach, B., Scrivener, K. and Hooton, R.D. (2011) 'Supplementary cementitious materials', *Cement and Concrete Research*, 41(12), pp. 1244–1256.
doi:10.1016/j.cemconres.2010.12.001.
181. Lutyński, M. and Pierzyna, P. (2017) 'Reuse of cement kiln dust for backfilling and co2 carbonation', *E3S Web of Conferences*, 18, p. 01014.
doi:10.1051/e3sconf/201712301014.
182. Luukkonen, T., Abdollahnejad, Z., Yliniemi, J., Kinnunen, P., Illikainen, M., 2018. One-part alkali-activated materials: A review. *Cement and Concrete Research*.
<https://doi.org/10.1016/j.cemconres.2017.10.001>
183. Lyu, Q., Chen, A. and Dai, P. (2023) 'Corrosion of ordinary Portland cement and Metakaolin-based geopolymer immersed in nitric acid solution', *Advances in Cement Research*, 35(6), pp. 276–286. doi:10.1680/jadcr.22.00108.
184. Ma, C., Zhao, B., Guo, S. (2019) 'Properties and characterization of green one-part geopolymer activated by composite activators', *Journal of Cleaner Production*, 220, pp. 188–199. doi:10.1016/j.jclepro.2019.02.159.
185. Madadi, A. and Wei, J. (2022) 'Characterization of calcium silicate hydrate gels with different calcium to silica ratios and polymer modifications', *Gels*, 8(2), p. 75.
doi:10.3390/gels8020075.
186. Mahoutian, M. and Shao, Y. (2016) 'Production of cement-free construction blocks from industry wastes', *Journal of Cleaner Production*, 137, pp. 1339–1346.
doi:10.1016/j.jclepro.2016.08.012.
187. Mangat, P. and Gurusamy, K., 1988. Corrosion resistance of steel fibres in concrete under marine exposure. *Cement and Concrete Research*, 18(1), pp.44-54.
188. Marku, J., Dumi, I., & Liço, E. (2013). The characterization and the utilization of cement kiln dust (CKD) as partial replacement of portland cement in mortar and concrete production. UDC:666.971.3.4.052
189. Maruyama, I., Sugimoto, H., Umeki, S., Kurihara, R. (2022) 'Effect of fineness of cement on drying shrinkage', *Cement and Concrete Research*, 161, p. 106961.
doi:10.1016/j.cemconres.2022.106961.
190. Maslehuddin, M., Al-Amoudi, O. S. B., Rahman, M. K., Ali, M. R., & Barry, M. S. (2009). Properties of cement kiln dust concrete. *Construction and Building Materials*, 23(6), 2357–2361. <https://doi.org/10.1016/j.conbuildmat.2008.11.002>
191. Maslehuddin, M., Al-Amoudi, O.S.B., Shameem, M., Rehman, M.K., Ibrahim, M., 2008. Usage of cement kiln dust in cement products - Research review and

- preliminary investigations. *Construction and Building Materials* 22, 2369–2375.
<https://doi.org/10.1016/j.conbuildmat.2007.09.005>
192. Matschei, T., Lothenbach, B. and Glasser, F.P. (2007) ‘The role of calcium carbonate in cement hydration’, *Cement and Concrete Research*, 37(4), pp. 551–558.
doi:10.1016/j.cemconres.2006.10.013.
193. McCoy, W. and Kriner, R., 1971. Use of Waste Kiln Dust for Soil Consolidation. *Lehigh Portland Cement Co.*,
194. McLellan, B. C., Williams, R. P., Lay, J., Van Riessen, A., & Corder, G. D. (2011). Costs and carbon emissions for geopolymers in comparison to ordinary portland cement. *Journal of Cleaner Production*, 19(9–10), 1080–1090.
<https://doi.org/10.1016/j.jclepro.2011.02.010>
195. Mejdoub, R., Hammi, H., Khitouni, M., Suñol, J. J., & M’nif, A. (2017a). The effect of prolonged mechanical activation duration on the reactivity of Portland cement: Effect of particle size and crystallinity changes. *Construction and Building Materials*, 152, 1041–1050. <https://doi.org/10.1016/j.conbuildmat.2017.07.008>
196. Mejdoub, R., Hammi, H., Khitouni, M., Suñol, J. J., & M’nif, A. (2017b). The effect of prolonged mechanical activation duration on the reactivity of Portland cement: Effect of particle size and crystallinity changes. *Construction and Building Materials*, 152, 1041–1050. <https://doi.org/10.1016/j.conbuildmat.2017.07.008>
197. Mellado, A. Catalan, C., Bouzon, N., Borrachero, M., Monzo, J., Paya, J. (2014) ‘Carbon footprint of Geopolymeric Mortar: Study of the contribution of the alkaline activating solution and assessment of an alternative route’, *RSC Adv.*, 4(45), pp. 23846–23852. doi:10.1039/c4ra03375b.
198. Mi, T. Liu, W. (2023) ‘The effect of carbonation on chloride redistribution and Corrosion of Steel Reinforcement’, *Construction and Building Materials*, 363, p. 129641. doi:10.1016/j.conbuildmat.2022.129641.
199. Min, D. and Mingshu, T., 1994. Formation and expansion of ettringite crystals. *Cement and Concrete Research*, 24(1), pp.119-126.
[https://doi.org/10.1016/0008-8846\(94\)90092-2](https://doi.org/10.1016/0008-8846(94)90092-2)
200. Mohamed, A.-M.O. (2023) ‘Carbonation of Cement Kiln Dust’, *Sustainable Utilization of Carbon Dioxide in Waste Management*, pp. 529–575.
doi:10.1016/b978-0-12-823418-1.00005-6.
201. Mohd Basri, M.S. Mustapha, F., Mazlan, N., Ishak, M. (2021) ‘Rice husk ash-based geopolymer binder: Compressive Strength, optimize composition, FTIR spectroscopy, microstructural, and potential as fire-retardant material’, *Polymers*, 13(24), p. 4373.
doi:10.3390/polym13244373.

202. Mollah, M. Y. A.; Lu, F.; Schennach, R.; Cocke, D. L.; Yousuf, M. An X-ray diffraction, fourier-transform infrared spectroscopy, and scanning electron microscopy/ energy-dispersive spectroscopic investigation of the effect of sodium lignosulfonate superplasticizer on the hydration of portland cement type V. *Polym.-Plast. Technol. Eng.* 1999, 38, 849–868. <https://doi.org/10.1080/03602559909351619>
203. Moon, H., Ramanathan, S., Suraneni, P., Shon, C.S., Lee, C.J., Chung, C.W., 2018. Revisiting the Effect of Slag in Reducing Heat of Hydration in Concrete in Comparison to Other Supplementary Cementitious Materials. *Materials* 2018, Vol. 11, Page 1847 11, 1847. <https://doi.org/10.3390/MA11101847>
204. Morsy, S.M. (2005) ‘Effect of Hydration Kinetics and Stability of Hydration Phases of Metakaolin-Lime Sludge-Silica Fume System’, *Ceramics* 49 (4) 225-229 (2005)
205. Moser, R. D., Jayapalan, A. R., Garas, V. Y., & Kurtis, K. E. (2010). Assessment of binary and ternary blends of metakaolin and Class C fly ash for alkali-silica reaction mitigation in concrete. *Cement and Concrete Research*, 40(12), 1664–1672. <https://doi.org/10.1016/j.cemconres.2010.08.006>
206. Mucsi, G., Rácz, Á. and Má dai, V. (2013) ‘Mechanical activation of cement in stirred media mill’, *Powder Technology*, 235, pp. 163–172. doi:10.1016/j.powtec.2012.10.005.
207. Muhammed, H.S., Ali, L.M. and Saeed, A.H. (2021) ‘Use of treated cement kiln dust as a nano material partially replaced in cement mortars’, *Journal of Physics: Conference Series*, 1973(1), p. 012016. doi:10.1088/1742-6596/1973/1/012016.
208. Nagataki, S. and Gomi, H., 1998. Expansive admixtures (mainly ettringite). *Cement and Concrete Composites*, 20(2-3), pp.163-170.
209. Nedunuri, S., Sertse, S. and Muhammad, S., 2020. Microstructural study of Portland cement partially replaced with fly ash, ground granulated blast furnace slag and silica fume as determined by pozzolanic activity. *Construction and Building Materials*, 238, p.117561.
210. Nematollahi, B., Sanjayan, J., Qiu, J., & Yang, E. H. (2017). Micromechanics-based investigation of a sustainable ambient temperature cured one-part strain hardening geopolymer composite. *Construction and Building Materials*, 131, 552–563. <https://doi.org/10.1016/j.conbuildmat.2016.11.117>
211. Neville, A., 2012. *Properties of concrete*. Harlow: Pearson Education.
212. Nikravan, M., Firdous, R. and Stephan, D. (2023) ‘Life cycle assessment of alkali-activated materials: A systematic literature review’, *Low-carbon Materials and Green Construction*, 1(1). doi:10.1007/s44242-023-00014-6.

213. Normann, F., Gardarsdottir, S.O. and Johnsson, F. (2019) ‘Techno-Economics of CO₂ Capture in industrialized regions with carbon-neutral heat and power generation– a case study of Sweden’, SSRN Electronic Journal [Preprint].
doi:10.2139/ssrn.3366073.
214. Nottidge, D.O., Balogun, R.B. and Njoku, N.R. (2009) ‘Effect of rice-husk ash on exchange acidity, growth and yield of groundnut in an acid ULTISOL.’, *Global Journal of Agricultural Sciences*, 8(1). doi:10.4314/gjass.v8i1.48514.
215. Oderji, S., Chen, B., Shakya, C., Ahmad, M. and Shah, S., 2019. Influence of superplasticizers and retarders on the workability and strength of one-part alkali-activated fly ash/slag binders cured at room temperature. *Construction and Building Materials*, 229, p.116891.
216. Olivier, J.G.J., Schure, K.M. and Peters, J.A.H.W. (2017) TRENDS IN GLOBAL CO₂ AND TOTAL GREENHOUSE GAS EMISSIONS. rep. Netherlands: PBL Publisher. Available at: https://www.pbl.nl/sites/default/files/downloads/pbl-2017-trends-in-global-co2-and-total-greenhouse-gas-emissions-2017-report_2674.pdf.
217. Oriola, F.O.P., Moses, G. and Afolayan, J.O. (2015) ‘EFFECTS OF COMBINING METAKAOLIN AND CEMENT KILN DUST AS CEMENT REPLACEMENT MATERIAL IN CONCRETE’, *Academy Journal of Science and Engineering* [Preprint].
218. Ouellet-Plamondon, C. and Habert, G. (2015) ‘Life cycle assessment (LCA) of alkali-activated cements and concretes’, *Handbook of Alkali-Activated Cements, Mortars and Concretes*, pp. 663–686. doi:10.1533/9781782422884.5.663.
219. Outer products form in the. (n.d.).
220. Özkan, I., & Yayla, Z. (2016). Evaluation of correlation between physical properties and ultrasonic pulse velocity of fired clay samples. *Ultrasonics*, 66, 4–10.
221. Peethamparan, S. and Olek, J., 2009. Closure to “Study of the Effectiveness of Cement Kiln Dusts in Stabilizing Na-Montmorillonite Clay” by Sulapha Peethamparan and Jan Olek. *Journal of Materials in Civil Engineering*, 21(11), pp.707-708.
222. Ping, Y., Kirkpatrick, R.J., Brent, P., McMillan, P.F., Cong, X., 1999. Structure of Calcium Silicate Hydrate (C-S-H): Near-, Mid-, and Far-Infrared Spectroscopy.

- Journal of the American Ceramic Society 82, 742–748.
<https://doi.org/10.1111/J.1151-2916.1999.TB01826.X>
223. Poon, C.-S., Lam, L., Kou, S. C., Wong, Y.-L., & Wong, R. (n.d.). Rate of pozzolanic reaction of metakaolin in high-performance cement pastes.
224. Provis, J. and van Deventer, J., 2016. *Alkali Activated Materials*. 1st ed. Melbourne, Australia: Springer.
225. Rabie, M., Irshidat, M.R. and Al-Nuaimi, N. (2022) ‘Ambient and heat-cured geopolymer composites: Mix Design Optimization and Life Cycle Assessment’, *Sustainability*, 14(9), p. 4942. doi:10.3390/su14094942.
226. Raupach, Michael & Dauberschmidt, Christoph & Eichler, Thorsten. (2004). Corrosion Behaviour of Steel Fibres in Concrete Containing Chlorides. EUROCORR 2004 - European Corrosion Conference: Long Term Prediction and Modelling of Corrosion.
227. Revilla-Cuesta, V., Serrano-López, R., Espinosa, A. B., Ortega-López, V., & Skaf, M. (2023). Analyzing the Relationship between Compressive Strength and Modulus of Elasticity in Concrete with Ladle Furnace Slag. *Buildings*, 13(12).
<https://doi.org/10.3390/buildings13123100>
228. Ritchie, I. and Bing-An, X., 1990. The kinetics of lime slaking. *Hydrometallurgy*, 23(2-3), pp.377-396.
229. Robayo-Salazar, R., Mejía-Arcila, J., Mejía de Gutiérrez, R. and Martínez, E., 2018. Life cycle assessment (LCA) of an alkali-activated binary concrete based on natural volcanic pozzolan: A comparative analysis to OPC concrete. *Construction and Building Materials*, 176, pp.103-111.
230. Rostami, V., Shao, Y. and Boyd, A.J. (2012) ‘Carbonation curing versus steam curing for precast concrete production’, *Journal of Materials in Civil Engineering*, 24(9), pp. 1221–1229. doi:10.1061/(asce)mt.1943-5533.0000462.
231. Rungchet, A., Chindaprasirt, P., Wansom, S. and Pimraksa, K., 2016. Hydrothermal synthesis of calcium sulfoaluminate–belite cement from industrial waste materials. *Journal of Cleaner Production*, 115, pp.273-283.
232. Sabir, B.B., Wild, S. and Bai, J. (2001) ‘Metakaolin and calcined clays as pozzolans for concrete: A Review’, *Cement and Concrete Composites*, 23(6), pp. 441–454. doi:10.1016/s0958-9465(00)00092-5.

233. Sadique, M. and Coakley, E. (2016) 'The influence of physico-chemical properties of fly ash and CKD on strength generation of high-volume fly Ash Concrete', *Advances in Cement Research*, 28(9), pp. 595–605. doi:10.1680/jadcr.15.00103.
234. Sagoe-Crentsil, K., Brown, T. and Taylor, A. (2013) 'Drying shrinkage and creep performance of Geopolymer Concrete', *Journal of Sustainable Cement-Based Materials*, 2(1), pp. 35–42. doi:10.1080/21650373.2013.764963.
235. Scholtzová, E., Kucková, L., Kožíšek, J., & Tunega, D. (2015). Structural and spectroscopic characterization of ettringite mineral -combined DFT and experimental study. *Journal of Molecular Structure*, 1100, 215–224.
<https://doi.org/10.1016/j.molstruc.2015.06.075>
236. Scrivener, K., Martirena, F., Bishnoi, S., & Maity, S. (2018). Calcined clay limestone cements (LC3). In *Cement and Concrete Research* (Vol. 114, pp. 49–56). Elsevier Ltd. <https://doi.org/10.1016/j.cemconres.2017.08.017>
237. Senff, L., Labrincha, J. A., Ferreira, V. M., Hotza, D., & Repette, W. L. (2009). Effect of nano-silica on rheology and fresh properties of cement pastes and mortars. *Construction and Building Materials*, 23(7), 2487–2491.
<https://doi.org/10.1016/j.conbuildmat.2009.02.005>
238. Seo, M., Lee, S.Y., Lee, C., Cho, S.S., 2019. Recycling of cement kiln dust as a raw material for cement. *Environments - MDPI* 6.
<https://doi.org/10.3390/environments6100113>
239. Seto, K. C., Davis, S. J., Mitchell, R. B., Stokes, E. C., Unruh, G., & Ürge-Vorsatz, D. (2016). Carbon Lock-In: Types, Causes, and Policy Implications. *Annual Review of Environment and Resources*, 41, 425–452. <https://doi.org/10.1146/annurev-environ-110615-085934>
240. Shao, Y. and Morshed, A.Z. (2013) 'Early carbonation for hollow-core concrete slab curing and carbon dioxide recycling', *Materials and Structures*, 48(1–2), pp. 307–319. doi:10.1617/s11527-013-0185-3.
241. Shao, Y., Mirza, M.S. and Wu, X. (2006) 'CO₂ sequestration using calcium-silicate concrete', *Canadian Journal of Civil Engineering*, 33(6), pp. 776–784.
doi:10.1139/105-105.
242. Sharma, D., Goyal, S., 2018. Accelerated carbonation curing of cement mortars containing cement kiln dust: An effective way of CO₂ sequestration and carbon footprint reduction. *Journal of Cleaner Production* 192, 844–854.
<https://doi.org/10.1016/j.jclepro.2018.05.027>

243. Shi, C., 2001. Studies on Several Factors Affecting Hydration and Properties of Lime-Pozzolan Cements. *Journal of Materials in Civil Engineering*, 13(6), pp.441-445.
244. Shi, C., He, F. and Wu, Y. (2012) 'Effect of pre-conditioning on CO₂ curing of lightweight concrete blocks mixtures', *Construction and Building Materials*, 26(1), pp. 257–267. doi:10.1016/j.conbuildmat.2011.06.020.
245. Shi, T., Gao, Y., Corr, D. J., & Shah, S. P. (2019). FTIR study on early-age hydration of carbon nanotubes-modified cement-based materials. *Advances in Cement Research*, 31(8), 353–361.
246. Shi, Z., Xu, G., Deng, J., Dong, M., Murugadoss, V., Liu, C., Shao, Q., Wu, S., & Guo, Z. (2019). Structural characterization of lignin from *D. sinicus* by FTIR and NMR techniques. In *Green Chemistry Letters and Reviews* (Vol. 12, Issue 3, pp. 235–243). Taylor and Francis Ltd. <https://doi.org/10.1080/17518253.2019.1627428>
247. Shoaib, M., Balaha, M. and Abdel-Rahman, A., 2000. Influence of cement kiln dust substitution on the mechanical properties of concrete. *Cement and Concrete Research*, 30(3), pp.371-377. [https://doi.org/10.1016/S0008-8846\(99\)00262-8](https://doi.org/10.1016/S0008-8846(99)00262-8)
248. Siddique, R. (2009) 'Cement kiln dust', *Waste Materials and By-Products in Concrete*, pp. 351–380. doi:10.1007/978-3-540-74294-4_11.
249. Siddique, R. (2018) 'Chapter 15 - Metakaolin', in *Waste and supplementary cementitious materials in concrete: Characterisation, properties and applications*. Cambridge, MA: Elsevier, pp. 493–511.
250. Siddique, R. and Klaus, J. (2009) 'Influence of metakaolin on the properties of mortar and concrete: A Review', *Applied Clay Science*, 43(3–4), pp. 392–400. doi:10.1016/j.clay.2008.11.007.
251. Siddique, R., 2006. Utilization of cement kiln dust (CKD) in cement mortar and concrete—an overview. *Resources, Conservation and Recycling*, 48(4), pp.315-338.
252. Sinngu, F., Ekolu, A., Naghizadeh, A., Quainoo, H.A. (2023) 'Evaluation of Metakaolin Pozzolan for cement in South Africa', *Developments in the Built Environment*, 14, p. 100154. doi:10.1016/j.dibe.2023.100154.
253. Soutsos, M., Vinai, R. and Rafeet, A., 2019. Alkali-activated concrete for the production of building blocks: research achievements and future challenges. In: *International Conference on Building Materials*. Hanoi.

254. Sreekrishnavilasam, A. and Caterina Santagata, M., 2006. *DEVELOPMENT OF CRITERIA FOR THE UTILIZATION OF CEMENT KILN DUST (CKD) IN HIGHWAY INFRASTRUCTURES*. Indiana: Purdue University.
255. Sreekrishnavilasam, A., King, S., Santagata, M., 2006. Characterization of fresh and landfilled cement kiln dust for reuse in construction applications. *Eng Geol* 85, 165–173. <https://doi.org/10.1016/j.enggeo.2005.09.036>
256. Sri Ravindrarajah, R., 1982. Usage of cement kiln dust in concrete. *International Journal of Cement Composites and Lightweight Concrete* 4, 95–102. [https://doi.org/10.1016/0262-5075\(82\)90013-6](https://doi.org/10.1016/0262-5075(82)90013-6)
257. Stepkowska, E., 2006. Simultaneous IR/TG study of calcium carbonate in two aged cement pastes. *Journal of Thermal Analysis and Calorimetry*, 84(1), pp.175-180. <https://doi.org/10.1007/s10973-005-7179-5>
258. Steuch, H., 1992. Review of Dust Return System. *Portland Cement Association*, (113).
259. Stevulova, N., Strigáč, J., Junak, J., Terpakova, E., & Holub, M. (2021). Incorporation of cement bypass dust in hydraulic road binder. *Materials*, 14(1), 1–16. <https://doi.org/10.3390/ma14010041>
260. Sultan, M.E., Abo-El-Enein, S.A., Sayed, A.Z., EL-Sokkary, T.M., Hammad, H.A., 2018. Incorporation of cement bypass flue dust in fly ash and blast furnace slag-based geopolymer. *Case Studies in Construction Materials* 8, 315–322. <https://doi.org/10.1016/j.cscm.2018.02.009>
261. Tait, M. and Cheung, W., 2016. A comparative cradle-to-gate life cycle assessment of three concrete mix designs. *The International Journal of Life Cycle Assessment*, 21(6), pp.847-860.
262. Tasiopoulou, T. et al. (2023) ‘Production-process simulation and life-cycle assessment of Metakaolin as supplementary cementitious material’, *Eng*, 4(1), pp. 761–779. doi:10.3390/eng4010046.
263. Teixeira, E., Mateus, R., Camões, A., Bragança, L. and Branco, F., 2016. Comparative environmental life-cycle analysis of concretes using biomass and coal fly ashes as partial cement replacement material. *Journal of Cleaner Production*, 112, pp.2221-2230.

264. Tkachenko, N. et al. (2023) 'Global database of cement production assets and upstream suppliers', *Scientific Data*, 10(1). doi:10.1038/s41597-023-02599-w.
265. Todres, H.A., Mishulovich, A., Ahmed, J., 1992. CEMENT KILN DUST MANAGEMENT: PERMEABILITY. RESEARCH AND DEVELOPMENT BULLETIN.
266. Toniolo, N., Rincón, A., Roether, J. A., Ercole, P., Bernardo, E., & Boccaccini, A. R. (2018). Extensive reuse of soda-lime waste glass in fly ash-based geopolymers. *Construction and Building Materials*, 188, 1077–1084. <https://doi.org/10.1016/j.conbuildmat.2018.08.096>
267. Torgal, F., Labrincha, J., Leonelli, C., Palomo Sánchez, A., Chindaprasirt, P., Habert, G. and Ouellet-Plamondon, C., n.d. *Handbook Of Alkali-Activated Cements, Mortars And Concretes*.
268. Torres-Carrasco, M. and Puertas, F. (2017) 'Waste glass as a precursor in alkaline activation: Chemical Process and hydration products', *Construction and Building Materials*, 139, pp. 342–354. doi:10.1016/j.conbuildmat.2017.02.071.
269. Torres-Carrasco, M. et al. (2015) 'Alkali activated slag cements using waste glass as alternative activators. Rheological behaviour', *Boletín de la Sociedad Española de Cerámica y Vidrio*, 54(2), pp. 45–57. doi:10.1016/j.bsecv.2015.03.004.
270. Turk, J., Cotix, Z., Mladenovic, A., Sajna, A. (2015) 'Environmental evaluation of green concretes versus conventional concrete by means of LCA', *Waste Management*, 45, pp. 194–205. doi:10.1016/j.wasman.2015.06.035.
271. Turner, L. and Collins, F., 2013. Carbon dioxide equivalent (CO₂-e) emissions: A comparison between geopolymer and OPC cement concrete. *Construction and Building Materials*, 43, pp.125-130.
272. U.A. Birnin-Yauri, F.P. Glasser, Friedel's salt, Ca₂Al(OH)₆(Cl, OH)·2H₂O: Its solid solutions and their role in chloride binding, *Cem. Concr. Res.* 28 (1998) 1713– 1723
273. Uliasz-Bocheńczyk, A. and Deja, J. (2023) *Potential application of cement kiln dust in carbon capture, utilisation, and Storage Technology* [Preprint]. doi:10.2139/ssrn.4499577.
274. Unluer, C. (2018) 'Carbon dioxide sequestration in magnesium-based binders', *Carbon Dioxide Sequestration in Cementitious Construction Materials*, pp. 129–173. doi:10.1016/b978-0-08-102444-7.00007-1.

275. Unluer, C. and Al-Tabbaa, A. (2013) 'Impact of hydrated magnesium carbonate additives on the carbonation of reactive mgo cements', *Cement and Concrete Research*, 54, pp. 87–97. doi:10.1016/j.cemconres.2013.08.009.
276. Vassilev, S.V. *et al.* (2013) 'An overview of the composition and application of biomass ash. part 1. phase–mineral and chemical composition and classification', *Fuel*, 105, pp. 40–76. doi:10.1016/j.fuel.2012.09.041.
277. von Greve-Dierfeld, S., Lothenbach, B., Vollpracht, A., Wu, B., Huet, B., Andrade, C., Medina, C., Thiel, C., Gruyaert, E., Vanoutrive, H., Saéz del Bosque, I. F., Ignjatovic, I., Elsen, J., Provis, J. L., Scrivener, K., Thienel, K. C., Sideris, K., Zajac, M., Alderete, N., ... De Belie, N. (2020). Understanding the carbonation of concrete with supplementary cementitious materials: a critical review by RILEM TC 281-CCC. *Materials and Structures/Materiaux et Constructions*, 53(6).doi:10.1617/s11527-020-01558-w.
278. W., T.H.F. (1997) *Cement Chemistry*. London: Thomas Telford.
279. Wang, K., Konsta-Gdoutos, M. and Shah, S., 2002. Hydration, Rheology, and Strength of Ordinary Portland Cement (OPC)-Cement Kiln Dust (CKD)-Slag Binders. *ACI Materials Journal*, 99(2). <https://doi.org/10.14359/11710>
280. Wang, K., Mishulovich, ; Alexander, Shah, S.P., n.d. Activations and Properties of Cementitious Materials Made with Cement-Kiln Dust and Class F Fly Ash. *Journal of Materials in Civil Engineering*, 19(1), pp.112-119. <https://doi.org/10.1061/ASCE0899-1561200719:1112>
281. Wang, X., Xu, J., Wang, Z., & Yao, W. (2022). Use of recycled concrete aggregates as carriers for self-healing of concrete cracks by bacteria with high urease activity. *Construction and Building Materials*, 337. <https://doi.org/10.1016/j.conbuildmat.2022.127581>
282. Way, S.J. and Shayan, A. (1993) 'Synthesis and characterisation of crystalline analogues of alkali-aggregate reaction products', *Cement and Concrete Research*, 23(2), pp. 471–479. doi:10.1016/0008-8846(93)90112-m.
283. Wedding, P., Daugherty, K., Funnell, J., 1983. The Incorporation of Low Levels of By-Products in Portland Cement and the Effects on Cement Quality. *Cement, Concrete and Aggregates* 5, 14–20. <https://doi.org/10.1520/CCA10245J>
284. Weil, M., Dombrowski, K. and Buchwald, A. (2009) 'Life-cycle analysis of geopolymers', *Geopolymers*, pp. 194–210. doi:10.1533/9781845696382.2.194.

285. Weil, M., Jeske, U. and Schebek, L., 2006. Closed-loop recycling of construction and demolition waste in Germany in view of stricter environmental threshold values. *Waste Management & Research*, 24(3), pp.197-206.
286. Whiteley et al. 2015 – Whiteley, B., Sheen, T. and Marsland, T. 2015. Cement Kiln Dust and By-Pass Dust from Cement Kilns. April 2015, Amec Foster Wheeler Environment & Infrastructure UK Limited. [Online] randd.defra.gov.uk/Document.aspx?Document=14051_36656FinalReport15150i3.pdf
287. Wild, S. and Khatib, J.M. (1997b) ‘Portlandite consumption in metakaolin cement pastes and mortars’, *Cement and Concrete Research*, 27(1), pp. 137–146. doi:10.1016/s0008-8846(96)00187-1.
288. Wild, S., Khatib, J.M. and Roose, L.J. (1998) ‘Chemical shrinkage and autogenous shrinkage of Portland Cement—metakaolin pastes’, *Advances in Cement Research*, 10(3), pp. 109–119. doi:10.1680/adcr.1998.10.3.109.
289. Wojtacha-Rychter, K., Król, M., Gołaszewska, M., Całus-Moszek, J., Magdziarczyk, M., & Smoliński, A. (2022). Dust from chlorine bypass installation as cementitious materials replacement in concrete making. *Journal of Building Engineering*, 51.
290. World Business Council for Sustainable Development, 2009. *Recycling Concrete*. The Cement Sustainability Initiative. p.3.
291. Xi, F., Davis, S. J., Ciais, P., Crawford-Brown, D., Guan, D., Pade, C., Shi, T., Syddall, M., Lv, J., Ji, L., Bing, L., Wang, J., Wei, W., Yang, K. H., Lagerblad, B., Galan, I., Andrade, C., Zhang, Y., & Liu, Z. (2016). Substantial global carbon uptake by cement carbonation. *Nature Geoscience*, 9(12), 880–883. <https://doi.org/10.1038/ngeo2840>
292. Xu, H., Zhao, Y., Vogel, S. C., Daemen, L. L., & Hickmott, D. D. (2007). Anisotropic thermal expansion and hydrogen bonding behavior of portlandite: A high-temperature neutron diffraction study. *Journal of Solid State Chemistry*, 180(4), 1519–1525. <https://doi.org/10.1016/j.jssc.2007.03.004>
293. Xuan, D., Zhan, B. and Poon, C.S. (2016) ‘Development of a new generation of eco-friendly concrete blocks by accelerated mineral carbonation’, *Journal of Cleaner Production*, 133, pp. 1235–1241. doi:10.1016/j.jclepro.2016.06.
294. Yan, Y., Ma, B., Miron, G. D., Kulik, D. A., Scrivener, K., & Lothenbach, B. (2022). Al uptake in calcium silicate hydrate and the effect of alkali hydroxide. *Cement and Concrete Research*, 162. <https://doi.org/10.1016/j.cemconres.2022.106957>

295. Yang, K.-H., Song, J.-K. and Song, K.-I. (2013) 'Assessment of CO₂ reduction of alkali-activated concrete', *Journal of Cleaner Production*, 39, pp. 265–272. doi:10.1016/j.jclepro.2012.08.001.
296. Yu, P., Kirkpatrick, J., Poe, B., McMillan, P., Cong, X. (1999) 'Structure of calcium silicate hydrate (c-s-h): Near-, mid-, and far-infrared spectroscopy', *Journal of the American Ceramic Society*, 82(3), pp. 742–748. doi:10.1111/j.1151-2916.1999.tb01826.x.
297. Yun, C. M., Rahman, M. R., Phing, C. Y. W., Chie, A. W. M., & Bakri, M. K. Bin. (2020). The curing times effect on the strength of ground granulated blast furnace slag (GGBFS) mortar. *Construction and Building Materials*, 260. <https://doi.org/10.1016/j.conbuildmat.2020.120622>
298. Zapala-Slaweta, J. (2017) 'Alkali silica reaction in the presence of Metakaolin - the significant role of calcium hydroxide', *IOP Conference Series: Materials Science and Engineering*, 245, p. 022020. doi:10.1088/1757-899x/245/2/022020
299. Zhang, D. and Shao, Y. (2016) 'Early age carbonation curing for precast reinforced concretes', *Construction and Building Materials*, 113, pp. 134–143. doi:10.1016/j.conbuildmat.2016.03.048.
300. Zhang, D., Ghoulah, Z. and Shao, Y. (2017) 'Review on carbonation curing of cement-based materials', *Journal of CO₂ Utilization*, 21, pp. 119–131. doi:10.1016/j.jcou.2017.07.003.
301. Zhang, L., Zha, X., Ning, J., & Li, W. (2023). Research Status on the Application Technology of Early Age Carbon Dioxide Curing. In *Buildings* (Vol. 13, Issue 4). MDPI. <https://doi.org/10.3390/buildings13040957>
302. Zhang, Q., Feng, P., Shen, X., Lu, J., Ye, S., Wang, H., Ling, T. C., & Ran, Q. (2023). Utilization of solid wastes to sequester carbon dioxide in cement-based materials and methods to improve carbonation degree: A review. In *Journal of CO₂ Utilization* (Vol. 72). Elsevier Ltd. <https://doi.org/10.1016/j.jcou.2023.102502>
303. Zhou, Z., Sofi, M., Lumantarna, E., Nicolas, R. S., Kusuma, G. H., & Mendis, P. (2019). Strength development and thermogravimetric investigation of high-volume fly ash binders. *Materials*, 12(20).
304. Zhu, M., Xie, G., Liu, L., Wang, R., Ruan, S., Yang, P., & Fang, Z. (2023). Strengthening mechanism of granulated blast-furnace slag on the uniaxial compressive strength of modified magnesium slag-based cemented backfilling material. *Process Safety and Environmental Protection*, 174, 722–733. <https://doi.org/10.1016/j.psep.2023.04.031>

Appendix

Appendix A: Chapter 3 Data

Below is a series of relevant raw data for the first paper from this research.

A.1 Sample Images



Figure A.1-1 - Top-down KGH cubes

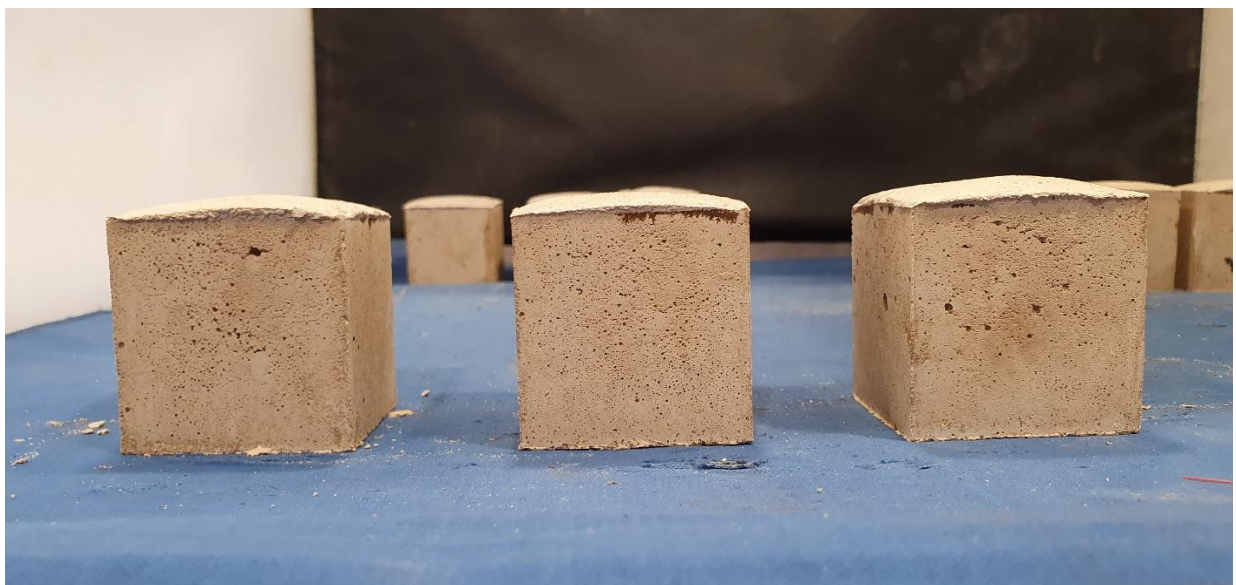


Figure A.1-2 - Side profile KGH cubes



Figure A.1-3 - Top-down KGA cubes



Figure A.1-4 - Side profile KGA cubes



Figure A.1-5 - Top-down KGCH cubes



Figure A.1-6 - Side profile KGCH cubes



Figure A.1-7 - Top-down KGCA cubes



Figure A.1-8 - Side profile KGCA cubes

A2. Flow Results

A.3 Compressive Strength and Density

Table A.3-0-1 - KGA strength and density results

	Dry (g)	Submerged (g)	Density (g/cm ³)	Load (N)	Strength (MPa)
KGA 1	247.03	118.39	1.92	3013	1.21
KGA 2	246.44	117.86	1.92	2920	1.17
KGA 3	250.07	119.83	1.92	2805	1.12
AVERAGE	247.85	118.69	1.92	2912.67	1.17
STDEV	1.02	0.61	0	85.07	0.03
KGA 4	246.61	119.1	1.93	12183	4.87
KGA 5	244.14	117.66	1.93	11425	4.57
KGA 6	245.72	118.06	1.92	11557	4.62
AVERAGE	245.49	118.27	1.93	11721.67	4.69
STDEV	1.59	0.83	0	330.63	0.13
KGA 7	246.40	118.23	1.92	18980.31	7.59
KGA 8	244.78	119.21	1.95	17463.78	6.99
KGA 9	250.66	120.81	1.93	19406.51	7.76
AVERAGE	247.28	119.41	1.93	18616.87	7.45
STDEV	2.48	1.60	0.01	833.71	0.33

Table A.3-0-2 - KGH strength and density results

	Dry (g)	Submerged (g)	Density (g/cm ³)	Load (N)	Strength (MPa)
KGH 1	249.95	115.69	1.86	9767.00	3.91
KGH 2	249.34	115.43	1.86	9289.00	3.72
KGH 3	248.83	115.08	1.86	9274.00	3.71
AVERAGE	249.37	115.40	1.86	9443.33	3.78
STDEV	0.46	0.25	0.00	228.95	0.09
KGH 4	250.18	116.14	1.87	11435.00	4.57
KGH 5	249.24	115.17	1.86	11495.00	4.60
KGH 6	248.36	115.15	1.86	12093.00	4.84
AVERAGE	249.26	115.49	1.86	11674.33	4.67
STDEV	0.74	0.46	0.00	297.05	0.12
KGH 7	251.89	116.91	1.87	16279.98	6.51
KGH 8	251.99	116.77	1.86	16554.74	6.62
KGH 9	252.26	117.21	1.87	16745.33	6.70
AVERAGE	252.05	116.96	1.87	16526.68	6.61
STDEV	0.16	0.18	0.00	191.01	0.08

Table A.3-0-3 - KGCA strength and density results

	Dry (g)	Submerged (g)	Density (g/cm ³)	Load (N)	Strength (MPa)
KGCA 1	241.79	118.22	1.96	4701	1.88
KGCA 2	243.39	119.44	1.96	4699	1.88
KGCA 3	246.36	120.65	1.96	4785	1.91
AVERAGE	243.85	119.44	1.96	4728.33	1.89
STDEV	1.89	0.99	0.00	40.08	0.02
KGCA 4	247.03	120.92	1.96	14699	5.88
KGCA 5	248.21	121.33	1.96	14801	5.92
KGCA 6	247.03	121.08	1.96	14953	5.98
AVERAGE	247.42	121.11	1.96	14817.67	5.93
STDEV	0.56	0.17	0.00	104.36	0.04
KGCA 7	249.7	122.47	1.96	22423	8.97
KGCA 8	249.26	122.4	1.96	22511	9.00
KGCA 9	248.72	121.95	1.96	22391	8.96
AVERAGE	249.23	122.27	1.96	22441.67	8.98
STDEV	0.40	0.23	0.00	50.74	0.02

Table A.3-0-4 - KGCH strength and density results

	Dry (g)	Submerged (g)	Density (g/cm ³)	Load (N)	Strength (MPa)
KGCH 1	251.59	119.49	1.90	11500	4.60
KGCH 2	255.74	121.5	1.91	11456	4.58
KGCH 3	249.8	118.68	1.91	11854	4.74
AVERAGE	252.38	119.89	1.90	11603.33	4.64
STDEV	2.49	1.19	0.00	178.16	0.07
KGCH 4	249.55	118.58	1.91	13511	5.40
KGCH 5	252.74	120.69	1.91	13587	5.43
KGCH 6	251.2	119.5	1.91	13201	5.28
AVERAGE	251.16	119.59	1.91	13433.00	5.37
STDEV	1.30	0.86	0.00	166.96	0.07
KGCH 7	252.79	121.11	1.92	18405	7.36
KGCH 8	253.34	123.3	1.95	18884	7.55
KGCH 9	254.78	122.8	1.93	18907	7.56
AVERAGE	253.64	122.40	1.93	18732.00	7.49
STDEV	0.84	0.94	0.01	231.41	0.09

A.4 Mercury Intrusion Porosimetry

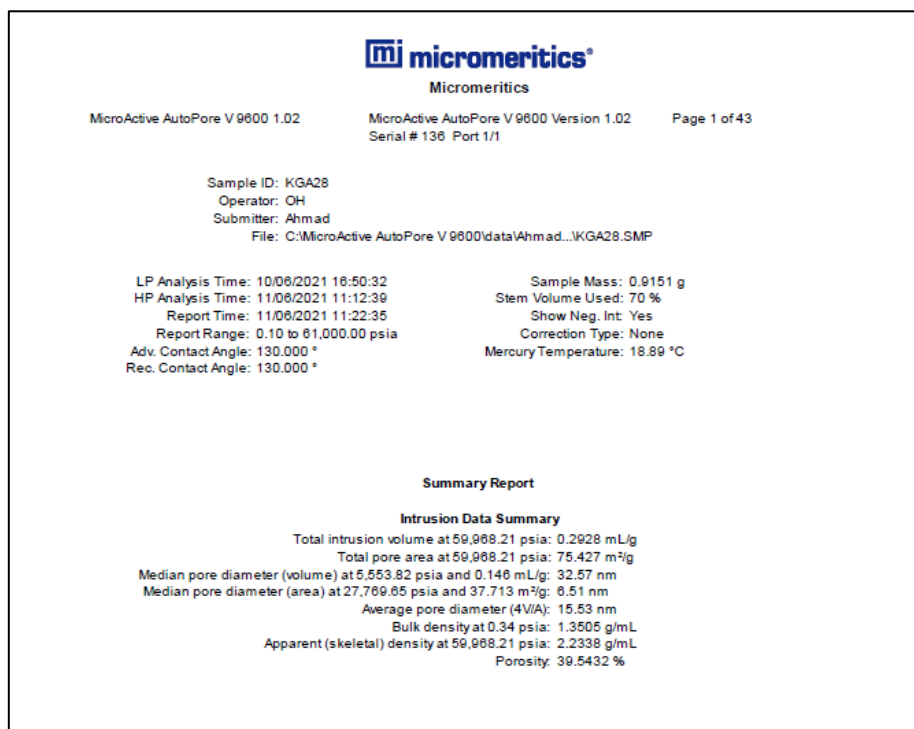


Figure A.4-1 – Porosity of KGA

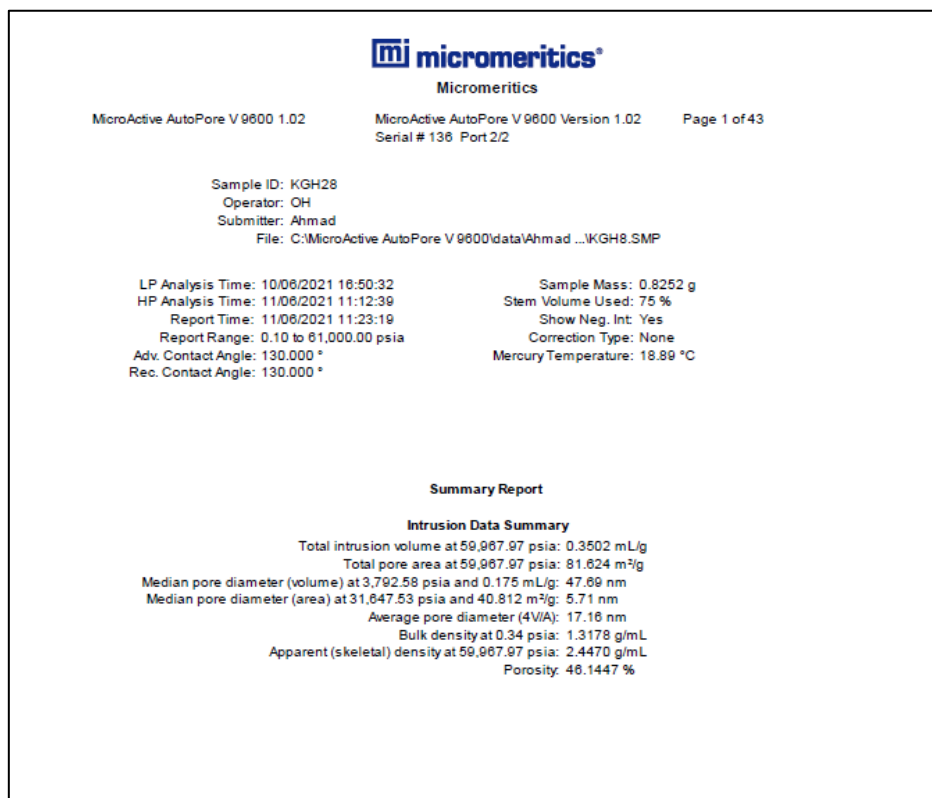


Figure A.4-2 – MIP for KGH

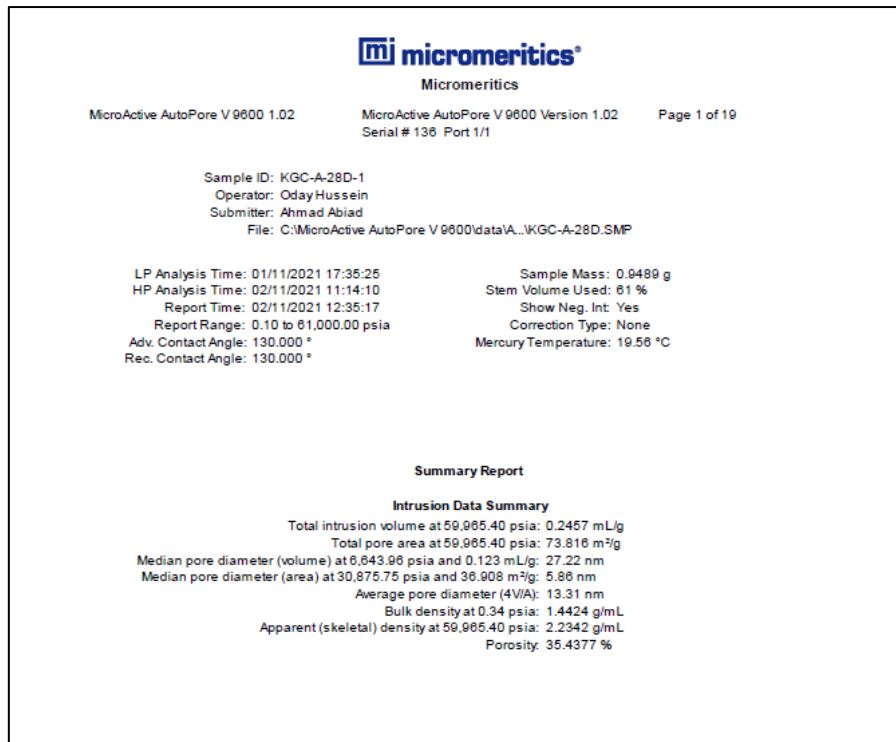


Figure A.4-3 – MIP Results for KGCA

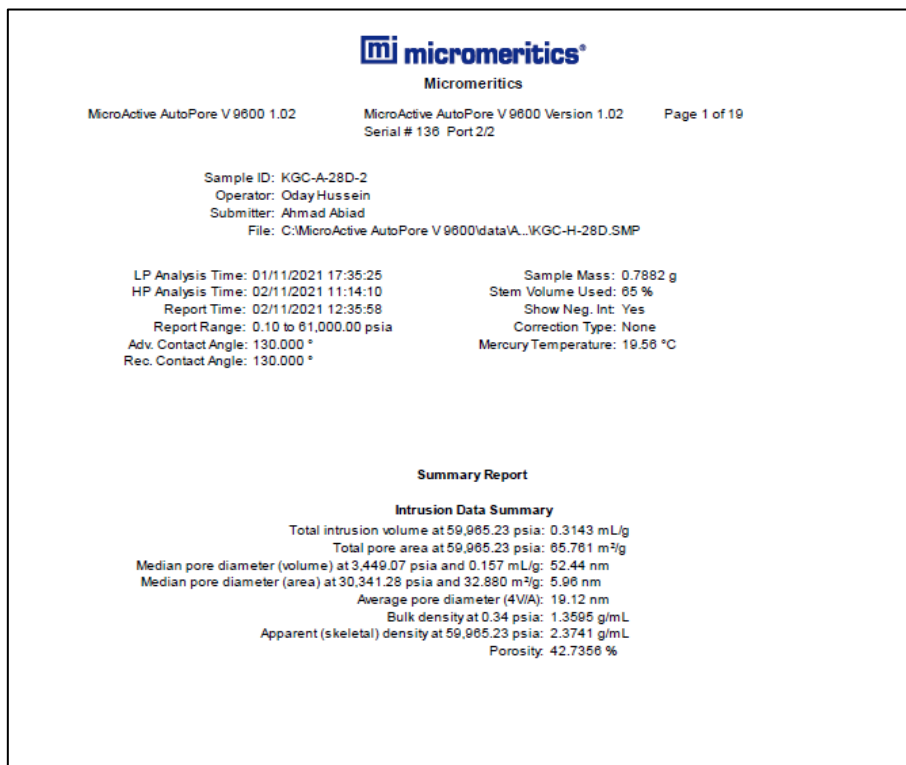


Figure A.4-4 – MIP Results for KGCH

Appendix B: Chapter 4 Data

Below is a series of relevant raw data for the second paper from this research.

B.1 Flow Table Test

Table B.1-1 - 50SBR flow

Flow Table (mm)		
61	60	134
59	63	133
60	60	135
64	57	134
134		

Table B.1-2 - 50SBL flow

Flow Table (mm)		
58	49	148
52	58	145
56	53	146
44	60	151
147.5		

Table B.1-3 - 30SBR flow

Flow Table (mm)		
53	49	153
46	61	148
46	59	150
50	55	150
150.25		

Table B.1-4 - 30SBL flow

Flow Table (mm)		
44	55	156
49	51	155
49	52	154
45	46	164
157.25		

Table B.1-5 - 10SBR flow

Flow Table (mm)		
43	48	164
42	49	164
46	48	161
39	52	164
163.25		

Table B.1-6 - 10SBL flow

Flow Table (mm)		
49	45	161
42	47	166
44	45	166
43	47	165
164.5		

Table B.1-7 - OPC flow

Flow Table (mm)		
58	38	159
38	57	160
52	41	162
56	38	161
160.5		



Figure B.1-1 – SB50L expansion during setting time tests

B.2 Compressive Strength Results

Table B.2-1 - 50SBR compressive strength

Code	Age	Load (N)	Compressive Strength (MPa)
50SBR-1	3 Days	4786.00	2.99
50SBR-2	3 Days	4367.00	2.73
50SBR-3	3 Days	4534.00	2.83
Average		4562.33	2.85
St. Deviation		172.23	0.11
50SBR-4	7 Days	15233.00	9.52
50SBR-5	7 Days	14864.00	9.29
50SBR-6	7 Days	14576.00	9.11
Average		14891.00	9.31
St. Deviation		268.90	0.17
50SBR-7	28 Days	24497.00	15.31
50SBR-8	28 Days	24015.00	15.01
50SBR-9	28 Days	24189.00	15.12
Average		24233.67	15.15
St. Deviation		199.29	0.12
50SBR-10	90 Days	29814.00	18.63
50SBR-11	90 Days	30206.00	18.88
50SBR-12	90 Days	29024.00	18.14
Average		29681.33	18.55
St. Deviation		491.58	0.31

Table B.2-2 - SB50L compressive strength

Code	Age	Load (N)	Compressive Strength (MPa)
50SBL-1	3 Days	9795.00	6.12
50SBL-2	3 Days	9704.00	6.07
50SBL-3	3 Days	9856.00	6.16
Average		9785.00	6.12
St. Deviation		62.46	0.04
50SBL-4	7 Days	14416.00	9.01
50SBL-5	7 Days	14638.00	9.15
50SBL-6	7 Days	14147.00	8.84
Average		14400.33	9.00
St. Deviation		200.76	0.13
50SBL-7	28 Days	20146.00	12.59
50SBL-8	28 Days	20174.00	12.61
50SBL-9	28 Days	19686.00	12.30
Average		20002.00	12.50
St. Deviation		223.74	0.14
50SBL-10	90 Days	24103.00	15.06
50SBL-11	90 Days	23898.00	14.94
50SBL-12	90 Days	24277.00	15.17
Average		24092.67	15.06
St. Deviation		154.90	0.10

Table B.2-3 - 30SBR compressive strength

Code	Age	Load (N)	Compressive Strength (MPa)
30SBR-1	3 Days	10005.00	6.25
30SBR-2	3 Days	10143.00	6.34
30SBR-3	3 Days	9635.00	6.02
Average		9927.67	6.20
St. Deviation		214.48	0.13
30SBR-4	7 Days	22298.00	13.94
30SBR-5	7 Days	22839.00	14.27
30SBR-6	7 Days	21828.00	13.64
Average		22321.67	13.95
St. Deviation		413.08	0.26
30SBR-7	28 Days	30951.00	19.34
30SBR-8	28 Days	33165.00	20.73
30SBR-9	28 Days	31873.00	19.92
Average		31996.33	20.00
St. Deviation		908.06	0.57
30SBR-10	90 Days	34934.00	21.83
30SBR-11	90 Days	36530.00	22.83
30SBR-12	90 Days	35654.00	22.28
Average		35706.00	22.32
St. Deviation		652.60	0.41

Table B.2-4 - 30SBL compressive strength

Code	Age	Load (N)	Compressive Strength (MPa)
30SBL-1	3 Days	10972.00	6.86
30SBL-2	3 Days	11655.00	7.28
30SBL-3	3 Days	10647.00	6.65
Average		11091.33	6.93
St. Deviation		420.08	0.26
30SBL-4	7 Days	20778.00	12.99
30SBL-5	7 Days	20584.00	12.87
30SBL-6	7 Days	19667.00	12.29
Average		20343.00	12.71
St. Deviation		484.52	0.30
30SBL-7	28 Days	30588.00	19.12
30SBL-8	28 Days	31594.00	19.75
30SBL-9	28 Days	29840.00	18.65
Average		30674.00	19.17
St. Deviation		718.65	0.45
30SBL-10	90 Days	34833.00	21.77
30SBL-11	90 Days	34977.00	21.86
30SBL-12	90 Days	33656.00	21.04
Average		34488.67	21.56
St. Deviation		591.71	0.37

Table B.2-5 - SB10R compressive strength

Code	Age	Load (N)	Compressive Strength (MPa)
10SBR-1	3 Days	15102.00	9.44
10SBR-2	3 Days	15530.00	9.71
10SBR-3	3 Days	15358.00	9.60
Average		15330.00	9.58
St. Deviation		175.85	0.11
10SBR-4	7 Days	26601.00	16.63
10SBR-5	7 Days	24286.60	15.18
10SBR-6	7 Days	23874.00	14.92
Average		24920.53	15.58
St. Deviation		1200.15	0.75
10SBR-7	28 Days	35548.00	22.22
10SBR-8	28 Days	36500.00	22.81
10SBR-9	28 Days	34898.00	21.81
Average		35648.67	22.28
St. Deviation		657.88	0.41
10SBR-10	90 Days	43087.00	26.93
10SBR-11	90 Days	43103.00	26.94
10SBR-12	90 Days	42829.00	26.77
Average		43006.33	26.88
St. Deviation		125.56	0.08

Table B.2-6 - 10SBL compressive strength

Code	Age	Load (N)	Compressive Strength (MPa)
10SBL-1	3 Days	16113.00	10.07
10SBL -2	3 Days	13878.00	8.67
10SBL -3	3 Days	15800.00	9.88
Average		15263.67	9.54
St. Deviation		988.11	0.62
10SBL -4	7 Days	24209.00	15.13
10SBL -5	7 Days	24674.00	15.42
10SBL -6	7 Days	24448.00	15.28
Average		24443.67	15.28
St. Deviation		189.86	0.12
10SBL -7	28 Days	35424.00	22.14
10SBL -8	28 Days	35683.00	22.30
10SBL -9	28 Days	35130.00	21.96
Average		35412.33	22.13
St. Deviation		225.91	0.14
10SBL -10	90 Days	40021.00	25.01
10SBL -11	90 Days	40466.00	25.29
10SBL -12	90 Days	40207.00	25.13
Average		40231.33	25.14
St. Deviation		182.48	0.11

Table B.2-7 - OPC compressive strength

Code	Age	Load (N)	Compressive Strength (MPa)
OPC-1	3 Days	19752.00	12.35
OPC-2	3 Days	17381.00	10.86
OPC-3	3 Days	19840.00	12.40
Average		18991.00	11.87
St. Deviation		1139.01	0.71
OPC-4	7 Days	27441.00	17.15
OPC-5	7 Days	26844.00	16.78
OPC-6	7 Days	28886.00	18.05
Average		27723.67	17.33
St. Deviation		857.27	0.54
OPC-7	28 Days	34721.00	21.70
OPC-8	28 Days	35073.00	21.92
OPC-9	28 Days	34296.00	21.44
Average		34696.67	21.69
St. Deviation		317.68	0.20
OPC-10	90 Days	38433.00	24.02
OPC-11	90 Days	38975.00	24.36
OPC-12	90 Days	39133.00	24.46
Average		38847.00	24.28
St. Deviation		299.76	0.19

B.3 Flexural Strength Results

Table B.3-1 - 50SBR flexural strength

Code	Age	Dry (g)	Submerged (g)	Density (g/cm ³)	Load (N)	Flexural Strength (MPa)
50SBR-1	3 Days	520.60	269.70	2.07	371.00	0.43
50SBR-2	3 Days	531.60	276.40	2.08	366.00	0.42
50SBR-3	3 Days	544.20	274.10	2.01	351.00	0.40
Average		532.13	273.40	2.06	362.67	0.42
St. Deviation		9.64	2.78	0.03	8.50	0.01
50SBR-4	7 Days	554.30	291.70	2.11	1301.00	1.36
50SBR-5	7 Days	539.80	284.40	2.11	1393.00	1.45
50SBR-6	7 Days	534.70	274.00	2.05	1344.00	1.40
Average		542.93	283.37	2.09	1346.00	1.40
St. Deviation		8.30	7.26	0.03	37.59	0.04
50SBR-7	28 Days	517.40	267.40	2.07	1870.00	2.14
50SBR-8	28 Days	541.70	286.60	2.12	2085.00	2.39
50SBR-9	28 Days	537.60	282.50	2.11	1935.00	2.22
Average		532.23	278.83	2.10	1963.33	2.25
St. Deviation		10.62	8.26	0.02	90.03	0.10
50SBR-10	90 Days	551.80	287.60	2.09	2123.00	2.43
50SBR-11	90 Days	544.00	287.60	2.12	2204.00	2.53
50SBR-12	90 Days	552.30	291.40	2.12	2084.00	2.39
Average		549.37	288.87	2.11	2137.00	2.45
St. Deviation		3.80	1.79	0.01	49.98	0.06

Table B.3-2 – 50SBL flexural strength

Code	Age	Dry (g)	Submerged (g)	Density (g/cm ³)	Load (N)	Flexural Strength (MPa)
50SBL-1	3 Days	557.00	285.20	2.05	1093.80	1.14
50SBL-2	3 Days	563.00	284.80	2.02	1061.63	1.11
50SBL-3	3 Days	583.00	300.40	2.06	712.00	0.74
Average		567.67	290.13	2.05	955.81	1.12
St. Deviation		11.12	7.26	0.02	172.90	0.18
50SBL-4	7 Days	569.40	291.70	2.05	1290.80	1.48
50SBL-5	7 Days	567.30	293.40	2.07	1361.52	1.56
50SBL-6	7 Days	576.40	298.40	2.07	1322.70	1.52
Average		571.03	294.50	2.06	1325.01	1.52
St. Deviation		3.89	2.84	0.01	28.92	0.03
50SBL-7	28 Days	579.90	305.10	2.11	1637.00	1.88
50SBL-8	28 Days	584.50	301.80	2.07	1810.00	2.07
50SBL-9	28 Days	543.00	281.40	2.08	1747.00	2.00
Average		569.13	296.10	2.08	1731.33	1.98
St. Deviation		18.57	10.48	0.02	71.49	0.08
50SBL-10	90 Days	579.90	305.10	2.11	1974.00	2.26
50SBL-11	90 Days	584.50	301.80	2.07	1916.00	2.20
50SBL-12	90 Days	588.40	307.40	2.09	1324.00	1.52
Average		584.27	304.77	2.09	1738.00	2.23
St. Deviation		3.47	2.30	0.02	293.70	0.34

Table B.3-3 - 30SBR flexural strength

Code	Age	Dry (g)	Submerged (g)	Density (g/cm ³)	Load (N)	Flexural Strength (MPa)
30SBR-1	3 Days	554.30	291.60	2.11	632.00	0.72
30SBR-2	3 Days	547.30	291.20	2.14	735.00	0.84
30SBR-3	3 Days	589.00	309.10	2.10	648.00	0.74
Average		563.53	297.30	2.12	671.67	0.77
St. Deviation		18.23	8.35	0.01	45.26	0.05
30SBR-4	7 Days	548.30	289.70	2.12	1548.00	1.77
30SBR-5	7 Days	558.20	299.30	2.16	1436.00	1.65
30SBR-6	7 Days	-	-	-	-	-
Average		553.25	294.50	2.14	1492.00	1.71
St. Deviation		4.95	4.80	0.02	56.00	0.06
30SBR-7	28 Days	546.40	291.50	2.14	2306.00	2.64
30SBR-8	28 Days	530.10	282.70	2.14	2118.00	2.43
30SBR-9	28 Days	532.10	285.40	2.16	2189.00	2.51
Average		536.20	286.53	2.15	2204.33	2.53
St. Deviation		7.26	3.68	0.01	77.51	0.09
30SBR-10	90 Days	527.10	283.10	2.16	2570.00	2.94
30SBR-11	90 Days	558.20	297.10	2.14	2227.00	2.55
30SBR-12	90 Days	499.70	268.10	2.16	2318.00	2.66
Average		528.33	282.77	2.15	2371.67	2.72
St. Deviation		23.90	11.84	0.01	145.08	0.17

Table B.3-4 - 30SBL flexural strength

Code	Age	Dry (g)	Submerged (g)	Density (g/cm ³)	Load (N)	Flexural Strength (MPa)
30SBL-1	3 Days	581.20	308.40	2.13	965.90	1.11
30SBL-2	3 Days	569.10	298.30	2.10	780.00	0.89
30SBL-3	3 Days	543.60	283.40	2.09	473.00	0.54
Average		564.63	296.70	2.11	872.95	1.00
St. Deviation		15.67	10.27	0.02	203.24	0.23
30SBL-4	7 Days	565.30	301.70	2.14	1840.00	2.11
30SBL-5	7 Days	540.60	281.40	2.09	1548.70	1.77
30SBL-6	7 Days	547.90	289.60	2.12	1697.00	1.94
Average		551.27	290.90	2.12	1695.23	1.94
St. Deviation		10.36	8.34	0.02	118.93	0.14
30SBL-7	28 Days	576.80	305.50	2.13	2171.00	2.49
30SBL-8	28 Days	559.50	301.40	2.17	1848.00	2.12
30SBL-9	28 Days	542.10	286.40	2.12	2063.00	2.36
Average		559.47	297.77	2.14	2027.33	2.32
St. Deviation		14.17	8.21	0.02	134.25	0.15
30SBL-10	90 Days	597.00	320.40	2.16	2288.00	2.62
30SBL-11	90 Days	568.00	304.30	2.15	2194.00	2.51
30SBL-12	90 Days	539.10	284.10	2.11	1477.00	1.69
Average		568.03	302.93	2.14	2241.00	2.57
St. Deviation		23.64	14.85	0.02	362.19	0.42

Table B.3-5 - 10SBR flexural strength

Code	Age	Dry (g)	Submerged (g)	Density (g/cm ³)	Load (N)	Flexural Strength (MPa)
10SBR-1	3 Days	535.70	287.90	2.16	1026.00	1.18
10SBR-2	3 Days	529.60	287.60	2.19	1008.00	1.16
10SBR-3	3 Days	544.90	294.30	2.17	1102.00	1.26
Average		536.73	289.93	2.17	1045.33	1.20
St. Deviation		6.29	3.09	0.01	40.74	0.05
10SBR-4	7 Days	534.30	288.60	2.17	1429.00	1.64
10SBR-5	7 Days	559.60	307.10	2.22	1575.00	1.80
10SBR-6	7 Days	529.00	285.10	2.17	1564.00	1.79
Average		540.97	293.60	2.19	1522.67	1.74
St. Deviation		13.35	9.65	0.02	66.38	0.08
10SBR-7	28 Days	559.80	304.10	2.19	2607.00	2.99
10SBR-8	28 Days	540.30	297.80	2.23	2432.00	2.79
10SBR-9	28 Days	532.70	287.30	2.17	2594.00	2.97
Average		544.27	296.40	2.20	2544.33	2.92
St. Deviation		11.41	6.93	0.02	79.61	0.09
10SBR-10	90 Days	537.00	294.20	2.21	2842.80	3.26
10SBR-11	90 Days	564.40	305.40	2.18	2610.00	2.99
10SBR-12	90 Days	548.10	301.10	2.22	2704.00	3.10
Average		549.83	300.23	2.20	2718.93	3.12
St. Deviation		11.25	4.61	0.02	95.63	0.11

Table B.3-6 - 10SBL flexural strength

Code	Age	Dry (g)	Submerged (g)	Density (g/cm ³)	Load (N)	Flexural Strength (MPa)
10SBL-1	3 Days	560.40	299.70	2.15	1042.00	1.19
10SBL-2	3 Days	548.60	293.90	2.15	1020.00	1.17
10SBL-3	3 Days	531.40	284.10	2.15	1011.00	1.16
Average		546.80	292.57	2.15	1024.33	1.17
St. Deviation		11.91	6.44	0.00	13.02	0.01
10SBL-4	7 Days	569.20	305.30	2.16	1771.00	2.03
10SBL-5	7 Days	569.40	306.10	2.16	1895.00	2.17
10SBL-6	7 Days	581.30	316.70	2.20	1841.00	2.11
Average		573.30	309.37	2.17	1835.67	2.10
St. Deviation		5.66	5.20	0.02	50.76	0.06
10SBL-7	28 Days	563.10	306.10	2.19	2189.00	2.51
10SBL-8	28 Days	566.00	302.30	2.15	2234.00	2.56
10SBL-9	28 Days	577.00	320.70	2.25	2094.00	2.40
Average		568.70	309.70	2.20	2172.33	2.49
St. Deviation		5.99	7.93	0.04	58.36	0.07
10SBL-10	90 Days	585.70	315.10	2.16	2581.00	2.96
10SBL-11	90 Days	597.40	329.00	2.23	2423.00	2.78
10SBL-12	90 Days	547.00	275.40	2.01	2507.00	2.87
Average		591.55	322.05	2.20	2503.67	2.87
St. Deviation		5.85	6.95	0.03	64.55	0.07

Table B.3-7 - OPC flexural strength

Code	Age	Dry (g)	Submerged (g)	Density (g/cm ³)	Load (N)	Flexural Strength (MPa)
OPC-1	3 Days	565.70	307.00	2.19	1258.00	1.44
OPC-2	3 Days	538.80	288.90	2.16	1287.00	1.47
OPC-3	3 Days	543.00	291.00	2.15	1341.00	1.54
Average		552.25	297.95	2.17	1272.50	1.48
St. Deviation		13.45	9.05	0.02	14.50	0.02
OPC-4	7 Days	554.00	298.60	2.17	1657.00	1.90
OPC-5	7 Days	567.20	304.40	2.16	1612.00	1.85
OPC-6	7 Days	577.60	311.30	2.17	1634.00	1.87
Average		566.27	304.77	2.17	1634.33	1.87
St. Deviation		6.60	2.90	0.01	22.50	0.03
OPC-7	28 Days	557.70	304.20	2.20	2372.00	2.72
OPC-8	28 Days	530.80	289.10	2.20	2457.00	2.82
OPC-9	28 Days	544.90	297.40	2.20	2344.00	2.69
Average		544.47	296.90	2.20	2391.00	2.74
St. Deviation		13.45	7.55	0.00	42.50	0.05
OPC-10	90 Days	547.70	299.30	2.20	2649.00	3.04
OPC-11	90 Days	530.80	288.80	2.19	2707.00	3.10
OPC-12	90 Days	550.40	303.20	2.23	2753.00	3.15
Average		542.97	297.10	2.21	2703.00	3.10
St. Deviation		8.45	5.25	0.01	29.00	0.03

B.4 Chemical Shrinkage Results

Table B.4-1 - Chemical Shrinkage of CBPD L, CBPD R and OPC

Time (Mins)	CBPD L	CBPD R	OPC
0	0	0	0
30	0.01316	-0.0171	-0.015
60	0.02368	-0.0186	-0.0188
90	0.05526	-0.0186	-0.0225
150	0.06974	-0.0171	-0.0263
250	0.07763	-0.0143	-0.03
330	0.08026	-0.01	-0.0363
500	0.08289	-0.0043	-0.0388
700	0.08553	0	-0.04
960	0.08684	0.00429	-0.04
1440	0.08947	0.00857	-0.0413
2160	0.08947	0.01286	-0.0413
2880	0.09079	0.015	-0.0425
3600	0.09079	0.01714	-0.0425
4320	0.09079	0.01714	-0.0425

Table B.4-2 - Chemical Shrinkage of SB50L, SB50R, SB30L, SB30R, SB10L and SB10R

Time (Mins)	SB50L	SB50R	SB30L	SB30R	SB10L	SB10R
0	0	0	0	0	0	0
30	0.00819	-0.0043	0.00952	-0.0043	-0.008	-0.013
60	0.01439	-0.0064	0.01429	-0.0064	-0.01	-0.015
90	0.03233	-0.0064	0.01905	-0.0043	-0.012	-0.018
150	0.04446	-0.0043	0.02381	-0.0043	-0.013	-0.024
250	0.0477	0	0.02857	-0.0021	-0.014	-0.028
330	0.04996	0.00213	0.03651	0	-0.017	-0.033
500	0.0516	0.00319	0.04127	0.00313	-0.019	-0.036
700	0.0526	0.00638	0.04444	0.00213	-0.023	-0.038
960	0.05211	0.00851	0.04762	0.00114	-0.025	-0.039
1440	0.05368	0.01064	0.04921	-0.0043	-0.028	-0.04
2160	0.05436	0.01277	0.04286	-0.0064	-0.033	-0.04
2880	0.05515	0.01383	0.0381	-0.0085	-0.035	-0.041
3600	0.05584	0.01489	0.03651	-0.0106	-0.036	-0.041
4320	0.05652	0.01489	0.03492	-0.011	-0.037	-0.041

B.5 Total Shrinkage Strain Results

B.5.1 Raw Data

Table B.5.1-1 - SB50R shrinkage strains

Days	Prism 1	Prism 2	Prism 3	Shrinkage Strain
1	0.016%	0.001%	0.003%	0.006%
3	0.022%	0.025%	0.007%	0.018%
6	0.034%	0.028%	0.019%	0.027%
7	0.039%	0.031%	0.023%	0.031%
9	0.049%	0.039%	0.033%	0.040%
10	0.052%	0.046%	0.037%	0.045%
13	0.067%	0.061%	0.055%	0.061%
14	0.073%	0.067%	0.062%	0.067%
15	0.078%	0.074%	0.068%	0.073%
16	0.079%	0.074%	0.069%	0.074%
21	0.094%	0.089%	0.082%	0.088%
23	0.098%	0.094%	0.089%	0.094%
24	0.100%	0.097%	0.090%	0.096%
28	0.113%	0.108%	0.102%	0.108%
36	0.133%	0.130%	0.123%	0.129%
42	0.147%	0.142%	0.138%	0.142%
44	0.151%	0.148%	0.142%	0.147%
49	0.158%	0.154%	0.148%	0.153%
52	0.160%	0.155%	0.151%	0.160%
65	0.183%	0.183%	0.180%	0.182%
75	0.194%	0.191%	0.187%	0.191%
90	0.200%	0.198%	0.193%	0.197%
131	0.219%	0.220%	0.212%	0.217%
137	0.221%	0.221%	0.213%	0.219%
143	0.229%	0.229%	0.223%	0.221%
150	0.228%	0.228%	0.219%	0.225%

Table B.5.1-2 - SB50L shrinkage strains

Days	Prism 1	Prism 2	Prism 3	Shrinkage Strain
1	0.002%	0.005%	0.002%	0.003%
3	0.001%	0.008%	0.012%	0.007%
6	0.006%	0.015%	0.019%	0.013%
7	0.009%	0.017%	0.021%	0.016%
9	0.014%	0.025%	0.026%	0.021%
10	0.017%	0.029%	0.028%	0.025%
13	0.027%	0.040%	0.039%	0.035%
14	0.032%	0.045%	0.044%	0.041%
15	0.036%	0.050%	0.047%	0.044%
16	0.039%	0.052%	0.047%	0.046%
21	0.054%	0.069%	0.068%	0.064%
23	0.064%	0.080%	0.076%	0.073%
24	0.067%	0.081%	0.079%	0.075%
28	0.084%	0.098%	0.097%	0.093%
36	0.115%	0.128%	0.126%	0.123%
44	0.135%	0.148%	0.147%	0.144%
46	0.140%	0.154%	0.153%	0.149%
49	0.146%	0.160%	0.158%	0.155%
52	0.155%	0.167%	0.166%	0.162%
65	0.188%	0.200%	0.203%	0.197%
75	0.198%	0.211%	0.211%	0.207%
90	0.204%	0.218%	0.218%	0.213%
131	0.212%	0.224%	0.228%	0.221%
137	0.213%	0.226%	0.226%	0.222%
143	0.220%	0.232%	0.235%	0.226%
150	0.219%	0.231%	0.234%	0.228%

Table B.5.1-3 - SB30R shrinkage strains

Days	Prism 1	Prism 2	Prism 3	Shrinkage Strain
1	0.003%	0.006%	0.014%	0.002%
2	0.017%	0.014%	0.023%	0.007%
3	0.014%	0.015%	0.025%	0.012%
5	0.019%	0.015%	0.031%	0.022%
6	0.021%	0.020%	0.032%	0.024%
7	0.021%	0.020%	0.033%	0.025%
8	0.025%	0.024%	0.037%	0.029%
15	0.060%	0.056%	0.070%	0.062%
19	0.076%	0.072%	0.086%	0.078%
20	0.080%	0.076%	0.090%	0.082%
21	0.085%	0.081%	0.093%	0.083%
22	0.085%	0.081%	0.094%	0.087%
26	0.091%	0.087%	0.099%	0.092%
28	0.094%	0.090%	0.103%	0.096%
30	0.097%	0.093%	0.105%	0.098%
35	0.100%	0.099%	0.110%	0.103%
42	0.114%	0.111%	0.124%	0.116%
48	0.121%	0.118%	0.130%	0.123%
55	0.125%	0.123%	0.135%	0.133%
68	0.143%	0.141%	0.154%	0.145%
78	0.152%	0.149%	0.161%	0.153%
90	0.154%	0.151%	0.162%	0.157%
134	0.188%	0.182%	0.195%	0.188%
140	0.192%	0.184%	0.196%	0.191%
146	0.195%	0.187%	0.200%	0.194%
150	0.196%	0.188%	0.201%	0.195%

Table B.5.1-4 - SB30L shrinkage strains

Days	Prism 1	Prism 2	Prism 3	Shrinkage Strain
0	0.000%	0.000%	0.000%	0.000%
1	0.006%	0.004%	0.003%	0.003%
2	0.050%	0.005%	0.006%	0.006%
3	0.050%	0.009%	0.009%	0.009%
5	0.057%	0.016%	0.009%	0.013%
7	0.065%	0.020%	0.018%	0.019%
15	0.093%	0.047%	0.043%	0.045%
19	0.110%	0.063%	0.060%	0.061%
20	0.115%	0.068%	0.064%	0.066%
21	0.119%	0.073%	0.070%	0.072%
22	0.123%	0.076%	0.071%	0.073%
26	0.128%	0.080%	0.078%	0.079%
28	0.135%	0.086%	0.083%	0.085%
30	0.138%	0.088%	0.085%	0.087%
35	0.145%	0.094%	0.092%	0.093%
42	0.162%	0.113%	0.110%	0.111%
48	0.172%	0.121%	0.121%	0.121%
50	0.177%	0.127%	0.125%	0.126%
68	0.207%	0.153%	0.155%	0.154%
78	0.213%	0.159%	0.161%	0.160%
90	0.220%	0.162%	0.169%	0.165%
134	0.253%	0.185%	0.202%	0.194%
140	0.258%	0.189%	0.206%	0.197%
150	0.261%	0.195%	0.211%	0.203%

Table B.5.1-5 - SB10R shrinkage strains

Days	Prism 1	Prism 2	Prism 3	Shrinkage Strain
1	0.009%	0.009%	0.018%	0.012%
2	0.017%	0.020%	0.021%	0.019%
3	0.022%	0.022%	0.030%	0.025%
4	0.026%	0.035%	0.037%	0.033%
5	0.032%	0.039%	0.039%	0.037%
6	0.037%	0.044%	0.047%	0.043%
7	0.040%	0.050%	0.050%	0.047%
8	0.046%	0.046%	0.050%	0.047%
9	0.055%	0.054%	0.065%	0.058%
10	0.056%	0.056%	0.064%	0.059%
11	0.055%	0.059%	0.066%	0.060%
15	0.057%	0.062%	0.069%	0.063%
21	0.084%	0.089%	0.095%	0.089%
25	0.094%	0.099%	0.104%	0.099%
26	0.098%	0.102%	0.108%	0.103%
27	0.100%	0.103%	0.109%	0.104%
28	0.099%	0.104%	0.109%	0.104%
32	0.101%	0.105%	0.109%	0.105%
34	0.102%	0.107%	0.112%	0.107%
35	0.102%	0.107%	0.112%	0.107%
40	0.101%	0.106%	0.111%	0.106%
47	0.107%	0.112%	0.117%	0.112%
53	0.109%	0.113%	0.119%	0.114%
60	0.111%	0.117%	0.121%	0.116%
73	0.120%	0.125%	0.131%	0.125%
83	0.125%	0.128%	0.135%	0.130%
90	0.123%	0.125%	0.134%	0.127%
140	0.123%	0.128%	0.135%	0.129%
146	0.142%	0.147%	0.152%	0.147%
150	0.149%	0.153%	0.158%	0.154%

Table B.5.1-6 - SB10L shrinkage strains

Days	Prism 1	Prism 2	Prism 3	Shrinkage Strain
1	0.014%	0.016%	0.013%	0.014%
2	0.027%	0.019%	0.016%	0.020%
3	0.027%	0.029%	0.024%	0.027%
4	0.038%	0.032%	0.029%	0.033%
5	0.043%	0.040%	0.036%	0.040%
6	0.045%	0.043%	0.038%	0.042%
7	0.048%	0.046%	0.044%	0.046%
8	0.063%	0.052%	0.041%	0.052%
9	0.059%	0.053%	0.048%	0.053%
10	0.059%	0.053%	0.049%	0.054%
11	0.061%	0.059%	0.054%	0.058%
12	0.063%	0.063%	0.055%	0.060%
21	0.092%	0.091%	0.086%	0.090%
25	0.102%	0.102%	0.096%	0.100%
26	0.102%	0.103%	0.099%	0.101%
28	0.103%	0.103%	0.100%	0.102%
30	0.109%	0.108%	0.102%	0.107%
32	0.110%	0.107%	0.102%	0.106%
34	0.112%	0.111%	0.105%	0.109%
35	0.113%	0.111%	0.105%	0.110%
40	0.114%	0.113%	0.105%	0.111%
47	0.121%	0.119%	0.111%	0.117%
53	0.123%	0.120%	0.113%	0.119%
60	0.123%	0.124%	0.116%	0.121%
73	0.135%	0.134%	0.127%	0.132%
83	0.141%	0.140%	0.133%	0.138%
90	0.140%	0.140%	0.130%	0.137%
97	0.142%	0.140%	0.133%	0.138%
140	0.157%	0.155%	0.151%	0.154%
146	0.158%	0.157%	0.155%	0.157%
150	0.165%	0.162%	0.160%	0.163%

Table B.5.1-7 - OPC shrinkage strains

Days	Prism 1	Prism 2	Prism 3	Shrinkage Strain
1	0.012%	0.011%	0.018%	0.014%
2	0.019%	0.016%	0.028%	0.021%
3	0.022%	0.017%	0.032%	0.024%
4	0.032%	0.029%	0.032%	0.031%
5	0.041%	0.032%	0.040%	0.038%
6	0.044%	0.039%	0.044%	0.042%
7	0.051%	0.042%	0.050%	0.048%
8	0.052%	0.044%	0.052%	0.049%
9	0.055%	0.047%	0.058%	0.054%
10	0.054%	0.050%	0.062%	0.055%
11	0.059%	0.052%	0.065%	0.059%
12	0.060%	0.055%	0.065%	0.060%
21	0.082%	0.075%	0.086%	0.081%
25	0.088%	0.081%	0.093%	0.087%
26	0.090%	0.083%	0.095%	0.089%
27	0.090%	0.085%	0.096%	0.090%
28	0.093%	0.085%	0.096%	0.091%
32	0.089%	0.083%	0.093%	0.088%
34	0.092%	0.085%	0.095%	0.090%
35	0.092%	0.087%	0.095%	0.091%
40	0.092%	0.087%	0.096%	0.091%
47	0.096%	0.089%	0.100%	0.095%
53	0.097%	0.091%	0.101%	0.096%
60	0.098%	0.093%	0.098%	0.096%
73	0.105%	0.099%	0.107%	0.104%
80	0.107%	0.102%	0.111%	0.107%
90	0.110%	0.104%	0.113%	0.109%
120	0.110%	0.108%	0.116%	0.112%
140	0.116%	0.116%	0.126%	0.119%
146	0.121%	0.119%	0.131%	0.123%
150	0.120%	0.119%	0.129%	0.123%

B.5.2 Shrinkage Plots

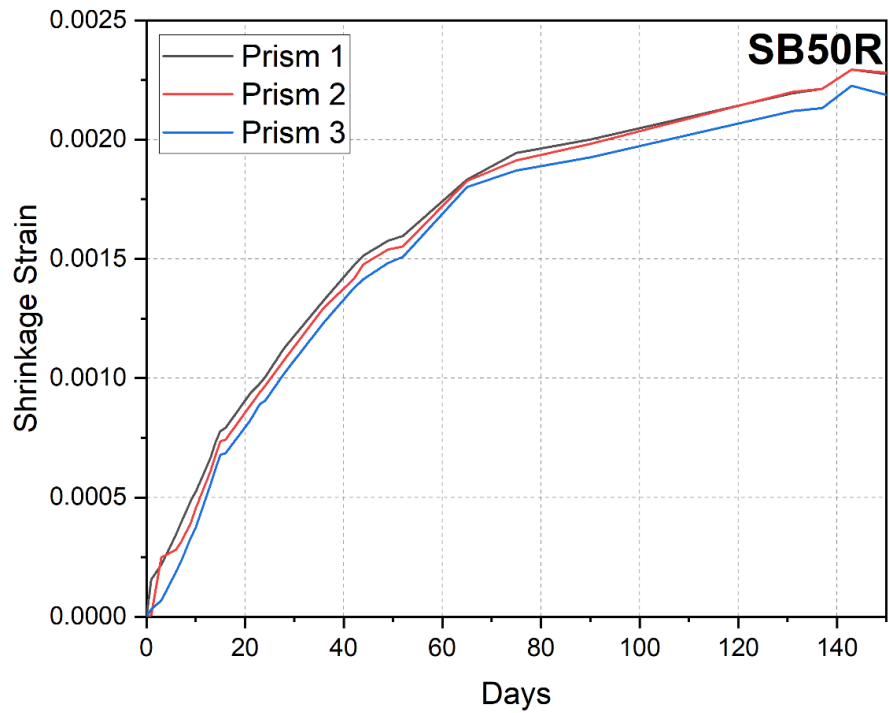


Figure B.5.2-1 – SB50R shrinkage strains

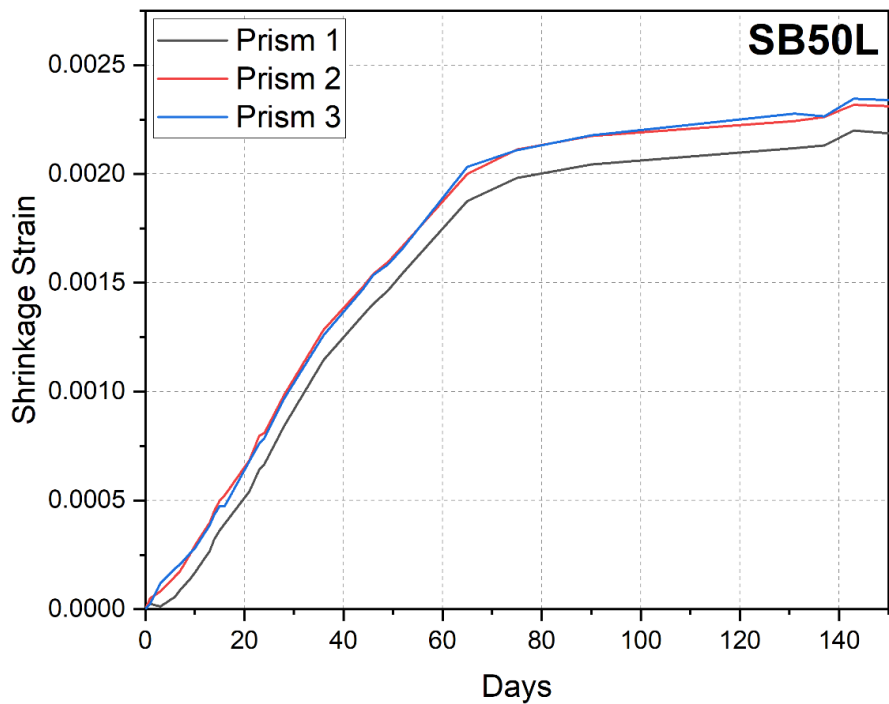


Figure B.5.2-2 – SB50L shrinkage strains

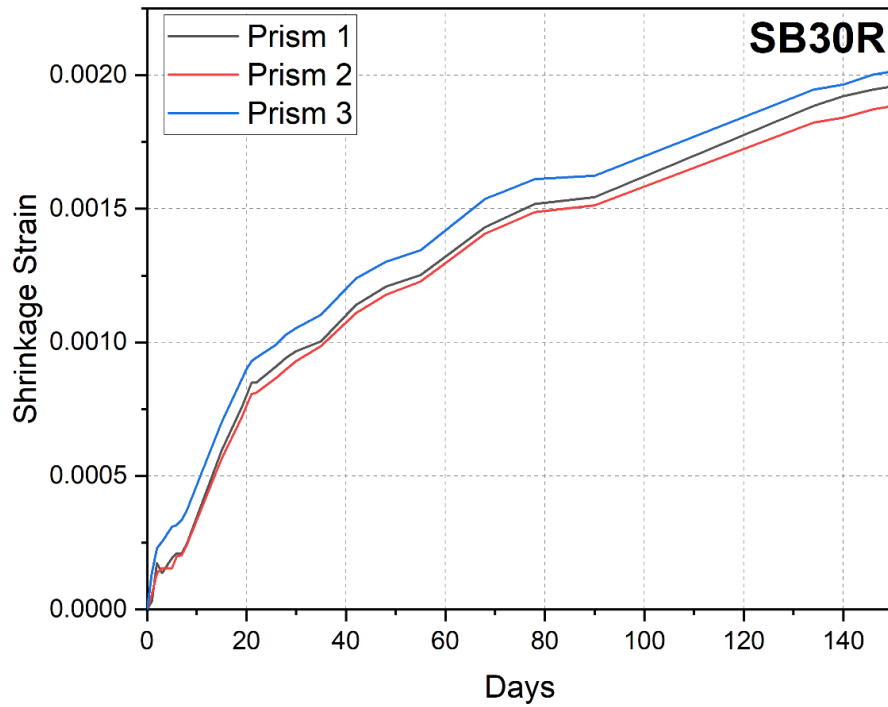


Figure B.5.2-3 – SB30R shrinkage strains

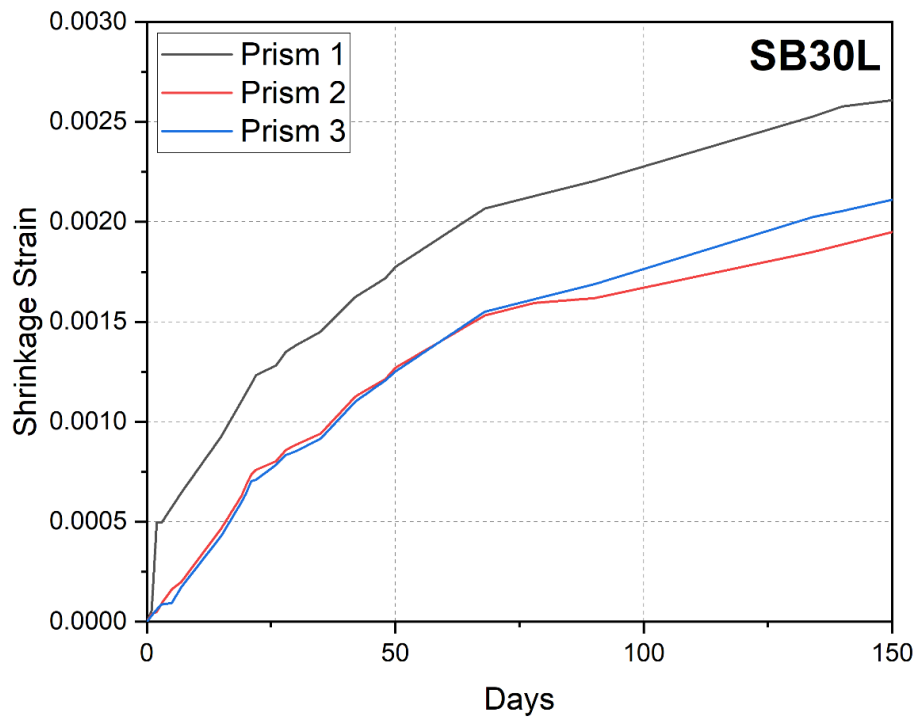


Figure B.5.2-4 - SB30L shrinkage strains

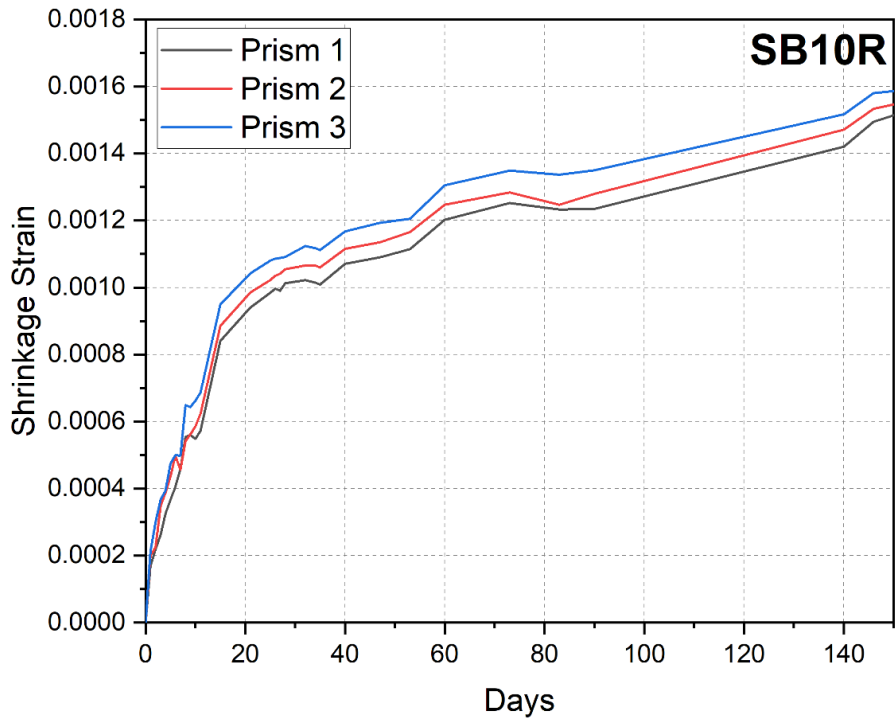


Figure B.5.2-5 – SB10R shrinkage strains

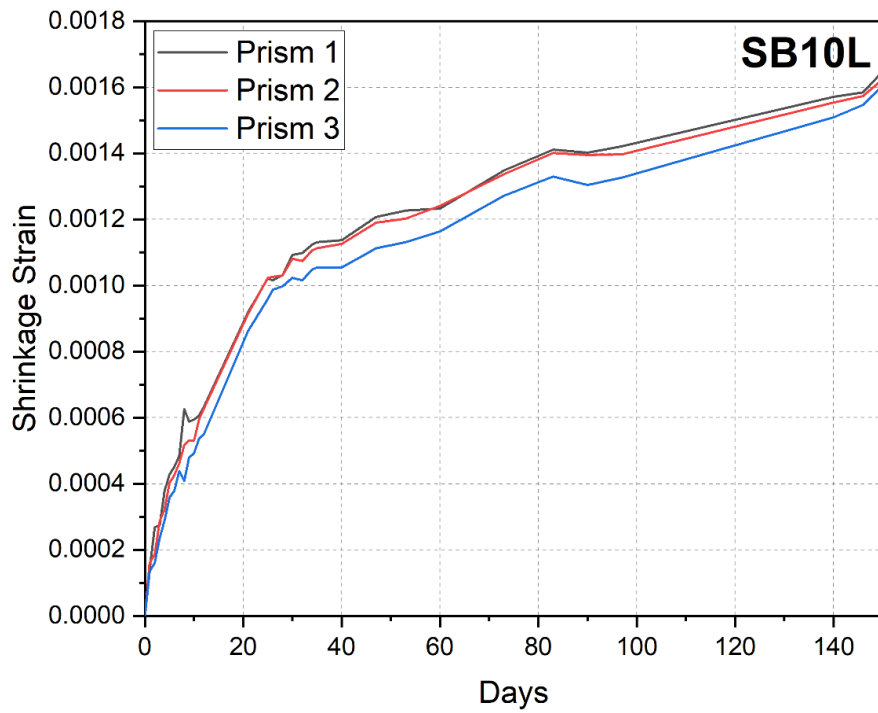


Figure B.5.2-6 – SB10L shrinkage strains

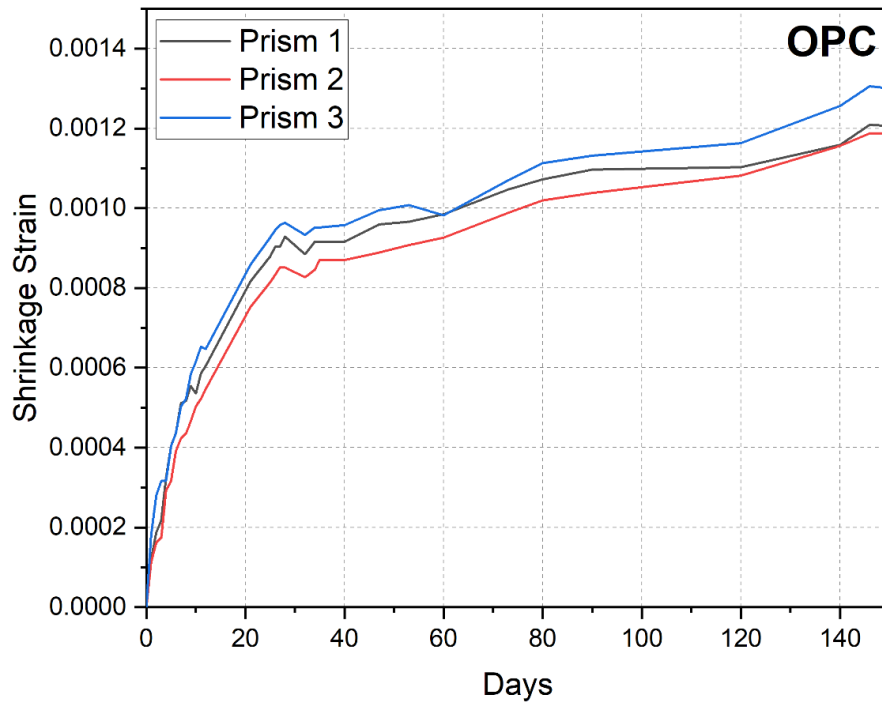


Figure B.5.2-7 – OPC shrinkage strains

Appendix C: Chapter 5 Data

C.1 Carbonation Strength Data



Figure C.1-1 - Carbonation chamber

Table C.1-1 – Compressive strength of SB50R

Code	Age	Load (N)	Compressive Strength (MPa)
50SBR-1	3 Days	1234.00	3.09
50SBR-2	3 Days	1294.00	3.24
50SBR-3	3 Days	1187.00	2.97
Average		1238.33	3.10
St. Deviation		43.79	0.03
50SBR-4	7 Days	4920.00	12.30
50SBR-5	7 Days	4971.00	12.43
50SBR-6	7 Days	5027.00	12.57
Average		4972.67	12.43
St. Deviation		43.70	0.11
50SBR-7	28 Days	6520.00	16.30
50SBR-8	28 Days	6602.00	16.51
50SBR-9	28 Days	6575.00	16.44
Average		6565.67	16.41
St. Deviation		34.12	0.09

Table C.1-2 - Compressive strength of SB50R-C

Code	Age	Load (N)	Compressive Strength (MPa)
50SBR-C-1	3 Days	1297.00	3.24
50SBR-C-2	3 Days	1274.00	3.19
50SBR-C-3	3 Days	1260.00	3.15
Average		1277.00	3.19
St. Deviation		15.25	0.01
50SBR-C-4	7 Days	5213.00	13.03
50SBR-C-5	7 Days	5114.00	12.79
50SBR-C-6	7 Days	5179.00	12.95
Average		5168.67	12.92
St. Deviation		41.07	0.10
50SBR-C-7	28 Days	6824.00	17.06
50SBR-C-8	28 Days	6876.00	17.19
50SBR-C-9	28 Days	6792.00	16.98
Average		6830.67	17.08
St. Deviation		34.62	0.09

Table C.1-3 - Compressive strength of SB50L

Code	Age	Load (N)	Compressive Strength (MPa)
50SBL-1	3 Days	2520.00	6.30
50SBL-2	3 Days	2571.00	6.43
50SBL-3	3 Days	2598.00	6.50
Average		2563.00	6.41
St. Deviation		32.34	0.02
50SBL-4	7 Days	4312.00	10.78
50SBL-5	7 Days	4423.00	11.06
50SBL-6	7 Days	4374.00	10.94
Average		4369.67	10.92
St. Deviation		45.42	0.11
50SBL-7	28 Days	5683.00	14.21
50SBL-8	28 Days	5777.00	14.44
50SBL-9	28 Days	5843.00	14.61
Average		5767.67	14.42
St. Deviation		65.65	0.16

Table C.1-4 - Compressive strength of SB50L-C

Code	Age	Load (N)	Compressive Strength (MPa)
50SBL-C-1	3 Days	3463.00	8.66
50SBL-C-2	3 Days	3542.00	8.86
50SBL-C-3	3 Days	3573.00	8.93
Average		3526.00	8.82
St. Deviation		46.31	0.03
50SBL-C-4	7 Days	6217.00	15.54
50SBL-C-5	7 Days	6114.00	15.29
50SBL-C-6	7 Days	6285.00	15.71
Average		6205.33	15.51
St. Deviation		70.30	0.18
50SBL-C-7	28 Days	8014.00	20.04
50SBL-C-8	28 Days	7923.00	19.81
50SBL-C-9	28 Days	8057.00	20.14
Average		7998.00	20.00
St. Deviation		55.86	0.14

Table C.1-5 - Compressive strength of SB30R

Code	Age	Load (N)	Compressive Strength (MPa)
30SBR-1	3 Days	2713.00	6.78
30SBR-2	3 Days	2646.00	6.62
30SBR-3	3 Days	2584.00	6.46
Average		2647.67	6.62
St. Deviation		52.68	0.03
30SBR-4	7 Days	6083.00	15.21
30SBR-5	7 Days	6114.00	15.29
30SBR-6	7 Days	6173.00	15.43
Average		6123.33	15.31
St. Deviation		37.33	0.09
30SBR-7	28 Days	8246.00	20.62
30SBR-8	28 Days	8319.00	20.80
30SBR-9	28 Days	8259.00	20.65
Average		8274.67	20.69
St. Deviation		31.79	0.08

Table C.1-6 - Compressive strength of SB30R-C

Code	Age	Load (N)	Compressive Strength (MPa)
30SBR-C-1	3 Days	2577.00	6.44
30SBR-C-2	3 Days	2512.00	6.28
30SBR-C-3	3 Days	2600.00	6.50
Average		2563.00	6.41
St. Deviation		37.26	0.02
30SBR-C-4	7 Days	6254.00	15.64
30SBR-C-5	7 Days	6170.00	15.43
30SBR-C-6	7 Days	6112.00	15.28
Average		6178.67	15.45
St. Deviation		58.29	0.15
30SBR-C-7	28 Days	8449.00	21.12
30SBR-C-8	28 Days	8412.00	21.03
30SBR-C-9	28 Days	8375.00	20.94
Average		8412.00	21.03
St. Deviation		30.21	0.08

Table C.1-7- Compressive strength of SB30L

Code	Age	Load (N)	Compressive Strength (MPa)
30SBL-1	3 Days	3034.00	7.59
30SBL-2	3 Days	3094.00	7.74
30SBL-3	3 Days	2987.00	7.47
Average		3038.33	7.60
St. Deviation		43.79	0.03
30SBL-4	7 Days	5220.00	13.05
30SBL-5	7 Days	5371.00	13.43
30SBL-6	7 Days	5427.00	13.57
Average		5339.33	13.35
St. Deviation		87.42	0.22
30SBL-7	28 Days	6920.00	17.30
30SBL-8	28 Days	7002.00	17.51
30SBL-9	28 Days	7090.00	17.73
Average		7004.00	17.51
St. Deviation		69.42	0.17

Table C.1-8 - Compressive strength of SB30L-C

Code	Age	Load (N)	Compressive Strength (MPa)
30SBL-C-1	3 Days	3397.00	8.49
30SBL-C-2	3 Days	3474.00	8.69
30SBL-C-3	3 Days	3460.00	8.65
Average		3443.67	8.61
St. Deviation		33.49	0.02
30SBL-C-4	7 Days	7013.00	17.53
30SBL-C-5	7 Days	7114.00	17.79
30SBL-C-6	7 Days	7199.00	18.00
Average		7108.67	17.77
St. Deviation		76.03	0.19
30SBL-C-7	28 Days	8824.00	22.06
30SBL-C-8	28 Days	8896.00	22.24
30SBL-C-9	28 Days	8942.00	22.36
Average		8887.33	22.22
St. Deviation		48.56	0.12

Table C.1-9 - Compressive strength of OPC

Code	Age	Load (N)	Compressive Strength (MPa)
OPC-1	3 Days	4534.00	11.34
OPC-2	3 Days	4591.00	11.48
OPC-3	3 Days	4487.00	11.22
Average		4537.33	11.34
St. Deviation		42.52	0.03
OPC-4	7 Days	7220.00	18.05
OPC-5	7 Days	7381.00	18.45
OPC-6	7 Days	7462.00	18.66
Average		7354.33	18.39
St. Deviation		100.58	0.25
OPC-7	28 Days	9633.00	24.08
OPC-8	28 Days	9905.00	24.76
OPC-9	28 Days	9742.00	24.36
Average		9760.00	24.40
St. Deviation		111.77	0.28

Table C.1-10 - Compressive strength of OPC-C

Code	Age	Load (N)	Compressive Strength (MPa)
OPC-C-1	3 Days	3897.00	9.74
OPC-C-2	3 Days	3743.00	9.36
OPC-C-3	3 Days	3746.00	9.37
Average		3795.33	9.49
St. Deviation		71.90	0.04
OPC-C-4	7 Days	6113.00	15.28
OPC-C-5	7 Days	6014.00	15.04
OPC-C-6	7 Days	6119.00	15.30
Average		6082.00	15.21
St. Deviation		48.15	0.12
OPC-C-7	28 Days	8783.00	21.96
OPC-C-8	28 Days	8929.00	22.32
OPC-C-9	28 Days	8811.00	22.03
Average		8841.00	22.10
St. Deviation		63.27	0.16

Appendix D: Chapter 6 Data

Below is a series of relevant raw data for the third paper from this research.

D.1 Compressive Strength Chapter 6

Table D.1-1 - 50SB compressive strength

Code	Age	Load (N)	Compressive Strength (MPa)
50SB-1	7 Days	26107.00	10.44
50SB-2	7 Days	25638.00	10.26
50SB-3	7 Days	25741.00	10.30
Average		25828.67	10.33
St. Deviation		201.25	0.08
50SB-4	28 Days	41146.00	16.46
50SB-5	28 Days	42174.00	16.87
50SB-6	28 Days	42686.00	17.07
Average		42002.00	16.80
St. Deviation		640.36	0.26

Table D.1-2 - 50SBM compressive strength

Code	Age	Load (N)	Compressive Strength (MPa)
50SBM-1	7 Days	34587.00	13.83
50SBM-2	7 Days	34108.00	13.64
50SBM-3	7 Days	35107.00	14.04
Average		34600.67	13.84
St. Deviation		407.95	0.16
50SBM-4	28 Days	53271	21.31
50SBM-5	28 Days	54815	21.93
50SBM-6	28 Days	55071	21.38
Average		54385.67	54385.67
St. Deviation		795.09	795.09

Table D.1-3 - 50SB 10MK compressive strength

Code	Age	Load (N)	Compressive Strength (MPa)
50SB 10MK-1	7 Days	46251.00	18.50
50SB 10MK-2	7 Days	46782.00	18.71
50SB 10MK-3	7 Days	45871.00	18.35
Average		46301.33	18.52
St. Deviation		373.61	0.15
50SB 10MK-4	28 Days	55982.00	22.39
50SB 10MK-5	28 Days	54794.00	21.92
50SB 10MK-6	28 Days	56249.00	22.50
Average		55675.00	22.27
St. Deviation		632.43	0.25

Table D.1-4 - 50SB 20MK compressive strength

Code	Age	Load (N)	Compressive Strength (MPa)
50SB 20MK-1	7 Days	42198.00	16.88
50SB 20MK-2	7 Days	42457.00	16.98
50SB 20MK-3	7 Days	41897.00	16.76
Average		42184.00	16.87
St. Deviation		228.83	0.09
50SB 20MK-4	28 Days	53809.00	21.52
50SB 20MK-5	28 Days	53696.00	21.48
50SB 20MK-6	28 Days	53245.00	21.30
Average		53583.33	21.43
St. Deviation		243.65	0.10

Table D.1-5 - 50SBM 10MK compressive strength

Code	Age	Load (N)	Compressive Strength (MPa)
50SBM 10MK-1	7 Days	66129.00	26.45
50SBM 10MK-2	7 Days	65888.00	26.36
50SBM 10MK-3	7 Days	52147.00	20.86
Average		61388.00	26.40
St. Deviation		6535.11	2.61
50SBM 10MK-4	28 Days	80547.00	32.22
50SBM 10MK-5	28 Days	82642.00	33.06
50SBM 10MK-6	28 Days	82249.00	32.90
Average		81812.67	32.73
St. Deviation		909.23	0.36

Table D.1-6 - 50SBM 20MK compressive strength

Code	Age	Load (N)	Compressive Strength (MPa)
50SBM 20MK-1	7 Days	62582.00	25.03
50SBM 20MK-2	7 Days	61604.00	24.64
50SBM 20MK-3	7 Days	62255.00	24.90
Average		62147.00	24.86
St. Deviation		406.50	0.16
50SBM 20MK-4	28 Days	78984.00	31.59
50SBM 20MK-5	28 Days	77422.00	30.97
50SBM 20MK-6	28 Days	78326.00	31.33
Average		78244.00	31.30
St. Deviation		640.31	0.26

Table D.1-7 - OPC compressive strength

Code	Age	Load (N)	Compressive Strength (MPa)
OPC-1	7 Days	48594.00	19.44
OPC-2	7 Days	47936.00	19.17
OPC-3	7 Days	47251.00	18.90
Average		47927.00	19.17
St. Deviation		548.31	0.22
OPC-4	28 Days	74599.00	29.84
OPC-5	28 Days	73827.00	29.53
OPC-6	28 Days	74864.00	29.95
Average		74430.00	29.77
St. Deviation		439.90	0.18

D.2 Shrinkage Strains

D.2.1 Shrinkage Raw Data

Table D.2.1-1 - SB50 10MK Shrinkage Strains

Days	Prism 1	Prism 2	Prism 3	Shrinkage Strain
0	0.00000%	0.00000%	0.00000%	0.00000%
1	0.00405%	0.00341%	0.00361%	0.00369%
3	0.00550%	0.00500%	0.00531%	0.00527%
7	0.01187%	0.01131%	0.01153%	0.01157%
8	0.01257%	0.01237%	0.01280%	0.01258%
12	0.01577%	0.01550%	0.01620%	0.01582%
20	0.02449%	0.02463%	0.02512%	0.02475%
27	0.03209%	0.03342%	0.03491%	0.03347%
36	0.03740%	0.03912%	0.04106%	0.03919%
40	0.04288%	0.04451%	0.04592%	0.04444%
49	0.04881%	0.04928%	0.05106%	0.04972%
56	0.05721%	0.05871%	0.05960%	0.05851%
66	0.06321%	0.06490%	0.06681%	0.06497%
78	0.07303%	0.07406%	0.07560%	0.07423%
85	0.07857%	0.07949%	0.08190%	0.07999%
92	0.08299%	0.08388%	0.08490%	0.08393%
100	0.08591%	0.08700%	0.08811%	0.08700%
120	0.08978%	0.09083%	0.09170%	0.09077%
140	0.09105%	0.09196%	0.09298%	0.09200%

Table D.2.1-2 - SB50M 10MK Shrinkage Strains

Days	Prism 1	Prism 2	Prism 3	Shrinkage Strain
0	0.00000%	0.00000%	0.00000%	0.00000%
1	0.00510%	0.00551%	0.00570%	0.00544%
3	0.00990%	0.00960%	0.01030%	0.00993%
7	0.01260%	0.01340%	0.01300%	0.01300%
8	0.01281%	0.01360%	0.01300%	0.01314%
12	0.01793%	0.01801%	0.01810%	0.01801%
20	0.03186%	0.03211%	0.03221%	0.03206%
27	0.03990%	0.04105%	0.04161%	0.04085%
36	0.04444%	0.04510%	0.04530%	0.04495%
40	0.04706%	0.04915%	0.05100%	0.04907%
49	0.05530%	0.05613%	0.05640%	0.05594%
56	0.06050%	0.06110%	0.06140%	0.06100%
66	0.06600%	0.06941%	0.07106%	0.06882%
78	0.07731%	0.07821%	0.07844%	0.07799%
85	0.08170%	0.08311%	0.08380%	0.08287%
92	0.08750%	0.08910%	0.08970%	0.08877%
100	0.09430%	0.09590%	0.09540%	0.09520%
120	0.09600%	0.10400%	0.09830%	0.09943%
140	0.09800%	0.10700%	0.10150%	0.10217%

Table D.2.1-3 - SB50 20MK Shrinkage Strains

Days	Prism 1	Prism 2	Prism 3	Shrinkage Strain
0	0.00000%	0.00000%	0.00000%	0.00000%
1	0.00261%	0.00280%	0.00311%	0.00284%
3	0.00902%	0.00981%	0.01124%	0.01002%
7	0.01510%	0.01540%	0.01751%	0.01600%
8	0.01513%	0.01521%	0.01768%	0.01600%
12	0.02271%	0.02218%	0.02413%	0.02300%
20	0.02791%	0.02866%	0.03044%	0.02900%
27	0.03198%	0.03290%	0.03413%	0.03300%
36	0.03805%	0.03871%	0.04025%	0.03900%
40	0.04098%	0.04198%	0.04306%	0.04201%
49	0.04578%	0.04688%	0.04833%	0.04700%
56	0.04884%	0.05000%	0.05118%	0.05001%
66	0.05278%	0.05409%	0.05513%	0.05400%
78	0.05784%	0.05845%	0.06071%	0.05900%
85	0.06477%	0.06589%	0.06735%	0.06600%
92	0.06871%	0.06984%	0.07145%	0.07000%
100	0.07305%	0.07382%	0.07514%	0.07400%
120	0.07403%	0.07477%	0.07620%	0.07500%
140	0.07614%	0.07678%	0.07809%	0.07700%

Table D.2.1-4 - SB50M 20MK Shrinkage Strains

Days	Prism 1	Prism 2	Prism 3	Shrinkage Strain
0	0.00000%	0.00000%	0.00000%	0.00000%
1	0.00213%	0.00287%	0.00350%	0.00284%
3	0.00830%	0.00890%	0.00979%	0.00900%
7	0.01649%	0.01721%	0.01790%	0.01720%
8	0.01758%	0.01822%	0.01897%	0.01826%
12	0.02310%	0.02397%	0.02488%	0.02398%
20	0.02990%	0.03088%	0.03220%	0.03099%
27	0.03387%	0.03488%	0.03655%	0.03510%
36	0.04072%	0.04271%	0.04399%	0.04247%
40	0.04430%	0.04571%	0.04760%	0.04587%
49	0.04739%	0.04851%	0.05188%	0.04926%
56	0.05171%	0.05310%	0.05579%	0.05353%
66	0.05704%	0.05871%	0.06111%	0.05895%
78	0.06078%	0.06271%	0.06502%	0.06284%
85	0.06858%	0.06943%	0.07210%	0.07004%
92	0.07247%	0.07361%	0.07602%	0.07403%
100	0.07502%	0.07585%	0.07790%	0.07625%
120	0.07871%	0.07988%	0.08192%	0.08017%
140	0.08320%	0.08505%	0.08680%	0.08502%

D2.2 Shrinkage Plots

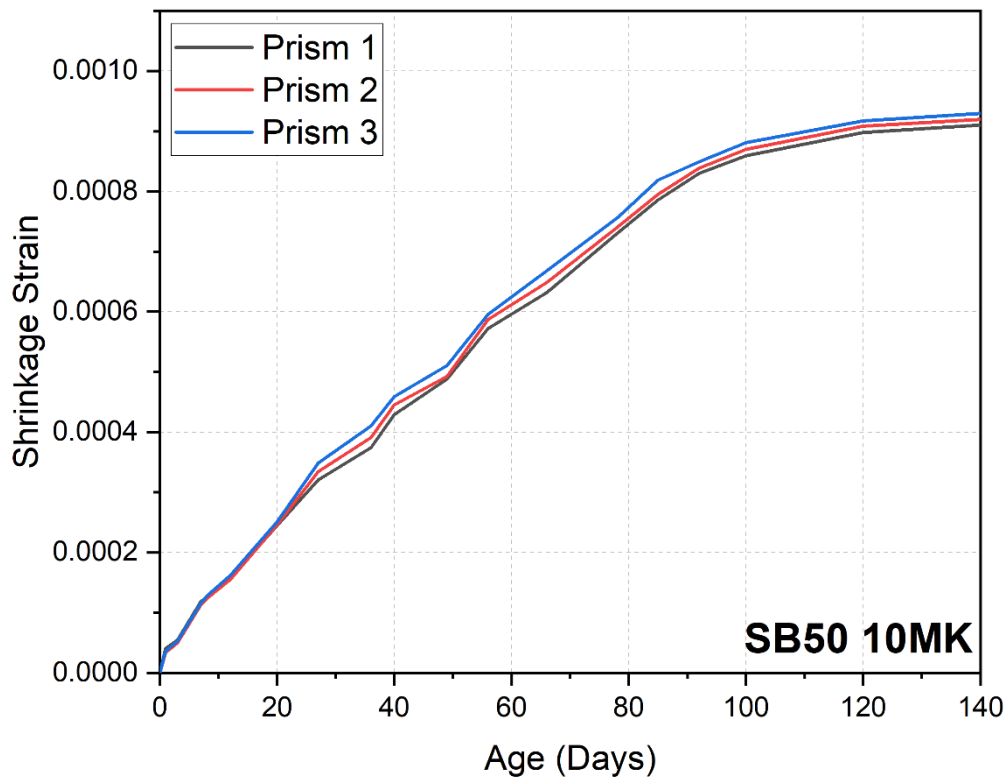


Figure D.2.2-1 - Total Shrinkage Strains SB50 10MK

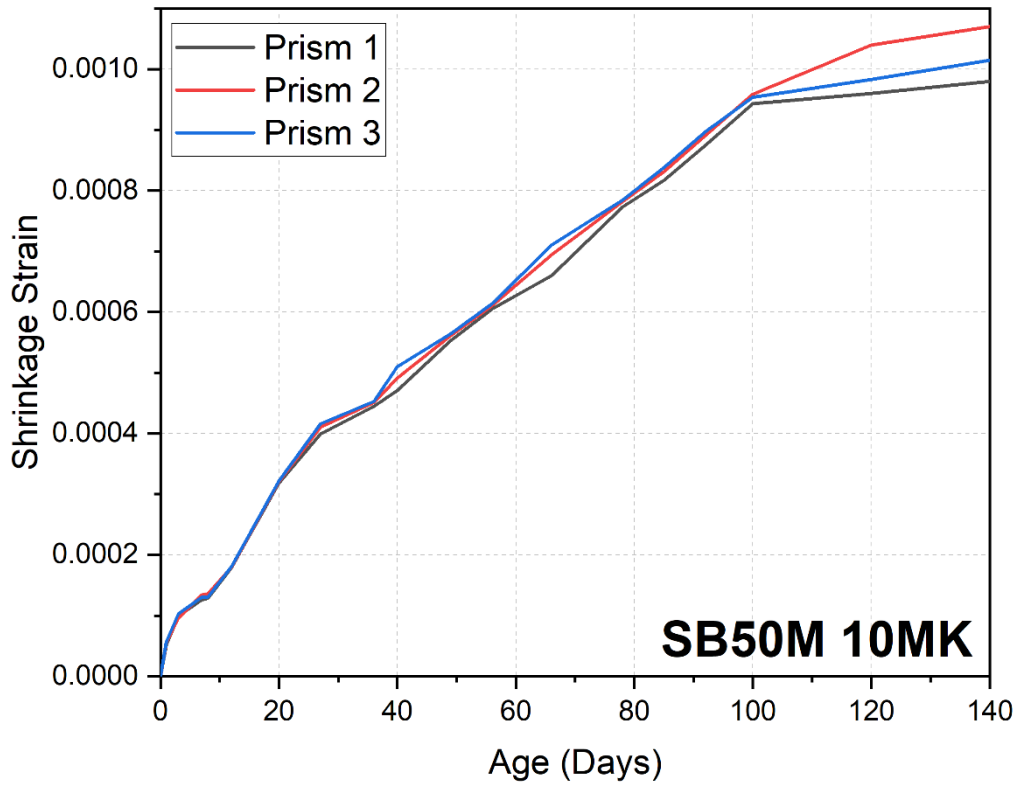


Figure D.2.2-2 - Total Shrinkage Strains SB50M 10MK

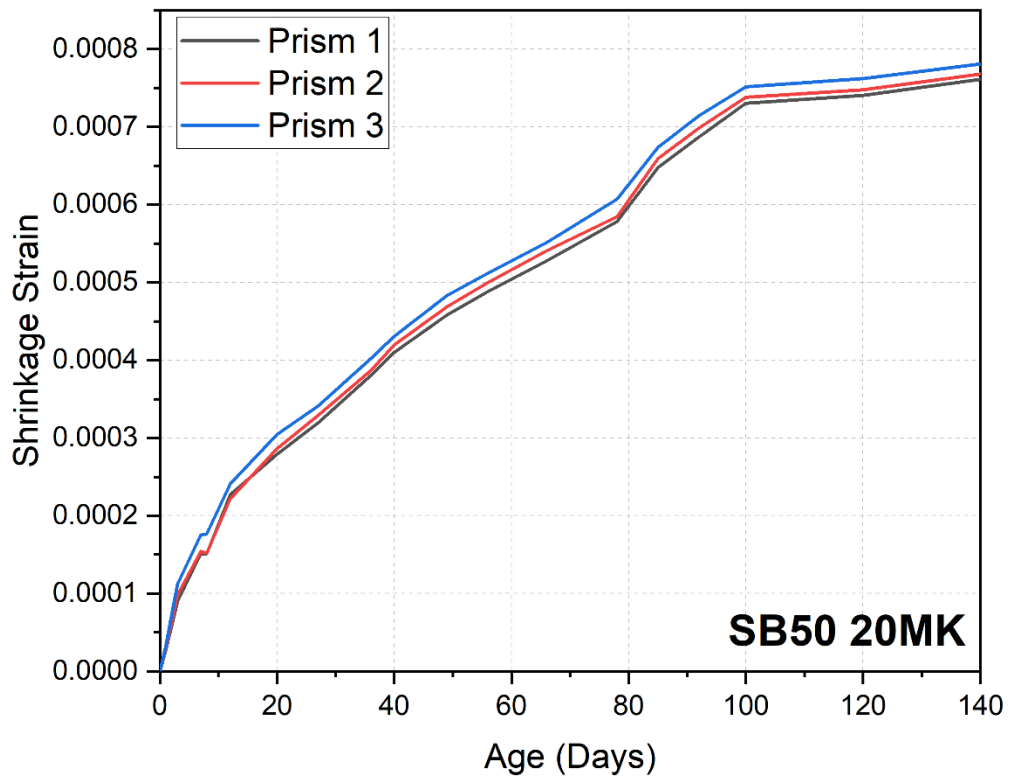


Figure D.2.2-3 - Total Shrinkage Strains SB50 20MK

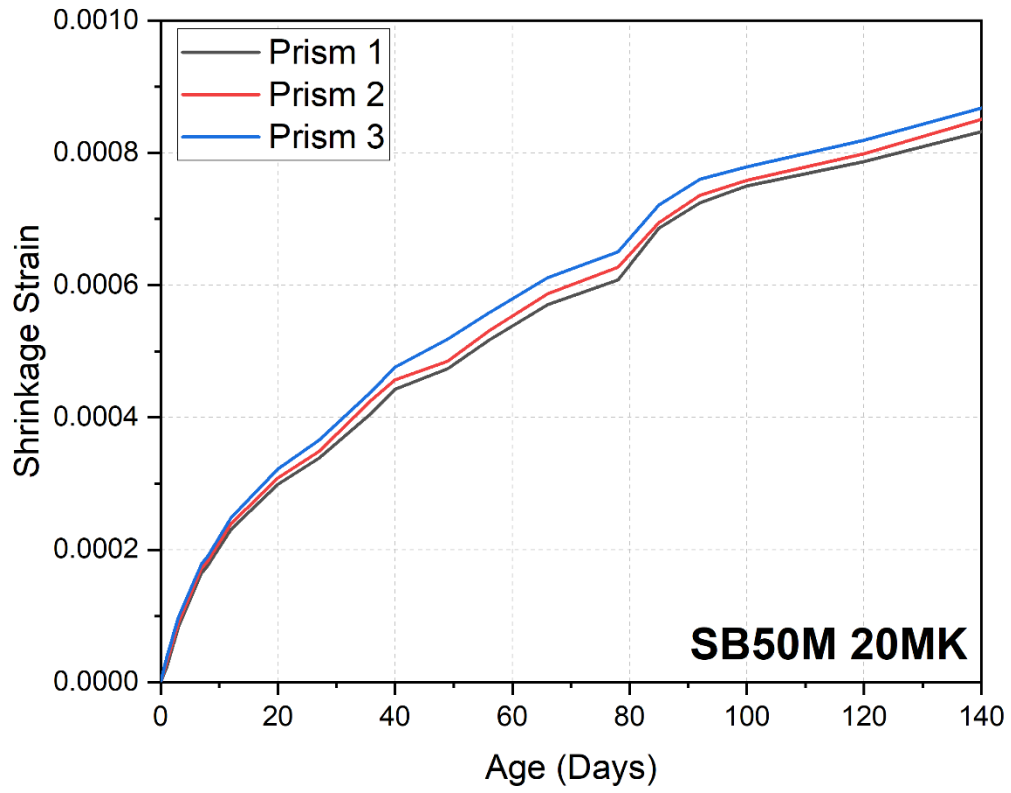


Figure D.2.2-4 - Total Shrinkage Strains SB50M 20MK

D.3 ASR Testing

D.3.1 Raw Data

Table D.3.1-1 – ASR of SB50M

Days	Prism 1	Prism 2	Prism 3	Total Expansion
0	0.00000%	0.00000%	0.00000%	0.00000%
2	0.00337%	0.00551%	0.00571%	0.00444%
5	0.00908%	0.00980%	0.01000%	0.00944%
10	0.02408%	0.02480%	0.02536%	0.02444%
14	0.03122%	0.03265%	0.03321%	0.03194%
19	0.03372%	0.03622%	0.03714%	0.03444%
23	0.03444%	0.03801%	0.03929%	0.03622%
28	0.03801%	0.04158%	0.04250%	0.03980%

Table D.3.1-2 – ASR of SB50M 10MK

Days	Prism 1	Prism 2	Prism 3	Total Expansion
0	0.00000%	0.00000%	0.00000%	0.00000%
2	0.00408%	0.00265%	0.00337%	0.00337%
5	0.00944%	0.00801%	0.00924%	0.00890%
10	0.02122%	0.01872%	0.02158%	0.02051%
14	0.02551%	0.02230%	0.02515%	0.02444%
19	0.02622%	0.02372%	0.02872%	0.02630%
23	0.02908%	0.02765%	0.03087%	0.02922%
28	0.03087%	0.02908%	0.03230%	0.03087%

Table D.3.1-3 – ASR of SB50M 20MK

Days	Prism 1	Prism 2	Prism 3	Total Expansion
0	0.00000%	0.00000%	0.00000%	0.00000%
2	0.00408%	0.00051%	0.00230%	0.00230%
5	0.00587%	0.00230%	0.00408%	0.00408%
10	0.00765%	0.00694%	0.00765%	0.00730%
14	0.01230%	0.00980%	0.01122%	0.01105%
19	0.01265%	0.01087%	0.01158%	0.01158%
23	0.01587%	0.01372%	0.01480%	0.01480%
28	0.01658%	0.01480%	0.01658%	0.01587%

Table D.3.1-4 – ASR of OPC

Days	Prism 1	Prism 2	Prism 3	Total Expansion
0	0.00000%	0.00000%	0.00000%	0.00000%
2	0.00730%	0.00765%	0.00765%	0.00747%
5	0.01372%	0.01480%	0.01444%	0.01444%
10	0.02801%	0.02908%	0.03087%	0.02944%
14	0.05051%	0.05158%	0.05230%	0.05158%
19	0.05337%	0.05408%	0.05515%	0.05408%
23	0.05587%	0.05551%	0.05765%	0.05622%
28	0.06015%	0.06122%	0.06265%	0.06122%

D.3.2 ASR Plots

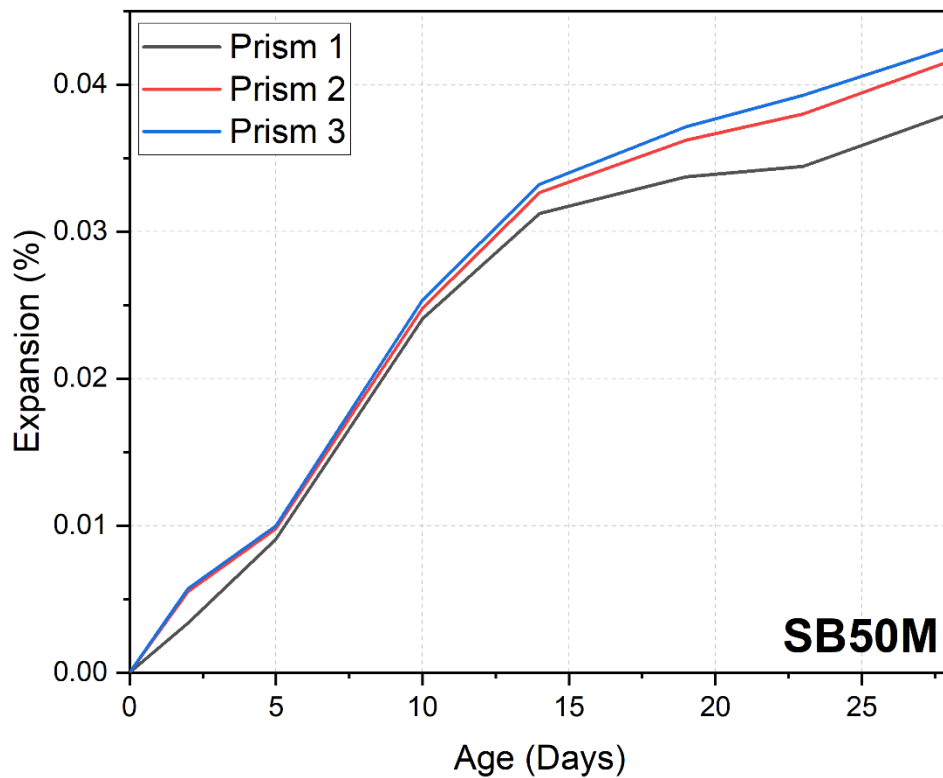


Figure D.3.2-1 – ASR of SB50M

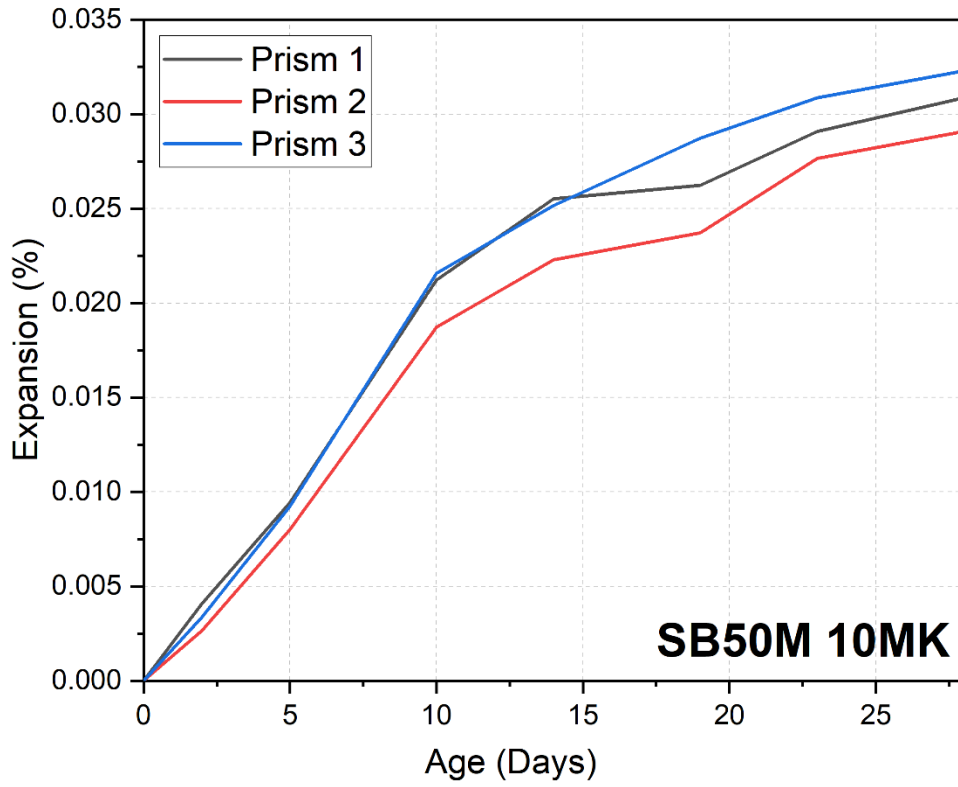


Figure D.3.2-2 - ASR of SB50M 10MK

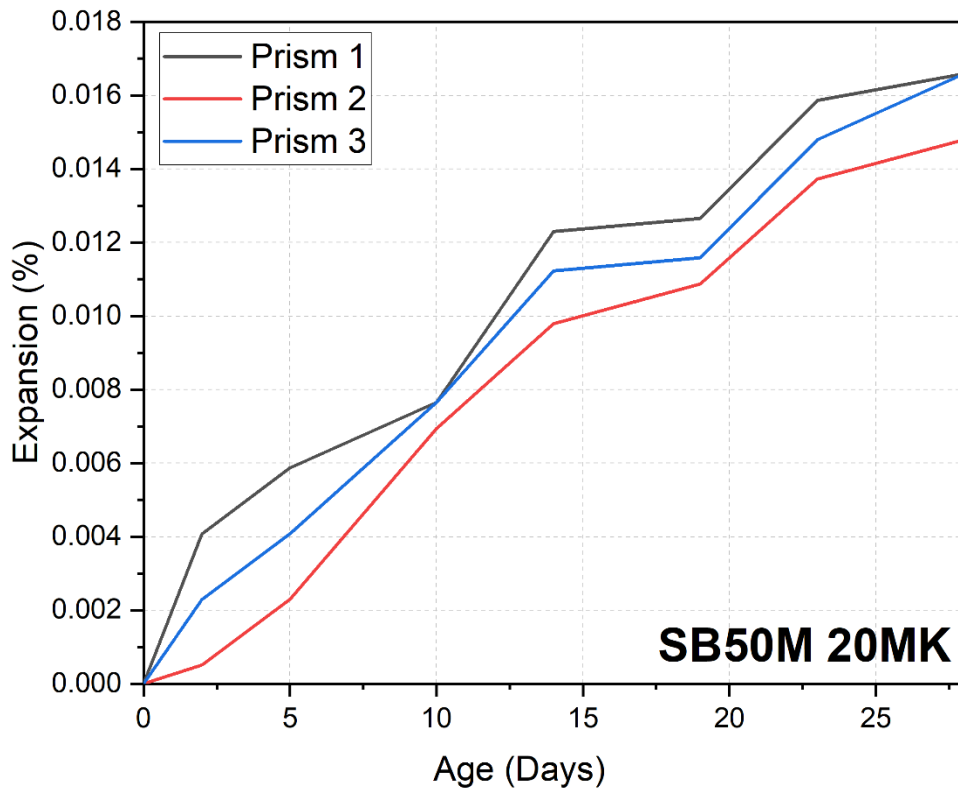


Figure D.3.2-3 - ASR of SB50M 20MK

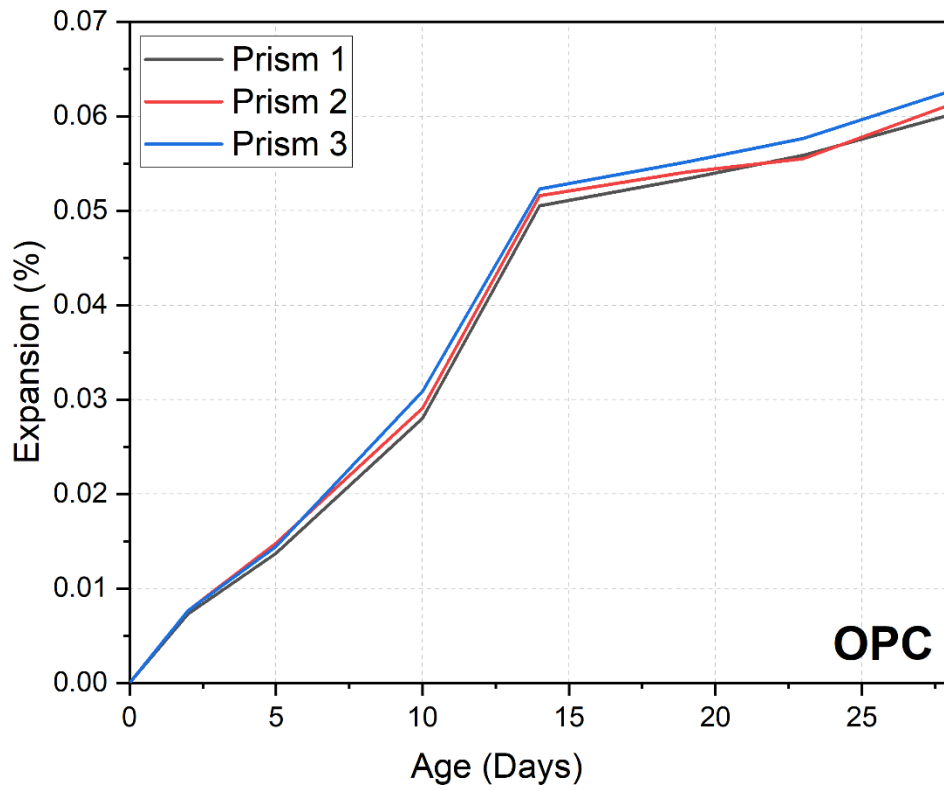


Figure D.3.2-4 ASR of OPC

D.4 Corrosion

D.4.1 Corrosion Images



Figure D.4.1-1 –Prisms exposed to corrosion acceleration



Figure D.4.1-2 – Agglomeration of corroded fibres



Figure D.4.1-3 - SB50M 20MK corrosion after 4 months



Figure D.4.1-4 - Side profile SB50M 10MK (4 month corrosion)



Figure D.4.1-5 – Corrosion of SB50M 20MK



Figure D.4.1-6 – Corrosion of SB50M



Figure D.4.1-7 – Corrosion of SB50M 10MK



Figure D.4.1-8 – Corrosion of OPC



Figure D.4.1-9 – Corrosion of SB50 20MK



Figure D.4.1-10 – Corrosion of SB50 10MK



Figure D.4.1-11 – Corrosion of SB50M



Figure D.4.1-12 – Corrosion of SB50



Figure D.4.1-13 – Samples used in the experiments

D.4.2 Corrosion Compressive Strength Results

Table D.4.2-1 – Compressive Strength of SB50

Code	Age	Load (N)	Compressive Strength (MPa)
SB50 1	4 Months	32067.00	20.04
SB50 2	4 Months	31959.00	19.97
SB50 3	4 Months	32163.00	20.10
Average		32063.00	20.04
St. Deviation		102.06	0.06
SB50 4	8 Months	35640.00	22.28
SB50 5	8 Months	35971.00	22.48
SB50 6	8 Months	34678.00	21.67
Average		35429.67	22.14
St. Deviation		671.67	0.42
SB50 NC 1	No Corrosion	34064.00	21.29
SB50 NC 2	No Corrosion	33897.00	21.14
SB50 NC 3	No Corrosion	33105.00	20.69
Average		33688.67	21.06
St. Deviation		512.32	0.32

Table D.4.2-2 Compressive Strength of SB50M

Code	Age	Load (N)	Compressive Strength (MPa)
SB50M 1	4 Months	42258.00	26.41
SB50M 2	4 Months	42885.00	26.80
SB50M 3	4 Months	42369.00	26.48
Average		42504.00	26.57
St. Deviation		334.59	0.21
SB50M 4	8 Months	48663.00	30.41
SB50M 5	8 Months	49075.00	30.67
SB50M 6	8 Months	49347.00	30.84
Average		49028.33	30.64
St. Deviation		344.38	0.22
SB50M NC 1	No Corrosion	45898.00	28.69
SB50M NC 2	No Corrosion	45362.00	28.35
SB50M NC 3	No Corrosion	46097.00	28.81

Average	45785.67	28.62
St. Deviation	380.16	0.24

Table D.4.2-3 Compressive Strength of SB50 10MK

Code	Age	Load (N)	Compressive Strength (MPa)
SB50 10MK 1	4 Months	43651.00	27.28
SB50 10MK 2	4 Months	43109.00	26.94
SB50 10MK 3	4 Months	43247.00	27.03
Average		43335.67	27.08
St. Deviation		281.67	0.18
SB50 10MK 4	8 Months	46256.00	28.91
SB50 10MK 5	8 Months	47246.00	29.53
SB50 10MK 6	8 Months	48103.00	30.06
Average		47201.67	29.50
St. Deviation		924.30	0.58
SB50 10MK NC 1	No Corrosion	45168.00	28.23
SB50 10MK NC 2	No Corrosion	45791.00	28.62
SB50 10MK NC 3	No Corrosion	45666.00	28.54
Average		45541.67	28.46
St. Deviation		329.59	0.21

Table D.4.2-4 Compressive Strength of SB50M 10MK

Code	Age	Load (N)	Compressive Strength (MPa)
SB50M 10MK 1	4 Months	65373.00	40.86
SB50M 10MK 2	4 Months	65507.00	40.94
SB50M 10MK 3	4 Months	65712.00	41.07
Average		65530.67	40.96
St. Deviation		170.73	0.11
SB50M 10MK 4	8 Months	58478.00	36.55
SB50M 10MK 5	8 Months	58711.00	36.69
SB50M 10MK 6	8 Months	59053.00	36.91
Average		58747.33	36.72
St. Deviation		289.22	0.18
SB50M 10MK NC 1	No Corrosion	61249.00	38.28
SB50M 10MK NC 2	No Corrosion	61753.00	38.60
SB50M 10MK NC 3	No Corrosion	61884.00	38.68
Average		61628.67	38.52
St. Deviation		335.26	0.21

Table D.4.2-5 Compressive Strength of SB50 20MK

Code	Age	Load (N)	Compressive Strength (MPa)
SB50 20MK 1	4 Months	42837.00	26.77
SB50 20MK 2	4 Months	33140.00	20.71
SB50 20MK 3	4 Months	41837.00	26.15
Average		39271.33	26.46
St. Deviation		5333.38	3.33
SB50 20MK 4	8 Months	44989.00	28.12
SB50 20MK 5	8 Months	43687.00	27.30
SB50 20MK 6	8 Months	43715.00	27.32
Average		44130.33	27.58
St. Deviation		743.76	0.46
SB50 20MK NC 1	No Corrosion	43099.00	26.94
SB50 20MK NC 2	No Corrosion	43205.00	27.00
SB50 20MK NC 3	No Corrosion	43401.00	27.13
Average		43235.00	27.02
St. Deviation		153.22	0.10

Table D.4.2-6 Compressive Strength of SB50M 20MK

Code	Age	Load (N)	Compressive Strength (MPa)
SB50M 20MK 1	4 Months	53887.00	33.68
SB50M 20MK 2	4 Months	54213.00	33.88
SB50M 20MK 3	4 Months	54869.00	34.29
Average		54323.00	33.95
St. Deviation		500.16	0.31
SB50M 20MK 4	8 Months	57184.00	35.74
SB50M 20MK 5	8 Months	57347.00	35.84
SB50M 20MK 6	8 Months	57501.00	35.94
Average		57344.00	35.84
St. Deviation		158.52	0.10
SB50M 20MK NC 1	No Corrosion	55866.00	34.92
SB50M 20MK NC 2	No Corrosion	55472.00	34.67
SB50M 20MK NC 3	No Corrosion	56078.00	35.05
Average		55805.33	34.88
St. Deviation		307.52	0.19

Table D.4.2-7 Compressive Strength of OPC

Code	Age	Load (N)	Compressive Strength (MPa)
OPC 1	4 Months	65373.00	40.86
OPC 2	4 Months	65507.00	40.94
OPC 3	4 Months	65712.00	41.07
Average		65530.67	40.96
St. Deviation		170.73	0.11
OPC 4	8 Months	60734.00	37.96
OPC 5	8 Months	61273.00	38.30
OPC 6	8 Months	60206.00	37.63
Average		60737.67	37.96
St. Deviation		533.51	0.33
OPC NC 1	No Corrosion	60159.00	37.60
OPC NC 2	No Corrosion	59437.00	37.15
OPC NC 3	No Corrosion	59811.00	37.38
Average		59802.33	37.38
St. Deviation		361.08	0.23

D.4.3 Corrosion Flexural Strength Results

Table D.4.3-1 - Flexural Strength of SB50

Code	Age	Load (N)	Compressive Strength (MPa)
SB50 1	4 Months	2204.00	2.53
SB50 2	4 Months	2097.00	2.40
SB50 3	4 Months	2307.00	2.64
Average		2202.67	2.52
St. Deviation		105.01	0.12
SB50 4	8 Months	2444.00	2.80
SB50 5	8 Months	2314.00	2.65
SB50 6	8 Months	2350.00	2.69
Average		2369.33	2.71
St. Deviation		67.12	0.08
SB50 NC 1	No Corrosion	1799.00	2.06
SB50 NC 2	No Corrosion	2227.00	2.55
SB50 NC 3	No Corrosion	2301.00	2.64
Average		2109.00	2.59
St. Deviation		271.01	0.31

Table D.4.3-2 - Flexural Strength of SB50M

Code	Age	Load (N)	Compressive Strength (MPa)
SB50M 1	4 Months	2450.00	2.81
SB50M 2	4 Months	2582.00	2.96
SB50M 3	4 Months	2410.00	2.76
Average		2480.67	2.84
St. Deviation		90.01	0.10
SB50M 4	8 Months	2677.00	3.07
SB50M 5	8 Months	2721.00	3.12
SB50M 6	8 Months	2754.00	3.16
Average		2717.33	3.11
St. Deviation		38.63	0.04
SB50M NC 1	No Corrosion	2602.00	2.98
SB50M NC 2	No Corrosion	2539.00	2.91
SB50M NC 3	No Corrosion	2515.00	2.88
Average		2552.00	2.92
St. Deviation		44.93	0.05

Table D.4.3-3 - Flexural Strength of SB50 10MK

Code	Age	Load (N)	Compressive Strength (MPa)
SB50 10MK 1	4 Months	2401.00	2.75
SB50 10MK 2	4 Months	2517.00	2.88
SB50 10MK 3	4 Months	2371.00	2.72
Average		2429.67	2.78
St. Deviation		77.11	0.09
SB50 10MK 4	8 Months	2615.00	3.00
SB50 10MK 5	8 Months	2689.00	3.08
SB50 10MK 6	8 Months	2514.00	2.88
Average		2606.00	2.99
St. Deviation		87.85	0.10
SB50 10MK NC 1	No Corrosion	2492.00	2.86
SB50 10MK NC 2	No Corrosion	2455.00	2.81
SB50 10MK NC 3	No Corrosion	2503.00	2.87
Average		2483.33	2.85
St. Deviation		25.15	0.03

Table D.4.3-4 - Flexural Strength of SB50M 10MK

Code	Age	Load (N)	Compressive Strength (MPa)
SB50M 10MK 1	4 Months	3225.00	3.70
SB50M 10MK 2	4 Months	3316.00	3.80
SB50M 10MK 3	4 Months	3271.00	3.75
Average		3270.67	3.75
St. Deviation		45.50	0.05
SB50M 10MK 4	8 Months	3601.00	4.13
SB50M 10MK 5	8 Months	3645.00	4.18
SB50M 10MK 6	8 Months	3544.00	4.06
Average		3596.67	4.12
St. Deviation		50.64	0.06
SB50M 10MK NC 1	No Corrosion	3443.00	3.95
SB50M 10MK NC 2	No Corrosion	3489.00	4.00
SB50M 10MK NC 3	No Corrosion	3528.00	4.04
Average		3486.67	4.00
St. Deviation		42.55	0.05

Table D.4.3-5 - Flexural Strength of SB50 20MK

Code	Age	Load (N)	Compressive Strength (MPa)
SB50 20MK 1	4 Months	2378.00	2.72
SB50 20MK 2	4 Months	2314.00	2.65
SB50 20MK 3	4 Months	2420.00	2.77
Average		2370.67	2.72
St. Deviation		53.38	0.06
SB50 20MK 4	8 Months	2423.00	2.78
SB50 20MK 5	8 Months	2484.00	2.85
SB50 20MK 6	8 Months	2569.00	2.94
Average		2492.00	2.86
St. Deviation		73.33	0.08
SB50 20MK NC 1	No Corrosion	2411.00	2.76
SB50 20MK NC 2	No Corrosion	2415.00	2.77
SB50 20MK NC 3	No Corrosion	2436.00	2.79
Average		2420.67	2.77
St. Deviation		13.43	0.02

Table D.4.3-6 - Flexural Strength of SB50M 20MK

Code	Age	Load (N)	Compressive Strength (MPa)
SB50M 20MK 1	4 Months	2789.00	3.20
SB50M 20MK 2	4 Months	2712.00	3.11
SB50M 20MK 3	4 Months	2853.00	3.27
Average		2784.67	3.19
St. Deviation		70.60	0.08
SB50M 20MK 4	8 Months	3247.00	3.72
SB50M 20MK 5	8 Months	3155.00	3.62
SB50M 20MK 6	8 Months	3363.00	3.85
Average		3255.00	3.73
St. Deviation		104.23	0.12
SB50M 20MK NC 1	No Corrosion	3130.00	3.59
SB50M 20MK NC 2	No Corrosion	3075.00	3.52
SB50M 20MK NC 3	No Corrosion	3281.00	3.76
Average		3162.00	3.62
St. Deviation		106.66	0.12

Table D.4.3-7 - Flexural Strength of OPC

Code	Age	Load (N)	Compressive Strength (MPa)
OPC 1	4 Months	3127.00	3.58
OPC 2	4 Months	3104.00	3.56
OPC 3	4 Months	3148.00	3.61
Average		3126.33	3.58
St. Deviation		22.01	0.03
OPC 4	8 Months	3322.00	3.81
OPC 5	8 Months	3375.00	3.87
OPC 6	8 Months	3436.00	3.94
Average		3377.67	3.87
St. Deviation		57.05	0.07
OPC NC 1	No Corrosion	3204.00	3.67
OPC NC 2	No Corrosion	3183.00	3.65
OPC NC 3	No Corrosion	3142.00	3.60
Average		3176.33	3.64
St. Deviation		31.53	0.04